

Modeling changes in the global carbon cycle-climate system

Inauguraldissertation

der Philosophisch–naturwissenschaftlichen Fakultät
der Universität Bern

vorgelegt von

Marco Steinacher

aus Basel (BS) und Frutigen (BE)

Leiter der Arbeit:

Prof. Dr. Fortunat Joos

Abteilung für Klima– und Umweltphysik
Physikalisches Institut der Universität Bern

Modeling changes in the global carbon cycle-climate system

Inauguraldissertation

der Philosophisch–naturwissenschaftlichen Fakultät
der Universität Bern

vorgelegt von

Marco Steinacher

aus Basel (BS) und Frutigen (BE)

Leiter der Arbeit:

Prof. Dr. Fortunat Joos

Abteilung für Klima– und Umweltphysik
Physikalisches Institut der Universität Bern

Von der Philosophisch–naturwissenschaftlichen Fakultät angenommen.

Bern, 22. Dezember 2011

Der Dekan

Prof. Dr. Silvio Decurtins

Thesis summary

There is strong evidence that human activities are altering the Earth's climate and biogeochemical cycles. Anthropogenic carbon emissions have increased the concentration of carbon dioxide (CO₂) in the atmosphere by about 40% since preindustrial times. The elevated CO₂ levels are the main drivers of changes in the atmosphere's radiative balance as well as in the ocean's chemistry. This thesis investigates consequences of the anthropogenic interference with the coupled carbon cycle-climate system. A main focus is on the acidification of the oceans caused by the uptake of anthropogenic CO₂. Further, interactions between climate and the carbon cycle are addressed. Numerical simulations with coupled carbon cycle-climate models are used to quantify future changes under several scenarios of CO₂ emissions, land-use change, and other forcings. Such projections are important for assessing potential impacts on ecological and socio-economic systems. Moreover, they provide a basis for developing mitigation and adaptation strategies and contribute to the understanding of the complex carbon cycle-climate system in general.

The introduction in chapter 1 provides an overview of the global carbon cycle with an emphasis on ocean biogeochemistry. Further, important concepts such as radiative forcing, feedbacks, and climate sensitivity are introduced. The influence of human activities, predominantly the emissions of CO₂, is summarized and discussed with respect to ocean acidification and the perturbation of the radiative balance, followed by an overview of the associated changes in climate and feedbacks within the coupled carbon cycle-climate system.

Chapter 2 consists of three publications presenting projections of ocean acidification with a special focus on the Arctic Ocean. The global coupled carbon cycle-climate model NCAR CSM1.4-carbon is applied to simulate ocean acidification for the industrial period and for the two IPCC SRES emission scenarios A2 and B1 (2000–2100). The results support the important finding of earlier studies that the ocean's chemistry is undergoing large and rapid changes in response to anthropogenic carbon emissions with potentially severe impacts on marine ecosystems. Ocean pH and the aragonite saturation state, a key variable governing impacts on calcifying organisms, decrease rapidly on a global scale. In the A2 scenario, water saturated by more than 300%, considered suitable for coral growth, vanishes by 2070 (CO₂ ≈ 630 ppm), and the ocean volume fraction occupied by saturated water decreases globally from 42% to 25% over this century. By extending the simulations from 2100 to 2500 under the assumption that carbon emissions are (unrealistically) reduced to zero in 2100, it is shown that the projected changes in the 21st century are largely irreversible for at least several hundred years.

The Arctic Ocean is identified to be particularly vulnerable with respect to ocean acidification. The largest projected pH changes ($\Delta\text{pH} = -0.45$) worldwide occur in Arctic surface waters. Aragonite undersaturation in the Arctic Ocean is imminent and expected to begin within the next decade for both scenarios. By the time atmospheric CO₂ exceeds 490 ppm (2040 in A2, 2050 in B1), more than half of the Arctic is projected to be undersaturated at the surface. By the end of the twenty-first century and for the A2 case, undersaturation in the Arctic Ocean also occurs with respect to calcite. The main reasons for the vulnerability of the

Arctic Ocean are its naturally low saturation state and that Arctic climate change amplifies the acidification, in contrast to other regions like the Southern Ocean, where no significant interaction of climate change and ocean acidification is found in our simulations. Freshening of surface waters and increased carbon uptake in response to sea ice retreat is projected to amplify the decrease in Arctic mean saturation and pH by more than 20%. The results imply that surface waters in the Arctic Ocean will become corrosive to aragonite, with potentially large implications for the marine ecosystem, if atmospheric CO₂ is not kept below 450 ppm.

In chapter 3, the response of the marine ecosystem productivity to climatic changes under the SRES A2 emission scenario is investigated with four comprehensive global coupled carbon cycle-climate models. The marine biological cycle is an important element of the carbon cycle and climate system, which influences the abundance of atmospheric CO₂. Yet the simulation of primary productivity in general circulation models is a relatively new field and remains challenging. The four models applied here, which include representations of marine ecosystems of different complexity and structure, all show a decrease between 2 and 13% in global mean net primary productivity by 2100. Despite differences in magnitude, a decrease in productivity over the 21st century is a robust result. Reduced nutrient supply to the productive zone in response to a shallower mixed layer depth and slowed circulation is identified as the dominant mechanism in the low- and mid-latitude ocean as well as in the North Atlantic. In parts of the Southern Ocean, on the other hand, an alleviation of light and/or temperature limitation leads to a productivity increase. The results are compared to recent projections relying on an empirical model approach, which suggest a productivity increase, and differences are discussed. Further, a method based on regional model skill metrics is developed to generate weighted multi-model means of projected changes in productivity. The multi-model estimate of the decrease in net primary production by 2100 is -2.9 GtC yr^{-1} (-8%).

In chapter 4, the Bern3D-LPX Earth System Model of Intermediate Complexity is applied to perform a large set of coupled climate-carbon cycle simulations over the last millennium and into the future under different scenarios. At first, the new model setup is presented and the newly implemented land surface albedo model component is described in detail and validated by comparing results with satellite observations. Further, the impact of land-use changes on the surface albedo and radiative forcing is quantified and compared to internal feedbacks. For the future projections, the model is forced as specified by the four representative concentration pathways (RCP), which have been selected for simulations with regard to the next Assessment Report of the IPCC, and their extensions up to 2300. Projections of global warming, steric sea level rise, and ocean acidification are provided and committed changes under different assumptions are quantified. Projected changes in the global mean temperature by 2100 range from 1.8 °C in the low mitigation scenario (RCP3-PD) to 4.6 °C in the high baseline scenario (RCP8.5). Further, changes in the carbon cycle are analyzed and simulations with prescribed CO₂ concentrations (diagnosed emissions) are compared to emission-driven simulations. When prescribing CO₂ emissions, the model simulates significantly higher CO₂ concentrations than specified for the RCP scenarios. This is a consequence of a relatively weak oceanic carbon sink, a considerable effect of land-use induced changes in the terrestrial sink capacity, and losses of carbon from soils. Finally, allowable emissions are quantified in four simulations where global mean temperatures are stabilized at 1.5 to 4 °C.

The impact of climate change mitigation on ocean acidification projections is discussed in chapter 5. A large set of baseline (no climate policy) and mitigation emission scenarios is explored in simulations with the Bern2.5CC and NCAR CSM1.4-carbon models. Emission scenarios provide an indication of the potential effect of mitigation policies but are often idealized and assume that new technologies and climate policies can be introduced over a relatively short period of time, especially in the lowest mitigation scenarios. The physical impacts in terms of ocean acidification are lower in mitigation than baseline scenarios. Early

decisions are required to meet specific mitigation targets. The low scenarios, which result in similar global mean surface carbonate saturation states by 2100 than observed today, depart from the corresponding baseline emissions around 2015–2020. They require socio-political and technical conditions that are very different from those now existing.

Chapter 6 presents a study that investigates the response of the carbon cycle to large changes in ocean circulation. Ensemble simulations with the NCAR CSM1.4-carbon model are forced with freshwater perturbations in the North Atlantic and in the Southern Ocean that lead to reductions of the Atlantic Meridional Overturning Circulation. Changes in the physical climate fields, in turn, affect the land and ocean biogeochemical cycles and cause a variations in the atmospheric CO₂ concentration by up to 20 ppm. The response depends on the location where the freshwater perturbation is applied. In the case of a North Atlantic perturbation, the land biosphere reacts with a strong reduction in carbon stocks and atmospheric CO₂ levels are increased. This response is strongest in the tropical regions due to a shift of the Intertropical Convergence Zone, and can be found most clearly in South America. The results are mainly discussed with respect to abrupt climatic changes in past and they are compared to proxy records. However, the results also have some relevance with respect to anthropogenic climate change. Many models project a reduction in the Atlantic Meridional Overturning Circulation under future scenarios and the simulated responses in the carbon cycle presented here illustrate potential feedback mechanisms.

Finally, an outlook in chapter 7 outlines how the work presented in this thesis will be continued in future studies. In the appendices, the coupling of the Bern3D and LPX models is documented along with several other technical improvements that have been implemented during this thesis.

Contents

Thesis summary	3
1 Introduction	9
1.1 Motivation	9
1.2 The global carbon cycle	9
1.3 Anthropogenic interference with biogeochemical cycles	17
1.4 Changes in the coupled carbon cycle-climate system	18
References	27
2 Arctic ocean acidification	37
2.1 Imminent ocean acidification in the Arctic	37
2.2 Modeling ocean acidification in the Arctic Ocean	59
2.3 Imminent and Irreversible Ocean Acidification	63
3 Projected decrease in marine productivity	67
4 Coupled carbon cycle-climate simulations with Bern3D-LPX	97
4.1 Introduction	97
4.2 Bern3D-LPX model description	97
4.3 Experimental setup	101
4.4 Results	106
4.5 Summary & Conclusions	124
References	127
5 Impact of climate change mitigation on ocean acidification	131
6 Fingerprints of changes in the terrestrial carbon cycle	153
7 Outlook	175
References	178

A	Coupling of the Bern3D and LPX models	179
A.1	Method	179
A.2	Mass-conserving mapping between LPX and Bern3D grids	180
A.3	Coupling LPX and Bern3D surface albedo	183
B	Implementation of new forcings and diagnostics in Bern3D	185
B.1	Sulphate aerosol forcing	185
B.2	Radiative forcing diagnostics	185
B.3	Sea level rise and ocean heat content	186
B.4	Temperature tracking	187
	References	189
C	Parallelization of the LPX model	191
D	Parallelization of the PISCES model	195
E	The Bern3D NetCDF Module	197
	Thanks	205
	Publications	207
	Erklärung gemäss RSL 05	209
	Curriculum vitæ	211

Chapter 1

Introduction

1.1 Motivation

In recent years climate change and the emission of greenhouse gases have been playing an increasingly prominent role in scientific, political, and public debates. This debate is fueled by (i) direct observation of climate change effects such as the rapid decline in Arctic summer sea ice extent (Stroeve et al., 2007), (ii) the growing evidence that human activities have significantly contributed to the observed global warming trend of 0.74 ± 0.18 °C from 1906 to 2005 (Solomon et al., 2007), (iii) the identification of potential negative consequences for ecosystems and society linked to increased atmospheric CO₂ such as ocean acidification (Royal Society, 2005; German Advisory Council on Global Change, 2006) or sea level rise (Anthoff et al., 2006), (iv) the assessment of potential economic costs associated with climate change (Stern, 2006), and (v) the increasing awareness that in view of the world's growing energy demand, policy actions are needed for “the stabilization of greenhouse gas concentrations in the atmosphere that would prevent dangerous anthropogenic interference with the climate system”, as required by the United Nations Framework Convention on Climate Change (United Nations, 1992). As a result, the European Union and several other countries have adopted a global warming limit of 2 °C as a target for mitigation efforts to reduce the risk of negative impacts (Council of the European Union, 2004). Further, certain levels of climate change, ocean acidification, and other global change impacts have been proposed as boundaries that must not be transgressed in order to prevent unacceptable environmental change (Rockström et al., 2009).

Assessing the risk of exceeding such limits and relating observed changes to human activities, such as the emission of greenhouse gases, requires an understanding of the coupled carbon cycle-climate system. An accurate quantification of potential future changes under different scenarios as well as their uncertainties is needed for decision making in politics, economics, and society in general. It provides an important basis of information for developing mitigation and adaptation strategies. This thesis is aimed at contributing to the understanding of the complex carbon cycle-climate system and it provides model projections that quantify potential impacts under future scenarios.

1.2 The global carbon cycle

Carbon is essential to life on Earth and it is found almost everywhere: in the atmosphere, in the oceans, in vegetation and soils on land, and in the Earth's crust. The total carbon inventory can be assumed constant over very long time scales because changes from radioactive processes (Damon & Sternberg, 1989) or due to the thermal escape of carbon from the

atmosphere to space (Tian et al., 2009) are very small. Yet within the earth system, carbon is constantly transformed between different forms and exchanged between reservoirs by many physical, chemical, and biological processes on various time scales (e.g. Field & Raupach, 2004). These processes are collectively referred to as the global carbon cycle.

Most of Earth’s carbon is stored in sediments. Estimates of this pool size are in the order of 60 million GtC¹ (Holmén, 1992). The fluxes from and to this reservoir, however, are relatively small (~ 0.2 GtC yr⁻¹) and therefore only relevant on time scales longer than several hundred years. On time scales up to some hundred years, the global carbon cycle is mainly determined by the exchange of carbon between the terrestrial biosphere, the ocean, and the atmosphere.

The atmosphere is the smallest of those fast-exchanging carbon pools. Atmospheric carbon exists mainly in the form of carbon dioxide (CO₂; more than 99%) and a small amount of methane (CH₄), which both are greenhouse gases. The atmospheric CO₂ concentrations measured in ice cores and ice-firn are in the range 280 ± 10 ppm² for about five thousand years before the industrial revolution (Indermühle et al., 1999). This corresponds to a preindustrial atmospheric carbon inventory of about 590 GtC. The oceans contained about 38 000 GtC and the land biosphere around 2000–3000 GtC by that time (Fig 1.1).

The relatively large gross exchange fluxes between the atmosphere and the ocean and land pools (~ 70 GtC yr⁻¹ and ~ 120 GtC yr⁻¹, respectively) yield mean residence times (inventory divided by flux) of about 3 yr (atmosphere), 20 yr (land), and 550 yr (ocean). Given the nearly constant atmospheric CO₂ concentration for several thousand years before the industrial time, it can be assumed that those three fast-exchanging carbon pools were close to equilibrium in preindustrial times (~ 1750 AD; Siegenthaler & Sarmiento, 1993).

While CO₂ in the atmosphere is relatively well-mixed, carbon is cycled within the oceans and the terrestrial biosphere. The carbon cycle in the ocean is mainly driven by the CO₂ gas-exchange with the atmosphere, physical transport, and biological activity in surface waters. On land, carbon fluxes are largely dominated by photosynthesis, respiration, and the decay of plants. In the following, these processes are explained in more detail.

1.2.1 Carbon cycling in the ocean

Most of the carbon in the ocean, about 98%, is in the form of dissolved inorganic carbon, defined as the sum of dissolved CO₂ gas³ ($\sim 0.5\%$), bicarbonate ions (HCO₃⁻, $\sim 90\%$), and carbonate ions (CO₃²⁻, $\sim 10\%$):

$$\text{DIC} = [\text{CO}_2] + [\text{HCO}_3^-] + [\text{CO}_3^{2-}] \quad (1.1)$$

The remaining 2% is present mainly in the form of dissolved organic matter (DOC; about 700 GtC) and only about 3 GtC is living biomass (Fig. 1.1). Today’s inventory and distribution of carbon in the oceans is relatively well known from several measurement campaigns (Key et al., 2004).

Various biological, chemical, and physical processes cause continuous fluxes of carbon within the ocean. Therefore, carbon is not distributed uniformly in the ocean interior. In the absence of those drivers, one would expect a relatively uniform distribution, similar to that of salinity. Instead, a vertical gradient in the DIC concentration is found with lower concentrations at the surface than at depth (Fig. 1.2). As an important consequence, this results in an increase in the carbon storage capacity of the oceans. If concentrations were higher at the surface, less

¹Gigatons of carbon (10^{12} kg)

²Parts per million; $0.0001\% = 10^{-6}$

³Here, CO₂ also includes carbonic acid, i.e. [CO₂] denotes the sum of [CO_{2(aq)}] and [H₂CO₃]. Square brackets are used to indicate concentrations of chemical species.

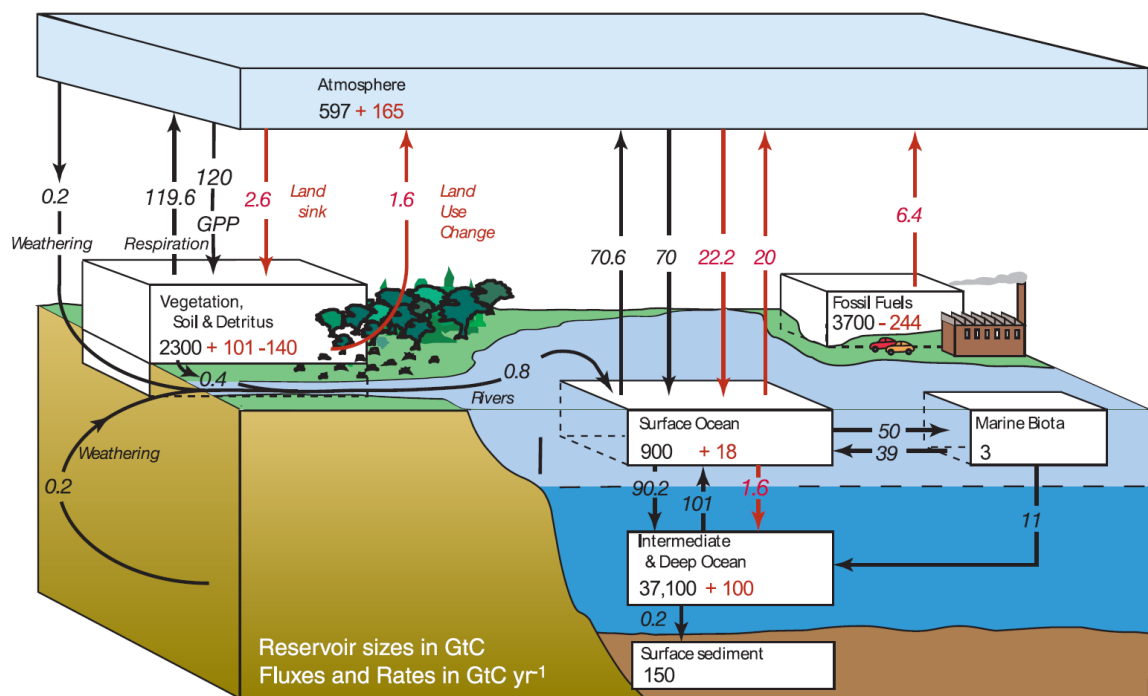


Figure 1.1: The global carbon cycle for the 1990s, showing the main annual fluxes in GtC yr^{-1} . The figure is taken from Denman et al. (2007). Preindustrial ‘natural’ fluxes and reservoir sizes are shown in black, and changes resulting from the anthropogenic perturbation in red. The net terrestrial loss of -39 GtC is inferred from cumulative fossil fuel emissions minus atmospheric increase minus ocean storage. The loss of -140 GtC from the ‘vegetation, soil & detritus’ compartment represents the cumulative emissions from land use change (Houghton, 2003), and requires a terrestrial biosphere sink of 101 GtC . Gross fluxes generally have uncertainties of more than $\pm 20\%$ but fractional amounts have been retained to achieve overall balance when including estimates in fractions of GtC yr^{-1} for riverine transport, weathering, deep ocean burial, etc. ‘GPP’ is annual gross (terrestrial) primary production. Atmospheric carbon content and all cumulative fluxes since 1750 are as of end 1994.

atmospheric CO_2 could enter the ocean and atmospheric CO_2 levels would be significantly higher (Sarmiento & Gruber, 2006). In the following, the drivers leading to this DIC gradient are discussed.

Air-sea gas exchange and physical transport

The unidirectional CO_2 fluxes between atmosphere and ocean are proportional to the partial pressures⁴ of CO_2 ($p\text{CO}_2$) in the atmosphere (air-sea flux) and in the surface ocean (sea-air flux), respectively. The net CO_2 exchange between atmosphere and ocean F_{ao} is determined by the partial pressure difference across the air-sea interface, the CO_2 solubility α , and a gas transfer velocity k_v : $F_{\text{ao}} = k_v \alpha (p\text{CO}_{2,a} - p\text{CO}_{2,o})$. The partial pressure difference can be measured and global syntheses of these data are available (Takahashi et al., 2002). The gas transfer velocity, however, is not easily measured and depends on wind speed, precipitation, sea ice and other factors (Watson & Orr, 2003). Usually, it is parametrized as a function of wind speed (e.g. Wanninkhof, 1992). Global mean gas transfer velocities for CO_2 at 20°C and different parametrization range from 11.2 cm h^{-1} to 20.0 cm h^{-1} (Sarmiento & Gruber, 2006; Müller et al., 2008). In contrast, the CO_2 solubility α is a well known function of temperature and salinity (Weiss, 1974).

⁴Using partial pressure instead of fugacity is a simplification. It assumes an ideal gas behavior of CO_2 , which is not entirely true. In practice, however, the difference is only about 1% (Watson & Orr, 2003).

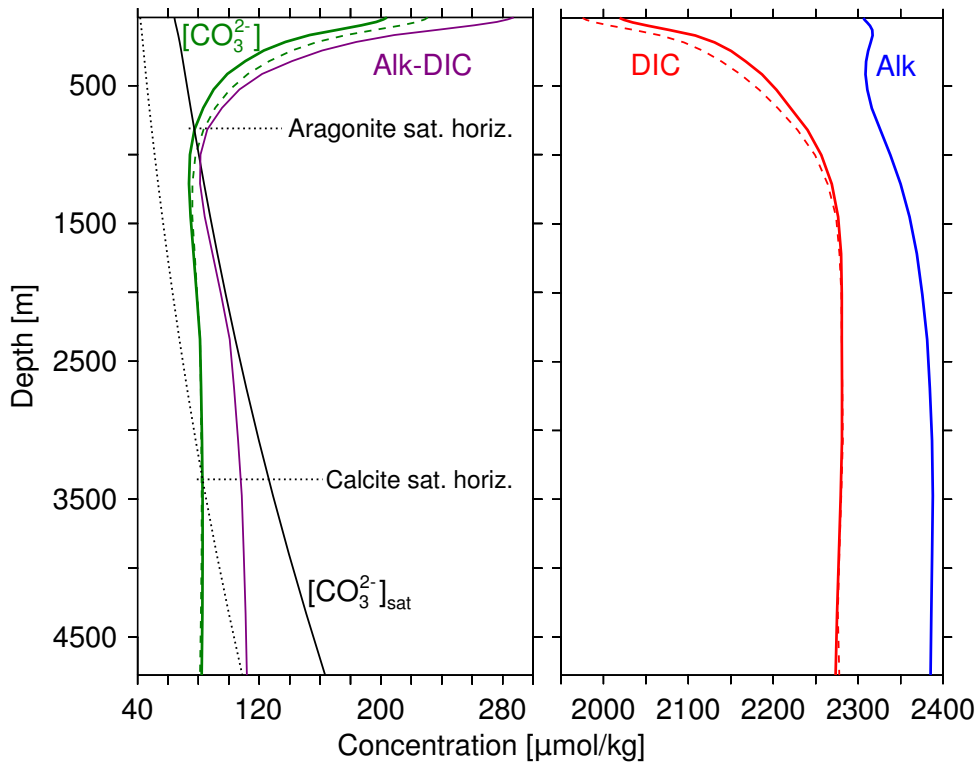
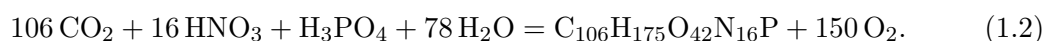


Figure 1.2: Depth profiles of observation-based global mean DIC (red), Alk (blue), and $[\text{CO}_3^{2-}]$ (green) in the ocean. The difference Alk-DIC (purple) is a rough approximation of $[\text{CO}_3^{2-}]$. Dashed lines indicate observation-based estimates of preindustrial DIC and CO_3^{2-} concentrations. The black lines in the left panel show the carbonate ion saturation concentrations $[\text{CO}_3^{2-}]_{\text{sat}}$ for aragonite (solid line) and calcite (dotted line), which depend on temperature, salinity, and pressure (depth). Horizontal lines indicate the corresponding saturation horizons, i.e. where $[\text{CO}_3^{2-}] = [\text{CO}_3^{2-}]_{\text{sat}}$. Please note that global mean values are shown here as an illustration. Saturation horizon depths vary considerably between different locations and ocean basins. $[\text{CO}_3^{2-}]$ and $[\text{CO}_3^{2-}]_{\text{sat}}$ are calculated from Alk, DIC, temperature, salinity, phosphate, and silicate as described in chapter 2. DIC and Alk data are from GLODAP and represent values around 1995 (Key et al., 2004), the other variables are from the World Ocean Atlas 2001 (Conkright et al., 2002). Preindustrial DIC estimates are obtained by subtracting observation-based estimates of anthropogenic DIC (Key et al., 2004) from the present-day data. For the calculation of preindustrial $[\text{CO}_3]$, present-day values were assumed for all variables except DIC.

CO_2 is more soluble in colder waters, resulting in elevated surface DIC concentrations at high latitudes. Deep water formation, the main driver of the thermohaline circulation (e.g. Stocker et al., 1992), also takes place at high latitudes, where surface waters become denser due to lower temperatures and higher salinity. Consequently, DIC-enriched waters are transported to the ocean interior. This ‘solubility pump’ accounts for about 10% of the vertical preindustrial DIC gradient found in the ocean (Sarmiento & Gruber, 2006).

Production and export of organic matter

In the sunlit surface ocean (the euphotic zone), inorganic materials are converted into organic matter by phytoplankton via oxygenic photosynthesis. By that process, which is called primary production (PP), CO_2 is fixed together with other nutrients in organic compounds. Based on ratios between carbon, nitrogen, and phosphorus found in sea water and also in samples of plankton (Redfield et al., 1963), PP can be summarized as



The primary production is limited by temperature, the available energy in the form of light, and the disposability of nutrients such as phosphate (PO_4^{3-}), nitrate (NO_3^-), or iron. The organic carbon that remains after subtracting the costs of all other metabolic processes by the phytoplankton themselves, is called net primary production (NPP; Lindeman, 1942). NPP is an important quantity because it represents the total flux of carbon that is fixed in organic matter and becomes available to heterotrophs.

The quantification of global NPP in the oceans is difficult. Local measurements with radiocarbon-methods together with phytoplankton pigment analyses have been used to calibrate models that estimate NPP from satellite images of ocean color (used as a proxy for chlorophyll concentrations), sea surface temperatures, and solar irradiance (Falkowski et al., 2003; Behrenfeld & Falkowski, 1997). The resulting estimates of global ocean NPP range from 30 to 70 GtC yr^{-1} (Carr et al., 2006), which is comparable to satellite-based estimates of terrestrial NPP (56 GtC yr^{-1} ; Field et al., 1998).

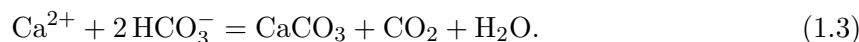
A large part of the organic matter produced in the euphotic zone is regenerated by heterotrophic respiration within the surface ocean. Yet some fraction of the primary producers and heterotrophs sinks below a certain gradient and cannot ascend back into the euphotic zone (Falkowski et al., 2003). Most of this organic matter is then respired by microbes in the ocean interior and only a small part sinks to the ground, where it is remineralized or buried in the sediments. The carbon flux leaving the production zone is called export production (EP). It removes carbon from the upper layers of the water column, thereby reducing $p\text{CO}_2$ in the surface ocean and in the atmosphere compared to a dead ocean. This mechanism is also known as the ‘soft tissue pump’ and is responsible for about 70% of the vertical DIC gradient in the ocean (Sarmiento & Gruber, 2006).

Like NPP, the global export production is not easy to estimate. Particle interceptor traps and radioactive tracers have been used to estimate local EP from the downward flux of particulate organic matter (Falkowski et al., 2003). By combining models with observational data, Laws et al. (2000) and Schlitzer (2000) estimated global EP around 11 GtC yr^{-1} .

CaCO_3 production

Apart from organic matter, some marine organisms also produce inorganic compounds such as opal⁵ or carbonate minerals. Most important for the carbon cycle is the production of calcium carbonate (CaCO_3), which occurs mostly in the form of calcite and aragonite. Aragonite has a different crystal structure and is less stable than calcite.

CaCO_3 in the ocean is mainly produced by three groups of marine organisms: Coccolithophorids, a phytoplankton group that form an outer sphere of calcite plates; foraminifera, amoebas that form calcite skeletons; and pteropods, a group of mollusks that produce aragonite crystals (Sarmiento & Gruber, 2006). The production of CaCO_3 (calcification) can be summarized as a reaction of calcium and bicarbonate ions:



This equation takes into account that the production of CaCO_3 from calcium (Ca^{2+}) and carbonate (CO_3^{2-}) ions also leads to the dissociation of HCO_3^- , which produces CO_2 (c.f. next section). Calcification therefore increases surface $p\text{CO}_2$ and the air-sea CO_2 flux is reduced, whereas the production of organic matter decreases surface $p\text{CO}_2$. Yet both processes reduce surface DIC by fixing carbon in compounds.

Most of the produced CaCO_3 is exported from the surface to deeper ocean layers. The global production and export of CaCO_3 is in the order of 1 GtC yr^{-1} (Sarmiento et al., 2002;

⁵Opal is an amorphous form of silica ($\text{SiO}_2 \cdot n(\text{H}_2\text{O})$).

Milliman et al., 1999) and contributes the remaining $\sim 20\%$ to the vertical DIC gradient (Sarmiento & Gruber, 2006). The dissolution of the exported CaCO_3 is an abiotic process driven by thermodynamics and depends on the saturation state of the water with respect to the corresponding mineral form of CaCO_3 (c.f. Fig. 1.2 and next section). Compared to organic carbon, CaCO_3 is generally exported to lower depths and a significant fraction reaches the ocean sediments. The mineral carbonates in the sediments provide a buffer mechanism against changes in alkalinity on longer time scales in the order of 10 000 yr (e.g. Archer, 2005; Tschumi et al., 2011).

Inorganic carbonate chemistry

The ratios between the three different species of DIC (CO_2 , HCO_3^- , and CO_3^{2-} ; Eq. 1.1) depend on the dissociation constants of carbonic acid, which are temperature, salinity, and pressure dependent (Millero, 1995):

$$K_1 = \frac{[\text{H}^+][\text{HCO}_3^-]}{[\text{CO}_2]}, K_2 = \frac{[\text{H}^+][\text{CO}_3^{2-}]}{[\text{HCO}_3^-]} \quad (1.4)$$

When the concentration of one of the DIC species changes, a new equilibrium is attained rapidly. As a result, the concentration of free protons, $[\text{H}^+]$, increases or decreases, which can be measured as change in pH^6 . The chemical speciation of DIC for a specific temperature, salinity, and pressure can therefore be expressed as non-linear functions of pH (Fig. 1.3).

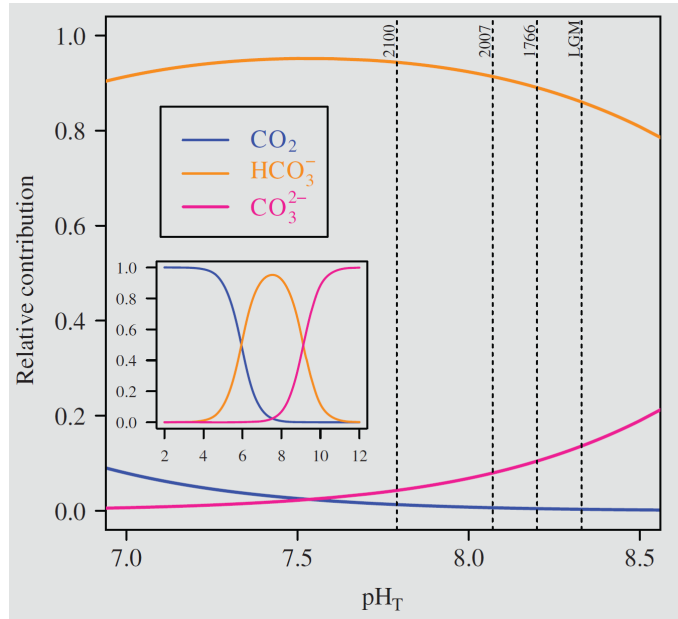


Figure 1.3: Bjerrum plot showing the relative contributions of carbon dioxide (CO_2), bicarbonate (HCO_3^-), and carbonate (CO_3^{2-}) to the dissolved inorganic carbon as a function of pH at 15°C and a salinity of 35. The figure is taken from Gattuso & Hansson (2011). K_1 and K_2 were calculated according to Lueker et al. (2000). The dashed vertical lines indicate the estimated average open-ocean surface pH during the Last Glacial Maximum (LGM), 1766, 2007, and 2100 (Gattuso & Lavigne, 2009). The projected value for 2100 is based on the IPCC SRES A2 emission scenario (c.f. Chap. 2; Plattner et al., 2001).

If, for example, ocean surface $[\text{CO}_2]$ increases due to gas exchange with the atmosphere, a part of it dissociates in order to maintain the equilibrium K_1 , and thus $[\text{H}^+]$ and $[\text{HCO}_3^-]$ are increased. This, in turn, changes the fraction K_2 , and HCO_3^- ions combine with H^+ to

⁶ $\text{pH} \approx -\log([\text{H}^+])$

re-establish the equilibrium. The net effect (in typical surface seawater) is an increase in $[\text{CO}_2]$ and $[\text{HCO}_3^-]$, while $[\text{CO}_3^{2-}]$ and pH decrease.

A quantity which is related to pH and the chemical speciation of DIC is total alkalinity, defined as

$$\text{Alk} = [\text{HCO}_3^-] + 2[\text{CO}_3^{2-}] + [\text{B}(\text{OH})_4^-] + [\text{OH}^-] - [\text{H}^+] + \text{minor compounds}. \quad (1.5)$$

Alkalinity is a measure of the charge balance in seawater (bases vs. acids) and can experimentally be determined by titration.

DIC and Alk can be used to describe the carbonate system state approximately. The advantage of using the quantities DIC and Alk is that both are conserved with respect to the chemical speciation of DIC (pH), and thus are temperature, salinity, and pressure independent (Sarmiento & Gruber, 2006). This property is particularly helpful if DIC and Alk are used as tracers in circulation models. Because HCO_3^- and CO_3^{2-} typically account for more than 90% of Alk in the ocean, the difference $\text{Alk} - \text{DIC}$ is a rough approximation of $[\text{CO}_3^{2-}]$ (Fig. 1.2). The uptake of atmospheric CO_2 , for example, increases DIC but does not change Alk, and consequently $[\text{CO}_3^{2-}]$ decreases. The production of 1 mol CaCO_3 reduces Alk by 2 mol and DIC by 1 mol, resulting in a reduction of pH and an increase in $p\text{CO}_2$.

The carbonate ion concentration is an important quantity for two reasons. First, calcifying organisms require a certain minimum concentration to be able to produce CaCO_3 (c.f. Sec. 1.4.2). Secondly, the vertical CO_3^{2-} profile determines the depth at which CaCO_3 starts to dissolve in the water column or from sediments (Fig. 1.2). CaCO_3 dissolves when $[\text{CO}_3^{2-}]$ is lower than the carbonate ion concentration in equilibrium with mineral CaCO_3 ($[\text{CO}_3^{2-}]_{\text{sat}}$). $[\text{CO}_3^{2-}]_{\text{sat}}$ is higher for aragonite than for the more stable calcite and further depends on temperature, salinity, and pressure, and thus increases with depth. The transition from over- to undersaturation (where $[\text{CO}_3^{2-}] = [\text{CO}_3^{2-}]_{\text{sat}}$) is called saturation horizon.

The carbonate saturation state is defined as

$$\Omega = \frac{[\text{Ca}^{2+}][\text{CO}_3^{2-}]}{K'_{\text{sp}}}, \quad (1.6)$$

where the $K'_{\text{sp}} = [\text{Ca}^{2+}]_{\text{sat}}[\text{CO}_3^{2-}]_{\text{sat}}$ is the solubility product of CaCO_3 (defined either for calcite or for aragonite; Mucci, 1983). Since $[\text{Ca}^{2+}]$ is linearly related to salinity it is nearly constant and the following approximate relationship can be obtained: $[\text{CO}_3^{2-}] \approx \Omega [\text{CO}_3^{2-}]_{\text{sat}}$.

1.2.2 Carbon on land

Most of the carbon in the preindustrial terrestrial biosphere is stored in soils and a smaller amount in the living vegetation (around 650 GtC). The terrestrial carbon stock is not as well known as the atmospheric and ocean inventories. Due to the relatively homogeneous distribution of carbon in the atmosphere and (to a lesser extent) in the ocean, local measurements can be extrapolated to get estimates of the global inventory. This is much more difficult on land because of large variations in soil and vegetation carbon content on small scales. By extending local soil measurements to a global map, a global soil carbon content of about 1500 GtC is estimated for the top soil layer of 1 m (Global Soil Data Task Group, 2000). About 70% of the soils have a carbon density of 5–15 kg m^{-2} , but values range up to 80 kg m^{-2} , mainly at high northern latitudes (Fig. 1.4). Due to the depth limit of 1 m, the contribution of peatlands and permafrost-affected soils is likely underestimated in this data set. Tarnocai et al. (2009) estimated that the northern permafrost region contains approximately 1670 Gt of organic carbon and Yu et al. (2010) quantified the global amount of carbon

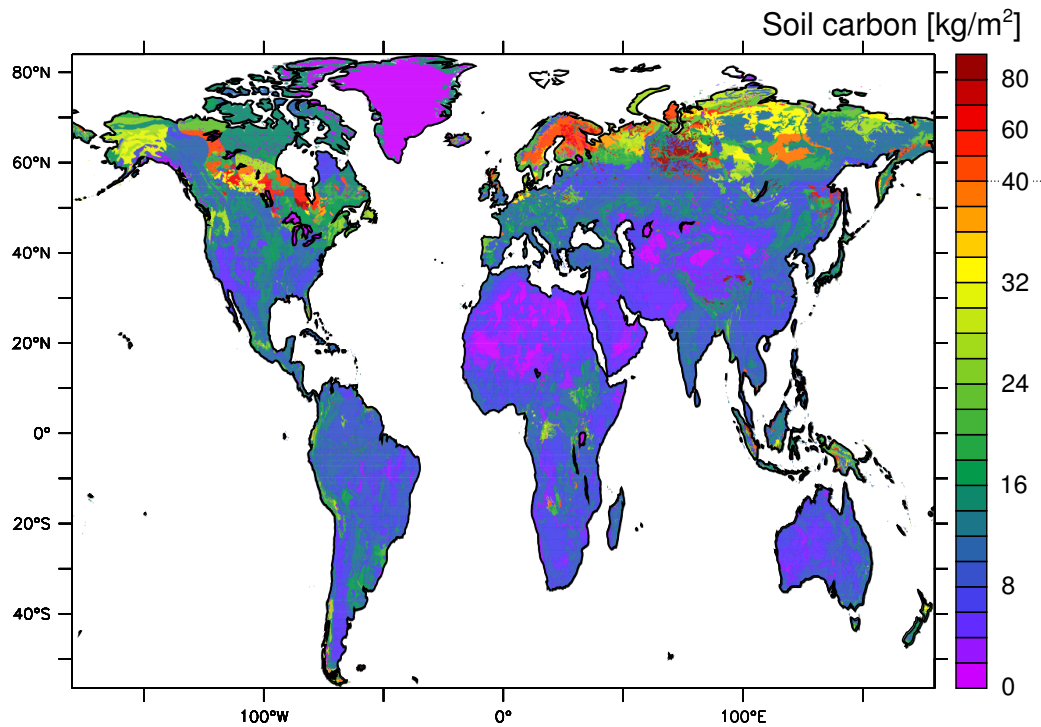


Figure 1.4: Observation-based estimates of soil carbon density in the top 1 m soil layer from the International Geosphere-Biosphere Programme’s Data and Information System (IGBP-DIS; Global Soil Data Task Group, 2000). Please note that the color scale is compressed at the high end from 40 to 85 kg m⁻².

stored in peatlands in the range of 500–700 GtC, with most of it in the boreal and subarctic zone (~90%).

The terrestrial biosphere exchanges large amounts of carbon with the atmosphere. The preindustrial gross fluxes are about 70% larger than those between ocean and atmosphere (Fig. 1.1). Atmospheric CO₂ is taken up by plants and fixed in organic compounds through photosynthesis. This carbon flux, referred to as gross primary production (GPP), is estimated at 123±8 GtC yr⁻¹ (Beer et al., 2010). A large part of GPP is lost from the ecosystem as autotrophic respiration associated with the costs for growth and maintenance of foliage, wood, and roots. The remaining net primary production (NPP) ranges from ca. 270 gC m⁻² yr⁻¹ (~30% of GPP) for evergreen boreal-humid biomes to ca. 850 gC m⁻² yr⁻¹ (~20% of GPP) for tropical-humid biomes (Luysaert et al., 2007). A global annual terrestrial NPP of 56 GtC yr⁻¹ (~45% of GPP) has been estimated by Field et al. (1998) based on satellite images and a NPP model.

The carbon incorporated in vegetation has a lifetime from years (foliage, fine roots) to centuries (old wood). Eventually, dead organic material is transferred to litter- and/or soil-carbon pools and subjected to decomposition by microbial activity (heterotrophic respiration). Typical turnover times range from years for litter pools (Matthews, 1997) to several hundred years for slow soil carbon pools (Gaudinski et al., 2000; Trumbore, 2000). The decomposition rates are linked to soil temperature and moisture (Bond-Lamberty & Thomson, 2010; Mahecha et al., 2010; Trumbore, 2000) and explain the high carbon content in some boreal soils.

The net CO₂ flux between the atmosphere and terrestrial ecosystems is largely determined by the difference between production and respiration, often denoted as net ecosystem production (NEP). There are, however, other fluxes that contribute to the total atmosphere-land carbon flux, e.g. from disturbances such as fires. It depends on the exact definition of NEP whether

those fluxes are also included or treated separately (Randerson et al., 2002).

1.3 Anthropogenic interference with biogeochemical cycles and the environment

Industrialization, the agricultural revolution, and medical advances have led to a rapid increase in the human population from about 1 billion in 1800 to estimated 7 billion in 2011 (United Nations, 2011). This increase is paralleled by a growing demand for energy, food, water, and other resources. To meet these demands, human activities have increasingly interfered with the environment and biogeochemical cycles.

Fossil fuels, at first coal and later also oil and natural gas, have become the primary energy source. By the extraction and combustion of fossil fuels, carbon that was stored in sediments, and thus subducted from the fast exchanging atmosphere-ocean-land system for million of years, is brought to the surface and released to the atmosphere. The burning of fossil fuel produces mainly CO_2 but also other pollutants such as nitrous oxide (N_2O), sulfur dioxide (SO_2), or volatile organic compounds (VOCs). Total carbon emissions for the period 1750 to 2008 from gaseous (14%), liquid (38%), and solid (45%) fossil fuels as well as from cement production and gas flaring (3%) are estimated at 315 GtC (Boden et al., 2011). Currently, CO_2 from fossil fuels is emitted at a rate of about 8.7 GtC yr^{-1} (1.3 t yr^{-1} per capita; Fig. 1.5). Apart from fossil fuel combustion, various industrial processes and biomass burning (e.g. Ito & Penner, 2005) release greenhouse gases, aerosols, synthetic chemicals, or other elements to the environment.

Increased food production, forestry, and urbanization have transformed the land surface significantly. Between one-third and one-half of the land surface has been transformed by human action (Vitousek et al., 1997). CO_2 emissions due to land-use changes, mostly from the conversion of natural vegetation to cropland and pastures, are estimated at 156 GtC for the period 1850 to 2000 (Houghton, 2003), which corresponds to about 55% of the fossil fuel emissions in the same period (286 GtC; Marland et al., 2008). Estimates of the annual fluxes during the 1980s and 1990s are 2.0 and 2.2 GtC yr^{-1} , respectively, dominated by the release of carbon from the tropics (Houghton, 2003). Estimating carbon emissions from land-use change is challenging. Estimates for tropical deforestation vary greatly and are sensitive to land-cover dynamics such as forest regrowth and successive clearing of secondary forest (Ramankutty et al., 2007).

Transformations of the land surface for agricultural or other uses can also change the albedo (diffuse reflectivity) of the Earth's surface. This has some consequences for the radiative balance because a larger (or smaller) fraction of the solar radiation is reflected by the land surface (Betts, 2000; Myhre et al., 2005).

Artificial nitrogen fertilizers are increasingly used to enhance food production. Those nitrogen additions affect the nitrogen cycle with far-reaching consequences, ranging from eutrophication of fresh waters and coastal zones to increased emissions of the potent greenhouse gas N_2O (Canfield et al., 2010) and ocean acidification (Doney et al., 2007). Further, the altered nitrogen cycle is expected to interact with other biogeochemical cycles, particularly with the carbon cycle, which may affect the ability of the earth system to absorb anthropogenic CO_2 in a positive or negative direction (Gruber & Galloway, 2008).

Human activities interfere in many other ways with the Earth's ecosystems, which are less important to the focus of this thesis. Those include, for example, alterations to river systems for providing freshwater to agriculture, over exploitation of fisheries, or chemical pollution by plastics, heavy metals, insecticides and the like (e.g. Rockström et al., 2009).

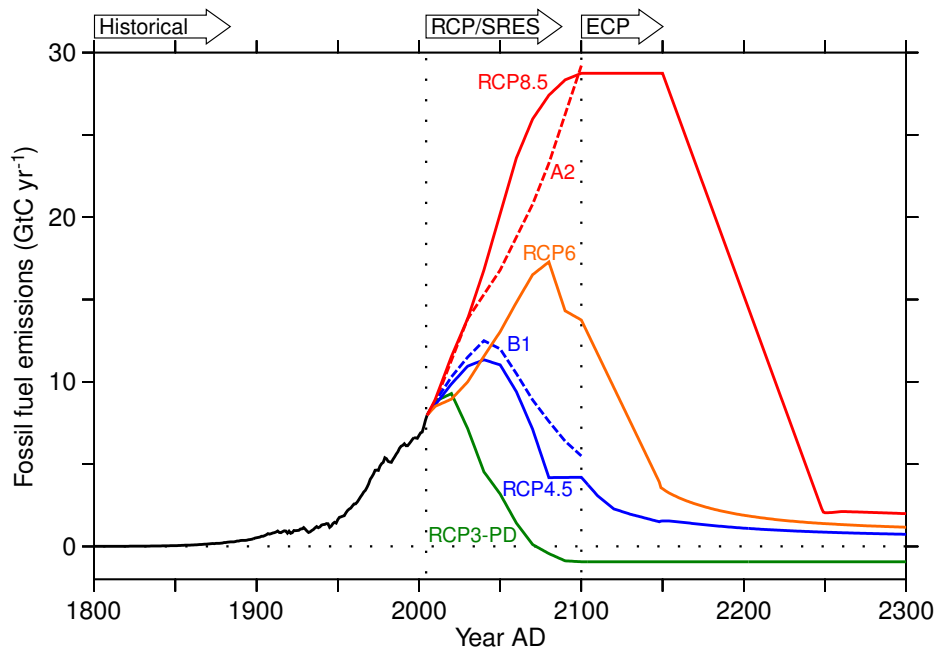


Figure 1.5: Historical fossil fuel CO₂ emissions (black line, 1800-2005; Marland et al., 2008) and several scenarios of future emissions. Solid lines show the emissions corresponding to the four Representative Concentration Pathways which have been selected for model experiments with regard to the next IPCC Assessment Report (AR5; Moss et al., 2010; van Vuuren et al., 2011), namely RCP8.5 (red), RCP6 (orange), RCP4.5 (blue), and RCP3-PD/2.6 (green). After 2100, the RCPs have been extended to 2300 (ECPs) for long term simulations (Meinshausen et al., 2011). The dashed lines show two of the SRES scenarios (2000-2100; Nakićenović et al., 2000), i.e. A2 (red) and B1 (blue), that have been used for the previous IPCC Assessment Report (AR4; Solomon et al., 2007). The SRES scenarios have been used for the simulations presented in chapters 2 and 3, while the future projections in chapter 4 are based on the extended RCP scenarios. In chapter 5, a wide range of scenarios (including SRES and RCPs) are used and described in more detail.

1.4 Changes in the coupled carbon cycle-climate system

1.4.1 Elevated atmospheric CO₂ and climate change

Anthropogenic emissions from fossil fuel burning and land-use change cause atmospheric CO₂ to rise. CO₂ concentrations have increased since preindustrial times by about 40% (110 ppm) to 389 ppm in 2010 (Conway & Tans, 2011). This is far above the natural range reconstructed for the last 800 000 years (Lüthi et al., 2008), and the 20th century increase in CO₂ occurred more than an order of magnitude faster than any sustained change during at least the past 22 000 years (Joos & Spahni, 2008). This has several implications for the carbon cycle and the climate system.

First, CO₂ is a greenhouse gas (GHG) and therefore affects the radiative balance between incoming shortwave radiation from the sun and the outgoing longwave (heat) radiation. Greenhouse gases absorb longwave radiation and re-emit it in all directions. By that process, the radiative flux which leaves the atmosphere into space is reduced. The effect is an increase in the near-surface temperature of the Earth until a new equilibrium between incoming and outgoing radiation is reached. This warming is the main driver of anthropogenic climate change and may have a wide range of consequences, such as sea level rise (Chap. 4; Domingues et al., 2008; Gregory & Huybrechts, 2006), a decrease of the thermohaline circulation, changed precipitation patterns, or the melting of sea-ice, ice sheets, and glaciers (Meehl et al., 2007). Those changes in turn may significantly affect ecosystems, biodiversity, and society (Parry et al., 2007).

The second major implication of elevated atmospheric CO₂ levels is an imbalance in the global carbon cycle, which was close to equilibrium at preindustrial times (Sec. 1.2). The excess CO₂ causes a net carbon flux from the atmosphere to the ocean and land carbon pools (Fig. 1.1). The oceanic uptake is driven by the imbalance of *p*CO₂ across the air-sea interface and increases DIC in surface waters. This leads to an acidification of the oceans (Chap. 2 and 5), with potentially negative effects for marine ecosystems.

Moreover, climate change is expected to influence the efficiency of the terrestrial and oceanic carbon sinks in absorbing anthropogenic CO₂ (Chap. 3 and 4). This in turn will affect the evolution of the atmospheric CO₂ concentrations and hence provides a feedback to climate change (climate-carbon cycle feedback).

In the following, first the mechanisms and effects of ocean acidification are discussed. Then an overview of changes in the Earth's radiative balance is given with a special focus on surface albedo changes. Finally, interactions and feedbacks in the coupled carbon cycle-climate system are discussed.

1.4.2 Ocean acidification

The uptake of anthropogenic CO₂ by the ocean changes its fundamental chemistry through well-understood reactions (Revelle & Suess, 1957; Broecker & Takahashi, 1966; Millero, 1979). The dissolution of CO₂ in seawater forms carbonic acid, which dissociates producing hydrogen ions. A large part of the hydrogen ions combine with carbonate ions (CO₃²⁻) to form bicarbonate (HCO₃²⁻), which causes a shift in the chemical speciation of DIC (see section 1.2.1 for more details). The net effect is a decrease in pH and carbonate ion concentrations. This process is called ocean acidification (Caldeira & Wickett, 2003; Orr et al., 2005).

The CaCO₃ saturation state, defined as

$$\Omega = \frac{[\text{Ca}^{2+}][\text{CO}_3^{2-}]}{K'_{\text{sp}}}, \quad (1.7)$$

has turned out to be a key variable for assessing biological impacts of ocean acidification (Gattuso et al., 1998; Kleypas et al., 2006; Doney et al., 2009). The solubility product K'_{sp} is either defined for calcite (Ω_{calc}) or the less stable mineral form aragonite (Ω_{arag}), and it is temperature, salinity, and pressure dependent (Mucci, 1983). Since $[\text{Ca}^{2+}]$ is linearly related to salinity it is nearly constant and changes in Ω are dominated by changes in $[\text{CO}_3^{2-}]$ and K'_{sp} . In undersaturated waters ($\Omega < 1$), CaCO₃ starts to dissolve (see also Sec. 1.2.1).

The decrease in surface pH, $[\text{CO}_3^{2-}]$, and Ω over the last 25 years is documented with accurate measurements. In the central North Pacific, at station ALOHA, where DIC and Alk is measured since 1989 and in situ pH for about half of that period, a declining long-term trend in pH of $-0.0019 \pm 0.0002 \text{ yr}^{-1}$ has been found (Fig. 1.6; Dore et al., 2009). Similarly, trends of $-0.0017 \pm 0.0003 \text{ yr}^{-1}$ and $-0.0018 \pm 0.0003 \text{ yr}^{-1}$ have been found at stations in the North Atlantic (BATS; Bates, 2007), and near the Canary Islands (ESTOC; González-Dávila et al., 2010), respectively. Global mean pH and Ω can be estimated from DIC and Alk measurements (Chap. 2). Further, observation-based estimates of anthropogenic DIC in the ocean (Key et al., 2004) allow the estimation of preindustrial values (Fig. 1.2; Orr et al., 2005). By using that method, a decline of 0.08 in global mean surface pH from 8.18 (preindustrial, 278 ppm atmospheric CO₂) to 8.10 (1994, 360 ppm) is estimated (Orr, 2011). Global annual mean Ω_{arag} has decreased by about -0.4 over the same period. Those estimates are largely compatible with model simulations (Chap. 2 and 4).

Large changes in pH and Ω are projected for future CO₂ emission scenarios (Caldeira & Wickett, 2003; Orr et al., 2005; Cao et al., 2007; McNeil & Matear, 2007; Gangstø et al.,

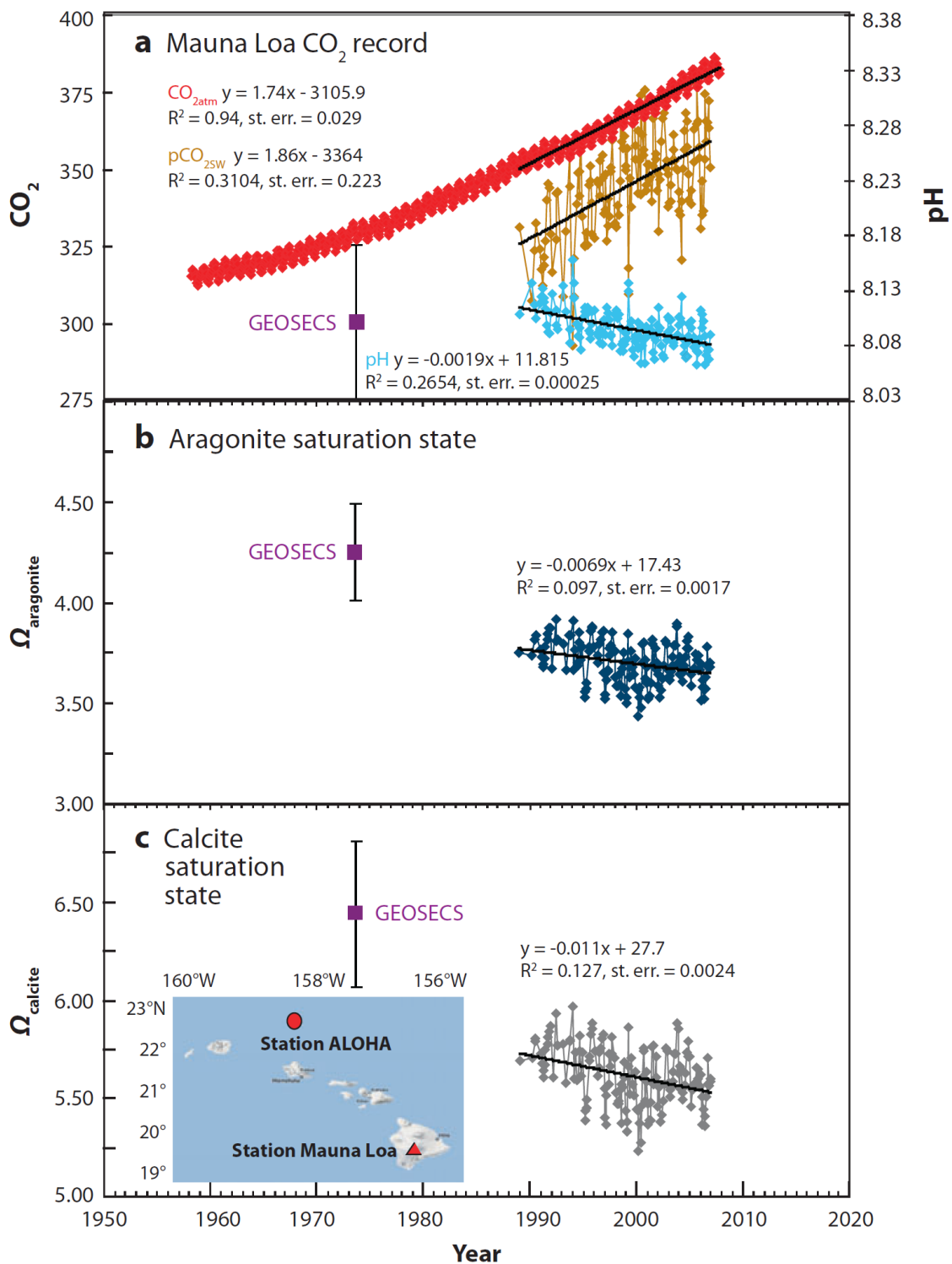


Figure 1.6: Time series of (a) atmospheric CO₂ (red; ppmv) at Mauna Loa (Conway & Tans, 2011), surface ocean pH (cyan), and pCO₂ (tan; μatm) at Ocean Station ALOHA in the subtropical North Pacific Ocean; and (b) aragonite saturation (dark blue) and (c) calcite saturation (gray) at Station ALOHA (Dore et al., 2009). The figure is taken from Doney et al. (2009). Note that the increase in oceanic CO₂ over the past 17 years is consistent with the atmospheric increase within the statistical limits of the measurements. Geochemical Ocean Section Study (GEOSECS) data are from a station near Station ALOHA collected in 1973 (Takahashi et al., 1980).

2008), which are largely irreversible on human timescales (Frölicher & Joos, 2010). In chapter 2, projections with the carbon cycle-climate model of the National Center for Atmospheric Research (NCAR CSM1.4-carbon) are discussed with a special focus on the Arctic Ocean. The Arctic Ocean, which already has a low saturation state (Jutterström & Anderson, 2005), currently takes up atmospheric CO₂ in the order of 0.07 to 0.20 GtCyr⁻¹ (Bates & Mathis, 2009), and thus is an important CO₂ sink. At the same time, polar amplification enhances the warming in the Arctic (Moritz et al., 2002; Serreze & Barry, 2011), sea ice is declining at a faster rate than expected (Stroeve et al., 2007), and surface waters experience substantial freshening (McPhee et al., 2009). The combination of these processes is likely to make the Arctic Ocean particularly vulnerable to ocean acidification (Chap. 2; Yamamoto-Kawai et al., 2011). Undersaturation of surface waters has been observed in the Canada Basin of the Arctic Ocean in 2008 (Yamamoto-Kawai et al., 2009) and more recently in the Bering Sea (Mathis et al., 2011). Those undersaturated areas are expected to become more widespread as atmospheric CO₂ levels increase.

The Southern Ocean and coastal upwelling systems are other regions that are fragile with respect to aragonite undersaturation. Like the Arctic Ocean, the Southern Ocean has a naturally low saturation state due to cold temperatures (Orr et al., 2005). Further, a large seasonal amplitude with an intense wintertime minimum in [CO₃²⁻] is observed. In combination with increased anthropogenic DIC, this could lead to seasonal aragonite undersaturation when anthropogenic CO₂ levels reach about 450 ppm (McNeil & Matear, 2008). In coastal upwelling systems, subsurface waters with a low saturation state are brought to the surface. The upwelling of waters which are increasingly enriched in anthropogenic DIC further decreases the saturation state at the surface and can lead to extended undersaturation. This has been observed (Feely et al., 2008) and simulated (Hauri et al., 2009) in the California Current System.

It has to be noted that despite the fact that the mentioned regions are particularly vulnerable to undersaturation at the surface, ocean acidification is a global phenomenon with large changes on the global scale. In the tropics, for example, a strong decrease in the surface saturation state is projected which could affect coral reefs. Further, as anthropogenic DIC invades the ocean interior, the saturation horizon, separating under- and oversaturated waters, starts to rise and the volume of undersaturated water increases globally (Chap. 2 and 5).

Ocean acidification poses a threat to marine organisms, ecosystem functions, and biodiversity (Fabry et al., 2008; Doney et al., 2009; Gattuso & Hansson, 2011) and may even impact fishery revenues (Cooley & Doney, 2009). Ocean warming and hypoxia are likely to amplify those impacts (Brewer & Peltzer, 2009; Poertner, 2008). The response of calcifying organisms to altered seawater carbonate chemistry has been investigated in many studies. Potentially dramatic responses have been found for corals (Gattuso et al., 1998; Langdon et al., 2000; Marubini et al., 2003), coral reef communities (Leclercq et al., 2000; Langdon, 2002), and planktonic organisms (Riebesell et al., 2000). The shells of pteropods, the major planktonic producers of aragonite, were shown to dissolve rapidly under undersaturated conditions with respect to aragonite (Orr et al., 2005; Fabry et al., 2008). Pteropods densities are high in polar and subpolar regions for which aragonite undersaturation is projected to occur first. Pteropods are an important part of the food-web and changes in their abundance could have severe consequences for the whole food chain up to higher levels. Yet several studies indicate a complicated nature of calcification responses by different organisms and the degree of sensitivity varies among species (Fabry, 2008; Doney et al., 2009). Further, studies exist only for a limited number of species and more research is clearly needed (Gattuso et al., 2009).

Climate mitigation actions that are aimed at reducing atmospheric CO₂ also help to mitigate

ocean acidification. This is discussed in chapter 5 by examining a large set of mitigation and non-mitigation scenarios for the 21st century. A common finding of several studies is that atmospheric CO₂ should be kept at or below ~ 450 ppm to avoid the risk of potentially severe implications for marine ecosystems (Chap. 2; McNeil & Matear, 2008). A stringent reduction in carbon emissions over the coming decades is required to reach this target (Chap. 5; Bernie et al., 2010).

1.4.3 Changes in the radiative balance

Radiative forcing and feedbacks

Climate and life on Earth is driven by energy fluxes along gradients. The primary energy source is the shortwave radiation from the hot sun, which is partially absorbed by the Earth, thereby heating its surface. The elevated surface temperature in turn causes a flux of longwave (heat) radiation back to the cold space. To maintain an equilibrium state, the incoming and outgoing radiation must be equal. While the amount of incoming radiation is mainly given by the solar activity (Delaygue & Bard, 2011) and Earth's orbit around the sun (Berger, 1978), many factors affect the amount of outgoing radiation. The reflectivity (albedo) of the Earth's surface and the amount of clouds, for example, largely determine how much of the shortwave radiation is reflected back to space. Greenhouse gases in the atmosphere control the amount of outgoing longwave radiation to a large extent by cascaded absorption and re-emission in all directions.

An imbalance between in- and outgoing radiation can be quantified as radiative forcing (Forster et al., 2007). The term 'forcing' refers to an external boundary condition for the climate system, such as the elevated atmospheric CO₂ concentrations as a result of anthropogenic emissions. Many other factors affect the radiative balance and can be of natural or anthropogenic origin. Major natural radiative forcings are changes in the total solar irradiance due to changes in the sun's activity, changes in Earth's orbit (orbital forcing), or stratospheric aerosols from volcanic eruptions (e.g. Schmidt et al., 2011). The main anthropogenic radiative forcing agents are long-lived greenhouse gases, ozone, surface albedo changes, and aerosols (Fig. 1.7).

CO₂ is the most important anthropogenic greenhouse gas for two reasons. First, it causes a radiative forcing that is larger than the forcing of all other GHGs (Fig. 1.7). The radiative forcing of a GHG is determined by its excess concentration and radiative efficiency. CO₂ has a much lower radiative efficiency than methane (CH₄, 26 times more potent) and nitrous oxide (N₂O, 216 times more potent) but CO₂ emissions are much higher, which results in a stronger forcing (Forster et al., 2007). Secondly, the lifetime of anthropogenic CO₂ in the atmosphere is very long. It is a chemically stable molecule and removed from the atmosphere only by oceanic or terrestrial uptake (Sec. 1.2), which is a slow process due to the equilibration time of the ocean in the order of several hundred to thousand of years.

In response to a radiative forcing, the climate system must react to restore the energy balance, resulting in changes of the near-surface temperature and other properties of the climate system. These changes in turn may again affect the radiative balance. Such changes in the radiative balance are termed 'feedbacks', rather than 'forcings'. The difference is that 'forcing' means an external influence that pushes the system into a new state. In contrast, a feedback is an internal mechanism of the system that will not change its steady state in the absence of external forcings. Such a feedback is, for example, the increase in atmospheric water vapor content in response to a warming. Because water vapor is a greenhouse gas, the original warming is amplified by the additional water vapor, thereby creating a positive feedback. Feedbacks are important mechanisms that often lead to complex non-linear responses of a

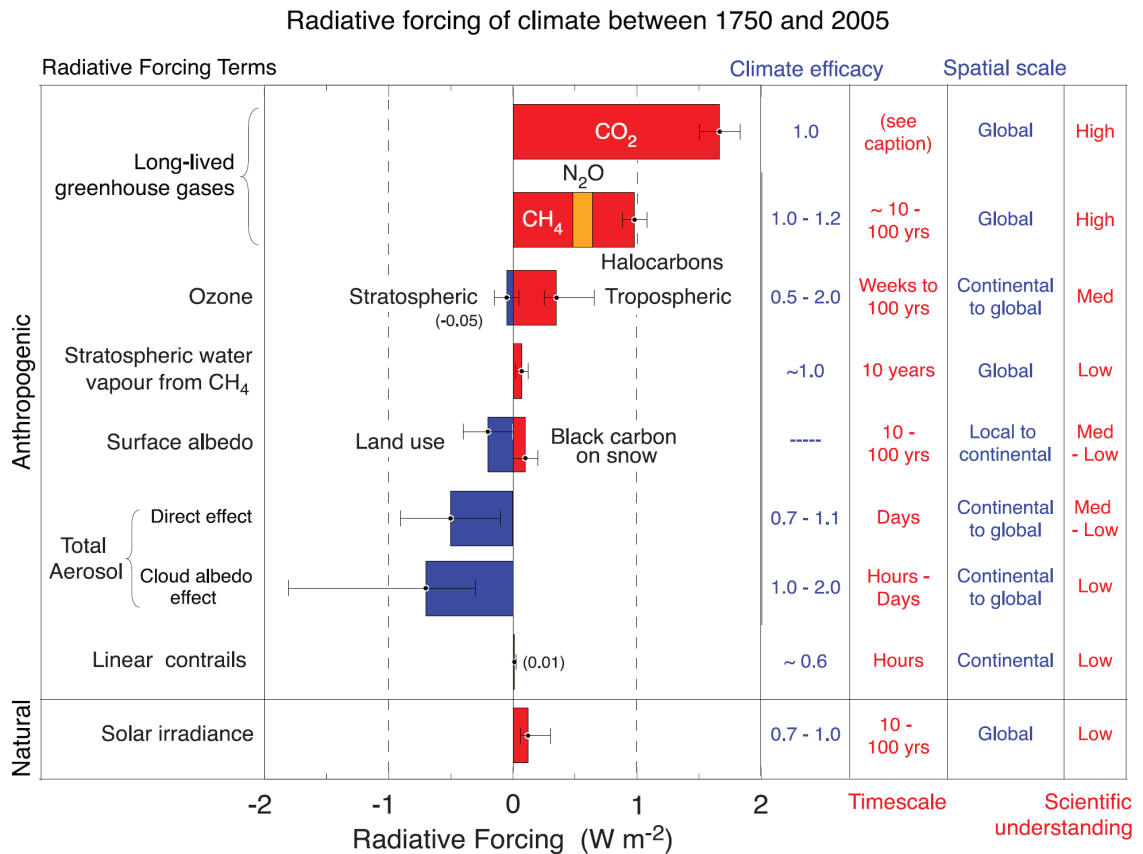


Figure 1.7: Global mean radiative forcings of the main agents between 1750 and 2005. The figure is taken from Forster et al. (2007). Anthropogenic forcings and the natural direct solar forcing are shown. Columns indicate other characteristics of the radiative forcing; efficacies (ratio of the climate sensitivity for a given agent to the climate sensitivity of CO₂) are not used to modify the radiative forcings shown. Time scales represent the length of time that a given forcing term would persist in the atmosphere after the associated emissions and changes ceased. No CO₂ time scale is given, as its removal from the atmosphere involves a range of processes that can span long time scales, and thus cannot be expressed accurately with a narrow range of lifetime values.

system through amplification or attenuation of initial changes. Therefore they are also a main reason for uncertainties when predicting system responses (Roe, 2009).

Surface albedo changes

Changes in the radiative balance in response to surface albedo changes can arise from both anthropogenic forcing or internal feedbacks. Simulated changes in albedo and radiative forcing with the Bern3D-LPX model are discussed in Chapter 4. Land-use changes alter the land surface by converting natural vegetation to agricultural land. This generally increases the surface albedo, mainly because of the much higher albedo of snow-covered non-forested areas than of forested regions (snow-masking effect; Betts, 2000), but also because the albedo of crops and pastures tend to be higher than that of forests (Myhre et al., 2005; Tian et al., 2004). Estimates of this negative forcing with respect to preindustrial times were found to be in the range from 0 to $-0.4 W m^{-2}$ with a best estimate at $-0.2 W m^{-2}$ (Fig. 1.7; Forster et al., 2007). The estimates are very sensitive to the assumed surface albedo for cropland (Myhre & Myhre, 2003). Myhre et al. (2005) estimated a smaller forcing of $-0.09 W m^{-2}$ (since pre-agricultural times) than earlier studies due to a lower albedo for crops and by using the present surface albedo from satellite data as limits on the pre-agricultural surface

albedo.

Surface albedo changes in response to climate change provide a feedback mechanism. In contrast to the generally negative forcing from land-use change, this feedback tends to be positive. Higher temperatures are expected to decrease the extent of the winter snow cover, resulting in a lower albedo, possibly contributing to Arctic amplification (Serreze & Barry, 2011; Serreze & Francis, 2006; Holland & Bitz, 2003). In addition to this mechanism, changes in climate may also lead to shifts in vegetation. As for anthropogenic land-use change, such changes could alter the surface albedo due to the snow-masking effect or because the foliage albedo of the new vegetation is different. Otto et al. (2011) investigated the contribution of forest expansion due to higher spring temperatures in the mid-Holocene and they found a relatively strong sensitivity of the warming to the strength of the snow-masking effect.

Climate sensitivity

The change in surface temperature per unit of radiative forcing is called climate sensitivity. It is often expressed as temperature change for a doubling of preindustrial atmospheric CO_2 , equivalent to a radiative forcing of about 3.71 W m^{-2} (Myhre et al., 1998). Due to uncertainties in the magnitude of feedback processes, the climate sensitivity is only weakly constrained. For example, it is not well understood how cloud cover and cloud properties change with increasing temperatures. Despite strong efforts in climate modeling and more available observational data, the uncertainty in climate sensitivity has not substantially decreased over the last two decades. In the Fourth Assessment Report (AR4) of the Intergovernmental Panel on Climate Change (IPCC) a likely range for climate sensitivity of 2-4.5 K has been estimated (Meehl et al., 2007). A more recent study found that climate sensitivities below 2.9 K are unlikely, while values larger than 4.5 K could not be excluded (Huber et al., 2011). Further, reconstructions of past radiative forcing and Last Glacial Maximum cooling suggest a range between 1.4 and 5.2 K, with a most likely value around 2.4 K, while values above 6 K are difficult to reconcile with the reconstructions (Koehler et al., 2010).

1.4.4 Carbon cycle dynamics and feedbacks

As already mentioned above, the imbalance in the carbon cycle caused by anthropogenic CO_2 emissions lead to net carbon fluxes from the atmosphere to the land and ocean pools (Fig. 1.1). In the ocean, this increases the DIC concentrations at the surface. Over time, anthropogenic DIC invades the ocean and the concentrations in the intermediate and deep ocean are increased as well. Eventually, a new equilibrium will be attained, but this is a slow process, mainly due to the relatively slow transport of DIC to the deep ocean. Depending on the initial magnitude of the imbalance and the effective strength of the oceanic and terrestrial carbon sinks, this can take hundred to thousands of years (Archer, 2005; Plattner et al., 2008; Frölicher & Joos, 2010). The evolution of atmospheric CO_2 for given emissions thus depends critically on the uptake of anthropogenic carbon by ocean and land (Chap. 4). Consequently, the quantification of the strength of these sinks in the past, present, and future is an important research question.

Since the net anthropogenic CO_2 fluxes are relatively small compared to the total gross fluxes between the reservoirs (Fig. 1.1), the quantification of the present sink fluxes is not easy. An oceanic carbon sink of $1.9 \pm 0.7 \text{ GtC yr}^{-1}$ to $2.2 \pm 0.3 \text{ GtC yr}^{-1}$ has been estimated with several data- and model-based methods for the 1990s (Le Quéré et al., 2003; Mikaloff Fletcher et al., 2006; Gruber et al., 2009). Canadell et al. (2007) estimated mean sink fluxes of $2.2 \pm 0.4 \text{ GtC yr}^{-1}$ (ocean), $2.8 \pm 0.7 \text{ GtC yr}^{-1}$ (land), and $4.1 \pm 0.04 \text{ GtC yr}^{-1}$ (atmosphere) for the period 2000-2006. By estimating land-use and fossil-fuel emissions, the global carbon

budget can be closed, which reduces the uncertainty in the combined land and ocean sink strength of $5.0 \pm 0.6 \text{ GtC yr}^{-1}$.

Estimates of the strength of natural sinks and sources in the recent past (Canadell et al., 2007; Bond-Lamberty & Thomson, 2010), reconstructions of past temperatures and CO_2 (Frank et al., 2010), and many models (Joos et al., 2001; Fung et al., 2005; Jones et al., 2006; Matthews, 2006; Friedlingstein et al., 2006; Plattner et al., 2008) suggest a considerable response of the carbon cycle to climate change. Most results indicate a positive feedback, i.e. that climate warming reduces the efficiency of the natural sinks to remove anthropogenic carbon from the atmosphere, resulting in an increase in the airborne fraction of anthropogenic CO_2 . Yet the estimated feedback strengths vary considerably and there are significant uncertainties associated with these feedbacks, which result in substantial uncertainties in carbon cycle-climate projections, particularly for high emissions scenarios and long-term projections (Friedlingstein et al., 2006; Plattner et al., 2008).

Several feedback mechanisms can affect the ability of the ocean to absorb anthropogenic CO_2 . The warming of the surface ocean reduces the CO_2 solubility and slows down the uptake of anthropogenic carbon from the atmosphere, providing a positive carbon cycle-climate feedback (Sarmiento & LeQuere, 1996; Joos et al., 1999). The dissolution of anthropogenic CO_2 in the surface ocean causes a shift in the composition of DIC from carbonate ions (CO_3^{2-}) towards bicarbonate (HCO_3^-) and undissociated CO_2 (Sec. 1.2.1). This reduces the buffer capacity (Revelle factor) of the ocean, and thus the efficiency in absorbing more CO_2 (Sabine et al., 2004).

Changes in the ocean circulation as documented in the past (Hughen et al., 2004; Muscheler et al., 2000) and projected by many models for future climate change scenarios (Meehl et al., 2007) could also affect the carbon cycle. Advection is important for the physical surface-to-deep transport of DIC (Müller et al., 2006), and thus a reduction in the thermohaline circulation could slow down the removal of anthropogenic DIC from the surface ocean. A decline in ocean circulation could further affect the carbon cycle by changing the nutrient supply to the productive zones (see below) or by inducing regional climatic changes which in turn affect the terrestrial biosphere. In chapter 6, the possibility of rapid changes in ocean circulation is investigated with regard to the response of the carbon cycle.

A key question is how the marine and terrestrial biospheres react to climate change in the future. In the ocean, a decrease in CaCO_3 production could provide a weak negative feedback to atmospheric CO_2 by decreasing surface pCO_2 (Sec. 1.2.1; Heinze, 2004; Gehlen et al., 2007; Ridgwell et al., 2007). On the other hand, many models project a decrease in the global export production (EP, Sec. 1.2.1) under global warming scenarios, which would act as a positive feedback (Chap. 3; Maier-Reimer et al., 1996; Joos et al., 1999; Bopp et al., 2001; Schmittner et al., 2008). A decrease in the nutrient supply to the surface ocean in response to increased stratification and a slowed thermohaline circulation has been identified as a main driver. Methods based on satellite observations also indicate a decrease in ocean productivity in response to increased stratification (Behrenfeld et al., 2006).

The simulation of marine productivity, however, is challenging and results vary considerably across models. This is particularly true for the net primary production, which is projected to increase under global warming in some studies (Schmittner et al., 2008; Sarmiento et al., 2004), while others show a decrease (Bopp et al., 2001; Moore et al., 2002; Boyd & Doney, 2002). In chapter 3 this is further discussed and results from four general circulation models with different representations of the carbon cycle and marine ecosystems are analyzed.

The response of the terrestrial biosphere on the global scale is probably largely controlled by temperature. Warmer temperatures will allow the treeline to migrate northwards and the expansion of boreal forests would likely result in additional carbon storage (Bigelow et al., 2003). On the other hand, the decay of soil and litter carbon increases strongly with

temperature (Bond-Lamberty & Thomson, 2010; Mahecha et al., 2010; Trumbore, 2000). Particularly soils in permafrost regions and wetlands with high carbon contents could become significant emission sources under continued warming (Tarnocai et al., 2009; Avis et al., 2011). In many models the release of soil and litter carbon dominates over the temperature effect on vegetation and show a strong positive temperature-feedback to atmospheric CO₂ (Chap. 4; Friedlingstein et al., 2006). Humidity and precipitation also affect plant growth significantly. Projections of changes in precipitation patterns, however, bear considerably more uncertainties than those of temperature.

Most models also predict a strong stimulation of GPP under elevated CO₂, which acts as a negative feedback to atmospheric CO₂ (Friedlingstein et al., 2006). This CO₂ fertilization is based on the leaf-level CO₂ assimilation rate, which depends on ambient CO₂ concentrations (Farquhar et al., 1980). In addition, CO₂ fertilization plays an important role in conjunction with land-use changes because the clearing of natural vegetation reduces the terrestrial sink capacity (Strassmann et al., 2008). In Chapter 4, projected changes in the terrestrial biosphere are discussed based on simulations with the Bern3D-LPX model under different scenarios.

There are many possibilities for other feedbacks and interactions between climate and the different biogeochemical cycles, which are not discussed here. Examples are expected interactions between the nitrogen and carbon cycles as already mentioned previously (Gruber & Galloway, 2008) and the increased methane emissions from wet ecosystems in response to a warming (Walter et al., 2006; Spahni et al., 2011). An overview of potential feedback mechanisms with respect to ocean biogeochemistry is given by Boyd & Doney (2003) and Gehlen et al. (2011).

Bibliography

- Anthoff, D., Nicholls, R. J., Tol, R. S. J., & Vafeidis, A. T., 2006. Global and regional exposure to large rises in sea-level: a sensitivity analysis, Working Paper 96, Tyndall Centre for Climate Change Research.
- Archer, D., 2005. Fate of fossil fuel CO₂ in geologic time, *J. Geophys. Res.-Oceans*, 110(C09S05).
- Avis, C. A., Weaver, A. J., & Meissner, K. J., 2011. Reduction in areal extent of high-latitude wetlands in response to permafrost thaw, *Nature Geosci.*, 4(7), 444–448.
- Bates, N. R., 2007. Interannual variability of the oceanic CO₂ sink in the subtropical gyre of the North Atlantic Ocean over the last 2 decades, *J. Geophys. Res.-Oceans*, 112(C09013).
- Bates, N. R. & Mathis, J. T., 2009. The Arctic Ocean marine carbon cycle: evaluation of air-sea CO₂ exchanges, ocean acidification impacts and potential feedbacks, *Biogeosciences*, 6(11), 2433–2459.
- Beer, C., Reichstein, M., Tomelleri, E., Ciais, P., Jung, M., Carvalhais, N., Roedenbeck, C., Arain, M. A., Baldocchi, D., Bonan, G. B., Bondeau, A., Cescatti, A., Lasslop, G., Lindroth, A., Lomas, M., Luysaert, S., Margolis, H., Oleson, K. W., Rouspard, O., Veenendaal, E., Viovy, N., Williams, C., Woodward, F. I., & Papale, D., 2010. Terrestrial gross carbon dioxide uptake: Global distribution and covariation with climate, *Science*, 329(5993), 834–838.
- Behrenfeld, M. J. & Falkowski, P. G., 1997. A consumer's guide to phytoplankton primary productivity models, *Limnol. Oceanogr.*, 42(7), 1479–1491.
- Behrenfeld, M. J., O'Malley, R. T., Siegel, D. A., McClain, C. R., Sarmiento, J. L., Feldman, G. C., Milligan, A. J., Falkowski, P. G., Letelier, R. M., & Boss, E. S., 2006. Climate-driven trends in contemporary ocean productivity, *Nature*, 444(7120), 752–755.
- Berger, A. L., 1978. Long-term variations of daily insolation and quaternary climatic changes, *J. Atmos. Sci.*, 35(12), 2362–2367.
- Bernie, D., Lowe, J., Tyrrell, T., & Legge, O., 2010. Influence of mitigation policy on ocean acidification, *Geophys. Res. Lett.*, 37(L15704).
- Betts, R. A., 2000. Offset of the potential carbon sink from boreal forestation by decreases in surface albedo, *Nature*, 408(6809), 187–190.
- Bigelow, N. H., Brubaker, L. B., Edwards, M. E., Harrison, S. P., Prentice, I. C., Anderson, P. M., Andreev, A. A., Bartlein, P. J., Christensen, T. R., Cramer, W., Kaplan, J. O., Lozhkin, A. V., Matveyeva, N. V., Murray, D. F., McGuire, A. D., Razzhivin, V. Y., Ritchie, J. C., Smith, B., Walker, D. A., Gajewski, K., Wolf, V., Holmqvist, B. H., Igarashi, Y., Kremenetskii, K., Paus, A., Pisaric, M. F. J., & Volkova, V. S., 2003. Climate change and Arctic ecosystems: 1. vegetation changes north of 55 degrees N between the last glacial maximum, mid-Holocene, and present, *J. Geophys. Res.-Atmos.*, 108(D19).
- Boden, T., Marland, G., & Andres, B., 2011. Global CO₂ emissions from fossil-fuel burning, cement manufacture, and gas flaring: 1751-2008, Data set, Carbon Dioxide Information Analysis Center, Oak Ridge National Laboratory, Oak Ridge, Tennessee 37831-6290, Available on-line: http://cdiac.ornl.gov/trends/emis/meth_reg.html.
- Bond-Lamberty, B. & Thomson, A., 2010. Temperature-associated increases in the global soil respiration record, *Nature*, 464(7288), 579–U132.
- Bopp, L., Monfray, P., Aumont, O., Dufresne, J. L., Le Treut, H., Madec, G., Terray, L., & Orr, J. C., 2001. Potential impact of climate change on marine export production, *Global Biogeochem. Cy.*, 15(1), 81–99.
- Boyd, P. W. & Doney, S. C., 2002. Modelling regional responses by marine pelagic ecosystems to global climate change, *Geophys. Res. Lett.*, 29(1806), 1–4.
- Boyd, P. W. & Doney, S. C., 2003. *Ocean Biogeochemistry: The Role of the Ocean Carbon Cycle in Global Change*, chap. 7: The Impact of Climate Change and Feedback Processes on the Ocean Carbon Cycle, pp. 157–193, Springer-Verlag, Berlin, Germany.
- Brewer, P. G. & Peltzer, E. T., 2009. Limits to marine life, *Science*, 324(5925), 347–348.
- Broecker, W. S. & Takahashi, T., 1966. Calcium carbonate precipitation on Bahama Banks, *J. Geophys. Res.*, 71(6), 1575–1602.

- Caldeira, K. & Wickett, M. E., 2003. Anthropogenic carbon and ocean pH, *Nature*, 425, 365.
- Canadell, J. G., Le Quere, C., Raupach, M. R., Field, C. B., Buitenhuis, E. T., Ciais, P., Conway, T. J., Gillett, N. P., Houghton, R. A., & Marland, G., 2007. Contributions to accelerating atmospheric CO₂ growth from economic activity, carbon intensity, and efficiency of natural sinks, *Proc. Nat. Acad. Sci. USA*, 104(47), 18866–18870.
- Canfield, D. E., Glazer, A. N., & Falkowski, P. G., 2010. The evolution and future of Earth's nitrogen cycle, *Science*, 330(6001), 192–196.
- Cao, L., Caldeira, K., & Jain, A. K., 2007. Effects of carbon dioxide and climate change on ocean acidification and carbonate mineral saturation, *Geophys. Res. Lett.*, 34(L05607).
- Carr, M.-E., Friedrichs, M. A. M., Schmeltz, M., Aita, M. N., Antoine, D., Arrigo, K. R., Asanuma, I., Aumont, O., Barber, R., Behrenfeld, M., Bidigare, R., Buitenhuis, E. T., Campbell, J., Ciotti, A., Dierssen, H., Dowell, M., Dunne, J., Esaias, W., Gentili, B., Gregg, W., Groom, S., Hoepffner, N., Ishizaka, J., Kameda, T., Le Quéré, C., Lohrenz, S., Marra, J., Melin, F., Moore, K., Morel, A., Reddy, T. E., Ryan, J., Scardi, M., Smyth, T., Turpie, K., Tilstone, G., Waters, K., & Yamanaka, Y., 2006. A comparison of global estimates of marine primary production from ocean color, *Deep-Sea Res. Pt. II*, 53(5-7), 741–770.
- Conkright, M. E., Antonov, J. I., Boyer, T. P., Locarnini, R. A., O'Brien, T. D., Stephens, C., & Garcia, H. E., 2002. *World Ocean Atlas 2001*, vol. 49-52 of NOAA Atlas NEDIS, US Govt. Printing Office, Washington, D. C.
- Conway, T. & Tans, P., 2011. Trends in atmospheric carbon dioxide, Data set, NOAA/ESRL, Available on-line: <http://www.esrl.noaa.gov/gmd/ccgg/trends/>.
- Cooley, S. R. & Doney, S. C., 2009. Anticipating ocean acidification's economic consequences for commercial fisheries, *Environ. Res. Lett.*, 4(2).
- Council of the European Union, 2004. 2610th council meeting: Environment, Press release 12908/04 (Presse 283).
- Damon, P. E. & Sternberg, R. E., 1989. Global production and decay of radiocarbon, *Radiocarbon*, 31(3), 697–703.
- Delaygue, G. & Bard, E., 2011. An antarctic view of beryllium-10 and solar activity for the past millennium, *Clim. Dynam.*, 36(11-12), 2201–2218.
- Denman, K., Brasseur, G., Chidthaisong, A., Ciais, P., Cox, P. M., Dickinson, R. E., Hauglustaine, D., Heinze, C., Holland, E., Jacob, D., Lohmann, U., Ramachandran, da Silva Dias, P. L., Wofsy, S., & Zhang, X., 2007. *Climate Change 2007: The Physical Science Basis. Contribution of Working Group I to the Fourth Assessment Report of the Intergovernmental Panel on Climate Change*, chap. 7: Couplings Between Changes in the Climate System and Biogeochemistry, pp. 499–587, Cambridge University Press, Cambridge, United Kingdom and New York, NY, USA.
- Domingues, C. M., Church, J. A., White, N. J., Gleckler, P. J., Wijffels, S. E., Barker, P. M., & Dunn, J. R., 2008. Improved estimates of upper-ocean warming and multi-decadal sea-level rise, *Nature*, 453(7198), 1090–U6.
- Doney, S. C., Mahowald, N., Lima, I., Feely, R. A., Mackenzie, F. T., Lamarque, J.-F., & Rasch, P. J., 2007. Impact of anthropogenic atmospheric nitrogen and sulfur deposition on ocean acidification and the inorganic carbon system, *Proc. Nat. Acad. Sci. USA*, 104(37), 14580–14585.
- Doney, S. C., Fabry, V. J., Feely, R. A., & Kleypas, J. A., 2009. Ocean acidification: the other CO₂ problem, *Ann. Rev. Mar. Sci.*, 1, 169–192.
- Dore, J. E., Lukas, R., Sadler, D. W., Church, M. J., & Karl, D. M., 2009. Physical and biogeochemical modulation of ocean acidification in the central North Pacific, *Proc. Nat. Acad. Sci. USA*, 106(30), 12235–12240.
- Fabry, V. J., 2008. Marine calcifiers in a high-CO₂ ocean, *Science*, 320, 1020–1022.
- Fabry, V. J., Seibel, B. A., Feely, R. A., & Orr, J. C., 2008. Impacts of ocean acidification on marine fauna and ecosystem processes, *ICES J. Mar. Sci.*, 65, 414–432.

- Falkowski, P. G., Laws, E. A., Barber, R. T., & Murray, J. W., 2003. *Ocean Biogeochemistry: The Role of the Ocean Carbon Cycle in Global Change*, chap. 4: Phytoplankton and Their Role in Primary, New, and Export Production, pp. 99–121, Springer-Verlag, Berlin, Germany.
- Farquhar, G. D., Caemmerer, S. V., & Berry, J. A., 1980. A biochemical-model of photosynthetic CO₂ assimilation in leaves of C-3 species, *Planta*, 149(1), 78–90.
- Feely, R. A., Sabine, C. L., Hernandez-Ayon, J. M., Ianson, D., & Hales, B., 2008. Evidence for upwelling of corrosive "acidified" water onto the continental shelf, *Science*, 320, 1490–1492, published online 22 May 2008.
- eds Field, C. B. & Raupach, M. R., 2004. *The global carbon cycle: Integrating Humans, Climate, and the Natural World*, SCOPE 62, Island Press.
- Field, C. B., Behrenfeld, M. J., Randerson, J. T., & Falkowski, P., 1998. Primary production of the biosphere: Integrating terrestrial and oceanic components, *Science*, 281(5374), 237–240.
- Forster, P., Ramaswamy, V., Artaxo, P., Berntsen, T., Betts, R., Fahey, D. W., Haywood, J., Lean, J., Lowe, D. C., Myhre, G., Nganga, J., Prinn, R., Raga, G., Schulz, M., & Dorland, R. V., 2007. *Climate Change 2007: The Physical Science Basis. Contribution of Working Group I to the Fourth Assessment Report of the Intergovernmental Panel on Climate Change*, chap. 2: Changes in Atmospheric Constituents and in Radiative Forcing, pp. 129–234, Cambridge University Press, Cambridge, United Kingdom and New York, NY, USA.
- Frank, D. C., Esper, J., Raible, C. C., Buentgen, U., Trouet, V., Stocker, B., & Joos, F., 2010. Ensemble reconstruction constraints on the global carbon cycle sensitivity to climate, *Nature*, 463(7280), 527–U143.
- Friedlingstein, P., Cox, P., Betts, R., Bopp, L., Von Bloh, W., Brovkin, V., Cadule, P., Doney, S., Eby, M., Fung, I., Bala, G., John, J., Jones, C., Joos, F., Kato, T., Kawamiya, M., Knorr, W., Lindsay, K., Matthews, H. D., Raddatz, T., Rayner, P., Reick, C., Roeckner, E., Schnitzler, K. G., Schnur, R., Strassmann, K., Weaver, A. J., Yoshikawa, C., & Zeng, N., 2006. Climate-Carbon Cycle Feedback Analysis: Results from the C⁴MIP model intercomparison: Evolution of carbon sinks in a changing climate, *J. Climate*, 19(14), 3337–3353.
- Frölicher, T. L. & Joos, F., 2010. Reversible and irreversible impacts of greenhouse gas emissions in multi-century projections with the NCAR global coupled carbon cycle-climate model, *Clim. Dynam.*, 34(Published online: 12 January 2010).
- Fung, I., Doney, S., Lindsay, K., & John, J., 2005. Evolution of carbon sinks in a changing climate, *Proc. Nat. Acad. Sci. USA*, 102(32), 11201–11206.
- Gangstø, R., Gehlen, M., Schneider, B., Bopp, L., Aumont, O., & Joos, F., 2008. Modeling the marine aragonite cycle: changes under rising carbon dioxide and its role in shallow water CaCO₃ dissolution, *Biogeosciences*, 5(4), 1057–1072.
- eds Gattuso, J.-P. & Hansson, L., 2011. *Ocean Acidification*, Oxford University Press, New York, USA.
- Gattuso, J.-P. & Lavigne, H., 2009. Technical note: Approaches and software tools to investigate the impact of ocean acidification, *Biogeosciences*, 6(10), 2121–2133.
- Gattuso, J.-P., Frankignoulle, M., Bourge, I., Romaine, S., & Buddemeier, R. W., 1998. Effect of calcium carbonate saturation of seawater on coral calcification, *Global Planet. Change*, 18, 37–46.
- Gattuso, J.-P., Hansson, L., & the EPOCA Consortium, 2009. European Project on Ocean Acidification (EPOCA): objectives, products and scientific highlights, *Oceanography*, 22(4), 190–201.
- Gaudinski, J. B., Trumbore, S. E., Davidson, E. A., & Zheng, S. H., 2000. Soil carbon cycling in a temperate forest: radiocarbon-based estimates of residence times, sequestration rates and partitioning of fluxes, *Biogeochemistry*, 51(1), 33–69.
- Gehlen, M., Gangstø, R., Schneider, B., Bopp, L., Aumont, O., & Etche, C., 2007. The fate of pelagic CaCO₃ production in a high CO₂ ocean: a model study, *Biogeosciences*, 4(4), 505–519.
- Gehlen, M., Gruber, N., Gangstø, R., Bopp, L., & Oschlies, A., 2011. *Ocean Acidification*, chap. 12: Biogeochemical consequences of ocean acidification and feedbacks to the earth system, pp. 230–248, Oxford University Press, New York, USA.

- German Advisory Council on Global Change, 2006. *The Future Oceans - Warming up, Rising High, Turning Sour*, WGBU Special Report, German Advisory Council on Global Change (WBGU), Berlin, Germany.
- Global Soil Data Task Group, 2000. Global gridded surfaces of selected soil characteristics (IGBP-DIS), Data set doi:10.3334/ORNLDAAC/569, Oak Ridge National Laboratory Distributed Active Archive Center, Oak Ridge, Tennessee, U.S.A., Available on-line: <http://www.daac.ornl.gov>.
- González-Dávila, M., Santana-Casiano, J. M., Rueda, M. J., & Llinás, O., 2010. The water column distribution of carbonate system variables at the ESTOC site from 1995 to 2004, *Biogeosciences*, 7(10), 3067–3081.
- Gregory, J. M. & Huybrechts, P., 2006. Ice-sheet contributions to future sea-level change, *Philos. T. Roy. Soc. A*, 364(1844), 1709–1731.
- Gruber, N. & Galloway, J. N., 2008. An Earth-system perspective of the global nitrogen cycle, *Nature*, 451(7176), 293–296.
- Gruber, N., Gloor, M., Mikaloff Fletcher, S. E., Doney, S. C., Dutkiewicz, S., Follows, M. J., Gerber, M., Jacobson, A. R., Joos, F., Lindsay, K., Menemenlis, D., Mouchet, A., Mueller, S. A., Sarmiento, J. L., & Takahashi, T., 2009. Oceanic sources, sinks, and transport of atmospheric CO₂, *Global Biogeochem. Cy.*, 23(GB1005).
- Hauri, C., Gruber, N., Plattner, G.-K., Alin, S., Feely, R. A., Hales, B., & Wheeler, P. A., 2009. Ocean acidification in the California current system, *Oceanography*, 22(4, SI), 60–71.
- Heinze, C., 2004. Simulating oceanic CaCO₃ export production in the greenhouse, *Geophys. Res. Lett.*, 31(L16308).
- Holland, M. M. & Bitz, C. M., 2003. Polar amplification of climate change in coupled models, *Clim. Dynam.*, 21(3-4), 221–232.
- Holmén, K., 1992. *Global Biogeochemical Cycles*, chap. 11: The global carbon cycle, pp. 239–262, Academic Press, London, UK.
- Houghton, R. A., 2003. Revised estimates of the annual net flux of carbon to the atmosphere from changes in land use and land management 1850-2000, *Tellus B*, 55(2), 378–390.
- Huber, M., Mahlstein, I., Wild, M., Fasullo, J., & Knutti, R., 2011. Constraints on climate sensitivity from radiation patterns in climate models, *J. Climate*, 24(4), 1034–1052.
- Hughen, K. A., Eglinton, T. I., Xu, L., & Makou, M., 2004. Abrupt tropical vegetation response to rapid climate changes, *Science*, 304(5679), 1955–1959.
- Indermühle, A., Stocker, T. F., Joos, F., Fischer, H., Smith, H. J., Wahlen, M., Deck, B., Mastroianni, D., Tschumi, J., Blunier, T., Meyer, R., & Stauffer, B., 1999. Holocene carbon-cycle dynamics based on CO₂ trapped in ice at Taylor Dome, Antarctica, *Nature*, 398(6723), 121–126.
- Ito, A. & Penner, J. E., 2005. Historical emissions of carbonaceous aerosols from biomass and fossil fuel burning for the period 1870-2000, *Global Biogeochem. Cy.*, 19(GB2028).
- Jones, C. D., Cox, P. M., & Huntingford, C., 2006. Climate-carbon cycle feedbacks under stabilization: uncertainty and observational constraints, *Tellus B*, 58(5), 603–613.
- Joos, F. & Spahni, R., 2008. Rates of change in natural and anthropogenic radiative forcing over the past 20,000 years, *Proc. Nat. Acad. Sci. USA*, 105(5), 1425–1430.
- Joos, F., Plattner, G.-K., Stocker, T. F., Marchal, O., & Schmittner, A., 1999. Global warming and marine carbon cycle feedbacks and future atmospheric CO₂, *Science*, 284(5413), 464–467.
- Joos, F., Prentice, I. C., Sitch, S., Meyer, R., Hooss, G., Plattner, G.-K., Gerber, S., & Hasselmann, K., 2001. Global warming feedbacks on terrestrial carbon uptake under the Intergovernmental Panel on Climate Change (IPCC) emission scenarios, *Global Biogeochem. Cy.*, 15(4), 891–907.
- Jutterström, S. & Anderson, L. G., 2005. The saturation of calcite and aragonite in the Arctic Ocean, *Mar. Chem.*, 94, 101–110.
- Key, R. M., Kozyr, A., Sabine, C. L., Lee, K., Wanninkhof, R., Bullister, J., Feely, R. A., Millero, F., Mordy, C., & Peng, T.-H., 2004. A global ocean carbon climatology: Results from Global Data Analysis Project (GLODAP), *Global Biogeochem. Cy.*, 18(GB4031+).

- Kleypas, J. A., Feely, R. A., Fabry, V. J., Langdon, C., Sabine, C. L., & Robbins, L. L., 2006. *Impacts of Ocean Acidification on Coral Reefs and Other Marine Calcifiers: A Guide for Future Research, report of a workshop held 18-20 April 2005, St. Petersburg, FL*, sponsored by NSF, NOAA, and the US Geological Survey.
- Koehler, P., Bintanja, R., Fischer, H., Joos, F., Knutti, R., Lohmann, G., & Masson-Delmotte, V., 2010. What caused Earth's temperature variations during the last 800,000 years? Data-based evidence on radiative forcing and constraints on climate sensitivity, *Quaternary Sci. Rev.*, 29(1-2, SI), 129–145.
- Langdon, C., 2002. Review of experimental evidence for effects of CO₂ on calcification of reef builders, in *Proceedings 9th International Coral Reef Symposium*, vol. 2, pp. 1091–1098.
- Langdon, C., Takahashi, T., Sweeney, C., Chipman, D., Goddard, J., Marubini, F., Aceves, H., Barnett, H., & Atkinson, M. J., 2000. Effect of calcium carbonate saturation state on the calcification rate of an experimental coral reef, *Global Biogeochem. Cy.*, 14(2), 639–654.
- Laws, E. A., Falkowski, P. G., Smith, W. O., Ducklow, H., & McCarthy, J. J., 2000. Temperature effects on export production in the open ocean, *Global Biogeochem. Cy.*, 14(4), 1231–1246.
- Le Quéré, C., Aumont, O., Bopp, L., Bousquet, P., Ciais, P., Francey, R., Heimann, M., Keeling, C. D., Keeling, R. F., Khesghi, H., Peylin, P., Piper, S. C., Prentice, I. C., & Rayner, P. J., 2003. Two decades of ocean CO₂ sink and variability, *Tellus B*, 55(2), 649–656.
- Leclercq, N., Gattuso, J.-P., & Jaubert, J., 2000. CO₂ partial pressure controls the calcification rate of a coral community, *Glob. Change Biol.*, 6, 329–334.
- Lindeman, R. L., 1942. The trophic-dynamic aspect of ecology, *Ecology*, 23(4), 399–418.
- Lueker, T. J., Dickson, A. G., & Keeling, C. D., 2000. Ocean pCO₂ calculated from dissolved inorganic carbon, alkalinity, and equations for K₁ and K₂: validation based on laboratory measurements of CO₂ in gas and seawater at equilibrium, *Mar. Chem.*, 70(1-3), 105–119.
- Lüthi, D., Le Floch, M., Bereiter, B., Blunier, T., Barnola, J.-M., Siegenthaler, U., Raynaud, D., Jouzel, J., Fischer, H., Kawamura, K., & Stocker, T. F., 2008. High-resolution carbon dioxide concentration record 650 000–800 000 years before present, *Science*, 453, 379–382.
- Luyssaert, S., Inglisma, I., Jung, M., Richardson, A. D., Reichstein, M., Papale, D., Piao, S. L., Schulzes, E.-D., Wingate, L., Matteucci, G., Aragao, L., Aubinet, M., Beers, C., Bernhoffer, C., Black, K. G., Bonal, D., Bonnefond, J.-M., Chambers, J., Ciais, P., Cook, B., Davis, K. J., Dolman, A. J., Gielen, B., Goulden, M., Grace, J., Granier, A., Grelle, A., Griffis, T., Gruenwald, T., Guidolotti, G., Hanson, P. J., Harding, R., Hollinger, D. Y., Hutrya, L. R., Kolar, P., Kruijt, B., Kutsch, W., Lagergren, F., Laurila, T., Law, B. E., Le Maire, G., Lindroth, A., Loustau, D., Malhi, Y., Mateus, J., Migliavacca, M., Misson, L., Montagnani, L., Moncrieff, J., Moors, E., Munger, J. W., Nikinmaa, E., Ollinger, S. V., Pita, G., Rebmann, C., Rouspard, O., Saigusa, N., Sanz, M. J., Seufert, G., Sierra, C., Smith, M.-L., Tang, J., Valentini, R., Vesala, T., & Janssens, I. A., 2007. CO₂ balance of boreal, temperate, and tropical forests derived from a global database, *Glob. Change Biol.*, 13(12), 2509–2537.
- Mahecha, M. D., Reichstein, M., Carvalhais, N., Lasslop, G., Lange, H., Seneviratne, S. I., Vargas, R., Ammann, C., Arain, M. A., Cescatti, A., Janssens, I. A., Migliavacca, M., Montagnani, L., & Richardson, A. D., 2010. Global convergence in the temperature sensitivity of respiration at ecosystem level, *Science*, 329(5993), 838–840.
- Maier-Reimer, E., Mikolajewicz, U., & Winguth, A., 1996. Future ocean uptake of CO₂: interaction between ocean circulation and biology, *Clim. Dynam.*, 12, 63–90.
- Marland, G., Boden, T. A., & Andres, R. J., 2008. *Global, Regional, and National Fossil Fuel CO₂ Emissions*, In Trends: A Compendium of Data on Global Change, Carbon Dioxide Information Analysis Center, Oak Ridge National Laboratory, U.S. Department of Energy, Oak Ridge, Tenn., U.S.A.
- Marubini, F., Ferrier-Pages, C., & Cuif, J. P., 2003. Suppression of skeletal growth in scleractinian corals by decreasing ambient carbonate-ion concentration: a cross-family comparison, *P. Roy. Soc. Lond. B Bio.*, 270, 179–184.
- Mathis, J. T., Cross, J. N., & Bates, N. R., 2011. The role of ocean acidification in systemic carbonate mineral suppression in the bering sea, *Geophys. Res. Lett.*, 38(L19602).

- Matthews, E., 1997. Global litter production, pools, and turnover times: Estimates from measurement data and regression models, *J. Geophys. Res.-Atmos.*, 102(D15), 18771–18800.
- Matthews, H. D., 2006. Emissions targets for CO₂ stabilization as modified by carbon cycle feedbacks, *Tellus B*, 58(5), 591–602.
- McNeil, B. I. & Matear, R. J., 2007. Climate change feedbacks on future oceanic acidification, *Tellus B*, 59, 191–198.
- McNeil, B. I. & Matear, R. J., 2008. Southern ocean acidification: A tipping point at 450-ppm atmospheric CO₂, *Proc. Nat. Acad. Sci. USA*, 105(48), 18860–18864.
- McPhee, M. G., Proshutinsky, A., Morison, J. H., Steele, M., & Alkire, M. B., 2009. Rapid change in freshwater content of the Arctic Ocean, *Geophys. Res. Lett.*, 36(L10602).
- Meehl, G. A., Stocker, T. F., Collins, W. D., Friedlingstein, P., Gaye, A. T., Gregory, J. M., Kitoh, A., Knutti, R., Murphy, J. M., Noda, A., Raper, S. C. B., Watterson, I. G., Weaver, A. J., & Zhao, Z.-C., 2007. *Climate Change 2007: The Physical Science Basis. Contribution of Working Group I to the Fourth Assessment Report of the Intergovernmental Panel on Climate Change*, chap. 10: Global Climate Projections, pp. 747–846, Cambridge University Press, Cambridge, United Kingdom and New York, NY, USA.
- Meinshausen, M., Smith, S. J., Calvin, K. V., Daniel, J. S., Kainuma, M., Lamarque, J.-F., Matsumoto, K., Montzka, S. A., Raper, S. C. B., Riahi, K., Thomson, A. M., Velders, G. J. M., & van Vuuren, D., 2011. The RCP greenhouse gas concentrations and their extension from 1765 to 2300, *Clim. Change*, 109, 213–241.
- Mikaloff Fletcher, S. E., Gruber, N., Jacobson, A. R., Doney, S. C., Dutkiewicz, S., Gerber, M., Follows, M., Joos, F., Lindsay, K., Menemenlis, D., Mouchet, A., Muller, S. A., & Sarmiento, J. L., 2006. Inverse estimates of anthropogenic CO₂ uptake, transport, and storage by the ocean, *Global Biogeochem. Cy.*, 20(GB2002).
- Millero, F. J., 1979. The thermodynamics of the carbonic acid system in seawater, *Geochim. Cosmochim. Ac.*, 43, 1651–1661.
- Millero, F. J., 1995. Thermodynamics of the carbon dioxide system in the oceans, *Geochim. Cosmochim. Ac.*, 59(4), 661–677.
- Milliman, J. D., Troy, P. J., Balch, W. M., Adams, A. K., Li, Y. H., & Mackenzie, F. T., 1999. Biologically mediated dissolution of calcium carbonate above the chemical lysocline?, *Deep-Sea Res.*, 46(10), 1653–1669.
- Moore, J. K., Doney, S. C., Kleypas, J. A., Glover, D. M., & Fung, I. Y., 2002. An intermediate complexity marine ecosystem model for the global domain, *Deep-Sea Res. Pt. II*, 49(1-3), 403–462.
- Moritz, R. E., Bitz, C. M., & Steig, E. J., 2002. Dynamics of recent climate change in the Arctic, *Science*, 297(5586), 1497–1502.
- Moss, R. H., Edmonds, J. A., Hibbard, K. A., Manning, M. R., Rose, S. K., van Vuuren, D. P., Carter, T. R., Emori, S., Kainuma, M., Kram, T., Meehl, G. A., Mitchell, J. F. B., Nakicenovic, N., Riahi, K., Smith, S. J., Stouffer, R. J., Thomson, A. M., Weyant, J. P., & Wilbanks, T. J., 2010. The next generation of scenarios for climate change research and assessment, *Nature*, 463(7282), 747–756.
- Mucci, A., 1983. The solubility of calcite and aragonite in seawater at various salinities, temperatures and 1 atmosphere total pressure, *Am. J. Sci.*, 238, 780–799.
- Müller, S. A., Joos, F., Edwards, N. R., & Stocker, T. F., 2006. Water mass distribution and ventilation time scales in a cost-efficient, three-dimensional ocean model, *J. Climate*, 19(21), 5479–5499.
- Müller, S. A., Joos, F., Plattner, G.-K., Edwards, N. R., & Stocker, T. F., 2008. Modeled natural and excess radiocarbon: Sensitivities to the gas exchange formulation and ocean transport strength, *Global Biogeochem. Cy.*, 22(3).
- Muscheler, R., Beer, J., Wagner, G., & Finkel, R. C., 2000. Changes in deep-water formation during the younger dryas event inferred from ¹⁰Be and ¹⁴C records, *Nature*, 408(6812), 567–570.
- Myhre, G. & Myhre, A., 2003. Uncertainties in radiative forcing due to surface albedo changes caused by land-use changes, *J. Climate*, 16(10), 1511–1524.

- Myhre, G., Highwood, E. J., Shine, K. P., & Stordal, F., 1998. New estimates of radiative forcing due to well mixed greenhouse gases, *Geophys. Res. Lett.*, 25(14), 2715–2718.
- Myhre, G., Kvalevag, M. M., & Schaaf, C. B., 2005. Radiative forcing due to anthropogenic vegetation change based on modis surface albedo data, *Geophys. Res. Lett.*, 32(21).
- Nakićenović, N., Alcamo, J., Davis, G., & colleagues, 2000. *Special Report on Emission Scenarios, Working Group III*, Intergovernmental Panel on Climate Change, Cambridge University Press, New York.
- Orr, J. C., 2011. *Ocean Acidification*, chap. 3: Recent and future changes in ocean carbonate chemistry, pp. 41–66, Oxford University Press, New York, USA.
- Orr, J. C., Fabry, V. J., Aumont, O., Bopp, L., Doney, S. C., Feely, R. A., Gnanadesikan, A., Gruber, N., Ishida, A., Joos, F., Key, R. M., Lindsay, K., Maier-Reimer, E., Matear, R., Monfray, P., Mouchet, A., Najjar, R. G., Plattner, G.-K., Rodgers, K. B., Sabine, C. L., Sarmiento, J. L., Schlitzer, R., Slater, R. D., Totterdell, I. J., Weirig, M. F., Yamanaka, Y., & Yool, A., 2005. Anthropogenic ocean acidification over the twenty-first century and its impact on calcifying organisms, *Nature*, 437, 681–686.
- Otto, J., Raddatz, T., & Claussen, M., 2011. Strength of forest-albedo feedback in mid-Holocene climate simulations, *Clim. Past*, 7, 1027–1039.
- eds Parry, M. L., Canziani, O. F., Palutikof, J. P., van der Linden, P. J., & E., H. C., 2007. *Climate Change 2007: Impacts, Adaptation and Vulnerability. Contribution of Working Group II to the Fourth Assessment Report of the Intergovernmental Panel on Climate Change*, Cambridge University Press, Cambridge, United Kingdom and New York, NY, USA.
- Plattner, G.-K., Joos, F., Stocker, T. F., & Marchal, O., 2001. Feedback mechanisms and sensitivities of ocean carbon uptake under global warming, *Tellus B*, 53(5), 564–592.
- Plattner, G.-K., Knutti, R., Joos, F., Stocker, T. F., von Bloh, W., Brovkin, V., Cameron, D., Driesschaert, E., Dutkiewicz, S., Eby, M., Edwards, N. R., Fichet, T., Hargreaves, J. C., Jones, C. D., Loutre, M. F., Matthews, H. D., Mouchet, A., Müller, S. A., Nawrath, S., Price, A., Sokolov, A., Strassmann, K. M., & Weaver, A. J., 2008. Long-term climate commitments projected with climate - carbon cycle models, *J. Climate*, 21(12), 2721–2751.
- Poertner, H.-O., 2008. Ecosystem effects of ocean acidification in times of ocean warming: a physiologist's view, *Mar. Ecol.-Prog. Ser.*, 373, 203–217.
- Ramankutty, N., Gibbs, H. K., Achard, F., Defriess, R., Foley, J. A., & Houghton, R. A., 2007. Challenges to estimating carbon emissions from tropical deforestation, *Glob. Change Biol.*, 13(1), 51–66.
- Randerson, J. T., Chapin, F. S., Harden, J. W., Neff, J. C., & Harmon, M. E., 2002. Net ecosystem production: A comprehensive measure of net carbon accumulation by ecosystems, *Ecol. Appl.*, 12(4), 937–947.
- Redfield, A. C., Ketchum, B. H., & Richards, F. A., 1963. *The influence of organisms on the composition of seawater*, vol. 2 of *The Sea*, pp. 26–77, Interscience.
- Revelle, R. & Suess, H. E., 1957. Carbon dioxide exchange between atmosphere and ocean and the question of an increase of atmospheric CO₂ during the past decades, *Tellus*, 9(1), 18–27.
- Ridgwell, A., Zondervan, I., Hargreaves, J. C., Bijma, J., & Lenton, T. M., 2007. Assessing the potential long-term increase of oceanic fossil fuel CO₂ uptake due to CO₂-calcification feedback, *Biogeosciences*, 4(4), 481–492.
- Riebesell, U., Zondervan, I., Rost, B., Tortell, P. D., Zeebe, R. E., & Morel, F. M. M., 2000. Reduced calcification of marine plankton in response to increased atmospheric CO₂, *Nature*, 407(6802), 364–367.
- Rockström, J., Steffen, W., Noone, K., Persson, A., Chapin, I. I. I., Lambin, E. F., Lenton, T. M., Scheffer, M., Folke, C., Schellnhuber, H. J., Nykvist, B., de Wit, C. A., Hughes, T., van der Leeuw, S., Rodhe, H., Sorlin, S., Snyder, P. K., Costanza, R., Svedin, U., Falkenmark, M., Karlberg, L., Corell, R. W., Fabry, V. J., Hansen, J., Walker, B., Liverman, D., Richardson, K., Crutzen, P., & Foley, J. A., 2009. A safe operating space for humanity, *Nature*, 461(7263), 472–475.
- Roe, G., 2009. Feedbacks, timescales, and seeing red, *Ann. Rev. Earth Pl. Sci.*, 37, 93–115.
- Royal Society, 2005. *Ocean acidification due to increasing atmospheric carbon dioxide*, Policy Document 12/05, Royal Society, London.

- Sabine, C. L., Feely, R. A., Gruber, N., Key, R. M., Lee, K., Bullister, J. L., Wanninkhof, R., Wong, C. S., Wallace, D. W. R., Tilbrook, B., Millero, F. J., Peng, T. H., Kozyr, A., Ono, T., & Rios, A. F., 2004. The oceanic sink for anthropogenic CO₂, *Science*, 305(5682), 367–371.
- Sarmiento, J. L. & Gruber, N., 2006. *Ocean Biogeochemical Dynamics*, Princeton University Press.
- Sarmiento, J. L. & LeQuere, C., 1996. Oceanic carbon dioxide uptake in a model of century-scale global warming, *Science*, 274(5291), 1346–1350.
- Sarmiento, J. L., Dunne, J., Gnanadesikan, A., Key, R. M., Matsumoto, K., & Slater, R., 2002. A new estimate of the CaCO₃ to organic carbon export ratio, *Global Biogeochem. Cy.*, 16(4), 1107.
- Sarmiento, J. L., Slater, R., Barber, R., Bopp, L., Doney, S. C., Hirst, A. C., Kleypas, J., Matear, R., Mikolajewicz, U., Monfray, P., Soldatov, V., Spall, S. A., & Stouffer, R., 2004. Response of ocean ecosystems to climate warming, *Global Biogeochem. Cy.*, 18(GB3003), 1–23.
- Schlitzer, R., 2000. *Inverse Methods in Biogeochemical Cycles*, chap. Applying the Adjoint Method for Global Biogeochemical Modeling, pp. 107–124, AGU, USA.
- Schmidt, G. A., Jungclaus, J. H., Ammann, C. M., Bard, E., Braconnot, P., Crowley, T. J., Delaygue, G., Joos, F., Krivova, N. A., Muscheler, R., Otto-Bliesner, B. L., Pongratz, J., Shindell, D. T., Solanki, S. K., Steinhilber, F., & Vieira, L. E. A., 2011. Climate forcing reconstructions for use in PMIP simulations of the last millennium (v1.0), *Geosci. Model Dev.*, 4(1), 33–45.
- Schmittner, A., Oschlies, A., Matthews, H. D., & Galbraith, E. D., 2008. Future changes in climate, ocean circulation, ecosystems, and biogeochemical cycling simulated for a business-as-usual CO₂ emission scenario until year 4000 ad, *Global Biogeochem. Cy.*, 22(GB1013), 1–21.
- Serreze, M. C. & Barry, R. G., 2011. Processes and impacts of Arctic amplification: A research synthesis, *Global Planet. Change*, 77(1-2), 85–96.
- Serreze, M. C. & Francis, J. A., 2006. The arctic amplification debate, *Clim. Change*, 76(3-4), 241–264.
- Siegenthaler, U. & Sarmiento, J. L., 1993. Atmospheric carbon-dioxide and the ocean, *Nature*, 365(6442), 119–125.
- Solomon, S., Qin, D., Manning, M., Alley, R. B., Berntsen, T., Bindoff, N. L., Chen, Z., Chidthaisong, A., Gregory, J. M., Hegerl, G. C., Heimann, M., Hewitson, B., Hoskins, B. J., Joos, F., Jouzel, J., Kattsov, V., Lohmann, U., Matsuno, T., Molina, M., Nicholls, N., Overpeck, J., Raga, G., Ramaswamy, V., Ren, J., Rusticucci, M., Somerville, R., Stocker, T. F., Whetton, P., Wood, R. A., & Wratt, D., 2007. *Climate Change 2007: The Physical Science Basis. Contribution of Working Group I to the Fourth Assessment Report of the Intergovernmental Panel on Climate Change*, chap. Technical Summary, Cambridge University Press, Cambridge, United Kingdom and New York, NY, USA.
- Spahni, R., Wania, R., Neef, L., van Weele, M., Pison, I., Bousquet, P., Frankenberg, C., Foster, P. N., Joos, F., Prentice, I. C., & van Velthoven, P., 2011. Constraining global methane emissions and uptake by ecosystems, *Biogeosciences*, 8(6), 1643–1665.
- Stern, N., 2006. *The Economics of Climate Change: The Stern Review*, Cabinet Office, HM Treasury, London, UK.
- Stocker, T. F., Wright, D. G., & Broecker, W. S., 1992. The influence of high-latitude surface forcing on the global thermohaline circulation, *Paleoceanography*, 7, 529–541.
- Strassmann, K. M., Joos, F., & Fischer, G., 2008. Simulating effects of land use changes on carbon fluxes: past contributions to atmospheric CO₂ increases and future commitments due to losses of terrestrial sink capacity, *Tellus B*, 60(4), 583–603.
- Stroeve, J., Holland, M. M., Meier, W., Scambos, T., & Serreze, M., 2007. Arctic sea ice decline: Faster than forecast, *Geophys. Res. Lett.*, 34(L09501).
- Takahashi, T., Broecker, W. S., Bainbridge, A. E., & Weiss, R. F., 1980. Carbonate chemistry of the Atlantic, Pacific, and Indian Oceans: The results of the GEOSECS expeditions, 1973–1978, , National Science Foundation, Washington D.C., USA.

- Takahashi, T., Sutherland, S. C., Sweeney, C., Poisson, A., Metzl, N., Tilbrook, B., Bates, N., Wanninkhof, R., Feely, R. A., Sabine, C., Olafsson, J., & Nojiri, Y., 2002. Global sea-air CO₂ flux based on climatological surface ocean pCO₂, and seasonal biological and temperature effects, *Deep-Sea Res. Pt. II*, 49(9-10), 1601–1622.
- Tarnocai, C., Canadell, J. G., Schuur, E. A. G., Kuhry, P., Mazhitova, G., & Zimov, S., 2009. Soil organic carbon pools in the northern circumpolar permafrost region, *Global Biogeochem. Cy.*, 23(GB2023).
- Tian, F., Kasting, J. F., & Solomon, S. C., 2009. Thermal escape of carbon from the early martian atmosphere, *Geophys. Res. Lett.*, 36.
- Tian, Y., Dickinson, R. E., Zhou, L., Myneni, R. B., Friedl, M., Schaaf, C. B., Carroll, M., & Gao, F., 2004. Land boundary conditions from MODIS data and consequences for the albedo of a climate model, *Geophys. Res. Lett.*, 31(5), 5 pp.
- Trumbore, S. E., 2000. Age of soil organic matter and soil respiration: radiocarbon constraints on belowground C dynamics, *Ecol. Appl.*, 10, 399–411.
- Tschumi, T., Joos, F., Gehlen, M., & Heinze, C., 2011. Deep ocean ventilation, carbon isotopes, marine sedimentation and the deglacial CO₂ rise, *Clim. Past*, 7(3), 771–800.
- United Nations, 1992. United Nations Framework Convention on Climate Change, Document FCCC/INFORMAL/84 GE.05-62220 (E) 200705.
- United Nations, 2011. World population prospects: The 2010 revision, Report, Department of Economic and Social Affairs, Population Division, Available on-line: <http://esa.un.org/unpd/wpp/>.
- van Vuuren, D. P., Edmonds, J., Kainuma, M. L. T., Riahi, K., Thomson, A., Matsui, T., Hurtt, G., Lamarque, J.-F., Meinshausen, M., Smith, S., Grainer, C., Rose, Hibbard, K. A., Nakicenovic, N., Krey, V., & Kram, T., 2011. Representative concentration pathways: an overview, *Clim. Change*.
- Vitousek, P. M., Mooney, H. A., Lubchenco, J., & Melillo, J. M., 1997. Human domination of Earth's ecosystems, *Science*, 277(5325), 494–499.
- Walter, K. M., Zimov, S. A., Chanton, J. P., Verbyla, D., & Chapin, I. I. I., 2006. Methane bubbling from siberian thaw lakes as a positive feedback to climate warming, *Nature*, 443(7107), 71–75.
- Wanninkhof, R., 1992. Relationship between wind-speed and gas-exchange over the ocean, *J. Geophys. Res.-Oceans*, 97(C5), 7373–7382.
- Watson, A. J. & Orr, J. C., 2003. *Ocean Biogeochemistry: The Role of the Ocean Carbon Cycle in Global Change*, chap. 5: Carbon Dioxide Fluxes in the Global Ocean, pp. 123–143, Springer-Verlag, Berlin, Germany.
- Weiss, R. F., 1974. Carbon dioxide in water and seawater: The solubility of a non-ideal gas, *Mar. Chem.*, 2, 203–215.
- Yamamoto-Kawai, M., McLaughlin, F. A., Carmack, E. C., Nishino, S., & Shimada, K., 2009. Aragonite undersaturation in the Arctic Ocean: Effects of ocean acidification and sea ice melt, *Science*, 326(5956), 1098–1100.
- Yamamoto-Kawai, M., McLaughlin, F. A., & Carmack, E. C., 2011. Effects of ocean acidification, warming and melting of sea ice on aragonite saturation of the Canada Basin surface water, *Geophys. Res. Lett.*, 38(L03601).
- Yu, Z., Loisel, J., Brosseau, D. P., Beilman, D. W., & Hunt, S. J., 2010. Global peatland dynamics since the last glacial maximum, *Geophys. Res. Lett.*, 37.

Chapter 2

Arctic ocean acidification

2.1 Imminent ocean acidification in the Arctic projected with the NCAR global coupled carbon cycle-climate model

Marco Steinacher, Fortunat Joos, Thomas L. Frölicher, Gian-Kasper Plattner, and Scott C. Doney

Published in *Biogeosciences*, Volume 6, pp. 515–533, 2009.

Biogeosciences, 6, 515–533, 2009
www.biogeosciences.net/6/515/2009/
© Author(s) 2009. This work is distributed under
the Creative Commons Attribution 3.0 License.



Imminent ocean acidification in the Arctic projected with the NCAR global coupled carbon cycle-climate model

M. Steinacher¹, F. Joos^{1,2}, T. L. Frölicher¹, G.-K. Plattner^{1,*}, and S. C. Doney³

¹Climate and Environmental Physics, Physics Institute, University of Bern, Sidlerstrasse 5, 3012 Bern, Switzerland

²Oeschger Centre for Climate Change Research, University of Bern, Erlachstrasse 9a, 3012 Bern, Switzerland

³Dept. of Marine Chemistry and Geochemistry, Woods Hole Oceanographic Institution, Woods Hole, MA 02543-1543, USA

*now at: Environmental Physics, Institute of Biogeochemistry and Pollutant Dynamics, ETH Zürich, Universitätstrasse 16, 8092 Zürich, Switzerland

Received: 22 September 2008 – Published in Biogeosciences Discuss.: 14 November 2008

Revised: 16 March 2009 – Accepted: 26 March 2009 – Published: 6 April 2009

Abstract. Ocean acidification from the uptake of anthropogenic carbon is simulated for the industrial period and IPCC SRES emission scenarios A2 and B1 with a global coupled carbon cycle-climate model. Earlier studies identified seawater saturation state with respect to aragonite, a mineral phase of calcium carbonate, as a key variable governing impacts on corals and other shell-forming organisms. Globally in the A2 scenario, water saturated by more than 300%, considered suitable for coral growth, vanishes by 2070 AD ($\text{CO}_2 \approx 630$ ppm), and the ocean volume fraction occupied by saturated water decreases from 42% to 25% over this century. The largest simulated pH changes worldwide occur in Arctic surface waters, where hydrogen ion concentration increases by up to 185% ($\Delta\text{pH} = -0.45$). Projected climate change amplifies the decrease in Arctic surface mean saturation and pH by more than 20%, mainly due to freshening and increased carbon uptake in response to sea ice retreat. Modeled saturation compares well with observation-based estimates along an Arctic transect and simulated changes have been corrected for remaining model-data differences in this region. Aragonite undersaturation in Arctic surface waters is projected to occur locally within a decade and to become more widespread as atmospheric CO_2 continues to grow. The results imply that surface waters in the Arctic Ocean will become corrosive to aragonite, with potentially large implications for the marine ecosystem, if anthropogenic carbon emissions are not reduced and atmospheric CO_2 not kept below 450 ppm.

1 Introduction

The continued emissions of CO_2 by human activities cause atmospheric CO_2 to rise, climate to warm, and the ocean pH to decrease (e.g. Feely et al., 2008; German Advisory Council on Global Change, 2006; Royal Society, 2005; Orr et al., 2005; Caldeira and Wickett, 2003). Today's atmospheric CO_2 concentration of 384 ppm is far above the natural range reconstructed for the last 800 000 years (172 to 300 ppm; Lüthi et al. (2008); Siegenthaler et al. (2005)) and probably the last 20 million years (Prentice et al., 2001). An important aspect of the human perturbation is its rate of change, as it codetermines the impacts of global warming and elevated CO_2 on natural and socioeconomic systems and their capabilities to adapt. The 20th century increase in CO_2 occurred more than an order of magnitude faster than any sustained change during at least the past 22 000 years (Joos and Spahni, 2008). Carbon cycle and climate change projections based on the latest set of mitigation and reference scenarios from the integrated assessment modelling community indicate that CO_2 and global mean surface temperature will continue to rise over the 21st century and decadal-scale rates of change in temperature and CO_2 will remain high for several decades even for stringent mitigation scenarios (Van Vuuren et al., 2008; Strassmann et al., 2008).

The purpose of this paper is to investigate the consequences of rising atmospheric CO_2 and climate change on ocean chemistry and the ocean's acid-base state with the Climate System Model CSM1.4-carbon of the US National Center for Atmospheric Research (NCAR). We investigate how the saturation state of seawater with respect to aragonite, a mineral phase of calcium carbonate (CaCO_3), will evolve over this century under two IPCC non-intervention



Correspondence to: M. Steinacher
(steinacher@climate.unibe.ch)

Table 1. Different levels of aragonite undersaturation ($\Omega_{\text{arag}} < 1$), atmospheric CO_2 concentration and year when these levels are reached in the Arctic for the A2 and B1 scenario. Levels are defined by the area fraction occupied by undersaturated surface waters in at least one month of the year, in the annual mean, and throughout the year.

Level (area fraction and seasonal occurrence)	CO_2 (ppm)	Year in A2	Year in B1
10%, ≥ 1 month	409	2016	2018
10%, annual mean	428	2023	2025
10%, year-round	450	2029	2034
50%, ≥ 1 month	520	2047	2068
50%, annual mean	534	2050	2085
50%, year-round	552	2054	–
100%, ≥ 1 month	634	2070	–
100%, annual mean	634	2070	–
100%, year-round	694	2080	–
Entire water column	765	2090	–

greenhouse gas emission scenarios. The emphasis here is on the Arctic Ocean, where large changes in CaCO_3 saturation (Gangstø et al., 2008; Steinacher, 2007; McNeil and Matear, 2007; Orr et al., 2008), freshwater balance, and sea ice (Stroeve et al., 2007; Holland et al., 2006) are expected under rising CO_2 . We also analyze how the ocean volume fraction of different saturation regimes is changing with increasing CO_2 and quantify seasonal and interannual variability worldwide.

A particular concern of rising atmospheric CO_2 is the impact on marine organisms and marine ecosystems (Doney et al., 2009). Recent work indicates that ocean acidification from the uptake of anthropogenic CO_2 has adverse consequences for many marine organisms via decreased CaCO_3 saturation, affecting calcification rates, and via disturbance to acid-base physiology (Fabry et al., 2008; Hoegh-Guldberg, 2005; Langdon, 2002). Particularly vulnerable appear organisms that build shells or other structures of calcium carbonate (CaCO_3) in the relatively soluble mineral forms of aragonite or high-magnesium CaCO_3 . Examples are pteropods (Orr et al., 2005), a major zooplankton group in high latitudes, corals (Kleypas et al., 2006; Langdon and Atkinson, 2005), and sea urchins (Fabry et al., 2008). Experimental evidence suggests a range of responses to ocean acidification (Fabry et al., 2008, Table 1) such as a reduction in foraminifera shell mass, shell dissolution for pteropods in water undersaturated with respect to aragonite, reduced calcification rates, reduced growth rates, reduced metabolisms, and increased mortality in molluscs or reduced fertility for a number of groups. Responses to acidification are likely to vary across species and life stages. Scleractinian corals were found to survive and recover after experiencing decalcification in acidic water (Fine and Tchernov, 2007). Currently experimental evidence is however limited with regard to the number of species tested at relevant CO_2 concentrations.

Uptake of anthropogenic carbon by the ocean changes the acid-base state of seawater. Currently, about a quarter of

the anthropogenic CO_2 emitted into the atmosphere is taken up by the ocean. The hydrolysis of CO_2 in seawater lowers ocean pH, making the oceans less basic (Caldeira and Wickett, 2003). Carbonate ion concentration (Feely et al., 2004) and the saturation state of water with respect to calcium carbonate (CaCO_3) is decreasing through the reaction:



The CaCO_3 saturation state, Ω , is the product of the concentrations of calcium ions (Ca^{2+}) and carbonate ions (CO_3^{2-}) divided by the apparent stoichiometric solubility product K'_{sp} :

$$\Omega = [\text{Ca}^{2+}][\text{CO}_3^{2-}]/K'_{\text{sp}} \quad (2)$$

The solubility product ($K'_{\text{sp}} = [\text{Ca}^{2+}]_{\text{sat}}[\text{CO}_3^{2-}]_{\text{sat}}$) is either defined for aragonite or calcite, two mineral phases of CaCO_3 secreted by marine organisms. The CO_3^{2-} saturation concentration is about 50% higher for the mineral phase calcite (Ω_{calc}) than for the less stable aragonite (Ω_{arag}). The concentration of Ca^{2+} is linearly related to salinity and nearly constant. It is thus convenient to express the saturation state as deviation of the CO_3^{2-} concentration from its saturation concentration: $\Delta[\text{CO}_3^{2-}] = [\text{CO}_3^{2-}] - [\text{CO}_3^{2-}]_{\text{sat}}$. Undersaturated seawater ($\Omega < 1$ or $\Delta[\text{CO}_3^{2-}] < 0$) is corrosive to CaCO_3 in the absence of protective mechanisms.

The CaCO_3 saturation state Ω_{arag} is a key variable for assessing biological impacts of ocean acidification. Available experimental and observational evidence suggests that the biogenic production and dissolution of CaCO_3 are mainly controlled by the ambient saturation state, rather than by pH or other factors. This has been shown for corals, coralline algae, coccolithophorids, foraminifera, echinoderms, mesocosm coral reef communities and natural coral reef ecosystems (Kleypas et al., 2006; Schneider and Erez, 2006; Hoegh-Guldberg, 2005; Orr et al., 2005; Gattuso et al., 1998). Tropical coral reef development was associated with

$\Omega_{\text{arag}} \geq 4.0$ by Kleypas et al. (1999), and Langdon and Atkinson (2005) project a 40–50% decrease of coral calcification rates by 2065 ($\Omega_{\text{arag}}=3.1$) relative to $\Omega_{\text{arag}}=4.6$, which corresponds to preindustrial conditions (year 1880) in the tropical ocean in their study.

A range of responses is found for pelagic calcifiers under changing Ω_{arag} (Fabry, 2008). Recently Iglesias-Rodriguez et al. (2008) reported laboratory evidence that calcification and net primary production per cell in the coccolithophore species *Emiliani huxleyi* are significantly increased by high CO_2 partial pressures. Yet the growth rates were found to be significantly lower at higher CO_2 levels. Such changes could have important implications for the overall community production of CaCO_3 relative to organic carbon, under increasing $p\text{CO}_2$. However, the implied feedback on atmospheric CO_2 has been estimated to be small in global modelling studies (Heinze, 2004; Gehlen et al., 2007; Ridgwell et al., 2007).

The main controls on 21st century Ω_{arag} are the uptake of anthropogenic carbon and the subsequent increase in dissolved inorganic carbon (DIC) (Orr et al., 2005). Second order changes in saturation state arises from alterations in the distribution of DIC and alkalinity (Alk) due to a reorganization of the marine biological cycle and ocean circulation as well as ocean warming (decreasing CO_2 solubility) and changes in the freshwater fluxes. Changes in sea ice affect Ω_{arag} by changing the air-sea gas exchange as well as the freshwater balance. The direct influence of temperature and salinity changes on the CaCO_3 solubility product (K'_{sp}) is negligible.

Large changes in Ω_{arag} and pH have been projected using ocean-only models (Kleypas et al., 1999; Caldeira and Wickett, 2003; Gangstø et al., 2008). Recently, the impact of climate change on ocean acidification also has been considered (Cao et al., 2007; McNeil and Matear, 2007; Orr et al., 2005, 2008). In most regions, a relatively small negative climate change feedback is found on changes in Ω_{arag} ($\approx 10\%$). An exception is the Arctic, where larger changes in Ω_{arag} are found for a simulation including climate change compared to one without climate change (McNeil and Matear, 2007). In a recent assessment, Orr et al. (2008) show by combining observations and model results that surface waters in the Arctic will become undersaturated within decades. They present an overview on the evolution of the saturation state in the Arctic with respect to both aragonite and calcite as inferred from three coupled models, including the NCAR CSM1.4-carbon.

Here, we complement earlier studies by using the fully coupled NCAR CSM1.4-carbon model to investigate the evolution of Ω_{arag} over the 21st century for the SRES A2 and B1 scenarios. In comparison to earlier work, we present a detailed analysis of the changes in the Arctic, including a quantification of underlying mechanisms, assess the global evolution of the ocean volume for different saturation regimes, and analyse spatio-temporal variability in saturation. In the next section, the model and experimental details are described. Then, model results are compared with observations, provid-

ing also statistical measures of data-model agreement. In the results section, projected global and regional changes in saturation state are described and climate feedbacks quantified. The change in Arctic saturation state is quantified both from direct model results and by combining observation-based estimates of the current saturation state (Jutterström and Andersson, 2005) with modeled changes following a similar approach as Orr et al. (2005, 2008). Before concluding, the projected anthropogenic changes are compared to modeled natural seasonal and interannual variations.

2 Methods

2.1 The NCAR CSM1.4-carbon model

Simulations were performed with the coupled climate-carbon cycle model NCAR CSM1.4-carbon (Doney et al., 2006; Fung et al., 2005). The core of the model used in this study is a modified version of the NCAR CSM1.4 coupled physical model, consisting of ocean, atmosphere, land and sea ice physical components integrated via a flux coupler without flux adjustments (Boville and Gent, 1998). The atmospheric model CCM3 is run with a spectral truncation resolution of $\approx 3.75^\circ$ (T31 grid) and 18 levels in the vertical (Kiehl et al., 1998). The ocean model is the NCAR CSM Ocean Model (NCOM) with 25 levels in the vertical and a resolution of 3.6° in longitude and 0.8° to 1.8° in latitude (T31x3 grid) (Gent et al., 1998). The sea ice component (CSIM) simulates the dynamic and thermodynamic evolution of ice concentration, thickness, temperature, velocity, and snow cover in response to forcing by the atmosphere and ocean (Bettge et al., 1996).

The model is known to simulate too much ice in the Northern Hemisphere (Weatherly et al., 1998). In particular the ice cover is too extensive in the North Pacific and North Atlantic. There is some contribution to the excess annual mean ice volume through larger-than-observed summer sea ice concentrations in the Arctic Ocean. The simulated preindustrial ice covered area in the Arctic Ocean is about 10% (summer) to 5% (winter) larger than estimated by Walsh (1978). The decreasing trend in summer sea ice cover during the last few decades is captured by the model but less pronounced. In the year 2000 the simulated ice covered area is about 40% (summer) to 10% (winter) larger than observed. Further, maximum thickness in the Arctic occurs against the Bering Strait, not against the Canadian Archipelago as observed (Weatherly et al., 1998).

The CSM1.4-carbon model combines the NCAR Land Surface Model (LSM) (Bonan, 1996) with the Carnegie-Ames-Stanford Approach (CASA) biogeochemical model (Randerson et al., 1997) and a derivative of the OCMIP-2 biotic carbon model (Najjar et al., 2007), where the nutrient uptake has been changed from a restoring to a prognostic formulation and an iron cycle has been added (Doney et al.,

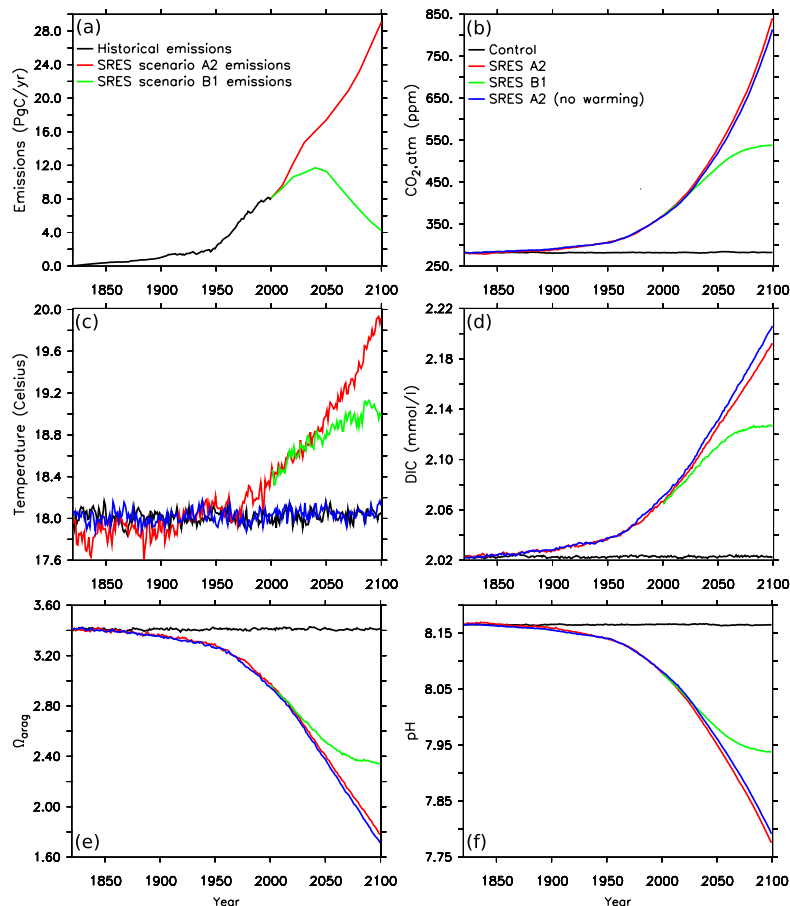


Fig. 1. Prescribed fossil fuel and land use CO₂ emissions (a) based on historical data (1820–2000, black) and the SRES-A2 (red) and B1 (green) scenarios (2000–2100). Simulated global annual mean atmospheric CO₂ (b), sea surface temperature (SST) (c), dissolved inorganic carbon (DIC) (d), aragonite saturation (Ω_{arag}) (e), and pH (f) at the ocean surface.

2006). Biological productivity is modulated by temperature, surface solar irradiance, mixed layer depth, and macro- and micronutrients (PO_4^{3-} , and iron). Following the OCMIP-2 protocols (Najjar et al., 2007), total biological productivity is partitioned 1/3 into sinking particulate organic matter (POC) flux and 2/3 into the formation of dissolved or suspended organic matter, where much of the latter is remineralised within the model euphotic zone. A constant export ratio of CaCO_3 to POC of 0.07 and constant Redfield ratios were used (Anderson and Sarmiento, 1994). A ratio of 0.07 is within (Yamanaka and Tajika, 1996; Sarmiento et al., 2002) or at the lower end (Jin et al., 2006; Kwon and Primeau, 2008) of the range given by others. Below the compensation depth of 75 m, 90% of the POC is remineralized within the first 1000 m, following a power-law parametrisation (Mar-

tin et al., 1987) and CaCO_3 is assumed to decrease exponentially with a depth scale of 3500 m. Any flux of POC or CaCO_3 reaching the sea floor is remineralized instantaneously. There is no feedback between changes in saturation state, pH or other carbonate chemistry variables and the biological carbon cycle implemented.

A sequential spin-up procedure including 1000 years of fully coupled simulation under preindustrial conditions was employed by Doney et al. (2006). Starting from this nearly steady state, four simulations over the period 1820 AD to 2100 AD were performed: (1) a 280 year long control simulation, two simulations with historical emissions over the industrial period followed by the (2) A2 IPCC emission scenario and (3) B1 IPCC emission scenario, and (4) a SRES A2 "no-warming case" simulation, where the concentrations of

greenhouse gases and other radiative agents were kept at their preindustrial values in the radiation module of the model. Differences in results between this no-warming simulation and the standard SRES A2 simulation are taken to reflect the impact of climate change on carbonate chemistry and other parameters.

The model was driven by emissions of CO₂ from fossil fuel and land use change (Fig. 1) as well as by anthropogenic sulfur emissions. Concentrations of the non-CO₂ greenhouse gases CH₄, N₂O, CFC-11, CFC-12 are prescribed according to reconstructions for 1820 to 2000 AD and as projected from emissions for 2000 to 2100 AD. The CFC-11 concentration is scaled to include the forcing of other halogenated species and SF₆. Emissions of non-CO₂ greenhouse gases were translated to concentration using formulations by Forster et al. (2007). A recurring annual cycle of ozone and natural sulfate aerosol were also included. Over the historical period, solar irradiance changes were prescribed following Wang et al. (2005) and spatially-explicit sulfate aerosols from explosive volcanic eruptions after Ammann et al. (2007). After year 2000, the solar irradiance was kept constant and no volcanic eruptions were assumed. Further details are given by Frölicher et al. (2009).

2.2 Carbonate chemistry and tracer data

For model evaluation, the gridded data from the Global Data Analysis Project (GLODAP) (Key et al., 2004) for DIC and Alk, and from the World Ocean Atlas 2001 (WOA01) (Conkright et al., 2002) for temperature (T), salinity (S), phosphate (PO_4^{3-}) and silicate ($\text{Si}(\text{OH})_4$) were used. The two data sets were regridded by multi-axis linear interpolation onto the model grid. The gridded GLODAP data have annual resolution and do not include the Arctic.

Carbonate chemistry, pH, carbonate ion concentration, and the saturation state have been calculated offline from modeled or observation-based quantities using the standard OCMIP carbonate chemistry routines (<http://www.ipsl.jussieu.fr/OCMIP/phase3/simulations/NOCES/HOWTO-NOCES-3.html>). In these routines, based on work by Dickson (2002), Millero (1995), and Mehrbach et al. (1973), the total pH scale (Lueker et al., 2000) is utilized. The apparent solubility product K'_{sp} is calculated after Mucci (1983) and the pressure dependency of chemical constants after Millero (1995). The observation-based carbonate variables were computed from monthly, seasonal, or annual means, depending on data availability. Annual means have been used for Alk and DIC, as well as for PO_4^{3-} and $\text{Si}(\text{OH})_4$ below 500 m. Seasonal means of T and S have been used below 1500 m. For the data-model comparison, annual averages from the simulated monthly carbonate data from 1990 to 1999 were used. Because the CSM model does not include $\text{Si}(\text{OH})_4$, a seasonal cycle of observation-based [$\text{Si}(\text{OH})_4$] from WOA01 has been used in all calculations of simulated pH and calcium carbonate saturation state.

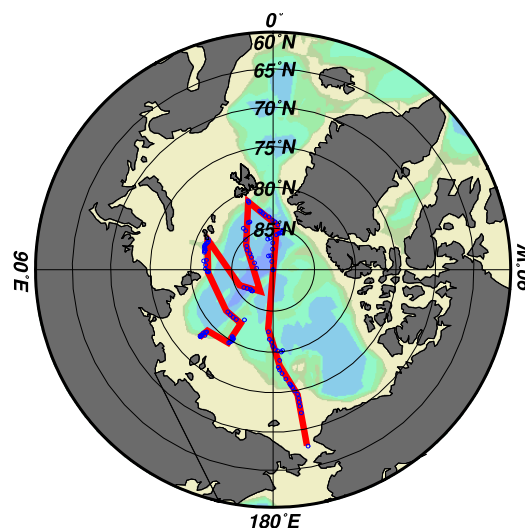


Fig. 2. Investigated Arctic Ocean transect where observation-based data is available from the ODEN-91, AOS-94, and ARCSYS-96 cruises.

Uncertainties in $[\text{CO}_3^{2-}]$ and Ω arising from this treatment of $\text{Si}(\text{OH})_4$ have been estimated to be less than 1% (Steinacher, 2007).

For the Arctic, observation-based estimates for Ω_{arag} and related variables were calculated from T , S , Alk, DIC, PO_4^{3-} , and $\text{Si}(\text{OH})_4$ measurements using the OCMIP chemistry routines and data from the Arctic Ocean Expedition 1991 (ODEN-91, cruise 77DN1991072), Arctic Ocean Section 1994 (AOS-94, cruise 18SN19940726), and the Arctic Climate System Study 1996 (ARCSYS-96, cruise 06AQ19960712) (Fig. 2, Jutterström and Anderson, 2005). These data are available from the preliminary CARINA database (http://cdiac.ornl.gov/oceans/CARINA/Carina_table.html). When not referring to this specific transect where observations are available, the Arctic Ocean is defined to be waters north of 65°N, except the Labrador Sea and the Greenland, Iceland, and Norwegian (GIN) Seas (<80°N and 35°W–18°E).

3 Results

3.1 Comparison of modeled aragonite saturation and CO_3^{2-} concentration with observation-based estimates

The modeled values and spatial pattern for Ω_{arag} and $[\text{CO}_3^{2-}]$ (averaged over the years 1990–1999 in the transient simulation) are compared with the data-based estimates in all major ocean basins (Fig. 3a). The correlation coefficient r between

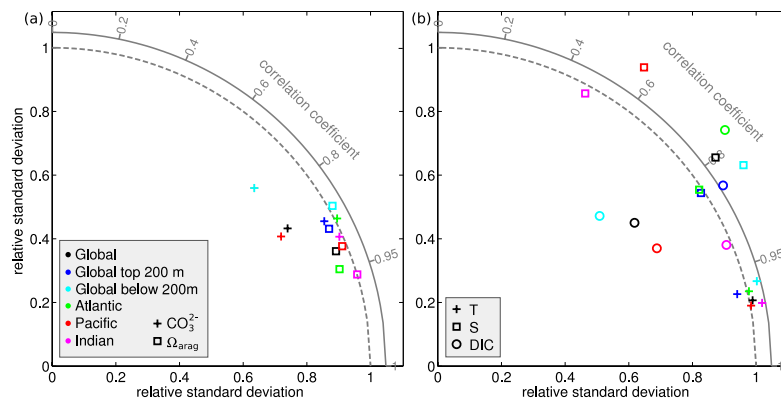


Fig. 3. (a) Taylor diagram (Taylor, 2001) conveying information about the pattern similarity between simulated and observation-based (GLODAP, WOA01) results for Ω_{arag} (squares) and $[\text{CO}_3^{2-}]$ (crosses). The observed field is represented by a point at unit distance from the origin along the abscissa. The distance from this point to the other points representing simulated fields, indicates the normalized r.m.s error. The simulated fields are averaged over the model years 1990–1999 and the results are shown for the entire global ocean (black), for the global ocean above (blue) and below (cyan) 200 m depth, as well as for the three major basins Atlantic (green), Pacific (red), and Indian Ocean (magenta), all of which include the respective part of the Southern Ocean. (b) Taylor diagram comparing simulated temperature (crosses), salinity (squares), and DIC (circles) fields with observation-based data for the same regions.

modeled and data-based Ω_{arag} is between 0.90 and 0.95 for the Atlantic, Pacific, and Global Ocean. The model represents the amplitude of variations in Ω_{arag} well in all major basins, as indicated by a relative standard deviation close to unity in the Taylor diagram (Fig. 3). Correlation coefficients are somewhat smaller (0.86 to 0.91) for $[\text{CO}_3^{2-}]$ than for Ω_{arag} because the data-model differences in Ω_{arag} decrease with depth relative to the differences in $[\text{CO}_3^{2-}]$. This results because the increase in the pressure-dependent solubility product K'_{sp} with depth decreases the weighting of the larger errors in deep-water $[\text{CO}_3^{2-}]$ (Fig. 4). Model biases in $[\text{CO}_3^{2-}]$ are particularly large in the Pacific where the relative standard deviation is smaller than indicated by observations.

The present distribution of $\Delta[\text{CO}_3^{2-}]$ (Fig. 4) and Ω_{arag} is governed by the distribution of DIC and Alk. $[\text{CO}_3^{2-}]$ is approximately proportional to the difference Alk–DIC. Consequently, the nutrient and carbon rich water of the North Pacific thermocline is undersaturated with respect to aragonite, while the relatively nutrient and carbon poor water of the North Atlantic thermocline is oversaturated. The increase of the solubility product K'_{sp} with pressure (depth) leads to a decrease of the saturation state in the deep ocean, although the carbonate ion concentration is relatively homogeneous below 1000 m.

Deviations in modeled and observation-based zonal mean $[\text{CO}_3^{2-}]$ and $\Delta[\text{CO}_3^{2-}]$ are less than $20 \mu\text{mol/l}$ in the deep Atlantic, the Southern Ocean, and the southern Pacific (Fig. 4). Larger deviations are found in the North Pacific and in the thermocline of the tropical Atlantic. $[\text{CO}_3^{2-}]$ is underesti-

ated in the tropical Atlantic related to too high DIC concentration in the model caused by nutrient trapping. On the other hand, the model underestimates export and remineralisation of organic matter in the North Pacific, causing too low DIC concentration and too high $[\text{CO}_3^{2-}]$ in the thermocline and at depth (Frölicher et al., 2009). Correspondingly, the modeled aragonite saturation horizon in the North Pacific is too deep compared with observation-based estimates.

In the Arctic Ocean, the modeled distribution of Ω_{arag} corresponds reasonably well to the observation-based estimates (years 1991–1996; Fig. 5). The observations suggest an oversaturation of around 50% in the top five hundred meter, around 25% at 1000 m depth and undersaturation below 2000 m. Horizontal gradients are relatively small along the transect. The model tends to underestimate Ω_{arag} at the surface (up to 0.3), while below 500 m Ω_{arag} is overestimated by 0.2 to 0.4. Correspondingly, the simulated saturation horizon is deeper than the observation-based horizon.

3.2 Projected global mean changes

Figure 1 provides projected global mean changes for a few key variables that broadly characterize the investigated scenarios. Anthropogenic carbon emissions increase to almost 30GtC yr^{-1} by the end of the century for the high-emission SRES A2, whereas emissions peak at around 12GtC yr^{-1} and decline thereafter in the more optimistic B1 scenario. Atmospheric CO_2 reaches 840 ppm and 538 ppm by the end of the century for the A2 and B1 scenario, respectively. Ocean surface DIC content increases on average by 8%

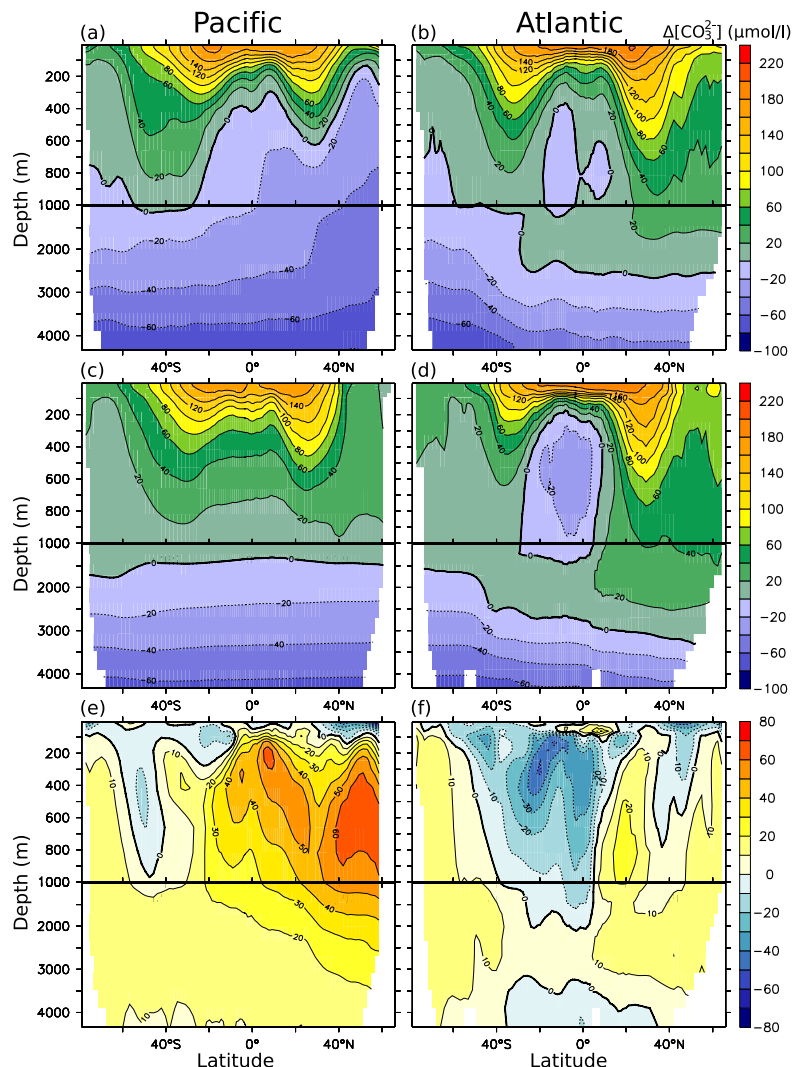


Fig. 4. Meridional sections through the Pacific (left) and the Atlantic (right) showing zonal mean of observed (top) and modeled (middle) supersaturation with respect to aragonite ($\Delta[\text{CO}_3^{2-}]$) in $\mu\text{mol/l}$. The saturation horizon is indicated by the thick line at $\Delta[\text{CO}_3^{2-}] = 0$. The bottom row shows the differences between model and measurements (model-observations). Simulated fields are averaged over the model years 1990–1999.

($0.17 \text{ mmol kg}^{-1}$) and by 5% ($0.10 \text{ mmol kg}^{-1}$). Mean aragonite saturation of surface water decreases from a preindustrial Ω_{arag} value of 3.4 to 1.8 (A2) and to 2.3 (B1) by the end of the century. Concomitant reductions in pH are 0.40 and 0.23 units. Global mean surface temperature increase is 1.97 and 0.94°C , reflecting the low climate sensitivity of the CSM1.4 (Friedlingstein et al., 2006).

Simulated climate change feedbacks on Ω_{arag} and pH are relatively small on the global scale. The CO_2 rise is slightly smaller in the no-warming case than in the standard SRES A2 simulation (Fig. 1), consistent with the low climate-carbon cycle feedback of the NCAR CSM1.4 (Fung et al., 2005). The increase in ocean surface DIC by the end of the century is about 8% larger without climate-feedback and consequently the decrease in surface Ω_{arag} is also slightly

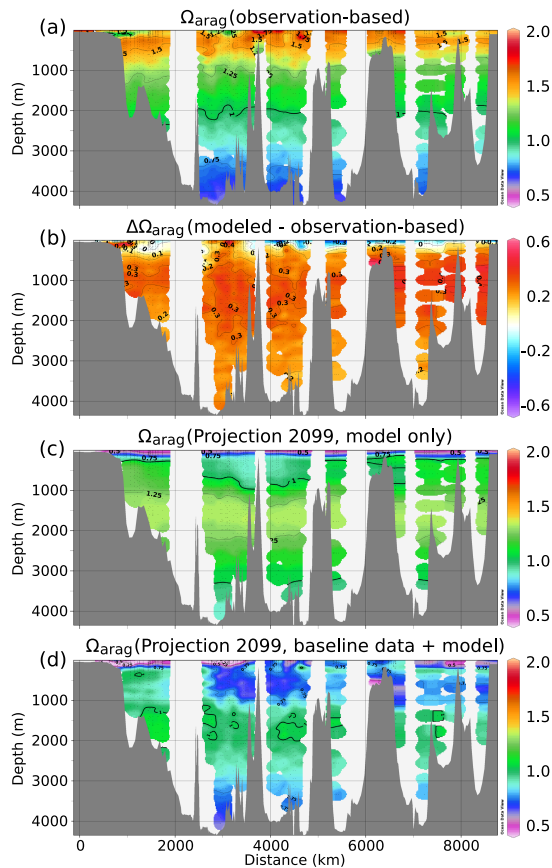


Fig. 5. (a) Observation-based present day aragonite saturation (Ω_{arag}) in the Arctic Ocean based on measurements from the ODEN-91, AOS-94, and ARCSYS-96 cruises during summer. The transect starts near the Bering Strait (0 km), leads then across the North Pole (2500 km) to Spitsbergen (3750 km), and from there to the Laptev Sea (8600 km), crossing the Eurasian Basin three times (see Fig. 2). (b) Difference between the modeled and the observation-based Ω_{arag} for the same transect and time. (c) Model-only projection of summer Ω_{arag} by 2099 under the A2 scenario, and (d) from combining modeled changes in Ω_{arag} and observation-based Ω_{arag} shown in (a).

enhanced (by about 4%). In contrast, the decrease in pH is about 4% smaller in the no-warming simulation. This opposite behavior is consistent with the analysis of Cao et al. (2007) for carbon emission scenarios, although they found a weaker effect on pH than on Ω_{arag} in their study with an Earth System Model of Intermediate Complexity. McNeil and Matear (2007) found a climate-change feedback reducing the change in Ω_{arag} by about 15% but almost no feedback on pH; they applied a scenario with prescribed CO_2 concen-

tration and not a scenario with prescribed carbon emission as done here (see Cao et al., 2007, for differences between emission and concentration scenarios).

Changes in DIC, Ω_{arag} , and pH are not linearly related to the atmospheric CO_2 increase (Thomas et al., 2007). The Revelle factor defined as the percentage change in CO_2 partial pressure divided by the percentage change in DIC increases with increasing CO_2 (Revelle and Suess, 1957; Takahashi et al., 1993). Doubling the atmospheric CO_2 from 280 to 560 ppm causes global mean surface DIC to increase by 6% (11 mmol kg^{-1}), whereas increasing CO_2 by a further 280 ppm to 840 ppm causes an additional DIC increase of only 3%. Therefore, a higher fraction of the emissions stays in the atmosphere for the high emission A2 scenario than for the low emission B1 scenario. On the other hand, surface mean aragonite saturation decreases by 1.1 unit for a doubling of CO_2 , but only by 0.5 units for the additional increase from 560 to 840 ppm. Similarly, pH decreases by 0.24 unit for the first 280 ppm increase and by 0.15 unit for the next 280 ppm.

3.3 Regional changes in saturation at the surface

It is projected that Ω_{arag} of surface waters will continue to decrease rapidly in all regions and that high latitude waters will become undersaturated (Figs. 6 and 7). Arctic surface waters are projected to become undersaturated with respect to aragonite within a few decades only, when following business as usual scenarios. Averaged over the entire Arctic, surface annual mean Ω_{arag} becomes less than unity in the model when atmospheric CO_2 exceeds 490 ppm (2040 AD in A2 and 2050 AD in B1). The Southern Ocean (65 to 80° S) becomes undersaturated on average about 20 years later in the A2 scenario, when atmospheric CO_2 concentration exceeds 580 ppm, consistent with Orr et al. (2005). By the end of the century, at 840 ppm, high latitude surface waters poleward of about 50° are projected to be undersaturated under the A2 scenario. Depending on the seasonal amplitude, short-time undersaturation during at least one month is reached several years earlier in many regions (Fig. 7b).

The biggest absolute changes in Ω_{arag} are found in tropical and subtropical surface waters. In the Tropics (30° N–30° S) Ω_{arag} is projected to drop from 4.2 (1820) to 2.3 in A2. For atmospheric CO_2 higher than 585 ppm, surface waters will have a zonal mean Ω_{arag} of less than three everywhere. These conditions are expected to have significant impacts on the ability of coral reef ecosystems to maintain their structures against the forces of erosion and dissolution (Kleypas et al., 2006).

Turning to the B1 scenario surface changes in Ω_{arag} are similar as for the A2 scenario until 2050, as both scenarios follow very similar pathways of atmospheric CO_2 . After 2050, the more gradual increase of atmospheric CO_2 in B1 slows down the decrease in Ω_{arag} . By 2100, undersaturation at the surface is limited to the Arctic Ocean and surface Ω_{arag}

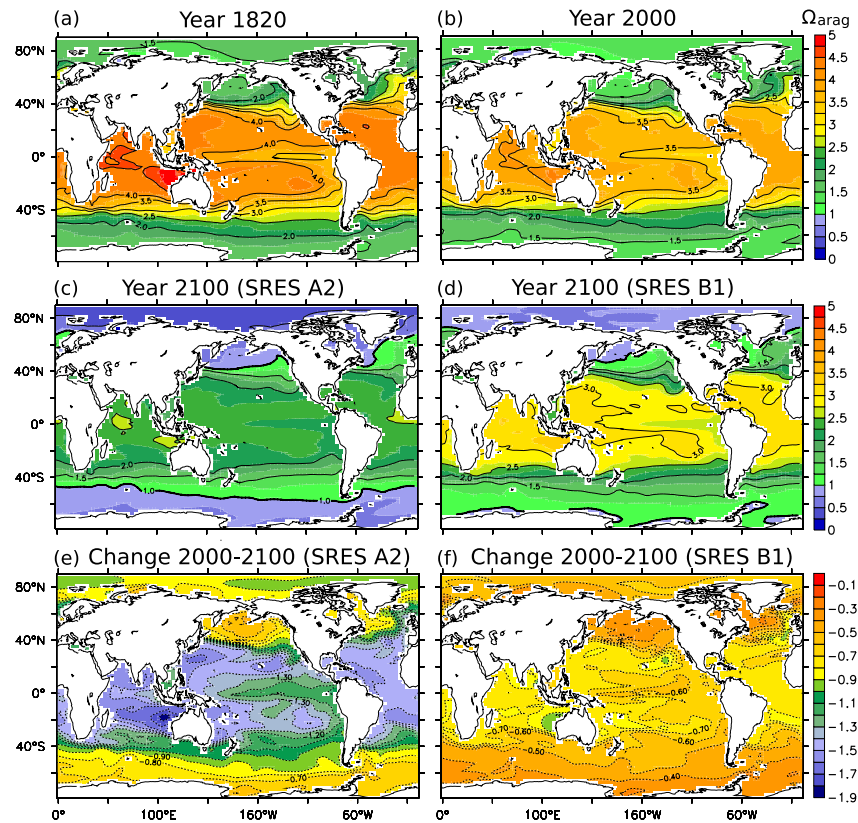


Fig. 6. Simulated aragonite saturation at the surface by the years 1820 (a), 2000 (b), and 2100 (c,d) for SRES scenarios A2 and B1. The largest changes in Ω_{arag} (e, f) are projected for the subtropics.

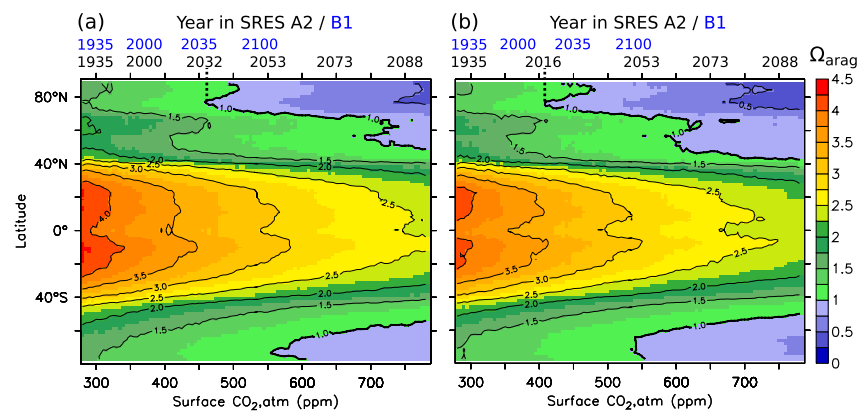


Fig. 7. Projected evolution of the (a) annual-mean and of the (b) lowest monthly mean zonally-averaged aragonite saturation Ω_{arag} for the SRES A2 scenario (model only). The evolution is plotted as a function of the annual-mean atmospheric CO_2 mixing ratio at the ocean surface. The corresponding years in the A2 and B1 scenarios are given at the top. The dotted line indicates the transition from supersaturation to undersaturation in zonal average Ω_{arag} at 77°N by 2032 and 2016, respectively.

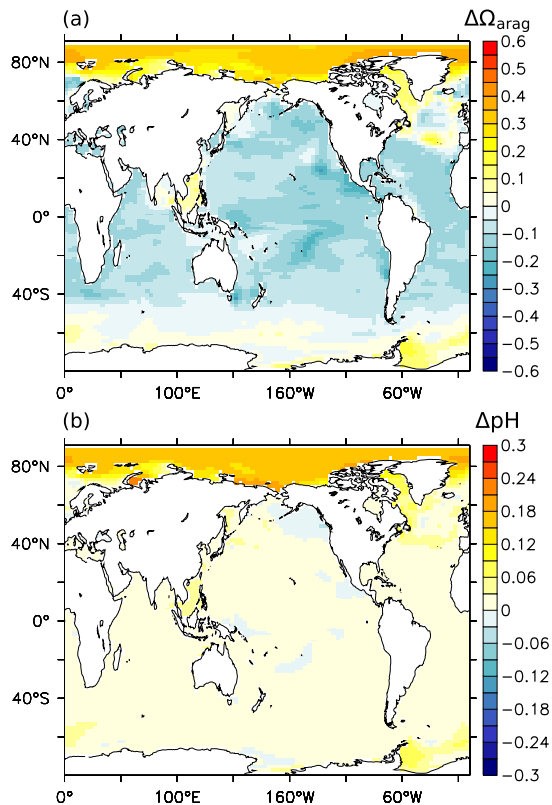


Fig. 8. Differences in projected surface Ω_{arag} (a) and pH (b) between the SRES A2 simulation with and without warming, averaged over the decade 2090–2099. Positive values indicate enhanced acidification by climate change, negative values indicate reduced acidification.

will stabilize at 2.5 to 3.0 in tropical and subtropical regions. The Southern Ocean surface remains slightly supersaturated throughout the B1 simulation.

The climate feedback on Ω_{arag} is negative in most regions of the oceans. Exceptions are the Arctic, the Labrador Sea and the high latitude North Atlantic, the Antarctic polar zone and a few coastal regions (Fig. 8). The modeled high latitude changes are linked to sea ice as discussed for the Arctic; we note that the model simulates too much sea ice in the North Atlantic and North Pacific (Weatherly et al., 1998) and the magnitude of the positive feedback in the high latitude North Atlantic may not be realistic. The climate feedback on pH is positive (or only slightly negative) in all regions.

3.4 Changes at depth and in the volume of supersaturated waters

Saturation is decreasing not only at the surface but also in the thermocline and the deep ocean as anthropogenic carbon continues to invade the ocean. This is illustrated by Hovmöller diagrams of $\Delta[\text{CO}_3^{2-}]$ for selected regions (Fig. 9). The thermocline changes in $[\text{CO}_3^{2-}]$ are relatively modest over the past 200 years. However, the modeled CO_3^{2-} concentrations decrease rapidly over this century and the saturation horizon, separating over- and undersaturated waters, shoals in most regions.

For the A2 scenario and over this century, the anthropogenic perturbation is projected to penetrate the top 3500 m in the North Atlantic, leading to a shoaling of the saturation horizon from 3250 m to 1300 m in mid and high latitudes and an extension of the undersaturated water masses in the low latitude Atlantic thermocline. In the Arctic and in the Southern Ocean supersaturation is already small today and the top 300 and 400 m will become undersaturated over the coming decades in the A2 scenario (Fig. 9). In the tropical Pacific the anthropogenic perturbation extends down to the depth of about 1000 m and the saturation horizon remains at 1500 m.

The anthropogenic perturbation causes a substantial loss of habitat for calcifying organisms. We introduce five classes of saturation levels: (i) more than 400% saturated ($\Omega_{\text{arag}} > 4$) as considered optimal for coral growth, (ii) 300 to 400% saturated, considered as adequate for coral growth, (iii) 200 to 300% saturated and (iv) 100 to 200% saturated, both considered as marginal to inadequate for coral growth (Langdon and Atkinson, 2005; Kleypas et al., 2006), and finally (v) undersaturated water ($\Omega_{\text{arag}} < 1$) considered to be unsuitable for pteropods (Feely et al., 2004; Orr et al., 2005). The volume of water that is more than 400% saturated is projected to vanish in the next three decades for the A2 and B1 scenario (Fig. 10). Water with Ω_{arag} larger than three is projected to vanish by 2070 ($\text{CO}_2 \approx 630$ ppm) in the A2 scenario and to be reduced to 11% of the respective preindustrial volume in the B1 scenario. Further, the volumes of waters with $2 < \Omega_{\text{arag}} < 3$ and $1 < \Omega_{\text{arag}} < 2$ are projected to decrease by about 75% and 30% over the industrial period and this century for the A2 scenario; corresponding changes are about half as large for B1 than for A2.

Overall the volume occupied by water oversaturated with respect to aragonite decreases from about 42% to 25% of the total ocean volume. We note that the model correctly simulates the total volume occupied by the first three classes, whereas the volume with an aragonite saturation between 100 and 200% is overestimated (crosses in Fig. 10). Therefore, these projections might be somewhat too optimistic.

3.5 Changes in the Arctic Ocean and climate feedbacks

Our projection that the Arctic ocean will become undersaturated with respect to aragonite in a few decades calls for a

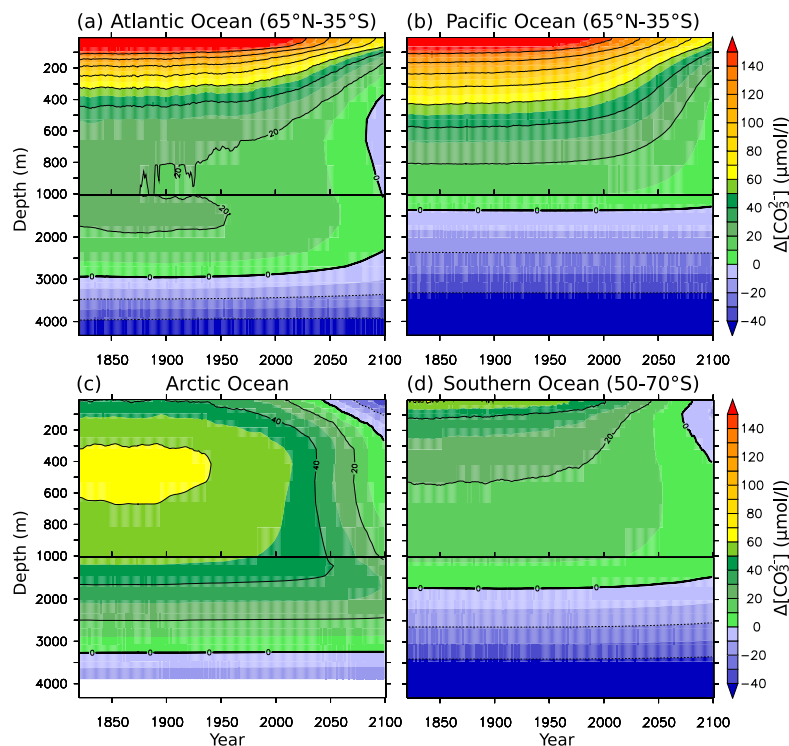


Fig. 9. Time-depth diagrams of simulated annual mean $\Delta[\text{CO}_3^{2-}]$ ($\mu\text{mol/l}$) with respect to aragonite for SRES A2; in the (a) Atlantic, (b) Pacific (c) Arctic, and (d) in the Southern Ocean.

more detailed analysis. We combine observation-based estimates of Ω_{arag} with the modeled changes to obtain an alternative estimate of the saturation state in the Arctic in 2100: $\Omega(t) = \Omega_{\text{obs.}}(t_0) + \Omega_{\text{model}}(t) - \Omega_{\text{model}}(t_0)$. In this way, Ω_{arag} is adjusted for known model biases similar to the approach of Orr et al. (2005), who applied simulated changes in DIC to observation-based estimates. The difference between adjusting Ω directly and calculating Ω from adjusted DIC and Alk concentrations is small ($<1\%$). In 2100 and for A2, the entire water column is projected to be undersaturated except some small regions at depths between 1000 m and 2000 m (Fig. 5). For comparison, the model-only projection also shows a distinct undersaturation in the top few hundred meters (Ω_{arag} between 0.25 and 0.75), whereas water remains oversaturated between 1000 and 3500 m in the model only projection as the modeled CO_3^{2-} concentration is biased high. In any case, the emerging undersaturation of the surface Arctic ocean is a robust feature and independent of these model biases.

Undersaturation occurs first in small regions and over short periods of the year. Its spatial and seasonal occurrence increases with rising atmospheric CO_2 as summarized in Table 1 for the investigated Arctic transect and for the

model-data approach. 10% of the surface area is projected to become undersaturated with respect to aragonite in at least one month of the year when atmospheric CO_2 has reached 409 ppm at year 2016 in the A2 and at year 2018 in the B1 scenario. At 428 ppm (2023 AD in A2, 2025 AD in B1) 10% of the surface is projected to become undersaturated in the annual mean, and at 450 ppm (2029 AD in A2, 2034 AD in B1) throughout the year. More than 50% of the surface waters of that section will become undersaturated at CO_2 levels of 534 ppm (2050 AD in A2, 2085 AD in B1), and at 765 ppm (2090 AD in A2) the entire water column is projected to become undersaturated.

The largest pH changes over the 21st century (-0.45 in A2, -0.23 in B1) are simulated in the Arctic Ocean. This turns the Arctic Ocean from a region with relatively high pH (0.06 units above the global average) to a region with very low pH (0.09 units below the global average by 2100 in A2). $[\text{H}^+]$ increases from 7.3 nmol/l to 20.8 nmol/l in A2 and to 12.35 nmol/l in B1, respectively.

Next the role of climate change and of different processes for the projected Arctic changes is addressed. Warming in the Arctic region is much higher than on global average

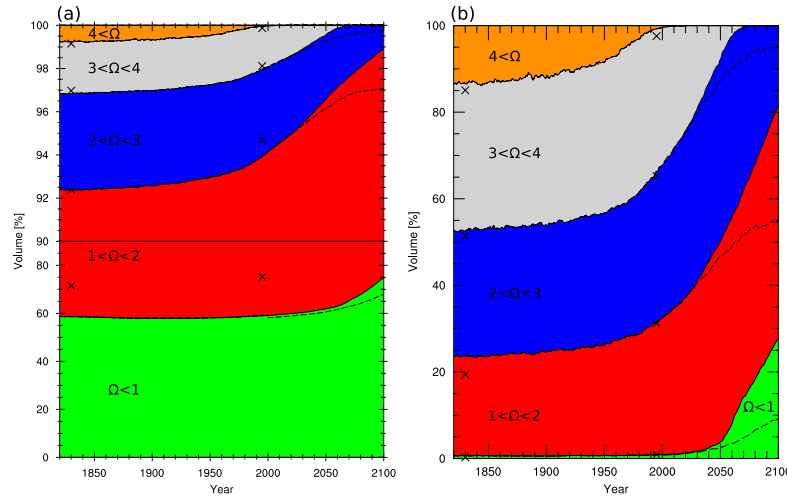


Fig. 10. Simulated global changes in the volume of supersaturated waters with respect to aragonite under the SRES A2. Panel (a) shows changes in the entire ocean volume, whereas panel (b) shows only changes for the top 200 m. Waters that are more than four times supersaturated (orange) are projected to vanish by the year 2010, and those that are 3 to 4 times supersaturated (gray) by the year 2070. The volumes of 2–3 and 1–2 times supersaturated waters (blue and red) decrease to 25% and 70% with respect to the preindustrial values by 2100. Thus the volume of undersaturated waters (green) increases by about 30% (or 17% of the total ocean volume) by 2100. The dashed lines indicate the volume changes under the SRES B1 scenario. The crosses denote the respective values derived from the GLODAP/WOA01 data set for 1995 and the estimated preindustrial values (1830) obtained by subtracting estimated anthropogenic CO_2 from DIC concentrations.

(polar amplification) and summer sea ice cover is projected to be significantly reduced. The Arctic Ocean is projected to become fresher in response to sea ice melt, altered evaporation and precipitation, and river input. Small climate feedbacks on Ω_{arag} and pH have been reported for the global ocean. However, climate change amplifies the decrease in average annual mean Arctic surface Ω_{arag} and pH by 22% and 27%, respectively (Fig. 8). In the simulation without global warming, alkalinity remains roughly constant in the Arctic, while the dissolved inorganic carbon concentration increases as a result of anthropogenic carbon uptake. Both surface Alk and DIC decrease in the simulation with global warming (Fig. 11). Additional freshwater input into the Arctic Ocean dilutes the tracer concentrations. The simulated decrease in DIC is smaller than that for Alk, mainly because the uptake of anthropogenic carbon tends to increase DIC. Overall, the difference between Alk and DIC, governing the CO_3^{2-} concentration, decreases more in the standard global warming simulation than in the simulation without climate change, thereby amplifying the changes in saturation state.

We can quantitatively attribute the changes of Alk and DIC, and thus $[\text{CO}_3^{2-}]$, to different mechanisms. A budget of the Alk and DIC fluxes entering and leaving the Arctic surface ocean (top 200 m) is established (Fig. 12) for the A2 scenario. The changes in the difference between Alk and DIC is taken as a proxy for changes in the CO_3^{2-} concen-

tration. This approximation works well in the Arctic surface ocean (inset of Fig. 12). We note that the regression slope is slightly different in the no-warming simulation (0.43, $r^2=0.94$) than in the standard global warming simulation (0.38, $r^2=0.90$). In the no-warming simulation, the freshwater balance, ocean circulation, the marine biological cycle and Alk remain mostly unperturbed. We note a small perturbation of the global hydrologic cycle, which arises most likely due to the interaction of increasing atmospheric CO_2 with the terrestrial biosphere. However, the most relevant changes are the uptake of anthropogenic (excess) carbon by gas exchange through the air-sea interface and the export of excess carbon out of the top 200 m by surface-to-deep and lateral (to the North Atlantic and through the Bering Strait) exchange. The resulting storage of anthropogenic carbon in the top 200 m increases DIC and decreases (Alk-DIC) by 0.10 mmol/l by 2100. In the standard global warming simulation, additional freshwater input dilutes both Alk and DIC. The decrease in Alk and DIC by freshwater input is proportional to their concentration and thus larger for Alk than for DIC. As a result, (Alk-DIC) is reduced by 0.035 mmol/l on average. The dilution of DIC by freshwater lowers the CO_2 partial pressure which in combination with an increase in ice-free area enhances uptake of anthropogenic carbon through gas exchange. Increased uptake is further promoted by the somewhat higher atmospheric CO_2 concentration in

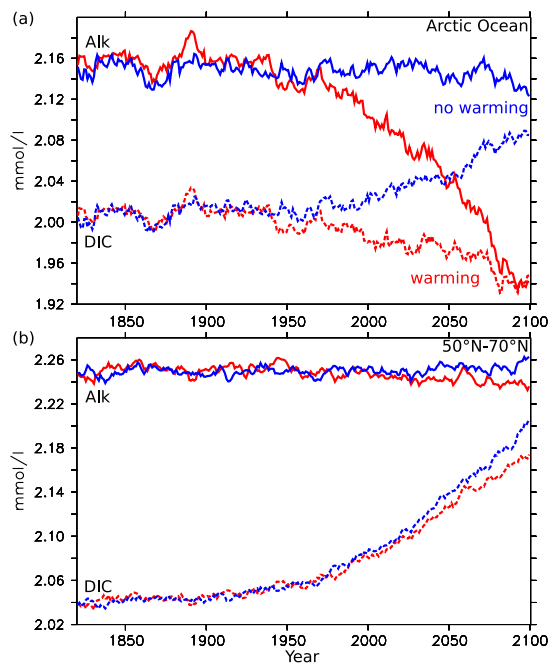


Fig. 11. Simulated annual mean alkalinity and DIC surface concentrations from 1820 to 2100 in the Arctic Ocean (a) and between 50° N and 70° N (b). Without warming (blue) both regions show similar changes. Including climate change (red) changes alkalinity and DIC in the North Pacific and North Atlantic only slightly and the difference Alk-DIC, which is approx. proportional to $[\text{CO}_3^{2-}]$, is almost constant. This is representative for all regions, except the Arctic, where the alkalinity is strongly reduced and the difference Alk-DIC is virtually zero by the end of the 21th century.

the warming than in the no-warming simulation. On the other hand the dilution of Alk increases the CO_2 partial pressure, which tends to decrease the uptake of anthropogenic carbon. The net effect is an increase in CO_2 uptake by about 40% in the warming simulation relative to the no-warming simulation. The export of excess carbon out of the top 200 m by physical transport is also enhanced in the warming simulation. Further, the projected changes in environmental conditions enhance marine biological productivity and the export of organic material and CaCO_3 out of the Arctic surface. As a result, surface (Alk-DIC) is increased by 0.013 mmol/l. Thus, the biological feedbacks partly counter the physically-driven climate feedback. Considering all fluxes, (Alk-DIC) decreases by 0.036 mmol/l (38%) more in the warming than in the no-warming simulation. This may be compared to a 0.013 mmol/l (34%) higher decrease in $[\text{CO}_3^{2-}]$.

Freshwater input at the ocean surface in the Arctic is increased due to melting of sea ice, as well as increased precipi-

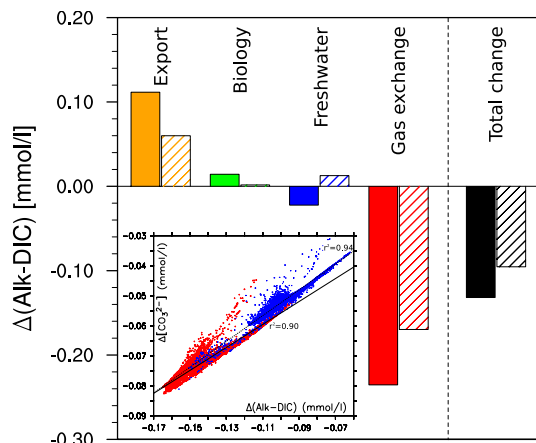


Fig. 12. Projected changes in the annual mean difference Alk-DIC, which is approximately proportional to $[\text{CO}_3^{2-}]$, from 1820 to 2100 under the A2 scenario in the top 200 m of the Arctic Ocean. The total change (black) is composed of changes in the net CO_2 uptake by gas-exchange with the atmosphere (red), changes in the freshwater flux at the ocean surface (blue), as well as changes in biology (green) and in the export of excess carbon by surface-to-deep and lateral exchange (orange). The difference between the simulation without warming (hatched) and the standard global warming simulation (solid) quantifies the impact of climate change on the individual components and on the total amplification of the carbonate ion reduction. The inset relates the changes in the difference Alk-DIC to the changes in $[\text{CO}_3^{2-}]$ for all grid boxes that contribute to the Arctic budget and for the warming (red) and no-warming (blue) simulations. The strong correlation indicates that the difference Alk-DIC is a reasonable proxy for $[\text{CO}_3^{2-}]$ in the Arctic surface ocean.

itation and reduced evaporation. In the CSM 1.4, rivers deliver pure freshwater to the ocean, with DIC and alkalinity set to zero. Land-ice is absent from the simulations. The annual mean sea ice volume in the Arctic Ocean is reduced by 69% in the A2 simulation from $3.48 \times 10^4 \text{ km}^3$ (preindustrial) to $1.07 \times 10^4 \text{ km}^3$ (2100). The summer sea ice cover is reduced by 74% from $8.7 \times 10^6 \text{ km}^2$ (preindustrial) to $2.3 \times 10^6 \text{ km}^2$ (2100), which corresponds to a cover of 88% and 23% of the total Arctic Ocean surface ($9.9 \times 10^6 \text{ km}^2$), respectively. The reduced sea ice cover allows gas exchange to occur in a larger area and the availability of light is increased in the ocean surface layer. The summer sea ice extent in the CSM is 10–40% higher than observed by 2000 (Fig. 13). The reduction in sea ice cover is at the lower end of the range of projections for the 21th century. More specifically, the simulated decrease from 2000 to 2100 in the A2 scenario is only slightly larger than the rapid reduction observed during the last decade. Holland et al. (2006) project abrupt reduction in summer Arctic sea ice and near ice-free conditions by 2040

528

M. Steinacher et al.: Arctic ocean acidification

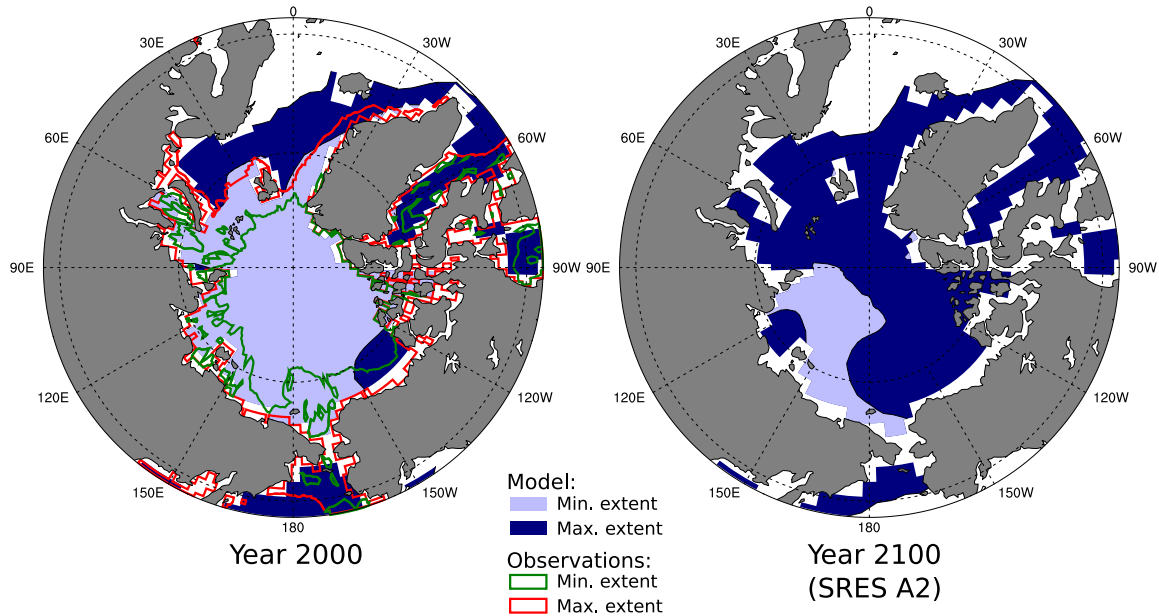


Fig. 13. Sea ice cover in the Arctic Ocean by the years 2000 and 2100. The color shading shows simulated minimum (light blue) and maximum (dark blue) sea ice extent. Lines indicate minimum (green) and maximum (red) sea ice extent as observed in the year 2000 (Walsh, 1978). The sea ice extent is defined here as the area where the sea ice concentration is above 50%.

for the SRES A1B scenario, whereas in our SRES A2 simulation summer sea ice cover remains above 70% of the total Arctic Ocean surface until about 2050. The simulated winter ice cover declines only little and remains larger than the observed present-day ice cover throughout the simulation. If the projections of rapid summer sea ice decline are true, the projected effects we see on the Arctic carbonate system will be even more pronounced than seen in the CSM simulations. Freshwater input and warming also cause an increase in stratification, here defined by the density difference between the surface and 200 m depth.

Modelled marine biological production in the Arctic increases due to a number of factors (Steinacher, 2007). Most importantly, enhanced availability of photosynthetic active radiation in response to reduced sea ice cover (and changes in cloud cover) and ocean surface warming stimulate productivity. Simulated shortwave irradiance increases by 200% at the air-water interface and sea surface temperature increases by 0.31°C in scenario A2 by 2100. On the other hand, iron and phosphate concentration decrease only by a few percent. We note that production is limited by temperature and light, but not by phosphate and iron. The averaged mixed layer depth remains roughly unchanged.

3.6 Seasonal and interannual variability of Ω_{arag}

The simulated seasonal and interannual variability of Ω_{arag} is small compared to the projected anthropogenic changes discussed above. The zonal mean seasonal cycle of Ω_{arag} shows the typical quadrupole space-time pattern (Fig. 14a, b) with largest positive seasonal deviations in summer and largest negative deviations in winter in both hemispheres and at mid-latitudes. This seasonal cycle is driven by low summer DIC and high winter DIC values linked to thermally driven air-sea exchange and nutrient drawdown during the spring and summer growing season, as well as winter convection and mixing. The seasonal variability of simulated Ω_{arag} is small in the high latitude and in the tropical surface ocean (± 0.1 in zonal mean Ω_{arag} ; less than 5%). In Northern Hemisphere mid-latitudes deviations up to 15–20% (0.35–0.40 in zonal mean Ω_{arag}) can be found, with maximum values from August to October and minimum values from February to April (Fig. 14). Largest seasonal amplitudes ($\Delta\Omega_{\text{arag}}$ up to 0.7) can be found around 40° N in the western Pacific and Atlantic, as well as in the South Atlantic near the coast of Argentina. These regions correspond to regions of high primary productivity and large seasonality in production. Surface Ω_{arag} is increased at the end and after the high production phase, when nutrient and DIC concentrations are reduced.

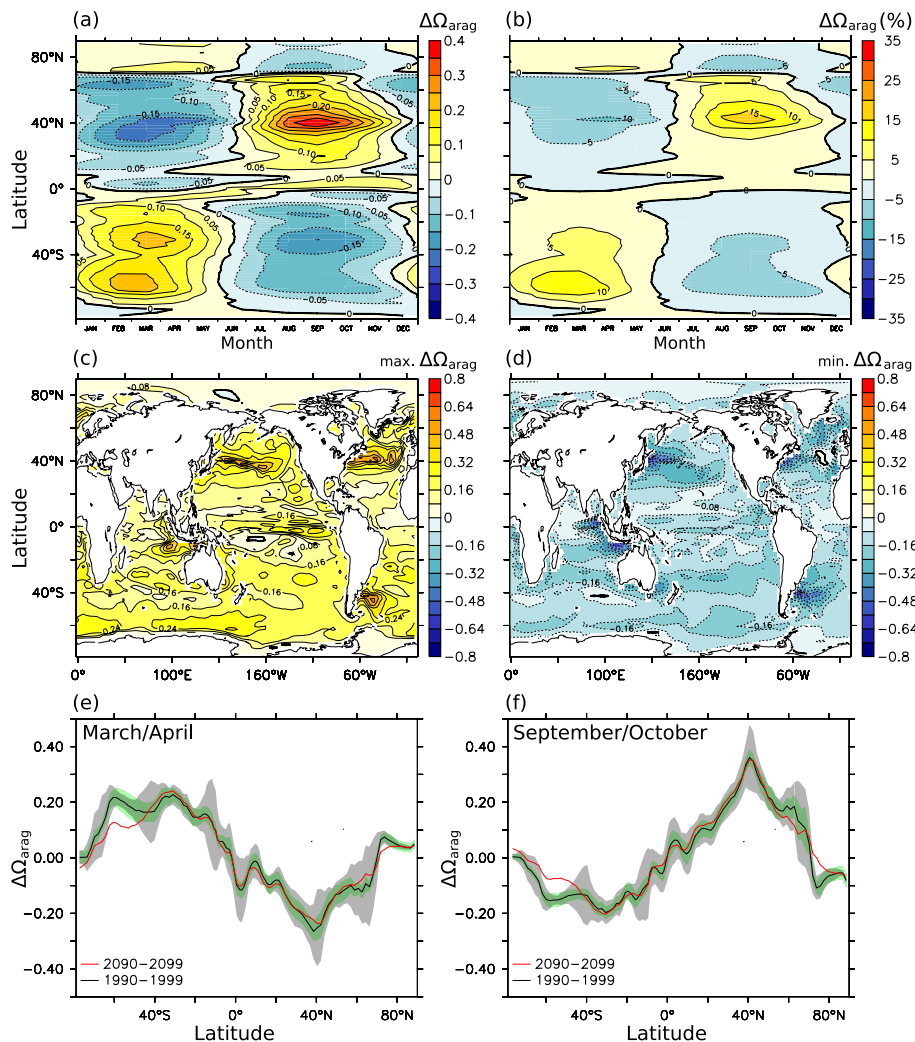


Fig. 14. Simulated seasonal variability of zonal mean surface Ω_{arag} . Average deviation from the annual mean for the decade 1990–1999, in absolute values (a) and relative to the annual mean Ω_{arag} (b, in percent). Maps of maximum positive (c) and negative (d) anomalies in surface Ω_{arag} for the decade 1990–1999 (maximum deviation from the decadal mean at each grid point and for every month). Average deviation from the annual mean in March/April (e) and September/October (f) for the decades 1990–1999 (black line) and 2090–2099 (red line) under SRES A2. The shaded areas indicate the interannual variability (green, $\pm\sigma$) and the variability across different longitudes (grey, $\pm\sigma$) for the decade 1990–1999.

The seasonal variability in the Arctic Ocean is out of phase with the general Northern Hemisphere seasonal signal and shows the same seasonal pattern as modeled for the Southern Hemisphere. Melting of Arctic sea ice decreases the supersaturation over the summer. The variability in sea ice cover and the associated freshwater input lead to a strong seasonal variability of alkalinity (up to $\pm 4\%$) and DIC, which outbal-

ances the relatively small variability in temperature. Overall, seasonal variability in Ω_{arag} is small (< 0.1) compared to the simulated anthropogenic changes in the Arctic.

The modeled large scale amplitudes and patterns of the seasonal variability do not show significant changes between 1820 and 2100 in the transient simulation under the A2 scenario in most regions. In the Southern Ocean (south of 40°S)

and around 50° N and 75° N the seasonal amplitude tends to be slightly reduced (Fig. 14). However, as the annual mean Ω_{arag} decreases with increasing CO_2 , the relative seasonal variability increases from about +10%/−5% at 40° N in 1820 to about +25%/−15% in 2100. Finally, we note that the interannual variability in zonal mean Ω is small (less than ± 0.1 in surface Ω_{arag}) both compared to the anthropogenic change as well as compared to zonal variability (Fig. 14). Because calcification is linearly coupled with production in the CSM1.4, interannual variability that could be caused by variations in the CaCO_3 /organic carbon formation and remineralization rates is not captured by the model.

4 Discussion and conclusions

The changes in the acid-base state of ocean waters in response to human induced carbon emissions have been analyzed with the NCAR CSM1.4-carbon coupled climate-carbon cycle model for two transient greenhouse gas emission scenarios. The model is able to reproduce the large-scale, contemporary distribution of carbonate and the saturation state with respect to aragonite reasonably well. A number of caveats are nevertheless worth mentioning. Results simulated for the North Pacific should be viewed with caution as the model overestimates saturation in this basin. The NCAR CSM1.4 model has a climate sensitivity near the lower bound of current estimates and simulated magnitudes of climate feedbacks on changes in saturation and pH might be somewhat low. However, these feedbacks play a minor role in most regions. Further, the model does not distinguish between different mineral phases (calcite, aragonite, high-Mg calcite) of calcium carbonate (Gangstø et al., 2008) and therefore has a single length-scale for calcium carbonate remineralization independent of seawater saturation state. The model does not include an active sediment reservoir or sediment burial and further research is needed to quantify the magnitude of a potential buffering of the simulated changes in saturation by re-dissolution of calcium carbonate from ocean sediments. Langdon (2002) suggests that dissolution rates on reefs, banks, and tropical shelves will not be able to buffer the $[\text{CO}_3^{2-}]$ decrease over the next 50–100 years.

Our study with a coupled climate-carbon cycle model supports the important finding of earlier studies that the acid-base state of the global ocean is currently undergoing large and rapid changes (Orr et al., 2005; Caldeira and Wickett, 2003) in response to anthropogenic carbon emissions with potentially large negative socio-economic impacts (Hoegh-Guldberg, 2005). The saturation state with respect to aragonite, calcite, or high-magnesium calcite is decreasing worldwide, causing a gradual worsening of living conditions for corals, pteropods, foraminiferas and coccolithophorides and potentially also for non-calcifying marine organisms (e.g. Fabry et al., 2008). Orr et al. (2005) have pointed out that the

Southern Ocean will become undersaturated for aragonite if atmospheric CO_2 increases beyond 560 ppm.

We highlight that the Arctic Ocean surface becomes undersaturated with respect to aragonite at even lower CO_2 concentration. The combination of observation-based estimates of Ω_{arag} in the Arctic (Jutterström and Anderson, 2005) with NCAR CSM1.4-carbon model projection indicates that 10% of the surface water along the investigated Arctic transect will become undersaturated for at least one month of the year when atmospheric CO_2 exceeds 409 ppm. This concentration is only 25 ppm higher than today's value and projected to be reached within the next decade for all SRES scenarios (Plattner et al., 2008; Meehl et al., 2007) and within the next two decades for the recent set of multi-gas mitigation scenarios (Van Vuuren et al., 2008; Strassmann et al., 2008). The entire water column in the Arctic is projected to become undersaturated within this century if anthropogenic carbon emissions continue to grow along the SRES A2 business-as-usual trajectory. Even under the relatively low- CO_2 scenario B1, more than 50% of the Arctic surface waters are projected to become undersaturated. These results are consistent with the study by (Orr et al., 2008) who analyzed Arctic acidification based on results from different AOGCMS, including the NCAR CSM1.4-carbon.

Atmospheric CO_2 will very likely exceed 400 ppm in the next one or two decades given current carbon emission trends and the inertia of the energy and the whole socio-economic system. The question is thus not whether undersaturation will occur in the Arctic, but how big its magnitude will be, how large an area will be affected by undersaturation, and over how many months of the year undersaturation will be prevalent. Our findings, combined with the emerging evidence on the impacts of aragonite undersaturation on marine organisms imply that not only radiative forcing or temperature, but also atmospheric CO_2 concentration should be included as a target in climate policy analyses and in the development of mitigation scenarios with integrated assessment models. Our subjective assessment is that atmospheric CO_2 should not exceed 450 ppm in order to avoid the risk of large changes in marine ecosystems.

The loss in volume of water with saturation has been quantified. We consider five saturation regimes for ease of discussion. Water with an aragonite saturation of more than 300%, considered suitable for coral growth, are projected to vanish completely in the second half of the century for the A2 scenario. Water with a saturation of more than 400%, considered optimal for coral growth, covered about 16% of the surface at preindustrial time and will be gone in the next few years. Overall, the volume of water supersaturated with respect to aragonite decreases strongly in the A2 and B1 scenarios considered here, with potentially adverse effect also on species living on the ocean floor and in the deep (Guinotte et al., 2006).

Our analysis shows that in addition to the uptake of anthropogenic carbon by air-sea gas exchange, freshwater input

M. Steinacher et al.: Arctic ocean acidification

531

from increased precipitation and ice melt contributes to the decrease in Arctic saturation state, while an increase in marine biological production slightly counteracts the decline. Additional freshwater input from land ice melt has not been considered here and is expected to slightly lower projected saturation states (Orr et al., 2008). Seasonal variability in saturation is significant in mid-latitudes regions, but small at high latitudes. The anthropogenic changes in saturation are superimposed on the seasonal variations. We did not find substantial changes in seasonal variability over this century in the NCAR model. Interannual variability in saturation is found to be small. These findings are consistent with results obtained at time series stations (HOT, BATS), which show that the anthropogenic signal is clearly distinguishable from seasonal and interannual variability (Bates, 2001; Brix et al., 2004; Kleypas et al., 2006).

In conclusion, human activities are perturbing the ocean and the habitats for marine organisms. The results of this study and of Feely et al. (2008) for the coastal North Pacific and Orr et al. (2008) for the Arctic show that undersaturation of surface waters with respect to aragonite is likely to become reality in a few years only.

Acknowledgements. This work was funded by the European Union projects CARBOOCEAN (511176-2) and EUROCEANS (511106-2) and is a contribution to the “European Project on Ocean Acidification” (EPOCA) which received funding from the European Community’s Seventh Framework Programme (FP7/2007-2013) under grant agreement no. 211384. Additional support was received from the Swiss National Science Foundation and SCD acknowledges support from the US National Science Foundation (NSF) grant ATM-0628582. Simulations were carried out at the Swiss National Supercomputing Centre (CSCS) in Manno, Switzerland.

Edited by: C. Heinze

References

- Ammann, C. M., Joos, F., Schimel, D. S., Otto-Bliesner, B. L., and Tomas, R. A.: Solar influence on climate during the past millennium: Results from transient simulations with the NCAR Climate System Model, *P. Natl. Acad. Sci. USA*, 104, 3713–3718, doi:10.1073/pnas.0605064, 2007.
- Anderson, L. A. and Sarmiento, J. L.: Redfield ratios of remineralization determined by nutrient data analysis, *Global Biogeochem. Cy.*, 8, 65–80, 1994.
- Bates, N. R.: Interannual variability of oceanic CO₂ and biogeochemical properties in the Western North Atlantic subtropical gyre, *Deep-Sea Res. Pt. II*, 48, 1507–1528, 2001.
- Bettge, T. W., Weatherly, J. W., Washington, W. M., Pollard, D., Briegleb, B. P., and Strand, W. G.: The CSM Sea Ice Model, NCAR Tech. Note NCAR/TN-425+STR, National Center for Atmospheric Research, Boulder, Colorado, USA, 1996.
- Bonan, G. B.: The NCAR Land Surface Model (LSM version 1.0) coupled to the NCAR Community Climate Model, NCAR Tech. Note NCAR/TN-429+STR, National Center for Atmospheric Research, Boulder, Colorado, USA, 1996.
- Boville, B. A. and Gent, P. R.: The NCAR Climate System Model, version one, *J. Climate*, 11, 1115–1130, 1998.
- Brix, H., Gruber, N., and Keeling, C. D.: Interannual variability of the upper ocean carbon cycle at station ALOHA near Hawaii, *Global Biogeochem. Cy.*, 18, GB4019, doi:10.1029/2004GB002245, 2004.
- Caldeira, K. and Wickett, M. E.: Anthropogenic carbon and ocean pH, *Nature*, 425, p. 365, 2003.
- Cao, L., Caldeira, K., and Jain, A. K.: Effects of carbon dioxide and climate change on ocean acidification and carbonate mineral saturation, *Geophys. Res. Lett.*, 34, L05607, doi:10.1029/2006GL028605, 2007.
- Conkright, M. E., Antonov, J. I., Boyer, T. P., Locarnini, R. A., O’Brien, T. D., Stephens, C., and Garcia, H. E.: World Ocean Atlas 2001, vol. 49–52 of NOAA Atlas NEDIS, US Govt. Printing Office, Washington, D. C., 2002.
- Dickson, A.: Handbook of methods of the analysis of the various parameters of the carbon dioxide system in seawater, US Dep. of Energy, Washington, D. C., 2002.
- Doney, S., Lindsay, K., Fung, I., and John, J.: Natural variability in a stable, 1000-yr global coupled climate-carbon cycle simulation, *J. Climate*, 19, 3033–3054, 2006.
- Doney, S. C., Fabry, V. J., Feely, R. A., and Kleypas, J. A.: Ocean acidification: the other CO₂ problem, *Ann. Rev. Mar. Sci.*, 1, 169–192, doi:10.1146/annurev.marine.010908.163834, 2009.
- Fabry, V. J.: Marine Calcifiers in a High-CO₂ Ocean, *Science*, 320, 1020–1022, 2008.
- Fabry, V. J., Seibel, B. A., Feely, R. A., and Orr, J. C.: Impacts of ocean acidification on marine fauna and ecosystem processes, *ICES J. Mar. Sci.*, 65, 414–432, 2008.
- Feely, R. A., Sabine, C. L., Kitack, L., Berelson, W., Kleypas, J., Fabry, V. J., and Millero, F. J.: Impact of Anthropogenic CO₂ on the CaCO₃ System in the Oceans, *Science*, 305, 362–366, 2004.
- Feely, R. A., Sabine, C. L., Hernandez-Ayon, J. M., Ianson, D., and Hales, B.: Evidence for Upwelling of Corrosive “Acidified” Water onto the Continental Shelf, *Science*, 320, 1490–1492, doi: 10.1126/science.1155676, published online 22 May 2008, 2008.
- Fine, M. and Tchernov, D.: Scleractinian Coral Species Survive and Recover from Decalcification, *Science*, 315, p. 1811, 2007.
- Forster, P., Ramaswamy, V., Artaxo, P., Bernsten, T., Betts, R., Fahey, D. W., Haywood, J., Lean, J., Lowe, D. C., Myhre, G., Nganga, J., Prinn, R., Raga, G., Schulz, M., and Dorland, R. V.: Climate Change 2007: The Physical Science Basis. Contribution of Working Group I to the Fourth Assessment Report of the Intergovernmental Panel on Climate Change, chap. Changes in Atmospheric Constituents and in Radiative Forcing, Cambridge University Press, Cambridge, United Kingdom and New York, NY, USA, 129–234, 2007.
- Friedlingstein, P., Cox, P., Betts, R., Bopp, L., Von Bloh, W., Brovkin, V., Cadule, P., Doney, S., Eby, M., Fung, I., Bala, G., John, J., Jones, C., Joos, F., Kato, T., Kawamiya, M., Knorr, W., Lindsay, K., Matthews, H. D., Raddatz, T., Rayner, P., Reick, C., Roeckner, E., Schnitzler, K. G., Schnur, R., Strassmann, K., Weaver, A. J., Yoshikawa, C., and Zeng, N.: Climate-Carbon Cycle Feedback Analysis: Results from the C⁴MIP Model Intercomparison: Evolution of carbon sinks in a changing climate, *J. Climate*, 19, 3337–3353, 2006.

- Frölicher, T. L., Joos, F., Plattner, G. K., Steinacher, M., and Doney, S. C.: Natural variability and anthropogenic trends in oceanic oxygen in a coupled carbon cycle-climate model ensemble, *Global Biogeochem. Cy.*, 23, 1–15, doi:10.1029/2008GB003316, 2009.
- Fung, I., Doney, S., Lindsay, K., and John, J.: Evolution of carbon sinks in a changing climate, *P. Natl. Acad. Sci. USA*, 102, 11201–11206, 2005.
- Gangstø, R., Gehlen, M., Schneider, B., Bopp, L., Aumont, O., and Joos, F.: Modeling the marine aragonite cycle: changes under rising carbon dioxide and its role in shallow water CaCO₃ dissolution, *Biogeosciences*, 5, 1057–1072, 2008, <http://www.biogeosciences.net/5/1057/2008/>.
- Gattuso, J.-P., Frankignoulle, M., Bourge, I., Romaine, S., and Buddemeier, R. W.: Effect of calcium carbonate saturation of seawater on coral calcification, *Global Planet. Change*, 18, 37–46, 1998.
- Gehlen, M., Gangstø, R., Schneider, B., Bopp, L., Aumont, O., and Ethe, C.: The fate of pelagic CaCO₃ production in a high CO₂ ocean: a model study, *Biogeosciences*, 4, 505–519, 2007, <http://www.biogeosciences.net/4/505/2007/>.
- Gent, P. R., Bryan, F. O., Danabasoglu, G., Doney, S. C., Holland, W. R., Large, W. G., and McWilliams, J. C.: The NCAR Climate System Model global ocean component, *J. Climate*, 11, 1287–1306, 1998.
- German Advisory Council on Global Change: The Future Oceans – Warming up, Rising High, Turning Sour, WGBU Special Report, German Advisory Council on Global Change (WBGU), Berlin, Germany, 2006.
- Guinotte, J., Orr, J., Cairns, S., Freiwald, A., Morgan, L., and George, R.: Will human-induced changes in seawater chemistry alter the distribution of deep-sea scleractinian corals?, *Front. Ecol. Environ.*, 4, 141–146, 2006.
- Heinze, C.: Simulating oceanic CaCO₃ export production in the greenhouse, *Geophys. Res. Lett.*, 31, L16308, doi:10.1029/2004GL020613, 2004.
- Hoegh-Guldberg, O.: Low coral cover in a high-CO₂ world, *J. Geophys. Res.*, 110, C09S06, doi:10.1029/2004JC002528, 2005.
- Holland, M. M., Bitz, C. M., and Tremblay, B.: Future abrupt reductions in the summer Arctic sea ice, *Geophys. Res. Lett.*, 33, L23503, doi:10.1029/2006GL028024, 2006.
- Iglesias-Rodriguez, M. D., Halloran, P. R., Rickaby, R. E. M., Hall, I. R., Colmenero-Hidalgo, E., Gittins, J. R., Green, D. R. H., Tyrrell, T., Gibbs, S. J., von Dassow, P., Rehm, E., Armbrust, E. V., and Boessenkool, K. P.: Phytoplankton Calcification in a High-CO₂ World, *Science*, 320, 336–340, doi:10.1126/science.1154122, 2008.
- Jin, X., Gruber, N., Dunne, J. P., Sarmiento, J. L., and Armstrong, R. A.: Diagnosing the contribution of phytoplankton functional groups to the production and export of particulate organic carbon, CaCO₃, and opal from global nutrient and alkalinity distributions, *Global Biogeochem. Cy.*, 20, 2, GB2015, doi:10.1029/2005GB002532, 2006.
- Joos, F. and Spahni, R.: Rates of change in natural and anthropogenic radiative forcing over the past 20000 years, *P. Natl. Acad. Sci. USA*, 105, 1425–1430, 2008.
- Jutterström, S. and Anderson, L. G.: The saturation of calcite and aragonite in the Arctic Ocean, *Mar. Chem.*, 94, 101–110, 2005.
- Key, R. M., Kozyr, A., Sabine, C. L., Lee, K., Wanninkhof, R., Bullister, J., Feely, R. A., Millero, F., Mordy, C., and Peng, T.-H.: A global ocean carbon climatology: Results from Global Data Analysis Project (GLODAP), *Global Biogeochem. Cy.*, 18, GB4031+, doi:10.1029/2004GB002247, 2004.
- Kiehl, J. T., Hack, J. J., Bonan, G. B., Boville, B. A., Williamson, D. L., and Rasch, P. J.: The National Center for Atmospheric Research Community Climate Model, *J. Climate*, 11, 1151–1178, 1998.
- Kleypas, J. A., Buddemeier, R. W., Archer, D., Gattuso, J.-P., Langdon, C., and Opdyke, B. N.: Geochemical Consequences of Increased Atmospheric Carbon Dioxide on Coral Reefs, *Science*, 284, 118–120, 1999.
- Kleypas, J. A., Feely, R. A., Fabry, V. J., Langdon, C., Sabine, C. L., and Robbins, L. L.: Impacts of Ocean Acidification on Coral Reefs and Other Marine Calcifiers: A Guide for Future Research, report of a workshop held 18–20 April 2005, St. Petersburg, FL, sponsored by NSF, NOAA, and the US Geological Survey, 2006.
- Kwon, E. Y. and Primeau, F.: Optimization and sensitivity of a global biogeochemistry ocean model using combined in situ DIC, alkalinity, and phosphate data, *J. Geophys. Res.-Oceans*, 113(C8), C08011, doi:10.1029/2007JC004520, 2008.
- Langdon, C.: Review of Experimental Evidence for Effects of CO₂ on Calcification of Reef Builders, in: Proceedings 9th International Coral Reef Symposium, vol. 2, 1091–1098, 2002.
- Langdon, C. and Atkinson, M. J.: Effect of elevated pCO₂ on photosynthesis and calcification of corals and interactions with seasonal change in temperature/irradiance and nutrient enrichment, *J. Geophys. Res.*, 110, C09S07, doi:10.1029/2004JC002576, 2005.
- Lueker, T. J., Dickson, A. G., and Keeling, C. D.: Ocean pCO₂ calculated from dissolved inorganic carbon, alkalinity, and equations for K-1 and K-2: validation based on laboratory measurements of CO₂ in gas and seawater at equilibrium, *Mar. Chem.*, 70, 105–119, 2000.
- Lüthi, D., Le Floch, M., Bereiter, B., Blunier, T., Barnola, J.-M., Siegenthaler, U., Raynaud, D., Jouzel, J., Fischer, H., Kawamura, K., and Stocker, T. F.: High-resolution carbon dioxide concentration record 650 000–800 000 years before present, *Science*, 453, 379–382, 2008.
- Martin, J. H., Knauer, G. A., Karl, D. M., and Broenkow, W. W.: VERTEX – Carbon cycling in the Northeast Pacific, *Deep-Sea Res.*, 34, 267–285, 1987.
- McNeil, B. I. and Matear, R. J.: Climate change feedbacks on future oceanic acidification, *Tellus B*, 59, 191–198, 2007.
- Meehl, G. A., Stocker, T. F., Collins, W. D., Friedlingstein, P., Gaye, A. T., Gregory, J. M., Kitoh, A., Knutti, R., Murphy, J. M., Noda, A., Raper, S. C. B., Watterson, I. G., Weaver, A. J., and Zhao, Z.-C.: Climate Change 2007: The Physical Science Basis. Contribution of Working Group I to the Fourth Assessment Report of the Intergovernmental Panel on Climate Change, chap. Global Climate Projections, Cambridge University Press, Cambridge, United Kingdom and New York, NY, USA, 747–846, 2007.
- Mehrbach, C., Culbertson, C. H., Hawley, J. E., and Pytkowicz, R. M.: Measurement of apparent dissociation-constants of carbonic-acid in seawater at atmospheric-pressure, *Limnol. Oceanogr.*, 18, 897–907, 1973.
- Millero, F. J.: Thermodynamics of the carbon dioxide system in the oceans, *Geochim. Cosmochim. Ac.*, 59, 661–677, 1995.
- Mucci, A.: The solubility of calcite and aragonite in seawater at

M. Steinacher et al.: Arctic ocean acidification

533

- various salinities, temperatures and 1 atmosphere total pressure, *Am. J. Sci.*, 238, 780–799, 1983.
- Najjar, R. G., Jin, X., Louanchi, F., Aumont, O., Caldeira, K., Doney, S. C., Dutay, J.-C., Follows, M., Gruber, N., Joos, F., Lindsay, K., Maier-Reimer, E., Matear, R. J., Matsumoto, K., Mouchet, A., Orr, J. C., Sarmiento, J. L., Schlitzer, R., Weirig, M. F., Yamanaka, Y., and Yool, A.: Impact of circulation on export production, dissolved organic matter, and dissolved oxygen in the ocean: Results from Phase II of the Ocean Carbon-cycle Model Intercomparison Project (OCMIP-2), *Global Biogeochem. Cy.*, 21, GB3007, doi:10.1029/2006GB002857, 2007.
- Orr, J. C., Fabry, V. J., Aumont, O., Bopp, L., Doney, S. C., Feely, R. A., Gnanadesikan, A., Gruber, N., Ishida, A., Joos, F., Key, R. M., Lindsay, K., Maier-Reimer, E., Matear, R., Monfray, P., Mouchet, A., Najjar, R. G., Plattner, G.-K., Rodgers, K. B., Sabine, C. L., Sarmiento, J. L., Schlitzer, R., Slater, R. D., Totterdell, I. J., Weirig, M. F., Yamanaka, Y., and Yool, A.: Anthropogenic ocean acidification over the twenty-first century and its impact on calcifying organisms, *Nature*, 437, 681–686, 2005.
- Orr, J. C., Jutterström, S., Bopp, L., Anderson, L. G., Fabry, V. J., Frölicher, T. L., Jones, P., Joos, F., Maier-Reimer, E., Segsneider, J., Steinacher, M., and Swingedouw, D.: Arctic ocean acidification, *Nature*, submitted, 2008.
- Plattner, G.-K., Knutti, R., Joos, F., Stocker, T. F., von Bloh, W., Brovkin, V., Cameron, D., Driesschaert, E., Dutkiewicz, S., Eby, M., Edwards, N. R., Fichefet, T., Hargreaves, J. C., Jones, C. D., Loutre, M. F., Matthews, H. D., Mouchet, A., Müller, S. A., Nawrath, S., Price, A., Sokolov, A., Strassmann, K. M., and Weaver, A. J.: Long-term climate commitments projected with climate – carbon cycle models, *J. Climate*, 21, 2721–2751, doi:10.1175/2007JCLI1905.1, 2008.
- Prentice, I. C., Farquhar, G. D., Fasham, M. J. R., Goulden, M. L., Heimann, M., Jaramillo, V. J., Kheshgi, H. S., Le Quéré, C., Scholes, R. J., and Wallace, D. W. R.: *Climate Change 2001: The Scientific Basis. Contribution of Working Group I to the Third Assessment Report of the Intergovernmental Panel on Climate Change*, chap. The Carbon Cycle and Atmospheric Carbon Dioxide, Cambridge University Press, Cambridge, United Kingdom and New York, NY, USA, 183–237, 2001.
- Randerson, J. T., Thompson, M. V., Conway, T. J., Fung, I. Y., and Field, C. B.: The contribution of terrestrial sources and sinks to trends in the seasonal cycle of atmospheric carbon dioxide, *Global Biogeochem. Cy.*, 11, 535–560, 1997.
- Revelle, R. and Suess, H. E.: Carbon dioxide exchange between atmosphere and ocean and the question of an increase of atmospheric CO₂ during the past decades, *Tellus*, 9, 18–27, 1957.
- Ridgwell, A., Zondervan, I., Hargreaves, J. C., Bijma, J., and Lenton, T. M.: Assessing the potential long-term increase of oceanic fossil fuel CO₂ uptake due to CO₂-calcification feedback, *Biogeosciences*, 4, 481–492, 2007, <http://www.biogeosciences.net/4/481/2007/>.
- Royal Society: Ocean acidification due to increasing atmospheric carbon dioxide, Policy Document 12/05, Royal Society, London, 2005.
- Sarmiento, J. L., Dunne, J., Gnanadesikan, A., Key, R. M., Matsumoto, K., and Slater, R.: A new estimate of the CaCO₃ to organic carbon export ratio, *Global Biogeochem. Cy.*, 16, 4, 1107, doi:10.1029/2002GB001919, 2002.
- Schlitzer, R.: Ocean Data View (Software), <http://odv.awi.de>, 2007.
- Schneider, K. and Erez, J.: The effect of carbonate chemistry on calcification and photosynthesis in the hermatypic coral *Acropora eurystoma*, *Limnol. Oceanogr.*, 51, 1284–1293, 2006.
- Siegenthaler, U., Stocker, T. F., Monnin, E., Lüthi, D., Schwander, J., Stauffer, B., Raynaud, D., Barnola, J.-M., Fischer, H., Masson-Delmotte, V., and Jouzel, J.: Stable carbon cycle-climate relationship during the late Pleistocene, *Science*, 310, 1313–1317, doi:10.1126/science.1120130, 2005.
- Steinacher, M.: Ocean acidification and changes in marine productivity in simulations with the fully coupled 3-D climate model CSM1.4-carbon, Master's thesis, University of Bern, Bern, Switzerland, 2007.
- Strassmann, K. M., Plattner, G.-K., and Joos, F.: CO₂ and non-CO₂ radiative forcings in climate projections for twenty-first century mitigation scenarios, *Clim. Dynam.*, doi:10.1007/s00382-008-0505-4, published online 20 Dec 2008, 2008.
- Stroeve, J., Holland, M. M., Meier, W., Scambos, T., and Serreze, M.: Arctic sea ice decline: Faster than forecast, *Geophys. Res. Lett.*, 34, L09501, doi:10.1029/2007GL029703, 2007.
- Takahashi, T., Olafsson, J., Goddard, J. G., Chipman, D. W., and Sutherland, S. C.: Seasonal-variation of CO₂ and nutrients in the high-latitude surface oceans – a comparative-study, *Global Biogeochem. Cy.*, 7, 843–878, 1993.
- Taylor, K. E.: Summarizing multiple aspects of model performance in a single diagram, *J. Geophys. Res.-Atmos.*, 106, 7183–7192, 2001.
- Thomas, H., Prowe, A. E. F., van Heuven, S., Bozec, Y., de Baar, H., Schiettecatte, L.-S., Suykens, K., Koné, M., Borges, A. V., Lima, I. D., and Doney, S. C.: Rapid decline of the CO₂ buffering capacity in the North Sea and implications for the North Atlantic Ocean, *Global Biogeochem. Cy.*, 21, GB4001, doi:10.1029/2006GB002825, 2007.
- Van Vuuren, D. P., Meinshausen, M., Plattner, G.-K., Joos, F., Strassmann, K. M., Smith, S. J., Wigley, T. M. L., Raper, S. C. B., Riahi, K., de la Chesnaye, F., den Elzen, M., Fujino, J., Jiang, K., Nakicenovic, N., Paltsev, S., and Reilly, J. M.: Temperature increase of 21st century mitigation scenarios, *P. Natl. Acad. Sci. USA*, 105, 15258–15262, doi:10.1073/pnas.0711129105, 2008.
- Walsh, J. E.: A data set on Northern Hemisphere sea ice extent, World Data Center-A for Glaciology (Snow and Ice), Glaciological Data, Report GD-2, part 1, 49–51, 1978.
- Wang, Y. M., Lean, J. L., and Sheeley, N. R.: Modeling the sun's magnetic field and irradiance since 1713, *Astrophys. J.*, 625, 522–538, 2005.
- Weatherly, J. W., Briegleb, B. P., Large, W. G., and Maslanik, J. A.: Sea Ice and Polar Climate in the NCAR CSM, *J. Climate*, 11, 1472–1486, 1998.
- Yamanaka, Y. and Tajika, E.: The role of the vertical fluxes of particulate organic matter and calcite in the oceanic carbon cycle: Studies using an ocean biogeochemical general circulation model, *Global Biogeochem. Cy.*, 10, 361–382, 1996.

2.2 Modeling ocean acidification in the Arctic Ocean

Marco Steinacher, Fortunat Joos, and Thomas L. Frölicher

Published as “Science Box 5” in the article “European Project on Ocean Acidification (EPOCA): Objectives, products, and scientific highlights” by Jean-Pierre Gattuso, Lina Hansson, and the EPOCA consortium, *Oceanography*, Volume 22, pp. 190–201, 2009.

Abstract The European Project on Ocean Acidification (EPOCA) is Europe’s first large-scale research initiative devoted to studying the impacts and consequences of ocean acidification. More than 100 scientists from 27 institutes and nine countries bring their expertise to the project, resulting in a multidisciplinary and versatile consortium. The project is funded for four years (2008 to 2012) by the European Commission within its Seventh Framework Programme. This article describes EPOCA and explains its different aspects, objectives, and products. Following a general introduction, six boxes highlight outcomes, techniques, and scientific results from each of the project’s core themes.

BOX 5. MODELING OCEAN ACIDIFICATION IN THE ARCTIC OCEAN

By Marco Steinacher, Fortunat Joos, and Thomas L. Frölicher

Ocean acidification in the Arctic is an important research focus in EPOCA. Oceanographic measurements demonstrate that Arctic surface water is already close to undersaturation with respect to aragonite (Jutterström and Anderson, 2005), and that undersaturation is imminent as fossil fuel carbon emissions continue to rise. Climate change is projected to amplify ocean acidification in the Arctic. Ocean acidification from business-as-usual, twenty-first century emissions is irreversible on human time scales.

Model results from nine modeling groups will become available within EPOCA to assess biogeochemical and ecosystem consequences of ocean acidification in the Arctic and in other regions of the world in a comprehensive analysis. EPOCA researchers will employ the full hierarchy of models from cost-efficient Earth System Models of Intermediate Complexity (EMICs), through high-resolution regional models, to state-of-the-art global coupled

climate-biogeochemical models.

As an example, we briefly discuss results obtained with the NCAR Climate System Model forced with rising carbon emissions for the two Intergovernmental Panel on Climate Change business-as-usual emission scenarios (A2 and B1) until 2100 (Steinacher et al., 2009). The NCAR Climate System Model is a global climate model with fully coupled atmosphere, ocean, land, and sea-ice components, and it includes an interactive global carbon cycle. Here, the carbonate ion concentration $[\text{CO}_3^{2-}]$ and the related saturation state for aragonite are used as indicators.

Undersaturation in the Arctic Ocean is imminent—expected to begin within the next decade for both scenarios (Figure B6). By the time atmospheric CO_2 exceeds 490 ppm (2040 in A2, 2050 in B1), more than half of the Arctic is projected to be undersaturated at the surface (annual mean). By the end of the twenty-first century and for the A2 case, undersaturation in the Arctic Ocean also occurs with respect to calcite.

The main reasons for the vulnerability of the Arctic Ocean are (1) its naturally low saturation state, as documented by several oceanographic cruises, and (2) Arctic climate change amplifies acidification, in contrast to other regions like the Southern Ocean, where climate change has almost no effect in our simulations. Amplified climate change in the Arctic leads to a reduction in sea ice cover and surface freshening through ice melting, altered precipitation and evaporation, and river input. The dilution of surface waters alters the CO_2 partial pressure, which in combination with an increase in ice-free area, enhances the uptake of anthropogenic CO_2 through gas exchange by about 40%. Further, freshwater input decreases $[\text{CO}_3^{2-}]$ by dilution, whereas increased export of excess carbon out of the upper ocean and enhanced marine productivity counteract the reduction in $[\text{CO}_3^{2-}]$. Our study does not

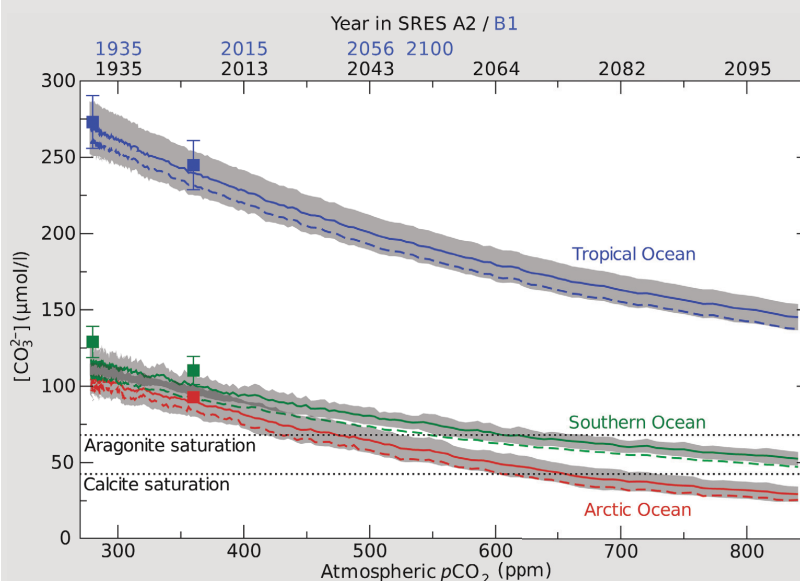


Figure B6. Projected surface water carbonate ion concentration versus projected atmospheric CO_2 (lower x-axis) and time (upper x-axis) for low (SRES B1) and high (SRES A2), business-as-usual emission scenarios. The figure shows modeled annual mean (solid line) and lowest monthly (dashed) concentrations averaged over the Arctic Ocean (red), the Southern Ocean (green), and the tropical ocean (blue), and spatial variability of annual mean concentrations within each region (shading, \pm one standard deviation). Squares indicate observation-based estimates for the Southern Ocean and tropics (Global Ocean Data Analysis Project and World Ocean Atlas 2001 [http://www.nodc.noaa.gov/OC5/WOA01/pr_woa01.html], annual mean), and for summer conditions in the Arctic Ocean (CARINA [CARbon dioxide IN the Atlantic Ocean] database; <http://cdiac.ornl.gov/oceans/datmet.html>), with "error bars" indicating the spatial variability. Model results are from the NCAR CSM1.4-carbon model.

account for changes in riverine carbon fluxes. Considering all effects, the decrease in surface $[\text{CO}_3^{2-}]$ in the Arctic Ocean is 34% higher than it would be without climate change in our model.

In contrast to other regions where the $[\text{CO}_3^{2-}]$ decrease is basically a function of increasing atmospheric CO_2 , the simulation of ocean acidification in the Arctic additionally relies on the model's ability to project climate change realistically. Major uncertainties are the magnitude and timing of sea ice cover reduction and changes in the freshwater balance. The simulated present-day ice cover in the NCAR model is larger than observed, and the projected reduction is moderate compared to other models. Considering the relatively low climate sensitivity of the model and recent projections of rapid summer sea ice decline, it is likely that the projected decrease in Arctic saturation represents a lower limit for a given scenario. Results from the EPOCA model suite will provide a more robust quantification of these effects.

Simulations in which emissions of carbon and other forcing agents are hypothetically stopped in years 2100 or 2000 allow us to investigate the legacy effects of historical and twenty-first century emissions. Undersaturation with respect to aragonite and calcite remains widespread in the Arctic for centuries even after cutting emissions in 2100 (recent work of authors Frölicher and Joos).

For the near future, it will be crucial that experimental scientists (see, e.g., Boxes 3 and 4) and modelers work hand in hand to improve understanding of how human carbon emissions affect the biogeochemical state of the ocean and how these changes affect the functioning and services provided by marine ecosystems. EPOCA's results will be needed to provide further guidance on emission reduction targets. Considering the precautionary principle mentioned in the United Nations Framework Convention on Climate Change, our subjective assessment is that atmospheric CO_2 should not exceed 450 ppm in order to avoid the risk of large-scale disruption to marine ecosystems.

Marco Steinacher (steinacher@climate.unibe.ch) is PhD Candidate, Division of Climate and Environmental Physics of the Physics Institute, and the Oeschger Centre for Climate Change Research, University of Bern, Switzerland. **Fortunat Joos** is Professor, Division of Climate and Environmental Physics of the Physics Institute, and the Oeschger Centre for Climate Change Research, University of Bern, Switzerland. **Thomas L. Frölicher** is Postdoctoral Research Fellow, Division of Climate and Environmental Physics of the Physics Institute, and the Oeschger Centre for Climate Change Research, University of Bern, Switzerland.

Atlantic, where water temperatures are low, promoting CO_2 dissolution and driving seawater toward undersaturation of calcium carbonate. Put simply, undersaturation will not only render calcification more difficult but may also lead to corrosion of existing shells and skeletons.

Fifteen EPOCA scientists recently returned from the first large-scale field experiment of the project—a five-week-long campaign in Svalbard aimed at investigating the impact of ocean acidification on Arctic benthic organisms such as echinoderms, mollusks, crustaceans, and calcareous algae. The organisms were exposed to different levels of $p\text{CO}_2$ using indoor mesocosm setups. In 2010, about 40 EPOCA scientists will return to Svalbard to study pelagic communities using offshore mesocosm facilities (see Box 4).

Guide to Best Practices in Ocean Acidification Research and Data Reporting

Standardized data protocols and reporting are crucial for meaningful comparisons and collaboration within the ocean acidification field. Together with IOC-UNESCO, and with funding support from the Scientific Council on Oceanic Research (SCOR), the US Ocean Carbon Biogeochemistry program, and the Kiel Excellence Cluster *The Future Ocean*, EPOCA organized an international workshop on Best Practices for Ocean Acidification Research that met in Kiel during November 2008. The meeting brought together around 40 scientists with expertise in different areas of ocean acidification research; the agenda covered seawater carbonate chemistry, experimental design of perturbation experiments, and measurements of

2.3 Imminent and Irreversible Ocean Acidification

Marco Steinacher, Thomas L. Frölicher, and Fortunat Joos

Published in *SOLAS news*, Issue 9, pp. 6–7, 2009.



Marco Steinacher obtained a MSc. in Physics at the University of Bern, Switzerland, where he is currently doing his PhD. in the Division of Climate- and Environmental Physics of the Physics Institute. His research interests include carbon cycle and climate modeling, ocean acidification, and probabilistic projections of future climate change.

Imminent and Irreversible Ocean Acidification

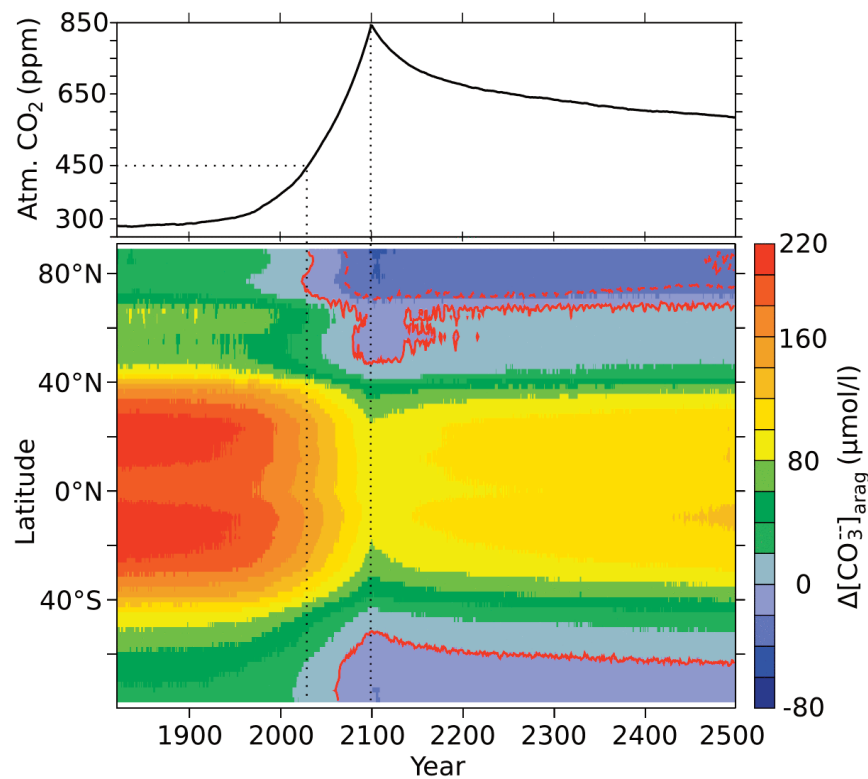
Marco Steinacher, Thomas L. Frölicher and Fortunat Joos

Climate and Environmental Physics, Physics Institute and Oeschger Centre for Climate Change Research, University of Bern, Switzerland Contact: steinacher@climate.unibe.ch



Anthropogenic carbon emissions force atmospheric CO_2 far above the natural range of the last million years and cause rapidly progressing global warming. Yet another issue linked to anthropogenic CO_2 has recently attracted wide attention. The uptake of anthropogenic CO_2 lowers ocean pH, the concentration of carbonate ions and the saturation state of seawater with respect to calcium carbonate (Orr et al., 2005). A particular concern of this "ocean acidification" is its impact on marine organisms and ecosystems (Doney et al., 2009).

We investigate ocean acidification with the comprehensive NCAR global coupled climate-carbon model forced with rising carbon emissions for the SRES A2 business-as-usual scenario until 2100 (Steinacher et al., 2009). Irreversible impacts of 21st century CO_2 emissions are quantified by extending the simulation (unrealistically) with zero emissions after 2100 (Frölicher and Joos, 2009). Here, the carbonate ion concentration $[\text{CO}_3^{2-}]$ and the related saturation state with respect to aragonite are used as indicators. Aragonite is a mineral phase of calcium carbonate secreted by



▲ Figure 1: Simulated evolution of atmospheric CO_2 and of zonal, annual mean surface carbonate ion concentration, shown as deviation from the saturation concentration with respect to aragonite. Red lines indicate the transitions from over- to undersaturation with respect to aragonite (solid) and calcite (dashed).

many marine organisms to build their shells and other structures. Aragonite shells dissolve in undersaturated water in the absence of protective mechanisms.

Surface water saturation decreases rapidly in all regions until 2100 (Fig. 1) and remains reduced for centuries. Undersaturation in the Arctic is imminent and starts already within the next decade. By the time atmospheric CO₂ exceeds 490 ppm (2040 in A2), more than half of the Arctic is undersaturated (annual mean). Similarly, the Southern Ocean becomes undersaturated on average, when atmospheric CO₂ exceeds 580 ppm and saturation in the tropics drops below 300%, threatening the survival of coral reefs. By the end of the 21st century, undersaturation in the Arctic Ocean also occurs with respect to calcite and remains widespread for centuries after cutting emissions in 2100.

The main reasons for the vulnerability of the Arctic Ocean is its naturally low saturation state and that Arctic climate change amplifies acidification, in contrast to other regions like the Southern Ocean, where climate change has almost no effect in our simulations. Enhanced uptake of atmospheric CO₂ in response to sea-ice retreat, surface freshening and other effects lead to a decrease in Arctic surface [CO₃²⁻] that is 34% higher than it would be without climate change.

Ocean acidification also affects the thermocline and the abyss as anthropogenic carbon continues to invade the ocean. Overall, the fraction of the ocean volume occupied by water oversaturated with respect to aragonite is

projected to decrease from about 42% to 25% by 2100 and to 10% by 2300. The fact that the volume fraction continues to decrease significantly after 2100 demonstrates that some impacts of 21st fossil fuel carbon emissions are strongly delayed and aggravate even for the extreme case of an immediate emission stop.

Undersaturation of Arctic surface waters with respect to aragonite is likely to become reality in a few years only (Steinacher et al., 2009) and ocean acidification from business-as-usual carbon emissions is irreversible on human timescales (Frölicher and Joos, 2009). Experimental evidence is emerging (Doney et al., 2009) that ocean acidification has negative impacts on many organisms and may severely affect cold and warm water corals or high-latitude species such as aragonite producing pteropods. Considering the precautionary principle mentioned in the United Nations Framework Convention on Climate Change, our subjective assessment is that atmospheric CO₂ should not exceed 450 ppm in order to avoid the risk of large-scale disruptions in marine ecosystems.

References

- Doney, S.C., Fabry, V.J., Feely, R.A., and Kleypas, J.A.: *Ann. Rev. Mar. Sci.*, 1, 169–192, 2009.
- Frölicher, T.L. and Joos, F.: submitted to *Clim. Dynam.*, 2009.
- Orr, J.C. et al.: *Nature*, 437, 681–686, 2005.
- Steinacher, M., Joos, F., Frölicher, T.L., Plattner, G.-K., and Doney, S.C.: *Biogeosciences*, 6, 515–533, 2009.

Chapter 3

Projected 21st century decrease in marine productivity: a multi-model analysis

M. Steinacher, F. Joos, T. L. Frölicher, L. Bopp, P. Cadule, V. Cocco, S. C. Doney, M. Gehlen, K. Lindsay, J. K. Moore, B. Schneider, and J. Segsneider

Published in *Biogeosciences*, Volume 7, pp. 979–1005, 2010.

Biogeosciences, 7, 979–1005, 2010
 www.biogeosciences.net/7/979/2010/
 © Author(s) 2010. This work is distributed under
 the Creative Commons Attribution 3.0 License.



Projected 21st century decrease in marine productivity: a multi-model analysis

M. Steinacher^{1,2}, F. Joos^{1,2}, T. L. Frölicher^{1,2}, L. Bopp³, P. Cadule³, V. Cocco^{1,2}, S. C. Doney⁴, M. Gehlen³, K. Lindsay⁵, J. K. Moore⁶, B. Schneider⁷, and J. Segschneider⁸

¹Climate and Environmental Physics, Physics Institute, University of Bern, Sidlerstrasse 5, 3012 Bern, Switzerland

²Oeschger Centre for Climate Change Research, University of Bern, Zähringerstrasse 25, 3012 Bern, Switzerland

³Laboratoire du Climat et de l'Environnement (LSCE), L'Orme des Merisiers Bât. 712, 91191 Gif sur Yvette, France

⁴Dept. of Marine Chemistry and Geochemistry, Woods Hole Oceanographic Institution, Woods Hole, MA 02543, USA

⁵Climate and Global Dynamics Division, National Center for Atmospheric Research, Boulder, CO 80307, USA

⁶Dept. of Earth System Science, University of California, Irvine, CA 92697, USA

⁷Institute of Geosciences, University of Kiel, Ludewig-Meyn-Str. 10, 24098 Kiel, Germany

⁸Max-Planck-Institut für Meteorologie, Bundesstrasse 53, 20146 Hamburg, Germany

Received: 21 July 2009 – Published in Biogeosciences Discuss.: 4 August 2009

Revised: 5 February 2010 – Accepted: 4 March 2010 – Published: 11 March 2010

Abstract. Changes in marine net primary productivity (PP) and export of particulate organic carbon (EP) are projected over the 21st century with four global coupled carbon cycle-climate models. These include representations of marine ecosystems and the carbon cycle of different structure and complexity. All four models show a decrease in global mean PP and EP between 2 and 20% by 2100 relative to preindustrial conditions, for the SRES A2 emission scenario. Two different regimes for productivity changes are consistently identified in all models. The first chain of mechanisms is dominant in the low- and mid-latitude ocean and in the North Atlantic: reduced input of macro-nutrients into the euphotic zone related to enhanced stratification, reduced mixed layer depth, and slowed circulation causes a decrease in macro-nutrient concentrations and in PP and EP. The second regime is projected for parts of the Southern Ocean: an alleviation of light and/or temperature limitation leads to an increase in PP and EP as productivity is fueled by a sustained nutrient input. A region of disagreement among the models is the Arctic, where three models project an increase in PP while one model projects a decrease. Projected changes in seasonal and interannual variability are modest in most regions. Regional model skill metrics are proposed to generate multi-model mean fields that show an improved skill in represent-

ing observation-based estimates compared to a simple multi-model average. Model results are compared to recent productivity projections with three different algorithms, usually applied to infer net primary production from satellite observations.

1 Introduction

Marine productivity and the marine biological cycle are important elements of the climate system. Biological processes influence, among other Earth system properties, the atmospheric abundance of radiative agents such as CO₂ (e.g. Volk and Hoffert, 1985; Siegenthaler and Wenk, 1984), N₂O (Suntharalingam and Sarmiento, 2000; Goldstein et al., 2003; Schmittner and Galbraith, 2008), dimethylsulphate (Bopp et al., 2003) and aerosols as well as the bio-optical properties of seawater and upper ocean physics (Timmermann and Jin, 2002; Manizza et al., 2008). However, the representation of ocean ecosystems (Sarmiento et al., 1993; Fasham et al., 1993; Six and Maier-Reimer, 1996; Moore et al., 2004; Le Quéré et al., 2005; Maier-Reimer et al., 2005; Aumont and Bopp, 2006; Vichi et al., 2007) and biogeochemical cycles in comprehensive atmosphere-ocean general circulation models (AOGCMs; Bopp et al., 2001; Fung et al., 2005; Wetzel et al., 2006; Crueger et al., 2008) is a relatively new field that requires further development to provide matured and robust results.



Correspondence to: M. Steinacher
 (steinacher@climate.unibe.ch)

The goal of this study is to provide a multi-model estimate of long-term trends in net primary productivity (PP) and export of particulate organic material (EP) using global warming simulations from four fully coupled atmosphere-ocean general circulation models and to identify the mechanisms behind these changes. These are the IPSL-CM4-LOOP model from the Institut Pierre Simon Laplace (IPSL), the COSMOS Earth System Model from the Max-Planck Institute for Meteorology (MPIM), and two versions of the Community Climate System Model (CSM1.4-carbon and CCSM3-BEC) from the National Center for Atmospheric Research. In this paper these models are referred to as IPSL, MPIM, CSM1.4, and CCSM3, respectively. The focus of the analysis is on how decadal-to-century scale changes in physical factors and nutrient availability affect global and regional PP and EP. The motivation is to provide an account on the performance of current climate-ecosystem models under global warming and to derive a best estimate of changes in productivity using regional model skill metrics. Our interest is further fueled by the contradicting projections for global PP from some “mechanistic” models, as used here, and a recent statistical model approach (Sarmiento et al., 2004).

A general finding across the hierarchy of mechanistic models is that global EP decreases in 21st century global warming simulations (Klepper and De Haan, 1995; Maier-Reimer et al., 1996; Joos et al., 1999; Matear and Hirst, 1999; Plattner et al., 2001; Bopp et al., 2001; Fung et al., 2005; Schmittner et al., 2008; Frölicher et al., 2009). Increased stratification and a slowed thermohaline circulation in response to surface warming and freshening cause a decrease in the delivery of nutrients to the surface. As a consequence, global EP and in some models also PP is reduced. In these models, the marine biological cycle is closed in the sense that nutrient uptake by phytoplankton, export of organic material into the thermocline, remineralization of organic material and transport of inorganic nutrients by the circulation is represented. In the simpler models, EP (or some approximation of PP) is tied to the availability of nutrients (such as phosphate or iron), light and temperature without considering food web dynamics, whereas in the more complex models the growth of phyto- and zooplankton, nitrogen fixation, and food web interactions and floristic shifts are explicitly taken into account, albeit in a simplified way. Large scale biogeochemical models often lack an explicit representation of the microbial loop. The energy and nutrient flows initiated by bacterial consumption of dissolved organic matter and grazing by bacterivores (Azam et al., 1983) are represented by a decay function for dissolved organic matter. The decay of dissolved organic matter releases nutrients which are in turn available for plankton consumption. Globally, the change in nutrient supply is the dominant mechanism for EP and PP changes in 21st century global warming simulations, whereas other factors such as changes in light availability and the growing season length due to sea ice retreat, altered oceanic mixing conditions, and cloud characteristics,

or the direct impact of elevated temperature on physiology considerably affect regional responses in productivity (Bopp et al., 2001). A decrease in global PP and new production by 5 to 8% is also projected in an off-line simulation with an ecosystem model (Moore et al., 2002) driven by the climate induced changes in ocean physics from an AOGCM simulation of the SRES A1 mid-range emission scenario (Boyd and Doney, 2002); the decrease is primarily attributed to the prescribed reduction in subsurface nutrients. In contrast, Sarmiento et al. (2004) projects an increase in global PP by 0.7 to 8.1% using an empirical model approach. We also note that Schmittner et al. (2008) find a strong increase in PP in 21st century CO₂ scenarios albeit new production and EP decrease. The increase in PP in their study results from an exponential dependency of phytoplankton growth rates on temperature (Eppley, 1972).

Schneider et al. (2008) present results for three (IPSL, MPIM, and CSM1.4) of the four Earth System models used in this study. They provide detailed information on the performance of these three models under current climate conditions and compare modeled physical (temperature, salinity, mixed layer depth, meridional overturning, ENSO variability) and biological (PP and EP, chlorophyll concentration) results with observation-based estimates. Of particular interest is the model performance with respect to seasonal and interannual variability as changes on these time scales may be linked to the century scale changes examined here. The models capture the general distribution of higher absolute PP and higher seasonal variability in the intermediate to high latitudes, though all models overestimate seasonal variability in intermediate southern latitudes. Interannual variability is largely controlled by the permanently stratified low-latitude ocean in all three models consistent with satellite data (Behrenfeld et al., 2006). However, the MPIM model strongly overestimates the amplitude and frequency of interannual PP variations, while the variability amplitude is slightly too low in the CSM1.4 model. Only the IPSL model is able to capture the correlation between observation-based PP, sea surface temperature and stratification in the low-latitude, stratified ocean. The MPIM model, and to a lesser degree, the CSM1.4 model, suffer from a too strong iron limitation compared to the real ocean. In the MPIM model, overall iron limitation is caused by the combination of low aeolian deposition and, more importantly, a high half-saturation value for iron. In the CSM1.4 model, iron appears to be too strongly scavenged, especially in the subtropical Pacific, also resulting in too strong iron limitation (Schneider et al., 2008). It remains difficult for any model to represent the iron cycle with its intricate coupling between physical transport, spatial and temporal varying iron sources by dust deposition (e.g. Mahowald et al., 2006) and sediments (e.g. de Baar et al., 1995; Dulaiova et al., 2009), iron sinks by particle scavenging, complexation by organic ligands (e.g. Parekh et al., 2008) and ecosystem and remineralization processes (Boyd et al., 2007).

The skill of the ocean component of the CCSM3 model in simulating PP and related variables has been assessed by Doney et al. (2009a). In that study, the model was forced with physical climate forcing from atmospheric reanalysis and satellite data products and atmospheric dust deposition. The results were then evaluated using data-based skill metrics. It was found that the model surface chlorophyll tend to be too high in the subtropical gyres and too low in the sub-polar gyres. This error pattern may result from a too weak grazing by zooplankton relative to PP in the picoplankton dominated subtropics and a too strong grazing in bloom environments. Further, their simulation shows excess surface macronutrients in the tropical Pacific, which is also true for the simulation in the present study. This is likely a result of a combination of physical circulation errors and too much iron scavenging. PP is found to be higher than observed in tropical and subtropical Pacific, suggesting that errors may also arise from other aspects of the biological cycling (e.g., export flux, subsurface remineralization; Doney et al., 2009a).

A challenge for any multi-model analysis is how to extract and distill the information contained in the individual models in a quantitative way. Ideally, the strengths of each individual model would be combined while weaknesses and failures would be removed to obtain an optimal multi-model mean. Here, we use regional weights to compute multi-model mean fields in PP and EP changes.

In this paper we analyze centennial-scale changes in PP and EP under anthropogenic climate warming. Unlike earlier studies, we make use of four interactively coupled global carbon cycle-climate models that include iron cycling and representations of the marine biogeochemistry of different complexities. The use of a multi-model ensemble increases the robustness of the results and allows us to explore uncertainties. The models are forced with prescribed CO₂ emissions from reconstructions (1860–2000 AD) and a high emission scenario, SRES A2 (2000–2100 AD). In the next section, models and experimental setup are described. In the result section, we first present projections for marine PP. Then, we investigate underlying physical and biogeochemical mechanisms, quantify model sensitivities, and also address changes in the seasonal cycle. Regional model skill metrics are used to compute multi-model mean changes. In the discussion section, results of the mechanistic models are compared with those of Sarmiento et al. (2004) and discussed in the light of earlier studies. Throughout this paper, the variables PP and EP are used to represent net primary productivity and export of particulate organic carbon (POC), respectively.

2 Methods

2.1 Models

All models used in this study are fully coupled 3-D atmosphere-ocean climate models that contributed to the IPCC Fourth Assessment Report (Solomon et al., 2007;

Meehl et al., 2007). In the case of the CCSM3 model a version without carbon cycle was used for the IPCC report. In this study, all model versions include carbon cycle modules for the terrestrial and oceanic components (Friedlingstein et al., 2006).

2.1.1 IPSL

The IPSL-CM4-LOOP (IPSL) model consists of the Laboratoire de Météorologie Dynamique atmospheric model (LMDZ-4) with a horizontal resolution of about $3^\circ \times 3^\circ$ and 19 vertical levels (Hourdin et al., 2006), coupled to the OPA-8 ocean model with a horizontal resolution of $2^\circ \times 2^\circ \cdot \cos\phi$ and 31 vertical levels and the LIM sea ice model (Madec et al., 1998). The terrestrial biosphere is represented by the global vegetation model ORCHIDEE (Krinner et al., 2005) and the marine carbon cycle is simulated by the PISCES model (Aumont et al., 2003). PISCES simulates the cycling of carbon, oxygen, and the major nutrients determining phytoplankton growth (PO_4^{3-} , NO_3^- , NH_4^+ , Si, Fe). The model has two phytoplankton size classes (small and large), representing nanophytoplankton and diatoms, as well as two zooplankton size classes (small and large), representing microzooplankton and mesozooplankton. Phytoplankton growth is limited by the availability of nutrients and light. The nanophytoplankton and diatom growth rates as well as the grazing rate of microzooplankton are temperature dependent and increase by a factor of 10 over the temperature range from -2°C to 34°C . The temperature sensitivity of the mesozooplankton grazing rate is slightly higher ($Q_{10} = 2.14$). For all species the C:N:P ratios are assumed constant (122:16:1; Takahashi et al., 1985), while the internal ratios of Fe:C, Chl:C, and Si:C of phytoplankton are predicted by the model. Iron is supplied to the ocean by aeolian dust deposition and from a sediment iron source. Iron is also added at the surface if the iron concentration falls below a lower limit of 0.01 nM. Iron is taken up by the plankton cells and released during remineralization of organic matter. Scavenging of iron onto particles is the sink for iron to balance external input. There are three non-living components of organic carbon in the model: semi-labile dissolved organic carbon (DOC), with a lifetime ranging from a few days to several years as a function of bacterial biomass and activity, and large and small detrital particles, which are fueled by mortality, aggregation, fecal pellet production and grazing. Small detrital particles sink through the water column with a constant sinking speed of 3 m day^{-1} , while for large particles the sinking speed increases with depth from a value of 50 m day^{-1} at the depth of the mixed layer, increasing to a maximum sinking speed of 425 m day^{-1} at 5000 m depth. For a more detailed description of the PISCES model see Aumont and Bopp (2006) and Gehlen et al. (2006). Further details and results from the fully coupled model simulation of the IPSL-CM4-LOOP model are given in Friedlingstein et al. (2006).

2.1.2 MPIM

The Earth System Model employed at the Max-Planck-Institut für Meteorologie (MPIM) consists of the ECHAM5 (Roeckner et al., 2006) atmospheric model of 31 vertical levels with the embedded JSBACH terrestrial biosphere model and the MPIOM physical ocean model, which includes a sea ice model (Marsland et al., 2003) and the HAMOCC5.1 marine biogeochemistry model (Maier-Reimer, 1993; Six and Maier-Reimer, 1996; Maier-Reimer et al., 2005). The coupling of the marine and atmospheric model components, and in particular the carbon cycles, is achieved by using the OASIS coupler.

HAMOCC5.1 is implemented into the MPIOM physical ocean model configuration using a curvilinear coordinate system with a 1.5° nominal resolution where the North Pole is placed over Greenland, thus providing relatively high horizontal resolution in the Nordic Seas. The vertical resolution is 40 layers, with higher resolution in the upper part of the water column (10 m at the surface to 13 m at 90 m). A detailed description of HAMOCC5.1 can be found in Maier-Reimer et al. (2005), while here only the main features relevant for the described experiments and analyses will be outlined. The marine biogeochemical model HAMOCC5.1 is designed to address large-scale, long-term features of the marine carbon cycle, rather than to give a complete description of the marine ecosystem. Consequently, HAMOCC5.1 is a NPZD model with one phytoplankton group (implicitly divided into calcite (coccolithophorids) and opal (diatoms) producers and flagellates) and one zooplankton species and particulate and dissolved dead organic carbon pools. The carbonate chemistry is identical to the one described in Maier-Reimer (1993).

PP depends on the availability of light (I) and nutrients. The local light supply is calculated from the temporally and spatially varying solar radiation at the sea surface, $I(0, t)$, as provided by the OGCM. Below the surface, light intensity is reduced due to attenuation by sea water (k_w) and chlorophyll (k_c) using a constant conversion factor for C:Chl, $R_{C:Chl}$:

$$I(z, t) = I(0, t) e^{-(k_w + k_c \text{PHY} 12 R_{C:P} / R_{C:Chl})z} \quad (1)$$

PP depends linearly on the availability of light, without saturation of growth rates for stronger irradiance (I). The growth rate $J(I(z, t))$, is calculated as $J(I) = \alpha_{\text{PHY}} I(z, t)$, where α_{PHY} is the slope of the production vs. light intensity curve. J is then multiplied by the nutrient limitation factor, which is calculated from a simple Monod function, limited by the least available nutrient (either phosphate, nitrate, or iron) to derive PP.

Particulate organic matter (POM), also termed detritus, is formed from dead phytoplankton and zooplankton, and zooplankton fecal pellets. POM production is taken to be proportional to the phytoplankton and zooplankton concentrations through constant mortality rates of plankton, and to the zooplankton grazing rate. POM sinks out of the euphotic

zone and is remineralized at depth. Furthermore, dissolved organic matter is produced by phytoplankton exudation and zooplankton excretion.

In the model version used in this study, all biological production rates (photosynthesis, mortality, grazing etc.) were temperature-independent, assuming that phytoplankton acclimate to local conditions. A constant climatology of global dust deposition fields from Stier et al. (2005) was used as source function of bioavailable iron. Removal of dissolved iron occurs through biological uptake and export, and by scavenging. Scavenging of iron is described as a relaxation to the deep-ocean iron concentration of 0.6 nM with a time scale of 200 years where the local concentration exceeds this value. The Fe:C ratio, also used to calculate the half-saturation value for iron, was set to a value of 5×10^{-6} (Johnson et al., 1997). With regard to the later discussions of results it should be noted here that the dust field of Stier et al. (2005) and the applied Fe:C ratio cause a too strong iron limitation of the model. Both using the Mahowald et al. (2006) dust fields or using an Fe:C ratio of 3×10^{-6} , which would be at the low end of the Johnson et al. (1997) estimates, would have avoided this. Unfortunately, the simulations with the coupled model were so computationally expensive that they could not be repeated until today, and the issue was only discovered when evaluating the experiment.

Export of detritus is simulated using prescribed settling velocities for opal (30 m day^{-1}), calcite shells (30 m day^{-1}) and organic carbon (10 m day^{-1}). Remineralization of organic matter depends on the availability of oxygen. In anoxic regions, remineralization occurs via denitrification. The model also includes cyanobacteria that take up nitrogen from the atmosphere if the local N:P ratio is below the Redfield ratio as a result of denitrification, and transform it directly into nitrate.

HAMOCC5.1 also includes an interactive sediment module. This component simulates pore water chemistry, the solid sediment fraction and interactions between the sediment and the oceanic bottom layer as well as between solid sediment and pore water constituents.

2.1.3 CSM1.4

The physical core of the NCAR CSM1.4 carbon climate model (Doney et al., 2006; Fung et al., 2005) is a modified version of the NCAR CSM1.4 coupled physical model, consisting of ocean, atmosphere, land and sea ice components integrated via a flux coupler without flux adjustments (Boville et al., 2001; Boville and Gent, 1998). The atmospheric model CCM3 is run with a horizontal resolution of 3.75° and 18 levels in the vertical (Kiehl et al., 1998). The ocean model is the NCAR CSM Ocean Model (NCOM) with 25 levels in the vertical and a resolution of 3.6° in longitude and 0.8° to 1.8° in latitude (Gent et al., 1998). The sea ice component model runs at the same resolution as the ocean model, and the land

surface model runs at the same resolution as the atmospheric model.

The CSM1.4-carbon model includes a modified version of the terrestrial biogeochemistry model CASA (Carnegie-Ames-Stanford Approach; Randerson et al., 1997), and a derivative of the OCMIP-2 (Ocean Carbon-Cycle Model Inter-comparison Project Phase 2) ocean biogeochemistry model (Najjar et al., 2007). In the ocean model, the biological source-sink term has been changed from a nutrient restoring formulation to a prognostic formulation inspired by Maier-Reimer (1993). Biological productivity is modulated by temperature (T), surface solar irradiance (I), mixed layer depth (MLD), and macro- and micro-nutrients (PO_4^{3-} , and iron):

$$\text{PP} = \frac{T + 2^\circ\text{C}}{T + 10^\circ\text{C}} \min\left(\frac{[\text{PO}_4]}{[\text{PO}_4] + \kappa_{\text{PO}_4}}, \frac{[\text{Fe}]}{[\text{Fe}] + \kappa_{\text{Fe}}}\right) \frac{I}{I + \kappa_I} \cdot \min\left([\text{PO}_4], \frac{[\text{Fe}]}{r_{\text{Fe:P}}}\right) \max\left(1, \frac{z_{\text{MLD}}}{z_c}\right) \frac{1}{\tau}, \quad (2)$$

where $\kappa_{\text{PO}_4} = 0.05 \mu\text{mol/l}$, $\kappa_{\text{Fe}} = 0.03 \text{ nmol/l}$, $\kappa_I = 20 \text{ W/m}^2$, $r_{\text{Fe:P}} = 5.85 \times 10^{-4}$, $\tau = 15$ days, and $z_c = 75$ m.

This empirical parameterization is intended to model the large-scale nutrient utilization by marine ecosystems. For example, the temperature function, together with iron limitation, forces a low productivity and nutrient utilization in water that is colder than about 2°C . On the other hand productivity depends only weakly on temperature in warmer waters. The temperature factor increases by less than two for a temperature increase from 4°C to 34°C ; this may be compared to an increase by a factor of seven in the IPSL model and no temperature-dependent growth rates in the MPIM model. Following the OCMIP-2 protocols (Najjar et al., 2007) total biological productivity is partitioned 1/3 into sinking POC flux, here taken to be equivalent to export productivity (EP), and 2/3 into the formation of dissolved or suspended organic matter, where much of the latter is remineralized within the model euphotic zone. Total productivity thus contains both new and regenerated production, though the regenerated contribution is probably lower than in the real ocean, as only the turnover of semi-labile dissolved organic matter (DOM) with a decay time scale of half a year is considered. CSM1.4 net primary productivity (PP) thus represents, rather, the carbon flux associated with net nutrient uptake and is not strictly equivalent to net primary production as measured by ^{14}C methods. It appears to be a reasonable proxy for the time and space variability of PP if somewhat underestimating the absolute magnitude (Schneider et al., 2008). For reasons of simplicity, net nutrient uptake times the C:P ratio of 117 (Anderson and Sarmiento, 1994) is considered here as PP, even though it is not exactly the same. The ocean biogeochemical model includes the main processes of the organic and inorganic carbon cycle within the ocean and air-sea CO_2 flux. A parametrization of the marine iron cycle (Doney et al., 2006) includes atmospheric dust deposition/iron dissolution, biological uptake, vertical particle transport and scavenging.

The CSM1.4-carbon source code is available online and described in detail in Doney et al. (2006).

2.1.4 CCSM3

The CCSM3 Biogeochemical Elemental Cycling (BEC) model includes several phytoplankton functional groups, one zooplankton group, semi-labile dissolved organic matter, and sinking particulates (Moore et al., 2004). Model-data skill metrics for the simulated marine ecosystem in uncoupled ocean experiments are reported in Doney et al. (2009a). The BEC includes explicit cycling of C, N, P, Fe, Si, O, and alkalinity. Iron has external sources from dust deposition and marine sediments, and the scavenging of iron onto particles balances these sources with 10% of scavenged iron presumed lost to the sediments (Moore and Braucher, 2008). Phytoplankton functional groups include diatoms, diazotrophs, picoplankton, and coccolithophores. The export ratio is largely a function of phytoplankton community composition with diatom production being exported more efficiently than production by small phytoplankton. Phytoplankton growth rates and zooplankton grazing rates are modified by a temperature function that includes a Q_{10} factor of 2.0. Thus, maximum growth rate would change by a factor of 8 for a temperature increase from 4°C to 34°C . Phytoplankton growth rates are also a function of nutrient and light limitation and these factors are multiplicative (Moore et al., 2004). Phytoplankton Fe/C, Chl/C, and Si/C ratios adjust dynamically to ambient nutrient and light, while the C/N/P ratios are fixed within each group (Moore et al., 2004). The CCSM3 ocean circulation model is a coarse resolution version of the parallel ocean program (POP) model with longitudinal resolution of 3.6 degrees and a variable latitudinal resolution from 1 – 2 degrees. There are 25 vertical levels with eight levels in the upper 103 m (Smith and Gent, 2004; Yeager et al., 2006).

2.2 Experiments and satellite-based productivity estimates

The models are forced by anthropogenic CO_2 emissions due to fossil fuel burning and land-use changes as reconstructed for the industrial period and following the SRES A2 emission scenario after 2000 AD. The CSM1.4, CCSM3, and MPIM models also include CH_4 and CFCs. N_2O , volcanic emissions, and changes in solar radiation are additionally taken into account by the CSM1.4 and CCSM3 models as described by Frölicher et al. (2009). Dust deposition fields were kept at a constant climatology in all experiments. All models were integrated for more than one thousand years for spin up (Schneider et al., 2008; Thornton et al., 2009). For analysis, all variables have been interpolated onto a common $1^\circ \times 1^\circ$ grid using a Gaussian weighted average of the data points within a radius of 4° with a mapping scale of 2° . Control simulations in which CO_2 emissions are set to zero and other forcings are set to constant preindustrial levels are

Table 1. Simulated global annual primary production (PP) and POC export (EP) for the four models IPSL, MPIM, CSM1.4, and CCSM3 under SRES A2. PP values are also given for weighted means of the four models derived from regional skill scores (PP^S), mean square errors (PP^E), and global skill scores ($PP^{S_{glob}}$), as well as for the arithmetic average (PP^{ave}). Global skill scores (S_{glob}) and root mean square errors (RMSE) indicate the ability of the individual models and the multi-model means to reproduce the satellite-based estimates of PP (average 1998–2005, see main text for details). Values are averaged over the periods 1860–1869 (1865), 1985–2004 (2000), and 2090–2099 (2095). ΔPP and ΔEP indicate changes between corresponding periods.

Primary production	IPSL	MPIM	CSM1.4	CCSM3	PP^S	PP^E	$PP^{S_{glob}}$	PP^{ave}
PP_{glob} 1865 [GtC yr ⁻¹]	34.9	23.9	27.5	49.4	37.1	35.9	36.3	33.8
PP_{glob} 2000 [GtC yr ⁻¹]	33.8	23.7	26.6	49.1	36.1	34.9	35.3	33.0
PP_{glob} 2095 [GtC yr ⁻¹]	30.3	21.6	25.6	48.4	34.2	33.0	33.5	31.2
ΔPP_{glob} 1865–2000 [GtC yr ⁻¹]	-1.1 (-3%)	-0.2 (-1%)	-0.9 (-3%)	-0.3 (-1%)	-1.0 (-3%)	-1.0 (-3%)	-1.0 (-3%)	-0.8 (-2%)
ΔPP_{glob} 2000–2095 [GtC yr ⁻¹]	-3.5 (-10%)	-2.1 (-9%)	-1.0 (-4%)	-0.7 (-1%)	-1.9 (-5%)	-1.9 (-5%)	-1.8 (-5%)	-1.8 (-5%)
ΔPP_{glob} 1865–2095 [GtC yr ⁻¹]	-4.6 (-13%)	-2.3 (-10%)	-1.9 (-7%)	-1.0 (-2%)	-2.9 (-8%)	-2.9 (-8%)	-2.8 (-8%)	-2.6 (-8%)
S_{glob}	0.49	0.16	0.37	0.46	0.40	0.33	0.30	0.25
RMSE [mgC m ⁻² day ⁻¹]	284	353	334	305	259	265	268	278
POC export	IPSL	MPIM	CSM1.4	CCSM3				
EP_{glob} 1865 [GtC yr ⁻¹]	9.1	5.0	9.1	7.2				
EP_{glob} 2000 [GtC yr ⁻¹]	8.7	5.0	8.8	7.1				
EP_{glob} 2095 [GtC yr ⁻¹]	7.3	4.5	8.4	6.8				
ΔEP_{glob} 1865–2000 [GtC yr ⁻¹]	-0.4 (-4%)	0.0 (0%)	-0.3 (-3%)	-0.1 (-1%)				
ΔEP_{glob} 2000–2095 [GtC yr ⁻¹]	-1.4 (-16%)	-0.5 (-10%)	-0.4 (-5%)	-0.3 (-4%)				
ΔEP_{glob} 1865–2095 [GtC yr ⁻¹]	-1.8 (-20%)	-0.5 (-10%)	-0.7 (-8%)	-0.4 (-6%)				

used to remove century-scale model drifts for each grid point and for each calendar month (Frölicher et al., 2009). Affected are the three-dimensional distribution of temperature, salinity, and nutrient concentrations in the IPSL and CSM1.4 models, as well as PP and EP in IPSL. For these variables, detrended values from the scenario simulations are used for analysis. We note that trends in surface values are small in the CSM1.4.

As a point of reference and following Schneider et al. (2008), we utilize throughout this study satellite-based estimates obtained with the Behrenfeld algorithm (VGPM; Behrenfeld and Falkowski, 1997b; Behrenfeld et al., 2006) for data-model comparison and to compute skill-score weighted multi-model averages. The satellite-derived estimates have uncertainties. For example, Carr et al. (2006) report that global PP estimates from twenty-four ocean-color-based models range over a factor of two. On a more positive side, ocean-color-based models agree with respect to the spatial pattern of chlorophyll distributions and correlations among the resulting fields are typically high. Given these substantial uncertainties in satellite-based productivity data, the comparison of model results with one single satellite-based data set should be viewed as an illustrative example.

3 Results

3.1 Projected annual mean net primary productivity and export production under SRES A2

We briefly discuss the magnitude and spatio-temporal patterns of net primary production (PP) in comparison with satellite-based estimates (see Schneider et al. (2008) for a more comprehensive analysis) and compare simulated e-ratios, i.e. the ratio of annual EP to PP, to field data compiled by Laws et al. (2000) before addressing long-term changes in PP. Global annual PP ranges between 24 Gt C yr⁻¹ (MPIM) and 49 Gt C yr⁻¹ (CCSM3) for modern conditions (Table 1, Fig. 1). Only the CCSM3 model lies within the satellite-based range of 35 to 70 Gt C yr⁻¹ (Behrenfeld et al., 2006; Carr et al., 2006). The range of the other three models is considerably lower. The very low PP in the MPIM model is likely linked to an overall too strong limitation of PP by iron (Schneider et al., 2008). This is supported by the fact that surface nitrate concentrations are largely overestimated by this model. PP in CSM1.4 represents carbon uptake associated with net nutrient uptake, rather than overall net primary productivity, and is thus underestimating real net primary production by design. There are also deficiencies in the regional representation of PP (Fig. 2). High PP along continental margins is not adequately represented in coarse resolution models. The MPIM model underestimates PP outside the equatorial regions, and the CSM1.4 model has too low PP in the equatorial Pacific. These deficiencies are related to the iron cycle of the two models. IPSL and CCSM3 appear to underestimate PP in high northern latitudes. The CCSM3

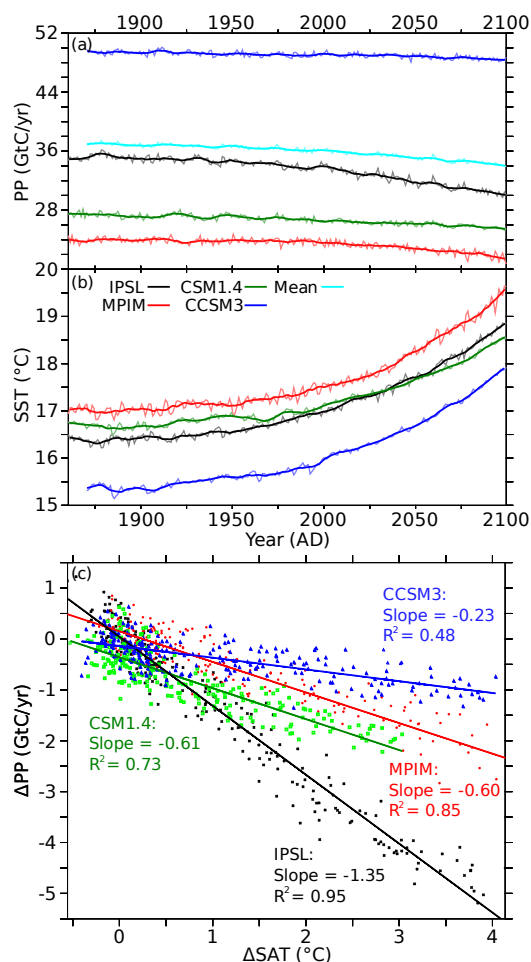


Fig. 1. (a) Global annual mean primary production (PP, $\frac{\text{GtC}}{\text{yr}}$) and (b) sea surface temperature (SST, $^{\circ}\text{C}$) simulated by the IPSL (black), MPIM (red), CSM1.4 (green), and CCSM3 (blue) models for the period 1860–2100 under SRES A2. The cyan line indicates the weighted mean PP derived from the regional skill scores of the four models. (c) ΔPP as a function of changes in global mean surface air temperature (SAT) for the same models and time period.

model clearly overestimates PP in the eastern tropical Pacific. The skill of individual models to represent the satellite-based PP field is rather low with correlations between modeled and satellite-based fields of less than 0.6 (Fig. 2b). The errors in the simulated PP fields reflect both deficiencies in the simulated physical fields and in the representation of ecosystem processes in the coupled AOGCM. Results from ocean only models with prescribed surface forcing compare typically better with observation-based estimates. We recall that the satellite-derived estimates have uncertainties; Carr

et al. (2006) report that global PP estimates from twenty-four ocean-color-based models range over a factor of two, but correlations among the resulting fields are typically high.

The e-ratio (EP:PP) is a measure of the contribution of regenerated production to total PP. The regenerated production is driven by nutrient recycling through the activities of heterotrophs, including bacteria. In the IPSL, MPIM, and CCSM3 models, the regenerational loop is described through the interaction of a limited number of different biomass pools and the production of dissolved organic matter (DOM) by plankton and the release of nutrients during DOM decay. Hence, the bacterial loop, which recycles nutrients to the food web by bacterial consumption of DOM and nutrient release by bacteria and grazing of bacteria by zooplankton, is implicitly described. In the CSM1.4 model, that features only one biomass pool, the e-ratio is fixed to 0.3. In the MPIM model, the annual-mean e-ratio shows a small spatial variability around a value of 0.2 (Fig. 3b,e). In the CCSM3 model the spatial variability is only slightly larger and the e-ratio ranges from 0.05 to 0.3 (Fig. 3c, f). In the IPSL, the e-ratio is low in mid- and low-latitude regions, intermediate in the Southern Ocean, North Pacific and North Atlantic and high in the Arctic (Fig. 3d). The spatial variability in the CCSM3 and IPSL models are driven mainly by phytoplankton community. Both models assume higher export for diatom production and with more diatom production at high latitudes the e-ratio increases. Following Laws et al. (2000), we compare the simulated e-ratio as a function of SST with field data from a few sites (Fig. 3a, b, c). The regression slope found for the IPSL model ($-0.0097\text{ }^{\circ}\text{C}^{-1}$) is somewhat lower than the slope of the field data ($-0.0198\text{ }^{\circ}\text{C}^{-1}$) but covers most of the data points, whereas the MPIM and CCSM3 models don't capture the observational range in the e-ratio. We note, however, that there are cold, iron-limited sites in the Southern Ocean that differ significantly from the regression line fitted to the data from the few sites selected by Laws et al. (2000). There is almost no correlation between the e-ratio and PP, consistent with observation-based estimates. Only the e-ratio in the CCSM3 model seems to be slightly biased towards higher values at locations with high PP.

Despite the deficiencies of individual models, the models as a class represent the pertinent features of the satellite-based observations such as a low PP in the oligotrophic gyres and the southern high latitudes (all models), high PP features in the North Atlantic (CSM1.4, IPSL, CCSM3), in the North Pacific (IPSL, CCSM3), around 30°S to 50°S (CSM1.4, IPSL, CCSM3), and in the equatorial and eastern boundary upwelling systems. Other reproduced features are the high seasonal variability in the North Atlantic and in southern intermediate latitudes (all), the low seasonal variability around the equator (CSM1.4) and in mid latitudes (all), and the correlation of temperature and stratification with PP on the interannual time scales for the low-latitude, permanently stratified ocean (IPSL) or the Nino3 region (IPSL, CSM1.4).

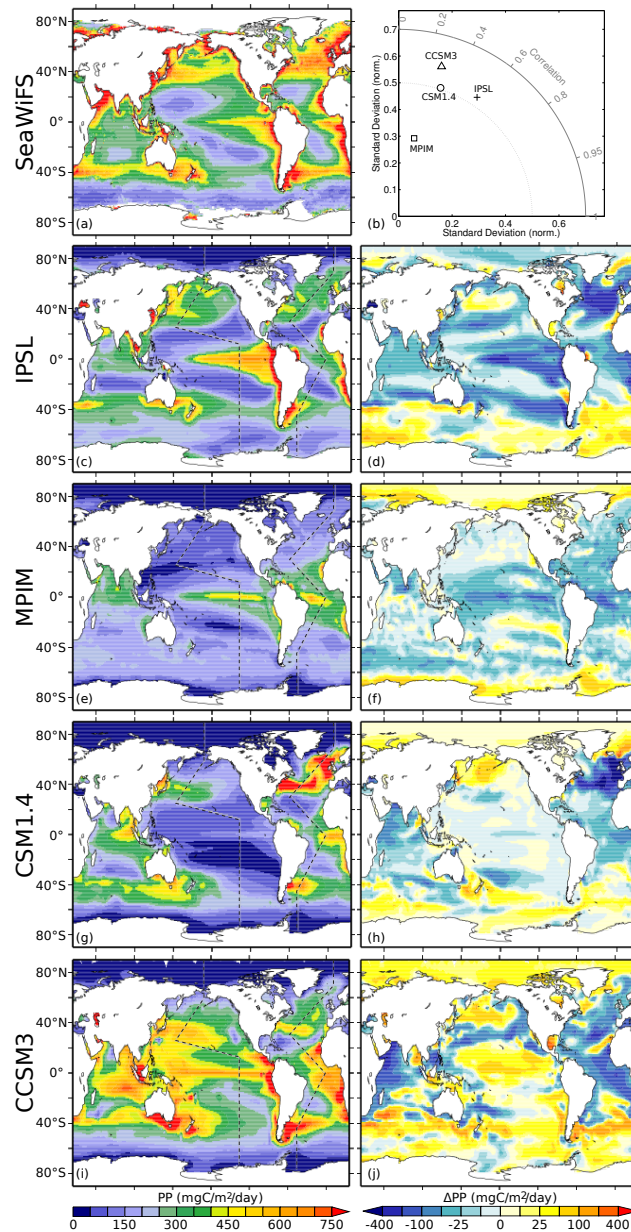


Fig. 2. Productivity (left) and projected changes by 2090–2099 (right). Vertically integrated annual mean primary production (PP , $\frac{\text{mgC}}{\text{m}^2 \text{ day}}$) derived from ocean color (a) (SeaWiFS; Behrenfeld et al., 2006; Behrenfeld and Falkowski, 1997b) and simulated by IPSL (c), MPIM (e), CSM1.4 (g), and CCSM3 (i) under preindustrial conditions (decadal mean 1860–1869). Dashed lines indicate the transects through the Atlantic and Pacific analyzed in this study. The Taylor diagram (b) shows the correspondence between model results and the satellite-based estimates (Taylor, 2001). In this diagram the polar coordinates represent the correlation coefficient R (polar angle) and the normalized standard deviation $\sigma_{\text{model}}/\sigma_{\text{obs}}$ (radius). Panels d, f, h, and j show the projected changes by the end of the 21st century under SRES A2 for the four models. The changes are shown on an exponential scale and represent the difference between 2090–2099 and 1860–1869 (decadal means).

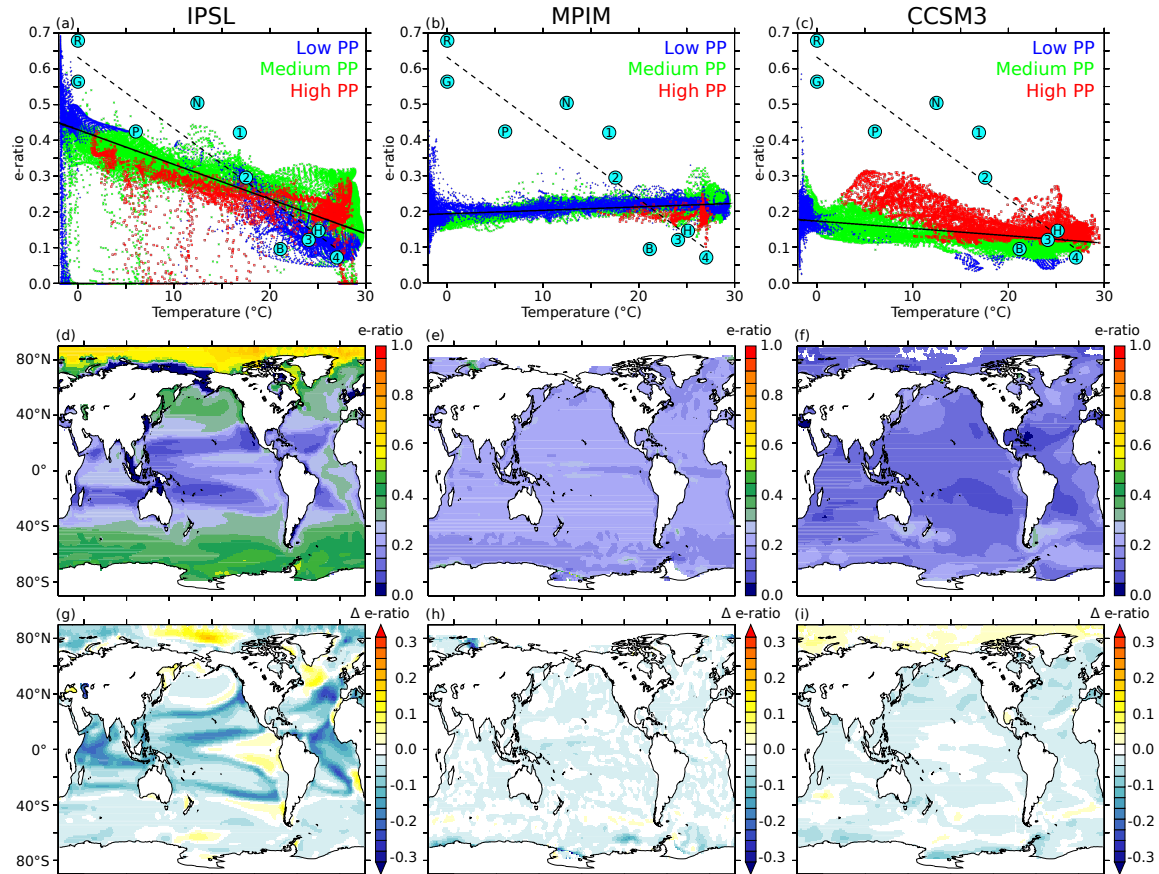


Fig. 3. Export ratio (e-ratio; EP:PP) simulated by the IPSL (left), MPIM (middle), and CCSM3 (right) models. The preindustrial (decadal mean 1860–1869) e-ratio is shown as a function of sea surface temperature (**a**, **b**, **c**). Each point represents one grid cell and the colors indicate low (blue; 10–150 mg C/m²/day), medium (green; 150–450 mg C/m²/day), and high (red; >450 mg C/m²/day) PP. Circles show field data (cf. Laws et al., 2000, Fig. 4) for the following locations: BATS (B), HOT and Arabian Sea (H), NABE (N), Peru-normal (1), Peru-El Niño (2), EqPac-normal (3), EqPac-El Niño (4), Ross Sea (R), Station-P (P), and Greenland polynya (G). The straight solid lines indicate the linear regression for IPSL ($r^2 = 0.58$, slope = -0.0097), MPIM ($r^2 = 0.21$, slope = 0.0010), and CCSM3 ($r^2 = 0.28$, slope = -0.0021), while the dashed line indicates the regression of the field data selected by Laws et al. (2000) ($r^2 = 0.86$, slope = -0.0198). Maps show the simulated e-ratio under preindustrial conditions (**d**, **e**, **f**) and the projected changes by the end of the 21st century under SRES A2 (**g**, **h**, **i**). Where PP is below a minimum threshold of 10 mg C/m²/day the e-ratio is not shown. In the CSM1.4 model the e-ratio is fixed at 0.3 and not shown in this figure.

This comparison with satellite-derived and in-situ estimates allows us to continue with some confidence as well as with caution to the discussion of 21st century projections.

All four models show a reduction in the globally integrated annual mean PP in the simulations from 1860 AD to 2100 AD under SRES A2 (Fig. 1, Table 1). The IPSL model shows the biggest changes. In that model PP declines by 4.6 GtC/yr by the end of this century, which is a reduction of the simulated preindustrial PP by 13%. The MPIM and CSM1.4 models show reductions of 10% (2.3 GtC/yr and

7% (1.9 GtC/yr), respectively. The CCSM3 model, which yields the highest PP, projects the smallest reduction of 2% (1.0 GtC/yr). Despite these small changes on the global scale, the CCSM3 model shows local changes of the same order of magnitude as the other models, but these changes tend to cancel out to some extent.

The projected PP decrease by the end of the century depends on the magnitude of the projected climate change and thus on the climate sensitivity of the models. A linear regression between global PP and global mean surface air

temperature is used to normalize PP changes with respect to climate change in order to account for the different climate sensitivities of the models (Fig. 1c). This yields a slope, i.e., the global PP decrease per °C warming, of $1.4 \text{ Gt C yr}^{-1} \text{ } ^\circ\text{C}^{-1}$ for the IPSL model, but only $0.6 \text{ Gt C yr}^{-1} \text{ } ^\circ\text{C}^{-1}$ for the MPIM and CSM1.4 models and $0.2 \text{ Gt C yr}^{-1} \text{ } ^\circ\text{C}^{-1}$ for CCSM3.

We identify a number of regions with large reductions (more than $50 \text{ mg C m}^{-2} \text{ day}^{-1}$) in PP (Fig. 2). These correspond to high PP areas. A large reduction in PP is found in the North Atlantic in the IPSL, CSM1.4, and CCSM3 models, around 35° S in the Pacific in the IPSL and less pronounced in the CSM1.4, in the upwelling regions off Africa in all models and in the equatorial Pacific in the MPIM and IPSL model. These reductions are qualitatively consistent across three out of the four models with the obvious caveat that no major reductions can be expected in regions where an individual model fails to simulate a significant preindustrial PP (e.g. MPIM outside the equator, CSM1.4 in the equatorial Pacific). An exception is the moderate increase in PP simulated by the CCSM3 model in parts of the tropical Pacific. Consistent moderate increases in PP are simulated in the high latitude Southern Ocean (all models) and around Svalbard, indicating that the high PP zone in the North Atlantic is moving northward with climate warming and sea ice retreat. An increase in PP is simulated in the Pacific north of 40° N in the IPSL, CSM1.4, and CCSM3 models. We note that sea ice extent is unrealistically high in this area in the CSM1.4 model (Steinacher et al., 2009; Weatherly et al., 1998). In summary, the model results suggest that PP will be reduced in most equatorial and mid-latitude regions and in the North Atlantic, and moderately enhanced in polar regions.

Climate change might not only affect PP, but also EP, and the relative contribution of new ($\approx e$) and recycled ($\approx 1 - e$) production. In the MPIM and CCSM3 models, the e-ratio remains spatially relatively uniform and shows almost no change during the simulation (Fig. 3e, h, f, i), much like in the simpler CSM1.4 model, where the e-ratio is fixed at 0.3. Thus, the relative reduction in EP follows closely the reduction in PP in these three models. The e-ratio in the IPSL model shows distinct regional changes by the end of this century (Fig. 3e). On global average, the (PP-weighted) e-ratio declines. Correspondingly, the reduction in EP is larger than in PP; EP declines by 20% and PP by 13% over the simulation period.

Turning to regional changes in the e-ratio, we find both positive and negative changes in the IPSL simulation (Fig. 3g). The attribution of simulated changes in the e-ratio is generally difficult as the set of equations describing PP and EP is complex and non-linear. Positive deviations in the e-ratio, e.g. as found in high-productive upwelling regions off South America and Africa, are small and difficult to ascribe to a forcing factor. The shifts to higher e-ratios south of Greenland and north of the Ross sea appear to be linked to the fact that these are the only two regions where a slight cooling

is simulated in the IPSL model; cooler temperatures are often associated with higher nutrient concentrations which tend to favor a higher e-ratio, consistent with the observation-based slope of e-ratio versus temperature (Fig. 3a). Large negative changes in the e-ratio of up to 0.25 are simulated at the border of highly productive regions where PP decreases from moderate to low values (e.g. at the edge of the subtropical gyres, (Fig. 3d, g)). The reasons for this decoupling of PP and EP in the IPSL model are a shift from diatoms and zooplankton to the smaller nanophytoplankton and the increased recycling of nutrients and carbon in the surface ocean (Bopp et al., 2005).

3.2 Mechanisms of long term shifts in PP under climate change

3.2.1 Attribution of PP changes to individual drivers in the CSM1.4 model

In order to identify links between long term shifts in PP and climate change, we first focus on the NCAR CSM1.4-carbon results. This model features the simplest formulations for biological production among the four models. PP is determined by the product $\text{PP} \propto F_N \cdot F_I \cdot F_T \cdot B$ (Eq. 2), where the first three factors represent nutrient, light, and temperature limitation and B is a biomass proxy derived from phosphate and iron concentrations. The relative changes in these factors (Fig. 4a–d) directly yield the relative changes in PP (Fig. 4e). Light availability is tied to the mixed layer depth and sea ice fraction in the CSM1.4 model. It increases when the mixed layer depth (MLD) exceeds 75 m. This unrealistic feature affects light limitation in the South Pacific (increased MLD/light availability) around 45° S and in a number of grid cells in the North Atlantic. We recall that the biomass proxy corresponds to the phosphate or (scaled) iron concentration (which ever is smaller) and thus directly represents nutrient concentrations.

The biomass proxy decreases in most areas of the world ocean (Fig. 4d). This can be attributed to a more efficient utilization of nutrients under global warming as found in previous work (e.g. Plattner et al., 2001; Frölicher and Joos, 2010). Reduced nutrient concentrations in combination with reduced export are indicative of reduced nutrient input from the thermocline into the mixed layer. Such conditions prevail in the Atlantic between 20° S and 65° N , in the western part of the Indian Ocean, and around 30° N and 35° S in the Pacific between 160° E and 140° W . PP shows little or no response to climate change in the tropical and subtropical Pacific, where PP is low due to an unrealistically strong iron limitation. On the other hand, sea ice retreat and warming in the Arctic alleviate the strong limitations by light and temperature and enhance Arctic PP. Similarly, a reduction in temperature limitation boosts PP around Antarctica in the model.

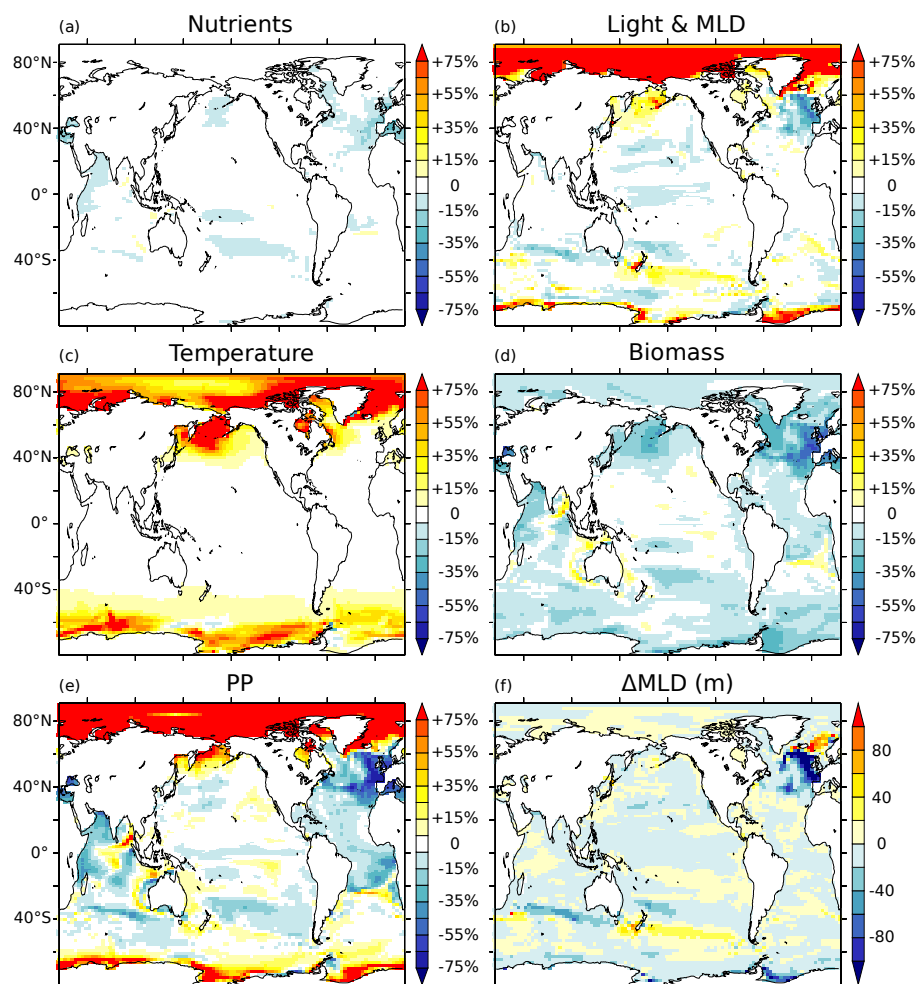


Fig. 4. Long-term changes in PP limitation by nutrients (a), light (b), and temperature (c) simulated by the CSM1.4 model. In the CSM1.4 model, these factors, together with changes in the biomass proxy (d), determine the changes in PP (e). Panels (a–e) show relative changes in percent from preindustrial (average 1860–1869) to projected future conditions under SRES A2 (average 2090–2099). Positive values indicate changes that enhance PP, negative values indicate changes that tend to reduce PP. All values are averaged over the compensation depth (75 m), where all of the production is restricted to occur. The light limitation factor (b) also accounts for changes in mixed layer depth (f).

In the North Atlantic, where the largest PP changes occur, the PP decrease is dominated by a decrease in the biomass proxy. Nutrients are used up more efficiently, and PP decreases likely in response to less surface-to-deep exchange, which is linked to a reduction in the North Atlantic thermohaline circulation (Frölicher et al., 2009) and a reduced deep wintertime convection. The model also simulates an increase in light limitation, mainly caused by the decrease in mixed layer depth, and a somewhat stronger limitation by iron in the east and by phosphate in the west. The slight increase in

PP in some areas in the Indian Ocean, around Australia, and in the South Atlantic around 25° S can mainly be attributed to an increased nutrient supply due to stronger upwelling.

In conclusion, PP changes in the CSM1.4 model are tightly linked to changes in nutrient input into the euphotic zone in combination with an alleviation of light and temperature limitations in high latitudes. A reduced nutrient input into the surface is expected in climate change scenarios as surface stratification tends to increase in response to warming and freshening. Next, we will investigate changes in physical

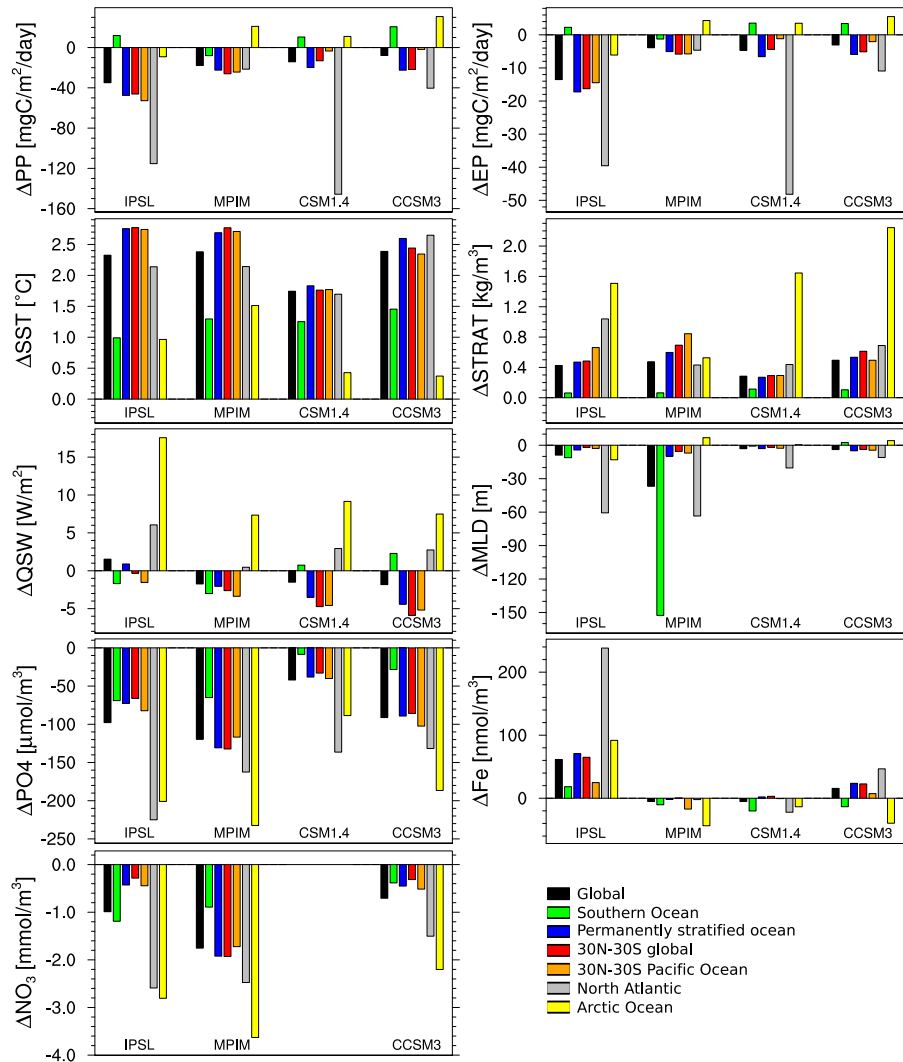


Fig. 5. Long-term trends of PP, EP and related properties simulated by the IPSL, MPIM, CSM1.4, and CCSM3 models under SRES A2. Each panel shows the projected changes of one property with respect to preindustrial conditions (average 2090–2099 minus average 1860–1869) for the following regions: Global oceans (black), Southern Ocean (green; south of 45° S), permanently stratified, low-latitude oceans (blue; annual mean SST > 15 °C), low-latitude oceans (red; 30° N–30° S), low-latitude Pacific (black, 30° N–30° S), North Atlantic (grey; 30° N–80° N), and Arctic Ocean (yellow). The properties are vertically integrated PP, POC export (EP), surface temperature (SST, averaged over top 75 m), stratification (STRAT), short wave heat flux (QSW) at the surface, mixed layer depth (MLD), and surface nutrient concentrations (PO₄, Fe, NO₃; averaged over top 75 m). NO₃ is not available for the CSM1.4 model.

factors such as stratification and upwelling as well as in nutrient availability and their link to PP for all four models.

3.2.2 Basin-scale changes in productivity, physical properties, and nutrient concentrations

There is a surprisingly good overall consistency in projected trends among the models on the basin-scale and for a range of variables. Figure 5 shows projected changes in selected large

regions for PP, EP, related physical properties, and nutrient concentrations for all four models. This comparison between changes in PP and in potential drivers is indicative of underlying mechanisms, albeit it does not allow for a stringent attribution as done in the previous section for the CSM1.4 model. Overall, the results are qualitatively consistent across models and regions. PP, EP, MLD, and surface nutrient concentrations are projected to decrease in all models and in almost all regions, while sea surface temperature (SST) and stratification increase. Next, we will show that the mechanisms identified for the CSM1.4 model are also key for the productivity changes in the IPSL, MPIM, and CCSM3 models. Namely, we find that a reduced nutrient input related to enhanced stratification, reduced MLD, and a slowed circulation tends to decrease PP and EP under transient global warming not only in the CSM1.4, but also in the other three models.

All models exhibit pronounced changes in MLD and stratification in the North Atlantic, which transform to strong reductions in surface macro-nutrient concentrations. Consequently, PP and EP decrease in the IPSL and CSM1.4 models by about 40% and 30%, respectively. In the CCSM3 model, PP is reduced by 13% and EP by 23%. In the MPIM model, preindustrial PP in the North Atlantic is unrealistically small due to too strong iron limitation and the 21st century reduction in PP is thus small as well.

All models show an increase in stratification and a decrease in MLD and macro-nutrients in the stratified ocean ($SST > 15^{\circ}\text{C}$). We again link this tentatively to a reduced nutrient input into the euphotic zone under global warming. Productivity and export decrease accordingly in all models.

In the Southern Ocean ($<45^{\circ}\text{S}$), relative PP trends are smaller than in other regions and vary in sign between different regions within the Southern Ocean. Changes that favor production, such as increased SST and light, and changes that tend to reduce production, such as reduced nutrient input, balance to some extent on the regional average. In the IPSL, CSM1.4, and CCSM3 simulations, PP increases on average, while MPIM shows a decrease of about 5%, which is probably linked to the very strong decrease in MLD. The CCSM3 model projects a relatively large PP increase around 40°S which results from the combination of a moderate to strong increase in SST and a reduction in nutrient limitation in some areas in that region. To some extent, this feature is also present in the CSM1.4 and IPSL simulations.

There are also some qualitative inconsistencies in projected trends between models. Most notable are the following three. (1) IPSL simulates a decrease in PP and EP in the Arctic Ocean, in contrast to MPIM, CSM1.4, and CCSM3 that project an increase (Fig. 5). (2) Surface iron concentration is projected to increase in all regions in IPSL and on global average in CCSM3, while MPIM and CSM1.4 project a decrease in most regions (Fig. 5). (3) CCSM3 projects an increase in PP in the central Pacific between 10°S and 20°N (Fig. 2), whereas the other models simulate a decrease.

In the Arctic Ocean, light availability in the surface ocean is strongly enhanced in all models due to sea ice retreat. The annual mean sea ice cover in the Arctic is reduced by 32% (IPSL), 25% (MPIM), 23% (CSM1.4) and 20% (CCSM3) with respect to preindustrial conditions. This leads, together with an increase in SST and MLD, to a strong increase in PP and EP in the MPIM (+130%), CSM1.4 (+215%), and CCSM3 (+150% for PP; +200% for EP) simulations, despite the strong (+90% in CSM1.4; +80% in CCSM3) and moderate (+20% in MPIM) increase in stratification and reduced surface nutrient concentrations. Although insolation and SST increase also strongly in IPSL, this model shows an opposite response in PP and EP. This can be explained with a strong increase in stratification of about 90% and the reduction in MLD and surface macro-nutrients of 50–70%.

The increase in surface iron concentration simulated by the IPSL model (20% in the global mean) is a consequence of the parametrization of the elemental ratio in phytoplankton. The ratio between carbon and nitrogen or phosphorus is kept constant. In contrast, the iron-to-carbon ratio of phytoplankton is assumed to decrease with increasing nutrient (and light) limitation. Consequently, lower macro-nutrient concentrations in the euphotic zone lead to a relatively lower uptake of iron compared to other nutrients by plankton and to a lower iron-to-carbon ratio in organic material. In turn, less iron is exported out of the euphotic zone and iron concentrations increase, while macro-nutrient concentrations decrease. In the IPSL model, surface iron concentrations are restored to a minimum value of 0.01 nM. This influences the interannual variability in PP (Schneider et al., 2008). However, this potential artificial iron source does not contribute significantly to the long-term trend in surface iron because, first, the number of grid cells and months where iron is restored is reduced during the simulation, and second, these regions do not correspond to the regions where large changes in surface iron are simulated. In the CCSM3 model, the iron-to-carbon ratio is also variable but this has only a small effect on surface iron concentrations. In the CSM1.4 and MPIM model, the iron-to-carbon and other elemental ratios are constant. Generally, surface iron tends to increase in regions with substantial aeolian iron input and increased stratification or reduced mixed layer depth, whereas it tends to decrease in parallel with macro-nutrient concentrations in the surface ocean in regions with little iron input. This leads to an increase in global mean surface iron of 4% in the CCSM3 model, while CSM1.4 and MPIM project a slight decrease of about 2%. In contrast to the IPSL model, these three models all project a decrease in surface iron in the Southern Ocean and in the Arctic.

Nutrient and light limitation factors are output variables of the CCSM3 model and therefore allow the direct attribution of changes in PP to changes in these factors. The PP increase projected by the CCSM3 model in the central Pacific between 10°S and 20°N is a result of a strong increase in SST and a slight reduction of iron limitation in combination with

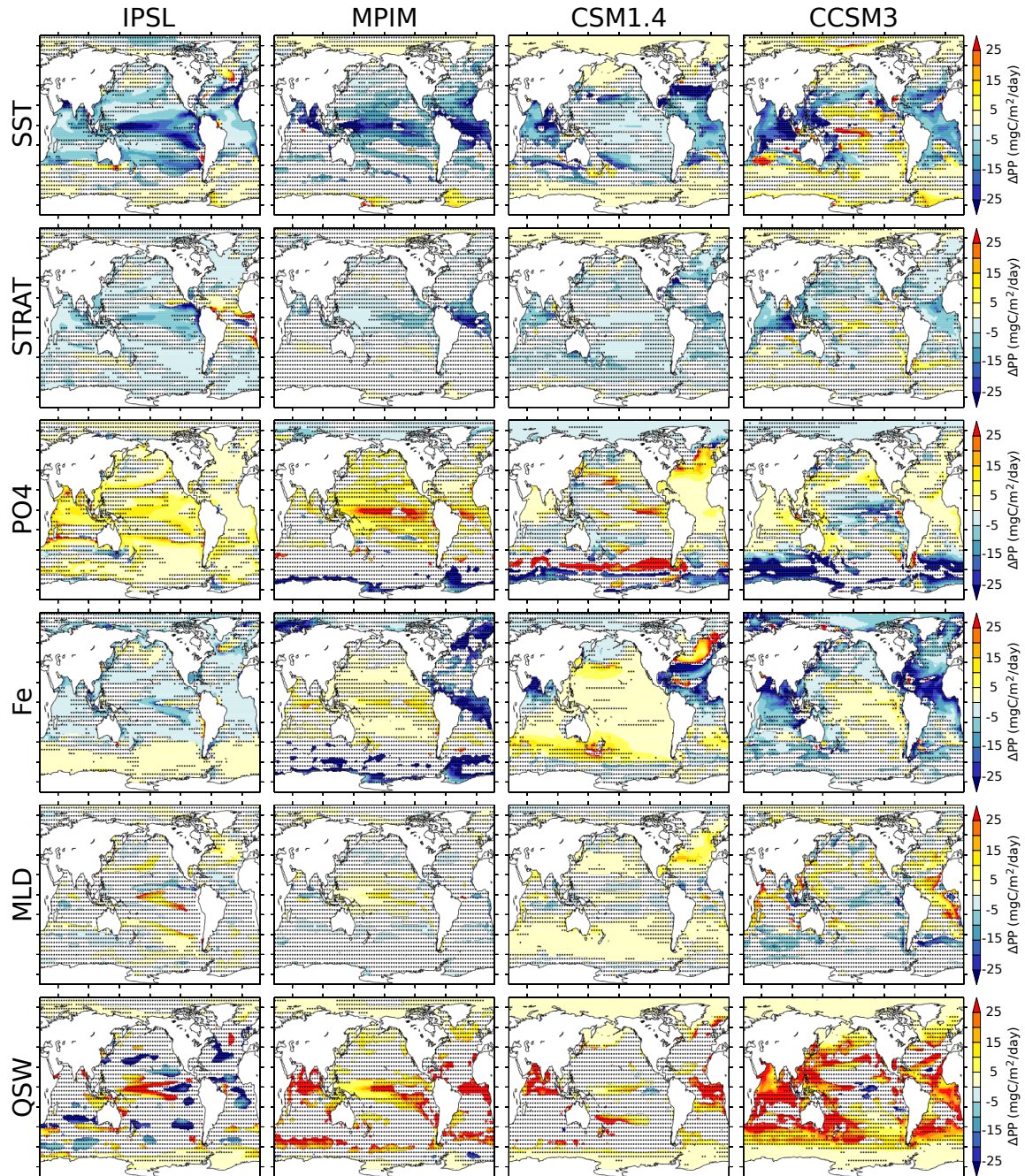


Fig. 6. Linear correlation between vertically integrated annual mean PP and surface temperature (SST), stratification index (STRAT), PO_4 , Fe, mixed layer depth (MLD), and light (QSW) for the IPSL, MPIM, CSM1.4, and CCSM3 models (columns from left to right). The regression has been calculated for simulated annual mean values in each grid cell from 1860 to 2100 (SRES A2). SST, PO_4 and Fe are averaged over top 75 m depth. Normalized regression slopes (ΔPP [$\text{mgC}/\text{m}^2/\text{day}$] per relative change of SST, STRAT, PO_4 , Fe, MLD, and QSW in percent) are shown where $R^2 > 0.1$. Areas where $R^2 < 0.5$ are shaded.

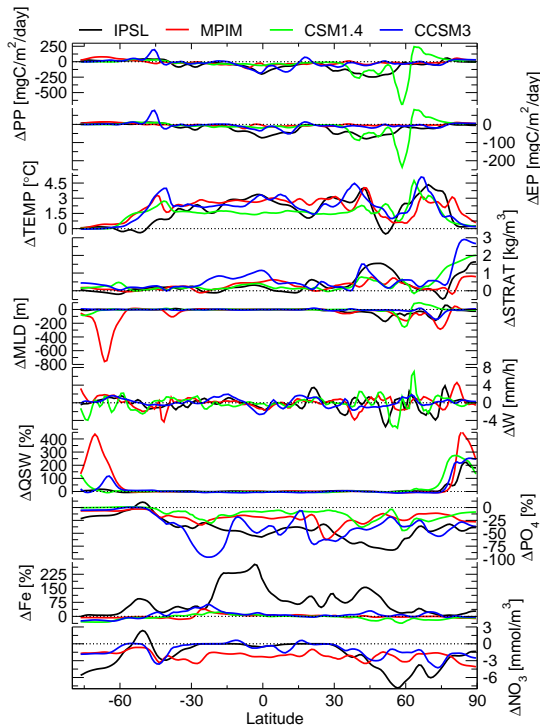


Fig. 7. Long-term trends of PP, EP and related properties simulated by the IPSL (black), MPIM (red), CSM1.4 (green), and CCSM3R (blue) models under SRES A2 for a transect through the Atlantic that covers major productivity features (dashed lines in Fig. 2c, e, g, i). Changes in vertical velocity (ΔW) are shown in addition to the parameters displayed in Fig. 5.

almost no change in macronutrient limitation and a moderate increase in light limitation. In this region, PO_4 and NO_3 concentrations are reduced in response to large changes in stratification and MLD and increased export, but they remain relatively high and PP limitation by macronutrients remains small. In contrast, a similar reduction in macronutrients leads to a significant increase in nutrient limitation around 30°N , and consequently to a pronounced reduction in PP. We note that the model overestimates present-day phosphate concentrations in the Pacific south of 40°N and that PP is too high in the eastern tropical and subtropical Pacific. Thus, the simulated macronutrient limitation might be too weak and the projected PP too high in this region. We also note that despite the moderate PP increase in the central equatorial Pacific, PP decreases slightly by 0.4% when averaged over the Pacific between 30°S and 30°N .

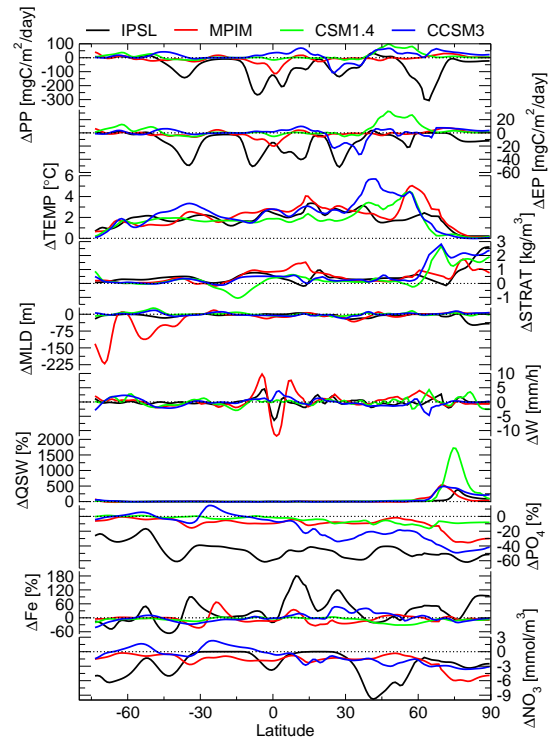


Fig. 8. Same as Fig. 7 but for a transect through the Pacific (dashed lines in Fig. 2c, e, g, i).

3.2.3 Local correlations between changes in PP and potential drivers

In this section, we address to which extent the features identified on the basin-scale are also evident on the local scale. We correlate simulated changes in annual mean PP with annual mean changes in SST, stratification, MLD, and shortwave radiation, as well as with phosphate and iron for each single grid cell (Fig. 6) and compare projected changes along two transects through the Atlantic (and Arctic), and the Pacific (Figs. 7 and 8). The transects, indicated in Fig. 2, are selected to cover major PP features in the two basins. The results tend to confirm the findings from the two previous sections, although the links between stratification, mixed layer depth and macro-nutrient concentrations are often somewhat obscured on the grid cell scale as evidenced by the small regression coefficient (R^2) found for many cells.

In the IPSL simulation, the PP decrease in the Pacific, North Atlantic and Indian Ocean correlates with enhanced stratification and decreased surface phosphate concentrations (Fig. 6). Changes in MLD correlate only weakly with PP trends; only in the North Atlantic and south-eastern Pacific are some relevant correlations found. Surface iron

concentrations correlate positively with PP because surface iron increases almost everywhere in the IPSL simulation. Correlations for EP are similar (not shown).

The MPIM model shows generally weak correlations, which can be explained with the strong iron limitation in that model. Under present climate conditions, PP is iron-limited in all regions except the tropical Atlantic (Schneider et al., 2008). Because surface iron concentrations decrease only slightly in most regions, no significant correlations are found. Exceptions are the low and mid latitudes of the Pacific, where surface iron concentrations decrease by about 20% and correlations of PP changes are found with surface iron (mainly in the subtropical gyres). Also, the PP decrease in the western tropical Pacific correlates with increased stratification and reduced MLD.

In the CSM1.4 simulation, increased stratification correlates to some extent with reduced PP and EP in the tropical and southern Pacific, as well as in the North Atlantic. This model shows a stronger correlation between PP and MLD than the other three. The latter may be an artifact of the model formulation for light limitation. Significant positive correlations are found in the North Atlantic, North Pacific, and in the Southern Ocean. Reduced surface nutrient concentrations mainly correlate where the respective nutrient is limiting; PO₄ in the low- and mid-latitude Atlantic and in the northern Indian Ocean, iron in the Pacific and southern Indian.

In the CCSM3 simulation, increased SST, enhanced stratification and reduced surface phosphate correlate with reduced PP and EP in the tropical and North Atlantic, in the Pacific around 30° N, and in the northern part of the Indian Ocean. There is almost no significant correlation between changes in MLD and PP. Enhanced PP at high latitudes and to some extent also in the tropical Indian and Atlantic correlates with increased light availability.

In conclusion the multi-model analysis confirms important conclusions obtained by attributing changes in PP and EP to individual drivers in the CSM1.4 model. We identify two different regimes for PP and EP changes in all models. First, a decrease in the concentrations of the limiting nutrient in combination with a decrease in EP is indicative of reduced nutrient input from the thermocline into the mixed layer. This first regime is dominant in the low- and mid-latitude ocean and in the North Atlantic in all four models and in the Arctic for the IPSL model. This regime is for example indicated by the positive slope between productivity (PP and EP) and limiting nutrient (yellow and red color in the panels for PO₄ and Fe in Fig. 6) and the negative slope between PP and stratification (blue color in the STRAT panel of Fig. 6) in areas where productivity is decreasing. For the second regime, an alleviation of light and temperature limitation leads to an increase in PP and EP, while PP and EP is fueled by a sustained or even increased nutrient input into the euphotic zone. This second regime is found in the Arctic in the CSM1.4 and MPIM model, to some extent in the tropical Pacific in the CCSM3

model, and in parts of the Southern Ocean in all four models. Globally, the first regime is most important and global PP and EP decreases in our 21st century global warming simulations.

3.3 A weighted multi-model mean of projected PP changes

In the previous sections, it is shown that the models as a class represent most of the pertinent features also seen in the satellite-based PP estimates and that the underlying mechanisms for changes in PP are broadly consistent across the range of models. However, individual models clearly fail to represent certain regional features.

The challenge is to combine the information from several models into a quantitative projection. In the assessments of the Intergovernmental Panel on Climate Change this has been achieved by averaging the results from individual models (Meehl et al., 2007). In this way, each model, whether skillful or not, is given equal weight. Obviously, such an approach is less than ideal as unrealistic features of a particular model influence the multi-model mean. For example, if one of the models simulates rainfall in a desert region, the multi-model mean will also show rainfall in the desert. An alternative would be to rely on the model with the best skill score with respect to suitable observations. However, this seems also less than ideal as each model has certain weaknesses and useful information from the other models is lost. Here, we suggest the use of regional skill scores as weights to compute a “best” or “optimal” estimate of projected changes. The goal is to take advantage of the skill of individual models in simulating regional features and to exclude or minimize the influence of regional results where a model is in conflict with observational evidence.

Technically, the multi-model mean is computed following the skill score metric developed by Taylor (2001). For each model m and grid cell at coordinates (i, j) a skill score

$$S_{m,i,j} = \frac{2(1 + R_{i,j})}{(\sigma_{i,j} + 1/\sigma_{i,j})^2}, \quad (3)$$

is calculated (Taylor, 2001), where $R_{i,j}$ is the distance-weighted correlation coefficient between the satellite-based estimates (PP_{obs}) and the simulated PP (PP _{m} ; average 1998–2005) and $\sigma_{i,j}$ is the corresponding standard deviation normalized by the standard deviation of the observations. This metric penalizes models that have normalized standard deviations either greater than or less than one by reducing the skill score. The weights are calculated using a two-dimensional Gaussian function

$$w(x, y)_{i,j} = \exp \left\{ - \left(\frac{(x - x_{i,j})^2}{2\rho^2} + \frac{(y - y_{i,j})^2}{2\rho^2} \right) \right\} \frac{A(x, y)}{\sum_{x,y} A(x, y)}, \quad (4)$$

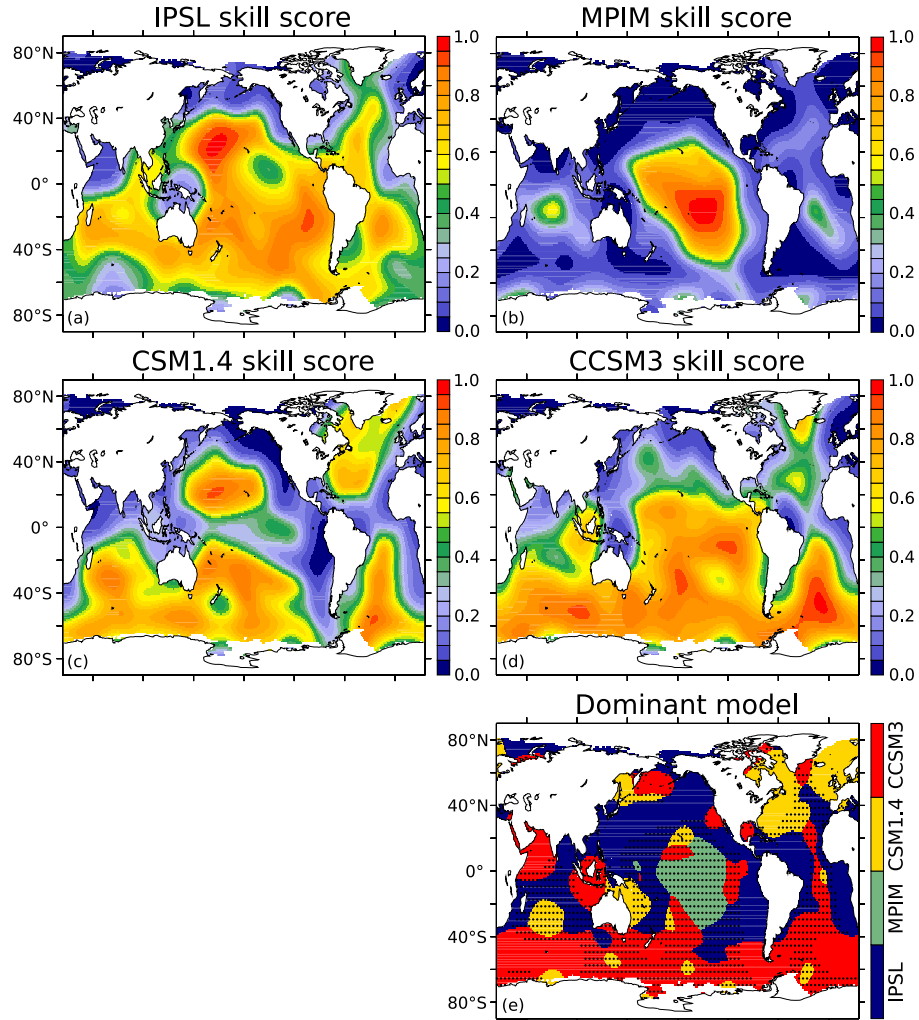


Fig. 9. Regional skill scores showing the ability of the IPSL (a), MPIM (b), CSM1.4 (c), and CCSM3 (d) models to reproduce the satellite-based estimates of PP. Panel (e) shows which model has the highest skill score at a specific point and therefore dominates the skill-score weighted multi-model mean shown in Fig. 10. The dotted areas indicate regions where the contribution of the model with the highest skill score to the multi-model mean is less than 40%.

where $x_{i,j}$ and $y_{i,j}$ are the longitude and latitude of the grid cell (i,j) , $A(x,y)$ is the area of the grid cell at coordinates (x,y) , and $\rho = 10^\circ$ characterizes the width of the distribution (the distance at which the weight has decreased from one to $1/\sqrt{e}$). We note that the results are not sensitive to the exact choice of ρ . The multi-model mean then is calculated in proportion to these regional skill scores (Fig. 9a–c):

$$\text{PP}_{i,j}^S = \sum_m \frac{S_{m,i,j}}{\sum_m S_{m,i,j}} \text{PP}_{m,i,j} \quad (5)$$

Where no observation-based data is available to calculate a skill score (e.g. in the Arctic) the model results are averaged using equal weights.

The above skill score metric emphasizes pattern similarities, but does not penalize offsets between the mean of the fields. Therefore, we also investigate an alternative metric, E , based on mean square errors:

$$E_{m,i,j} = \sum_{x,y} w(x,y)_{i,j} (\text{PP}_{\text{obs}}(x,y) - \text{PP}_m(x,y))^2 \quad (6)$$

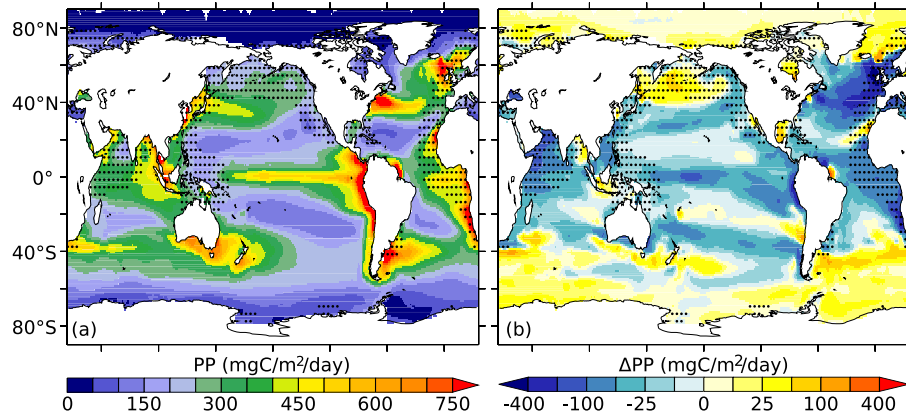


Fig. 10. (a) Multi-model mean of vertically integrated annual mean PP under preindustrial conditions (decadal mean 1860–1869) and (b) projected changes by the end of the 21st century under SRES A2. The changes are shown on an exponential scale and represent the difference between 2090–2099 and 1860–1869 (decadal means). The multi-model means have been computed by using the regional skill scores shown in Fig. 9 as weights. The dotted areas indicate that none of the regional skill scores is higher than 0.5. Where no observation-based data is available to calculate skill scores (e.g. in the Arctic) the arithmetic mean of the model results is shown.

The weights $w(x, y)_{i, j}$ used here are the same as given above. The multi-model mean with this second metric is calculated as

$$PP_{i, j}^E = \sum_m \frac{E_{m, i, j}^{-1}}{\sum_m E_{m, i, j}^{-1}} PP_{m, i, j}. \quad (7)$$

In addition, we have computed the arithmetic mean from all models (PP^{ave}) as well as the mean obtained by weighting individual models with their global ($\rho = \infty$) skill score ($PP^{\text{S}_{\text{glob}}}$).

Next, global skill scores (S_{glob}) and global root mean square errors (RMSE) are computed for the individual model results and for the multi-model fields obtained by the four different averaging methods (Table 1). The global skill score for the first field (PP^{S}) is considerably higher than for the others. All averaging methods result in a lower global skill score than that of the two best models (IPSL and CCSM3). However, the RMSE is lower for the PP^{S} field than for each individual model and for the other multi-model fields. In the following, we discuss results from this metric only. We note that differences in the results obtained by the first two metrics (PP^{S} and PP^E) are generally small.

This skill score method accounts for the different skills of the models at reproducing regional features of the satellite based estimates, while not degrading the overall skill in representing the satellite-based field compared to the best individual model. For example, the CSM1.4 model reproduces the high PP tongue around 40° N in the North Atlantic. The IPSL model captures most of the high PP features along the coasts of South America and Africa. The MPIM model has a high skill in the central Pacific and the most realistic latitudinal extension of the equatorial PP belt, while the CCSM3

captures best the magnitude and pattern of PP around 40° S. Therefore these models dominate the mean in those regions (Fig. 9d), and all these features are present in the multi-model mean (Fig. 10a). There remain weaknesses. All models underestimate PP in the Arabian Sea and off the west coast of North America. Consequently, the multi-model mean also misses these features. Overall, this method improves the multi-model mean significantly compared to simpler averaging methods (Table 1).

Regional skill scores are applied to calculate the multi-model mean of preindustrial PP and of the projected changes by the end of the 21st century (Fig. 10) and as a function of the global mean surface air temperature (SAT_{glob} , Fig. 11d). The globally integrated annual mean PP decreases from 37.1 GtC yr⁻¹ (preindustrial) to 33.0 GtC yr⁻¹ by 2100 AD (−2.9 GtC yr⁻¹; −8%) for the multi-model mean (Fig. 1, Table 1). Large decreases in PP are projected for the North Atlantic, off the coast of Africa in the South Atlantic, in the Pacific around the equator and around 30°, and in the northern part of the Indian Ocean; a slight increase in PP is found in the Southern Ocean and in the Arctic (Fig. 10b). Calculating the mean by 2100 has the disadvantage that PP changes are merged that correspond to different temperature changes as the models have different climate sensitivities. One way to avoid this is to calculate the regression slope $\Delta PP / \Delta SAT_{\text{glob}}$ for each grid cell (Fig. 11a–c) as done for the global PP in Fig. 1c. The patterns of the resulting PP change per centigrade SAT increase are broadly consistent with the patterns of the projected PP change by 2100.

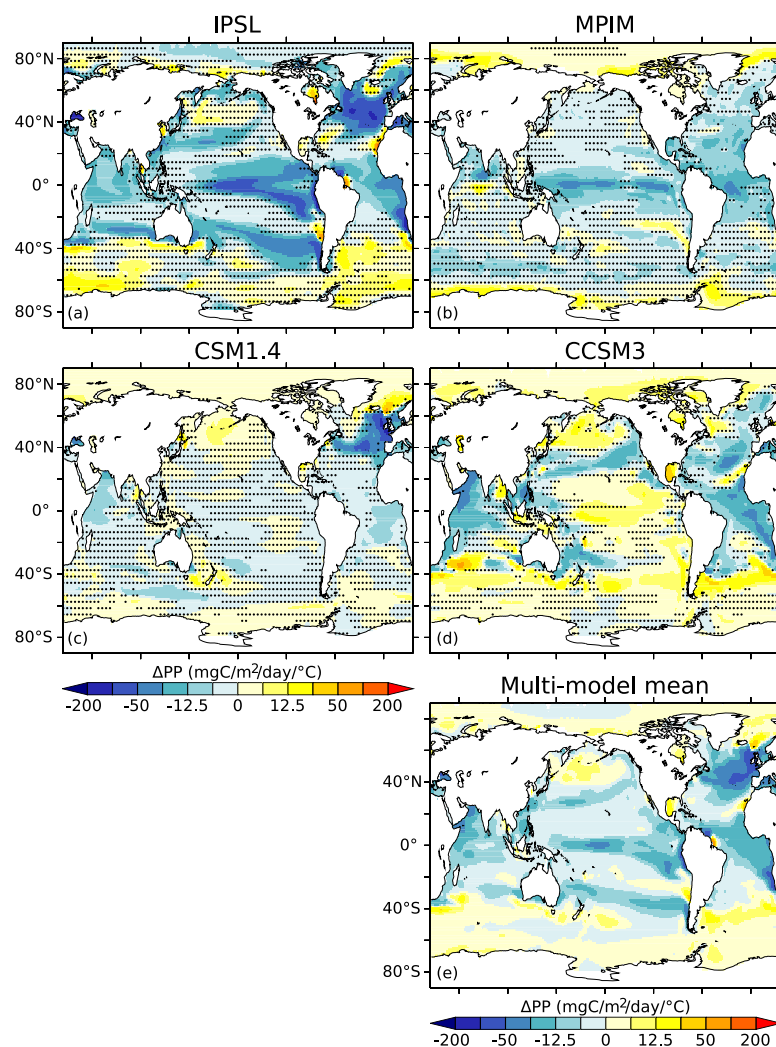


Fig. 11. Projected changes in vertically integrated annual mean primary production for a nominal increase in global mean surface air temperature (SAT_{glob}) of $1\text{ }^{\circ}\text{C}$. The panels show the slope $\Delta PP/\Delta SAT_{glob}$ at each grid cell for the IPSL (a), MPIM (b), CSM1.4 (c), and CCSM3 (d) models. The multi-model mean (e) is the weighted mean (based on regional skill scores) of the individual slopes. The color code is on an exponential scale and changes are calculated from a linear regression of annual mean values over the period 1860–2099. Areas where $R^2 < 0.1$ are shaded in panels (a–d).

3.4 Changes in the seasonal cycle

One aspect of the simulations to explore is how the seasonal cycle and interannual variability are modified under global warming. Here, we compare the simulated maximum seasonal PP amplitudes (annual maximum minus annual minimum) and their interannual variations for the decades 1860–1869 and 2090–2099 along the two sections in the Atlantic and the Pacific shown in Fig. 2 and for the global zonal mean (Fig. 12).

In the global zonal mean, the seasonal amplitude is projected to decrease everywhere in the IPSL simulation. Largest reductions of about $200\text{ mg C m}^{-2}\text{ day}^{-1}$ can be found at $40^{\circ}\text{ N}–70^{\circ}\text{ N}$, where the reduction is clearly distinguishable from preindustrial interannual variability. Further, a marked reduction is found at low latitudes around $20^{\circ}–30^{\circ}$ and in the Arctic Ocean north of 80° N . The reduction in the north is linked to a large reduction in PP in the Atlantic between 30° N and 60° N from April to July and in the Pacific between 55° N and 70° N from April to September

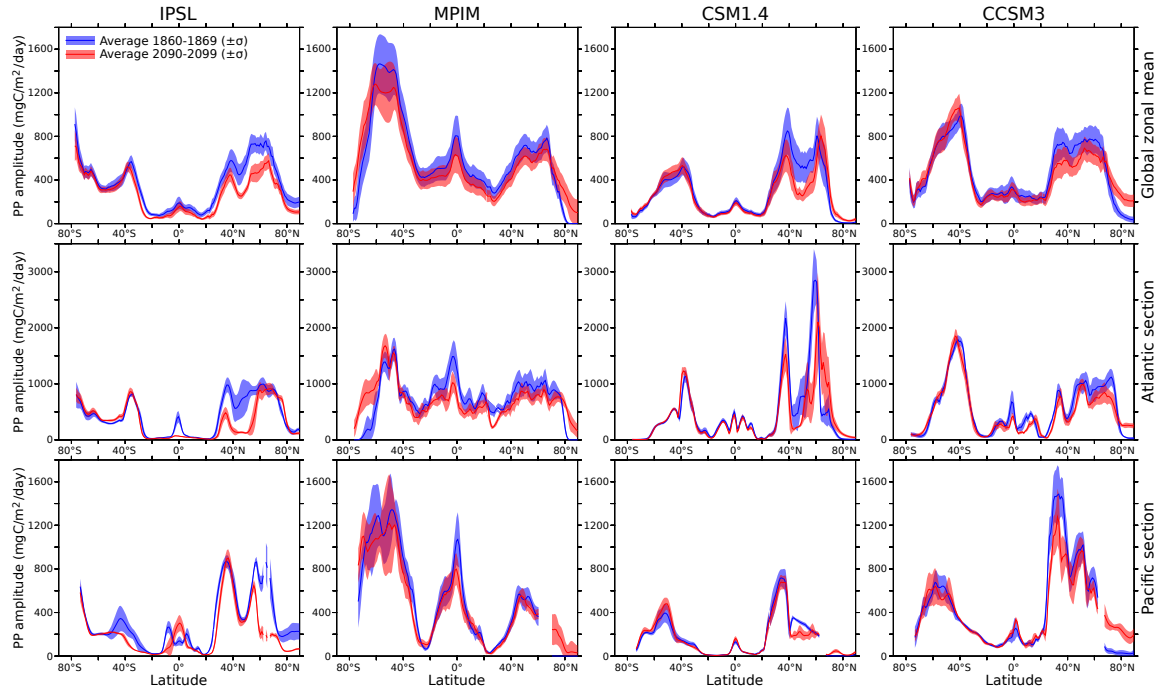


Fig. 12. Seasonal PP amplitude (maximum – minimum) zonally averaged (top), and for specific sections in the Atlantic (middle) and Pacific (bottom) as simulated by the four models IPSL, MPIM, CSM1.4, and CCSM3 (columns from left to right) for preindustrial conditions (blue; decade 1860–1869) and projected by the end of the century (red; decade 2090–2099). Lines indicate the decadal mean and shadings the interannual variability ($\pm\sigma$). Please note that the scale of the vertical axis is different for the Atlantic section.

(not shown). Not only the seasonal amplitude, but also the interannual variability in PP is projected to decrease for most latitudes.

The zonally averaged seasonal PP amplitude in the MPIM simulation is also reduced between 70° N and 60° S. Largest reductions of about $200 \text{ mg C m}^{-2} \text{ day}^{-1}$ are located in the Southern Ocean and around the equator. South of 60° S and north of 70° N the seasonal amplitude increases, consistent with an increase in PP in these areas. The MPIM model exhibits a larger interannual variability than the other two models, and at most latitudes the projected changes are within the range of preindustrial interannual variability. Maximum changes in PP occur from December to February in the Southern Ocean and during July/August in the Arctic Ocean.

In the CSM1.4 model the zonally averaged seasonal PP amplitude is reduced by up to $300 \text{ mg C m}^{-2} \text{ day}^{-1}$ between 40° N and 60° N. An increase is found north of 60° N, in the Southern Ocean (40° S– 60° S), and in the Arctic Ocean. Changes are small in other regions. The changes in the north are dominated by the Atlantic where PP is strongly reduced between 40° N and 60° N (March–June) and enhanced between 60° N and 70° N (April–June).

In the global zonal mean, the seasonal amplitude projected by the CCSM3 model decreases between 30° N and 70° N by about $200 \text{ mg C m}^{-2} \text{ day}^{-1}$, broadly consistent with the results of the other models. In the Arctic Ocean the amplitude increases by about the same amount. A slight increase is also found around 45° N. The reduction around 60° N can be attributed to changes in the North Atlantic, while the changes around 30° N are dominated by the Pacific. In the tropical Atlantic the amplitude tends to be reduced slightly.

In summary, changes in seasonal cycle amplitude are relatively small, though there are exceptions. The seasonal amplitude tends to become smaller when overall PP decreases. Interannual variability in the seasonal amplitude is substantial and projected to decrease in two of the four models (IPSL and CSM1.4).

4 Discussion and conclusions

The trends in ocean productivity in response to anthropogenic climate change have been analyzed with four coupled carbon cycle-climate models that incorporate marine biogeochemical-ecosystem models of different complexity. The decreasing trend in global net primary production (PP)

and particulate organic carbon export (EP) is a robust result, but relative and absolute magnitudes differ among models and regions.

The underlying mechanisms of change are qualitatively consistent across the models, except in the Arctic and in parts of the tropical Pacific. All four models show a consistent change in physical drivers, surface concentrations of macro-nutrients, and PP when considering regional averages (Fig. 5). Namely, the models project an increase in sea surface temperature and stratification in all regions and an increase in available light in the Arctic in response to sea ice retreat. Macro-nutrient concentrations in the euphotic zone are projected to decrease in all regions and for all models. Two different regimes for change in PP and EP are identified, that were already discussed previously in the literature (Bopp et al., 2001; Sarmiento et al., 1998). First, all models indicate a decrease in PP and EP in the low- and mid-latitude ocean and in the North Atlantic in response to reduced nutrient delivery to the surface ocean linked to enhanced stratification, reduced mixed-layer depth and slowed ocean circulation. This is broadly consistent with earlier projections using box models, Earth System Models of Intermediate Complexity or general circulation models (Klepper and De Haan, 1995; Maier-Reimer et al., 1996; Joos et al., 1999; Matear and Hirst, 1999; Plattner et al., 2001; Bopp et al., 2001; Fung et al., 2005; Frölicher et al., 2009). Second, light and temperature limitation is reduced in the high-latitude ocean, whereas nutrient supply remains sufficient to support an increase in PP and EP. This second regime is found in the Arctic in the CSM1.4 and MPIM model and in parts of the Southern Ocean in all four models. A qualitative difference among models is found in the Arctic, where IPSL projects a decrease in PP and EP related to a reduced supply of macro-nutrients, whereas CSM1.4, MPIM, and CCSM3 project a PP and EP increase due to reduced light and temperature limitation. In any case, absolute changes in PP in the Arctic and the Southern Ocean are relatively small in the IPSL, MPIM, and CSM1.4 models. An exception is the CCSM3 model where the PP increase in the Arctic and Southern Ocean is of the same order of magnitude as the decrease in the tropics and in the North Atlantic. This explains the relatively small decrease in PP on the global scale projected by that model.

The models project also a different evolution of iron. The MPIM and CSM1.4 models use constant elemental ratios in their production algorithms and consequently surface iron concentration are decreasing in parallel with macro-nutrient concentrations in regions without substantial aeolian iron input. In the IPSL model, the iron-to-carbon ratio of assimilated material is reduced under nutrient stress. As a consequence, iron concentration increases in the euphotic zone as less iron is exported to depth in the form of organic matter. The CCSM3 model also features a variable iron-to-carbon ratio but the effect on surface iron concentrations is rather small and changes are mainly driven by physical processes such as increased stratification.

The cycling of iron is quantitatively not well understood and difficult to represent in ocean models. It involves a temporally and spatially variable aeolian dust source, sediment sources, as well as complex physical and chemical processes such as complexation to organic ligands and scavenging by particles (e.g. Parekh et al., 2004). All models in this study have atmospheric iron deposition and the IPSL and CCSM3 models also have a sediment source. Sensitivity studies with the ocean only model of MPIM showed a decrease in EP of 0.4 GtC in response to a 30% decrease of dust deposition in a $2\times\text{CO}_2$ climate as predicted by Mahowald et al. (2006). Tagliabue et al. (2008) found a NPP reduction of about 3% in response to a 60% reduction in iron input from dust in a 21st century simulation with the IPSL model. Variations in the dust input of iron significantly impact nitrogen fixation, export production, and air-sea CO_2 exchange in the CCSM3 model (Moore et al., 2006; Moore and Braucher, 2008; Doney, et al., 2009b). This suggests that there may be a significant even though not first order impact on atmospheric CO_2 . The predicted change and even the sign of change in dust deposition, however, are still highly uncertain and, therefore, dust climatologies were kept constant in this study.

None of the models used here explicitly represents bacterial pools. The microbial loop describing the energy and nutrient flow initiated by bacterial consumption of dissolved organic matter and grazing by bacterivores is implicitly represented in the models. Dissolved organic matter is assumed to decay and released nutrients are then available to fuel productivity. Three of the models show a lower global PP than observation-based estimates and one might be tempted to link to the low productivity to the missing explicit representation of bacteria. However, the PP of 49 Gt C yr^{-1} simulated by the CCSM3 model falls well within the satellite-based range of 35 to 70 Gt C yr^{-1} and the PP of the IPSL model is with 34 Gt C yr^{-1} only slightly lower than the satellite-based range. As already discussed, PP in the MPIM model is too strongly limited by iron and the simple empirical formulation of productivity in the CSM1.4 is biased low by design. Taken together, this suggests that the missing explicit representation of bacteria does not necessarily cause an underestimation of PP.

The formulation of the temperature dependency of growth rates and other processes vary qualitatively and quantitatively among the four models. An exponential temperature dependency is used for growth rates, microzooplankton grazing, and POC remineralization in the IPSL and CCSM3 models with Q_{10} values of 1.9 and 2.0, respectively. This is comparable to the temperature dependency for growth rates proposed by Eppley (1972) and applied by Schmitzner et al. (2008). In contrast, growth rates are temperature-independent in the MPIM model, thereby assuming that phytoplankton acclimate to local temperature. The temperature limitation for productivity in CSM1.4 corresponds formally to a Michaelis-Menton type formulation (Eq. 2) and has a

1000

concave shape in contrast to the exponential-type formulations. In other words, the nominal sensitivity of PP to a temperature change is highest at low temperatures in CSM1.4, in contrast to CCSM3 and IPSL where the sensitivity of growth rates is highest in the warm ocean. Interestingly, global PP is decreasing in all four models under global warming, in contrast to the model of Schmittner et al. (2008). The IPSL model with the highest temperature sensitivity for growth rates and a realistic relationship between the export ratio and temperature (Fig. 3) yields the largest decrease in PP per nominal change in surface temperature (Fig. 1c). Apparently, increasing nutrient limitation is more important in regulating PP on the global scale than the direct temperature effect on growth rates in the IPSL model and in the other models applied here.

Quantitatively, the four models show large differences in regional responses. These are often linked to differences in the simulation of the mean PP fields. For example, iron limitation is too strong in the MPIM in the low and mid-latitude ocean and in the CSM1.4 model in the equatorial Pacific. Consequently, PP in these regions is very low for these models and the projected decrease is also small by necessity. Other differences are related to the climate sensitivity of the models. The CSM1.4 model has the smallest climate sensitivity and shows a smaller surface warming and smaller changes in low-latitude stratification than the IPSL and MPIM model. The comparison between observation-based PP estimates and simulated PP (Fig. 2; Schneider et al., 2008) suggests that it is not advisable to simply average the results from the four models as obvious shortcomings of the models would unfavorably influence the multi-model mean projection.

We have applied regional model skill metrics as weights in the computation of multi-model means. Here, we have used the satellite-based PP estimates (average of annual mean PP for the period 1998 to 2005) of Behrenfeld et al. (2006) as an example target against which the performance of individual models is assessed; in the future it might be useful to compare models to the ensemble of satellite-based reconstructions of PP and chlorophyll given their uncertainties. Other metrics, such as how well the models reproduce current surface nutrient distributions, could be used as additional targets (Doney et al., 2009a). A scale length is introduced for the regional skill score calculation that can be adjusted for the problem considered. Here, the scale length has been selected to be representative for the spatial scale of marine biogeographical provinces ($\approx 10^\circ$); the exact choice of the numerical value is not crucial for our application. The multi-model mean PP changes are expressed as PP change per a nominal increase in global mean surface air temperature of 1°C to account for the different climate sensitivities of the models. The use of regional metrics has advantages. It results in an improved skill in representing the satellite-based PP field compared to a conventional, IPCC-type multi-model average where each model is given equal weight. Most weight is at-

M. Steinacher et al.: Projected decrease in marine productivity

tached to the model that represents an individual regional feature best, whereas little weight is attached to the models that fail to reproduce the regional feature. The regional metrics quantify the regional performance of each model (Fig. 9). Features that all models fail to represent as evidenced by low skills can be flagged in the multi-model average. Disadvantages are that suitable target fields have to be defined and scale lengths to be determined. The choice of an annual mean climatological field as a target is debatable. Additional targets including seasonal or interannual variability (Santer et al., 2009) may be applied. Most preferable would be observation-based data that include decadal scale trends when evaluating projections of the 21st century. Further, our approach, as any weighting scheme, is based on the assumption that the relative skill of the model remains about the same over time. A more fundamental caveat is worth mentioning. Each individual model provides an internally consistent representation of heat and mass fluxes, nutrient cycling, and ecosystem dynamics taking fully into account first order principles such as mass and energy conservation. By using regional weights, regional features from different models are combined to a new global mean field which may lack internal consistency. We believe that our regional weight approach is preferable compared to the conventional “one model, one vote” approach to generate a multi-model mean projection of PP. However, we caution that this might not be the case for other applications.

Our results are contradictory to the results of Sarmiento et al. (2004) on the global scale and in most regions (Fig. 13). Sarmiento et al. (2004) project an increase in global PP by 0.7 to 8.1% and not a decrease. These authors rely on an empirical model approach in combination with output for physical variables from AOGCM global warming simulations. The cycling of nutrients and nutrient concentrations are not explicitly considered. Seven physics-based diagnostics (surface temperature, salinity and density, upwelling and vertical density gradient in the top layers, mixed layer depth, and ice cover) are used to define 33 biogeographical provinces. An empirical chlorophyll model, describing chlorophyll as an exponential function of temperature, salinity, mixed layer depth and growing season length, is fitted to the SeaWiFS chlorophyll data for each province and used to project 21st century changes in chlorophyll from the AOGCM output. Finally, PP is estimated from the chlorophyll concentration for three different productivity algorithms (Behrenfeld and Falkowski, 1997a; Carr, 2002; Marra et al., 2003). This chain of models yield an increase in PP almost in the entire ocean for the Marra et al. algorithm and, to a lesser extent for the Carr algorithm, whereas the Behrenfeld and Falkowski algorithm yields a decrease in PP in low and mid latitudes and an increase in high-latitudes. Only the projected decrease in low and mid latitudes with the Behrenfeld and Falkowski algorithm is consistent with this and an earlier analysis with the IPSL model (Bopp et al., 2001). On the global scale, the increase in PP projected by Sarmiento et al. (2004) is in the

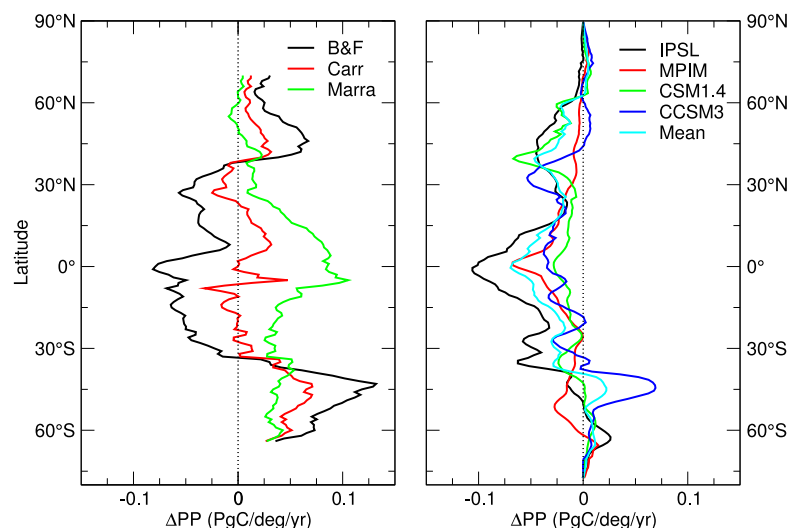


Fig. 13. Changes in zonally integrated PP under global warming as found with an empirical approach (left; cf. Fig. 11 in Sarmiento et al., 2004) and simulated with the mechanistic models IPSL, MPIM, CSM1.4, and CCSM3 (right). In the left panel the productivity is calculated with the three different primary production algorithms of Behrenfeld and Falkowski (1997a, B&F), Carr (2002), and Marra et al. (2003). The multi-model mean shown in the right panel (cyan) has been calculated using regional skill scores.

range of about 0.2% to 2% per nominal change in surface air temperature of 1°C for the three algorithms. The corresponding range is −4% to −0.5% for the four models used here, whereas the model of Schmittner et al. (2008) shows a more than five times larger sensitivity than inferred by the empirical approach.

What are the reasons for the discrepancies between results from the empirical approach and those from process-based climate-biogeochemical-ecosystem models used in this study? A fundamental conceptual difference is that the cycling of nutrients and nutrient availability is explicitly considered in the process-based models, whereas nutrient limitation is only implicitly included in the empirical approach of Sarmiento et al. (2004) and the satellite productivity algorithms. As nutrients are a key factor for phytoplankton growth and PP, it appears necessary to take the decadal-to-century scale evolution of nutrient cycling into account as done in the process-based models. As discussed by Sarmiento et al. (2004), projected changes in chlorophyll are small for their empirical approach, and their changes in PP depend critically on the applied satellite algorithm. Sarmiento et al. (2004) highlight the importance of the assumed relationship between temperature and PP for a given chlorophyll concentration. This temperature sensitivity of PP is very different among the satellite algorithms. For example, PP increases with temperature by a factor of about two between 18°C and 30°C for the Marra et al. algorithm, but decreases by a factor of two over the same temperature range for the Behrenfeld and Falkowski algorithm. Consequently,

PP is projected to decrease in low and mid latitudes with the Behrenfeld and Falkowski algorithm and to increase with the Marra et al. algorithm in transient warming scenarios. These discrepancies between algorithms may reflect the difficulties to separate light and nutrient effects on PP (Behrenfeld et al., 2008). We note that observation-based changes in global chlorophyll and inferred global PP by Behrenfeld et al. (2006) evolve in parallel. An implicit assumption in the empirical approach is that the spatial relationship between PP and physical forcing found for the modern ocean can be applied to temporal changes into the future. However, Schneider et al. (2008) find that the relationship between PP and temperature in the low-latitude ocean is different for inter-annual variations of the last decades and the century-scale trends in transient warming simulations.

Process-based models are far from perfect (Schneider et al., 2008) and their results must be interpreted with some caution. However, it appears evident from our analysis that the cycling of nutrients and changes in the supply to the surface and in the concentration of nutrients must be realistically represented to project changes in PP and EP with some realism. What is required for further progress is to combine satellite, field, and laboratory observations, empirical approaches and process-based models to further improve our quantitative understanding. Novel metrics such as (multivariate) regional skill scores may prove useful to synthesize results from models and observational studies in a quantitative and transparent way. As far as modeling is concerned, factorial experiments dedicated to quantify the link between

1002

PP and individual parameters will be helpful to improve the understanding of model behavior and to compare model results with experimental data. Improved parametrizations of ecosystem processes that take into account emerging results from field and laboratory studies are required to close gaps in understanding.

Acknowledgements. We would like to thank J. Sarmiento and R. Slater for providing us with the data from their study. We also thank the SeaWiFS Project and M. Behrenfeld for providing data from satellite observations. Furthermore, we thank J. Sarmiento and M. Behrenfeld for their valuable comments that helped to improve the manuscript and K. Taylor for sharing his expertise on model skill metrics. This work was funded by the European Union projects CARBOOCEAN (511176-2) and EUROCEANS (511106-2) and is a contribution to the “European Project on Ocean Acidification” (EPOCA) which received funding from the European Community’s Seventh Framework Programme (FP7/2007–2013) under grant agreement no. 211384. Additional support was received from the Swiss National Science Foundation. SCD acknowledges support from the NASA Ocean Biology and Biogeochemistry Program (NNX07AL80G). LB acknowledges support from the EU Project MEECE (Marine Ecosystem Evolution in a Changing Environment, grant agreement 212085).

Edited by: C. P. Slomp

References

- Anderson, L. A. and Sarmiento, J. L.: Redfield ratios of remineralization determined by nutrient data analysis, *Global Biogeochem. Cycles*, 8, 65–80, 1994.
- Aumont, O. and Bopp, L.: Globalizing results from ocean in situ iron fertilization studies, *Global Biogeochem. Cycles*, 20, 1–15, 2006.
- Aumont, O., Maier-Reimer, E., Blain, S., and Monfray, P.: An ecosystem model of the global ocean including Fe, Si, P colimitations, *Global Biogeochem. Cycles*, 17, 1060, doi:10.1029/2001GB001745, 2003.
- Azam, F., Fenchel, T., Field, J. G., Gray, J. S., Meyerreil, L. A., and Thingstad, F.: The ecological role of water-column microbes in the sea, *Mar. Ecol.-Prog. Ser.*, 10, 257–263, 1983.
- Behrenfeld, M. J. and Falkowski, P. G.: A consumer’s guide to phytoplankton primary productivity models, *Limnol. Oceanogr.*, 42, 1479–1491, 1997a.
- Behrenfeld, M. J. and Falkowski, P. G.: Photosynthetic rates derived from satellite-based chlorophyll concentration, *Limnol. Oceanogr.*, 42, 1–20, 1997b.
- Behrenfeld, M. J., O’Malley, R. T., Siegel, D. A., McClain, C. R., Sarmiento, J. L., Feldman, G. C., Milligan, A. J., Falkowski, P. G., Letelier, R. M., and Boss, E. S.: Climate-driven trends in contemporary ocean productivity, *Nature*, 444, 752–755, 2006.
- Behrenfeld, M. J., Halsey, K. H., and Milligan, A. J.: Evolved physiological responses of phytoplankton to their integrated growth environment, *Philos. T. R. Soc. B*, 363, 2687–2703, doi:10.1098/rstb.2008.0019, 2008.
- Bopp, L., Monfray, P., Aumont, O., Dufresne, J. L., Le Treut, H., Madec, G., Terray, L., and Orr, J. C.: Potential impact of climate change on marine export production, *Global Biogeochem. Cycles*, 15, 81–99, 2001.
- Bopp, L., Aumont, O., Belviso, S., and Monfray, P.: Potential impact of climate change on marine dimethyl sulfide emissions, *Tellus B*, 55, 11–22, 2003.
- Bopp, L., Aumont, O., Cadule, P., Alvain, S., and Gehlen, M.: Response of diatoms distribution to global warming and potential implications: a global model study, *Geophys. Res. Lett.*, 32, 1–4, 2005.
- Boville, B. A. and Gent, P. R.: The NCAR Climate System Model, version one, *J. Climate*, 11, 1115–1130, 1998.
- Boville, B. A., Kiehl, J. T., Rasch, P. J., and Bryan, F. O.: Improvements to the NCAR CSM-1 for transient climate simulations, *J. Climate*, 14, 164–179, doi:10.1029/2002JD003026, 2001.
- Boyd, P. W. and Doney, S. C.: Modelling regional responses by marine pelagic ecosystems to global climate change, *Geophys. Res. Lett.*, 29, 1806, doi:10.1029/2001GL014130, 2002.
- Boyd, P. W., Jickells, T., Law, C. S., Blain, S., Boyle, E. A., Bueseler, K. O., Coale, K. H., Cullen, J. J., de Baar, H. J. W., Follows, M., Harvey, M., Lancelot, C., Levasseur, M., Owens, N. P. J., Pollard, R., Rivkin, R. B., Sarmiento, J., Schoemann, V., Smetacek, V., Takeda, S., Tsuda, A., Turner, S., and Watson, A. J.: Mesoscale iron enrichment experiments 1993–2005: Synthesis and future directions, *Science*, 315, 612–617, doi:10.1126/science.1131669, 2007.
- Carr, M.-E.: Estimation of potential productivity in Eastern Boundary Currents using remote sensing, *Deep-Sea Res. Pt. II*, 49, 59–80, 2002.
- Carr, M.-E., Friedrichs, M. A. M., Schmeltz, M., Aita, M. N., Antoine, D., Arrigo, K. R., Asanuma, I., Aumont, O., Barber, R., Behrenfeld, M., Bidigare, R., Buitenhuis, E. T., Campbell, J., Ciotti, A., Dierssen, H., Dowell, M., Dunne, J., Esaias, W., Gentili, B., Gregg, W., Groom, S., Hoepffner, N., Ishizaka, J., Kameda, T., Le Quéré, C., Lohrenz, S., Marra, J., Melin, F., Moore, K., Morel, A., Reddy, T. E., Ryan, J., Scardi, M., Smyth, T., Turpie, K., Tilstone, G., Waters, K., and Yamanaka, Y.: A comparison of global estimates of marine primary production from ocean color, *Deep-Sea Res. Pt. II*, 53, 741–770, doi:10.1016/j.dsr2.2006.01.028, 2006.
- Crueger, T., Roeckner, E., Raddatz, T., Schnur, R., and Wetzol, P.: Ocean dynamics determine the response of oceanic CO₂ uptake to climate change, *Clim. Dynam.*, 31, 151–168, doi:10.1007/s00382-007-0342-x, 2008.
- de Baar, H. J. W., de Jong, J. T. M., Bakker, D. C. E., Löscher, B. M., Veth, C., Bathmann, U., and Smetacek, V.: Importance of iron for plankton blooms and carbon dioxide drawdown in the Southern Ocean, *Nature*, 373, 412–415, 1995.
- Doney, S., Lindsay, K., Fung, I., and John, J.: Natural variability in a stable, 1000-yr global coupled climate-carbon cycle simulation, *J. Climate*, 19, 3033–3054, 2006.
- Doney, S. C., Lima, I., Moore, J. K., Lindsay, K., Behrenfeld, M. J., Westberry, T. K., Mahowald, N., Glover, D. M., and Takahashi, T.: Skill metrics for confronting global upper ocean ecosystem-biogeochemistry models against field and remote sensing data, *J. Marine Syst.*, 76, 95–112, doi:10.1016/j.jmarsys.2008.05.015, 2009a.
- Doney, S. C., Lima, I., Feely, R. A., Glover, D. M., Lindsay, K., Mahowald, N., Moore, J. K., and Wanninkhof, R.: Mechanisms governing interannual variability in upper-ocean inorganic car-

- bon system and air-sea CO₂ fluxes: Physical climate and atmospheric dust, *Deep-Sea Res.*, 56, 640–655, doi:10.1016/j.dsr2.2008.12.006, 2009b.
- Dulaiova, H., Ardelan, M. V., Henderson, P. B., and Charette, M. A.: Shelf-derived iron inputs drive biological productivity in the southern Drake Passage, *Global Biogeochem. Cycles*, 23, doi:10.1029/2008GB003406, 2009.
- Eppley, R. W.: Temperature and phytoplankton growth in sea, *Fish. Bull.*, 70, 1063–1085, 1972.
- Fasham, M. J. R., Sarmiento, J. L., Slater, R. D., Ducklow, H. W., and Williams, R.: Ecosystem behavior at Bermuda Station-S and Ocean Weather Station India – A general-circulation model and observational analysis, *Global Biogeochem. Cycles*, 7, 379–415, 1993.
- Friedlingstein, P., Cox, P., Betts, R., Bopp, L., Von Bloh, W., Brovkin, V., Cadule, P., Doney, S., Eby, M., Fung, I., Bala, G., John, J., Jones, C., Joos, F., Kato, T., Kawamiya, M., Knorr, W., Lindsay, K., Matthews, H. D., Raddatz, T., Rayner, P., Reick, C., Roeckner, E., Schnitzler, K. G., Schnur, R., Strassmann, K., Weaver, A. J., Yoshikawa, C., and Zeng, N.: Climate-Carbon Cycle Feedback Analysis: Results from the C⁴MIP Model Intercomparison: Evolution of carbon sinks in a changing climate, *J. Climate*, 19, 3337–3353, 2006.
- Frölicher, T. L. and Joos, F.: Reversible and irreversible impacts of greenhouse gas emissions in multi-century projections with the NCAR global coupled carbon cycle-climate model, *Clim. Dynam.*, 34, published online first, doi:10.1007/s00382-009-0727-0, 2010.
- Frölicher, T. L., Joos, F., Plattner, G. K., Steinacher, M., and Doney, S. C.: Natural variability and anthropogenic trends in oceanic oxygen in a coupled carbon cycle-climate model ensemble, *Global Biogeochem. Cycles*, 23, 1–15, doi:10.1029/2008GB003316, 2009.
- Fung, I., Doney, S., Lindsay, K., and John, J.: Evolution of carbon sinks in a changing climate, *P. Natl. Acad. Sci. USA*, 102, 11201–11206, 2005.
- Gehlen, M., Bopp, L., Emprin, N., Aumont, O., Heinze, C., and Ragueneau, O.: Reconciling surface ocean productivity, export fluxes and sediment composition in a global biogeochemical ocean model, *Biogeosciences*, 3, 521–537, 2006, <http://www.biogeosciences.net/3/521/2006/>.
- Gent, P. R., Bryan, F. O., Danabasoglu, G., Doney, S. C., Holland, W. R., Large, W. G., and McWilliams, J. C.: The NCAR Climate System Model global ocean component, *J. Climate*, 11, 1287–1306, 1998.
- Goldstein, B., Joos, F., and Stocker, T. F.: A modeling study of oceanic nitrous oxide during the Younger Dryas cold period, *Geophys. Res. Lett.*, 30, 1092, doi:10.1029/2002GL016418, 2003.
- Hourdin, F., Musat, I., Bony, S., Braconnot, P., Codron, F., Dufresne, J.-L., Fairhead, L., Filiberti, M.-A., Friedlingstein, P., Grandpeix, J.-Y., Krinner, G., Levan, P., Li, Z.-X., and Lott, F.: The LMDZ4 general circulation model: climate performance and sensitivity to parametrized physics with emphasis on tropical convection, *Clim. Dynam.*, 19, 3445–3482, 2006.
- Johnson, K. S., Gordon, R. M., and Coale, K. H.: What controls dissolved iron concentrations in the world ocean?, *Mar. Chem.*, 57, 137–161, 1997.
- Joos, F., Plattner, G. K., Stocker, T. F., Marchal, O., and Schmittner, A.: Global warming and marine carbon cycle feedbacks and future atmospheric CO₂, *Science*, 284, 464–467, 1999.
- Kiehl, J. T., Hack, J. J., Bonan, G. B., Boville, B. A., Williamson, D. L., and Rasch, P. J.: The National Center for Atmospheric Research Community Climate Model, *J. Climate*, 11, 1151–1178, 1998.
- Klepper, O. and De Haan, B. J.: A sensitivity study of the effect of global change on ocean carbon uptake, *Tellus B*, 47, 490–500, 1995.
- Krinner, G., Viovy, N., de Noblet-Ducoudre, N., Ogee, J., Polcher, J., Friedlingstein, P., Ciais, P., Sitch, S., and Prentice, I. C.: A dynamic global vegetation model for studies of the coupled atmosphere-biosphere system, *Global Biogeochem. Cycles*, 19, 1–33, 2005.
- Laws, E. A., Falkowski, P. G., Smith, W. O., Ducklow, H., and McCarthy, J. J.: Temperature effects on export production in the open ocean, *Global Biogeochem. Cycles*, 14, 1231–1246, 2000.
- Le Quéré, C., Harrison, S. P., Prentice, I. C., Buitenhuis, E. T., Aumont, O., Bopp, L., Claustre, H., Da Cunha, L. C., Geider, R., Giraud, X., Klaas, C., Kohfeld, K. E., Legendre, L., Manizza, M., Platt, T., Rivkin, R. B., Sathyendranath, S., Uitz, J., Watson, A. J., and Wolf-Gladrow, D.: Ecosystem dynamics based on plankton functional types for global ocean biogeochemistry models, *Glob. Change Biol.*, 11, 2016–2040, doi:10.1111/j.1365-2468.2005.01004.x, 2005.
- Madec, G., Delecluse, P., Imbard, M., and Levy, C.: OPA 8.1 ocean general circulation model reference manual, Notes du Pôle de Modélisation 11, Institut Pierre Simon Laplace des Sciences de l'Environnement Global, Paris, France, 1998.
- Mahowald, N. M., Muhs, D. R., Levis, S., Rasch, P. J., Yoshioka, M., Zender, C. S., and Luo, C.: Change in atmospheric mineral aerosols in response to climate: Last glacial period, preindustrial, modern, and doubled carbon dioxide climates, *J. Geophys. Res.-Atmos.*, 111, D10202, doi:10.1029/2005JD006653, 2006.
- Maier-Reimer, E.: Geochemical cycles in an ocean general circulation model. Preindustrial tracer distributions, *Global Biogeochem. Cycles*, 7, 645–677, 1993.
- Maier-Reimer, E., Mikolajewicz, U., and Winguth, A.: Future ocean uptake of CO₂: interaction between ocean circulation and biology, *Clim. Dynam.*, 12, 63–90, 1996.
- Maier-Reimer, E., Kriest, I., Segsneider, J., and Wetzol, P.: The HAMBURG Ocean Carbon Cycle model HAMOCC5.1, Berichte zur Erdsystemforschung 14/2005, Max Planck-Institut für Meteorologie, Hamburg, Germany, 2005.
- Manizza, M., Le Quéré, C., Watson, A. J., and Buitenhuis, E. T.: Ocean biogeochemical response to phytoplankton-light feedback in a global model, *J. Geophys. Res.-Oceans*, 113, C10010, doi:10.1029/2007JC004478, 2008.
- Marra, J., Ho, C., and Trees, C. C.: An alternative algorithm for the calculation of primary productivity from remote sensing data, Tech. rep., Lamont-Doherty Earth Obs., Palisades, N.Y., USA, 2003.
- Marsland, S. J., Haak, H., Jungclaus, J. H., Latif, M., and Roske, F.: The Max-Planck-Institute global ocean/sea ice model with orthogonal curvilinear coordinates, *Ocean Model.*, 5, 91–127, 2003.
- Matear, R. J. and Hirst, A. C.: Climate change feedback on the future oceanic CO₂ uptake, *Tellus B*, 51, 722–733, 1999.
- Meehl, G. A., Stocker, T. F., Collins, W. D., Friedlingstein, P., Gaye,

1004

M. Steinacher et al.: Projected decrease in marine productivity

- A. T., Gregory, J. M., Kitoh, A., Knutti, R., Murphy, J. M., Noda, A., Raper, S. C. B., Watterson, I. G., Weaver, A. J., and Zhao, Z.-C.: Climate Change 2007: The Physical Science Basis. Contribution of Working Group I to the Fourth Assessment Report of the Intergovernmental Panel on Climate Change, chap. Global Climate Projections, 747–846, Cambridge University Press, Cambridge, United Kingdom and New York, NY, USA, 2007.
- Moore, J. K. and Braucher, O.: Sedimentary and mineral dust sources of dissolved iron to the world ocean, *Biogeosciences*, 5, 631–656, 2008, <http://www.biogeosciences.net/5/631/2008/>.
- Moore, J. K., Doney, S. C., Kleypas, J. A., Glover, D. M., and Fung, I. Y.: An intermediate complexity marine ecosystem model for the global domain, *Deep-Sea Res. Pt. II*, 49, 403–462, doi:10.1016/S0967-0645(01)00108-4, 2002.
- Moore, J. K., Doney, S. C., and Lindsay, K.: Upper ocean ecosystem dynamics and iron cycling in a global three-dimensional model, *Global Biogeochem. Cycles*, 18, GB4028, doi:10.1029/2004GB002220, 2004.
- Moore, J. K., Doney, S. C., Lindsay, K., Mahowald, N., and Michaels, A. F.: Nitrogen fixation amplifies the ocean biogeochemical response to decadal timescale variations in mineral dust deposition, *Tellus B*, 58, 560–572, doi:10.1111/j.1600-0889.2006.00209.x, 2006.
- Najjar, R. G., Jin, X., Louanchi, F., Aumont, O., Caldeira, K., Doney, S. C., Dutay, J.-C., Follows, M., Gruber, N., Joos, F., Lindsay, K., Maier-Reimer, E., Matear, R. J., Matsumoto, K., Mouchet, A., Orr, J. C., Sarmiento, J. L., Schlitzer, R., Weirig, M. F., Yamanaka, Y., and Yool, A.: Impact of circulation on export production, dissolved organic matter, and dissolved oxygen in the ocean: Results from Phase II of the Ocean Carbon-cycle Model Intercomparison Project (OCMIP-2), *Global Biogeochem. Cycles*, 21, GB3007, doi:10.1029/2006GB002857, 2007.
- Parekh, P., Follows, M. J., and Boyle, E.: Modeling the global ocean iron cycle, *Global Biogeochem. Cycles*, 18, GB1002, doi:10.1029/2003GB002061, 2004.
- Parekh, P., Joos, F., and Mueller, S. A.: A modeling assessment of the interplay between aeolian iron fluxes and iron-binding ligands in controlling carbon dioxide fluctuations during Antarctic warm events, *Paleoceanography*, 23, PA4202, doi:10.1029/2007PA001531, 2008.
- Plattner, G.-K., Joos, F., Stocker, T. F., and Marchal, O.: Feedback mechanisms and sensitivities of ocean carbon uptake under global warming, *Tellus B*, 53, 564–592, 2001.
- Randerson, J. T., Thompson, M. V., Conway, T. J., Fung, I. Y., and Field, C. B.: The contribution of terrestrial sources and sinks to trends in the seasonal cycle of atmospheric carbon dioxide, *Global Biogeochem. Cycles*, 11, 535–560, 1997.
- Roegner, E., Brokopf, R., Esch, M., Giorgetta, M., Hagemann, S., Kornbluh, L., Manzini, E., Schlese, U., and Schulzweida, U.: Sensitivity of simulated climate to horizontal and vertical resolution in the ECHAM5 atmosphere model, *J. Climate*, 19, 3771–3791, 2006.
- Santer, B. D., Taylor, K. E., Gleckler, P. J., Bonfils, C., Barnett, T. P., Pierce, D. W., Wigley, T. M. L., Mears, C., Wentz, F. J., Brueggemann, W., Gillett, N. P., Klein, S. A., Solomon, S., Stott, P. A., and Wehner, M. F.: Incorporating model quality information in climate change detection and attribution studies, *P. Natl. Acad. Sci. USA*, 106, 14778–14783, doi:10.1073/pnas.0901736106, 2009.
- Sarmiento, J. L., Slater, R. D., Fasham, M. J. R., Ducklow, H. W., Toggweiler, J. R., and Evans, G. T.: A seasonal 3-dimensional ecosystem model of nitrogen cycling in the North-Atlantic euphotic zone, *Global Biogeochem. Cycles*, 7, 417–450, 1993.
- Sarmiento, J. L., Hughes, T. M. C., Stouffer, R. J., and Manabe, S.: Simulated response of the ocean carbon cycle to anthropogenic climate warming, *Nature*, 393, 245–249, 1998.
- Sarmiento, J. L., Slater, R., Barber, R., Bopp, L., Doney, S. C., Hirst, A. C., Kleypas, J., Matear, R., Mikolajewicz, U., Monfray, P., Soldatov, V., Spall, S. A., and Stouffer, R.: Response of ocean ecosystems to climate warming, *Global Biogeochem. Cycles*, 18, GB3003, doi:10.1029/2003GB002134, 2004.
- Schmittner, A. and Galbraith, E. D.: Glacial greenhouse-gas fluctuations controlled by ocean circulation changes, *Nature*, 456, 373–376, doi:10.1038/nature07531, 2008.
- Schmittner, A., Oesch, A., Matthews, H. D., and Galbraith, E. D.: Future changes in climate, ocean circulation, ecosystems, and biogeochemical cycling simulated for a business-as-usual CO₂ emission scenario until year 4000 AD, *Global Biogeochem. Cycles*, 22, GB1013, doi:10.1029/2007GB002953, 2008.
- Schneider, B., Bopp, L., Gehlen, M., Segsneider, J., Frlicher, T. L., Cadule, P., Friedlingstein, P., Doney, S. C., Behrenfeld, M. J., and Joos, F.: Climate-induced interannual variability of marine primary and export production in three global coupled climate carbon cycle models, *Biogeosciences*, 5, 597–614, 2008, <http://www.biogeosciences.net/5/597/2008/>.
- Siegenthaler, U. and Wenk, T.: Rapid atmospheric CO₂ variations and ocean circulation, *Nature*, 308, 624–626, 1984.
- Six, K. D. and Maier-Reimer, E.: Effects of plankton dynamics on seasonal carbon fluxes in an ocean general circulation model, *Global Biogeochem. Cycles*, 10, 559–583, 1996.
- Smith, R. and Gent, P.: Reference Manual for the Parallel Ocean Program (POP). Ocean Component of the Community Climate System Model (CCSM2.0 and 3.0), Tech. Rep. LAUR-02-2484, Los Alamos National Laboratory, Los Alamos, New Mexico, USA, 2004.
- Solomon, S., Qin, D., Manning, M., Alley, R. B., Berntsen, T., Bindoff, N. L., Chen, Z., Chidthaisong, A., Gregory, J. M., Hegerl, G. C., Heimann, M., Hewitson, B., Hoskins, B. J., Joos, F., Jouzel, J., Kattsov, V., Lohmann, U., Matsuno, T., Molina, M., Nicholls, N., Overpeck, J., Raga, G., Ramaswamy, V., Ren, J., Rusticucci, M., Somerville, R., Stocker, T. F., Whetton, P., Wood, R. A., and Wratt, D.: Climate Change 2007: The Physical Science Basis, contribution of Working Group I to the Fourth Assessment Report of the Intergovernmental Panel on Climate Change, chap. Technical Summary, Cambridge University Press, Cambridge, United Kingdom and New York, NY, USA, 2007.
- Steinacher, M., Joos, F., Frlicher, T. L., Plattner, G.-K., and Doney, S. C.: Imminent ocean acidification in the Arctic projected with the NCAR global coupled carbon cycle-climate model, *Biogeosciences*, 6, 515–533, 2009, <http://www.biogeosciences.net/6/515/2009/>.
- Stier, P., Feichter, J., Kinne, S., Kloster, S., Vignati, E., Wilson, J., Ganzeveld, L., Tegen, I., Werner, M., Balkanski, Y., Schulz, M., Boucher, O., Minikin, A., and Petzold, A.: The aerosol-climate model ECHAM5-HAM, *Atmos. Chem. Phys.*, 5, 1125–1156, 2005,

- <http://www.atmos-chem-phys.net/5/1125/2005/>.
- Suntharalingam, P. and Sarmiento, J. L.: Factors governing the oceanic nitrous oxide distribution: Simulations with an ocean general circulation model, *Global Biogeochem. Cycles*, 14, 429–454, 2000.
- Tagliabue, A., Bopp, L., and Aumont, O.: Ocean biogeochemistry exhibits contrasting responses to a large scale reduction in dust deposition, *Biogeosciences*, 5, 11–24, 2008, <http://www.biogeosciences.net/5/11/2008/>.
- Takahashi, T., Broecker, W. S., and Langer, S.: Redfield ratio based on chemical-data from isopycnal surfaces, *J. Geophys. Res.-Oceans*, 90, 6907–6924, 1985.
- Taylor, K. E.: Summarizing multiple aspects of model performance in a single diagram., *J. Geophys. Res.-Atmos.*, 106, 7183–7192, 2001.
- Thornton, P. E., Doney, S. C., Lindsay, K., Moore, J. K., Mahowald, N., Randerson, J. T., Fung, I., Lamarque, J.-F., Feddema, J. J., and Lee, Y.-H.: Carbon-nitrogen interactions regulate climate-carbon cycle feedbacks: results from an atmosphere-ocean general circulation model, *Biogeosciences*, 6, 2099–2120, 2009, <http://www.biogeosciences.net/6/2099/2009/>.
- Timmermann, A. and Jin, F. F.: Phytoplankton influences on tropical climate, *Geophys. Res. Lett.*, 29, 2104, doi:10.1029/2002GL015434, 2002.
- Vichi, M., Pinardi, N., and Masina, S.: A generalized model of pelagic biogeochemistry for the global ocean ecosystem. Part I: Theory, *J. Marine Syst.*, 64, 89–109, doi:10.1016/j.jmarsys.2006.03.006, 2007.
- Volk, T. and Hoffert, M. I.: The Carbon Cycle and Atmospheric CO₂: Natural Variations Archean to Present, chap. Ocean carbon pumps: Analysis of relative strengths and efficiencies in ocean-driven atmospheric CO₂ changes., 99–110, *Geophys. Monogr. Ser. 32*, AGU, Washington, DC, USA, 1985.
- Weatherly, J. W., Briegleb, B. P., Large, W. G., and Maslanik, J. A.: Sea Ice and Polar Climate in the NCAR CSM, *J. Climate*, 11, 1472–1486, 1998.
- Wetzel, P., Maier-Reimer, E., Botzet, M., Jungclaus, J., Keenlyside, N., and Latif, M.: Effects of ocean biology on the penetrative radiation in a coupled climate model, *J. Climate*, 19, 3973–3987, 2006.
- Yeager, S. G., Shields, C. A., Large, W. G., and Hack, J. J.: The low-resolution CCSM3, *J. Climate*, 19, 2545–2566, 2006.

Chapter 4

Coupled carbon cycle-climate simulations with the Bern3D-LPX model

4.1 Introduction

The Bern3D-LPX Earth System Model of Intermediate Complexity (EMIC) is applied to perform a suite of simulations over the last millennium and future projections for different scenarios (Table 4.1). Most of these simulations are done in the context of the ‘EMIC AR5’ project¹, a joint effort by several groups, that will become a contribution of the EMIC modeling community to the 5th Assessment Report (AR5) of IPCC Working Group 1. The experimental setup follows closely the recommendations of the Paleoclimate Modelling Intercomparison Project (PMIP3², Schmidt et al., 2011) and the Coupled Model Intercomparison Project Phase 5 (CMIP5³, Taylor et al., 2009).

The aim of this chapter is to document and validate the model setup and to provide an overview of main results. A more extensive analysis, including the results from all participating groups, will be done within the ‘EMIC AR5’ project. In the following, the coupled Bern3D-LPX model is described in the next section and a detailed description of the newly implemented land surface albedo model is given. Then, the experimental setup is explained. In the results section, the new albedo model is validated and the impact on the radiative forcing is discussed. Then, future projections of global warming, steric sea level rise, and ocean acidification under the four RCP scenarios are presented. Finally, projected changes in the carbon cycle and their impacts on allowable emissions and atmospheric CO₂ are discussed for the RCP scenarios as well as for the temperature stabilization scenarios.

4.2 Bern3D-LPX model description

The Bern3D-LPX is an earth system model of intermediate complexity consisting of components that represent the ocean and sea ice, the ocean sediments, the atmosphere, and the terrestrial biosphere with a fully coupled carbon cycle. Below these components are briefly described. More information on the already published parts of the model can be found in the given references. This study is the first application of the model with a fully coupled

¹<http://climate.uvic.ca/EMICAR5>

²<http://pmip3.lsce.ipsl.fr/>

³<http://cmip-pcmdi.llnl.gov/cmip5/>

carbon cycle. Also, a dynamic surface albedo model has been added, which is presented in the following subsection. The technical aspects of coupling the LPX vegetation model to the Bern3D model are described in Appendix A and more information on newly implemented forcings and diagnostics is given in Appendix B.

The Bern3D ocean component is a seasonally forced three-dimensional frictional geostrophic global ocean model with a horizontal resolution of 36×36 boxes and 32 vertical layers. The integration time step is about a week. The physical ocean model is based on the model by Edwards et al. (1998) and described in detail by Müller et al. (2006). Marine biogeochemical cycles and air-sea gas-exchange are implemented following OCMIP-2 (Orr & Najjar, 1999; Najjar et al., 1999) with the addition of prognostic formulations for marine biological productivity as well as representations for the cycling of iron (Parekh et al., 2008), silica (Tschumi et al., 2008), ^{13}C , and ^{14}C . The sedimentary component described in Tschumi et al. (2011) is based on the model by Gehlen et al. (2006) and Heinze et al. (1999) which represents sediment diagenesis in the top 10 cm beneath the seafloor.

The atmosphere is represented by a single-layer energy and moisture balance model (EBM) with the same horizontal resolution as the ocean component (Ritz et al., 2011). Depth-integrated horizontal heat fluxes are parametrized in terms of eddy-diffusive fluxes with uniform zonal and meridional diffusivities. For the calculation of vertical shortwave radiation fluxes, incoming solar radiation (Berger, 1978), zonally averaged fractional cloud cover (from ECMWF ERA-40), and the surface albedo are taken into account (Bintanja, 1996). Following Weaver et al. (2001), the outgoing longwave radiation fluxes are parameterized after Thompson & Warren (1982) with additional radiative forcings due to CO_2 , other greenhouse gases, volcanic aerosols, and a feedback term, which is tuned to produce an equilibrium climate sensitivity of 3°C . The CO_2 forcing is calculated from the deviation of CO_2 concentrations from the preindustrial reference value (Myhre et al., 1998). Following Strassmann et al. (2009), the global mean radiative forcing from non- CO_2 greenhouse gases is calculated as the product of concentrations and radiative efficiencies as given in Forster et al. (2007). The radiative forcing from volcanic aerosols are specified explicitly with time series of global mean values. Sulphate aerosols are taken into account by changing the surface albedo locally according to the parametrization by Reader & Boer (1998) as described in Appendix B.

The terrestrial biosphere component LPX (Land-surface Processes and eXchanges) is based on the Lund-Potsdam-Jena (LPJ) Dynamic Global Vegetation Model at $3.75^\circ \times 2.5^\circ$ resolution as used by Joos et al. (2001), Gerber et al. (2003), and described in detail by Sitch et al. (2003). Vegetation is represented by 12 plant functional types and the fertilization of plants by increasing atmospheric CO_2 concentrations is modeled according to the modified Farquhar scheme (Farquhar et al., 1980). The model has been extended with a land-use module (Strassmann et al., 2008; Stocker et al., 2011) and more recently with a new hydrology scheme (Gerten et al., 2004; Wania et al., 2009a) that allows for the simulation of permafrost dynamics and peatlands (Wania et al., 2009a,b; Spahni et al., in prep.). Land surface albedo is calculated from vegetation cover, vegetation type, and snow cover after Otto et al. (2011) as described in section 4.2.1.

Here, the LPX component is driven by global mean atmospheric CO_2 concentrations and changes in global mean surface air temperature relative to a reference period. The global mean temperature deviations are used to scale climate anomaly fields (temperature, precipitation, and cloud cover) obtained from global warming simulations with the NCAR AOGCM. These anomalies are then added to the 31-year baseline climatology (Stocker et al., 2011). The terrestrial biosphere interacts with the rest of the model through the exchange of CO_2 with the atmosphere and changes in surface albedo due to vegetation and land-use changes (Appendix A). A schematic view of the coupled model is depicted in Fig. 4.1.

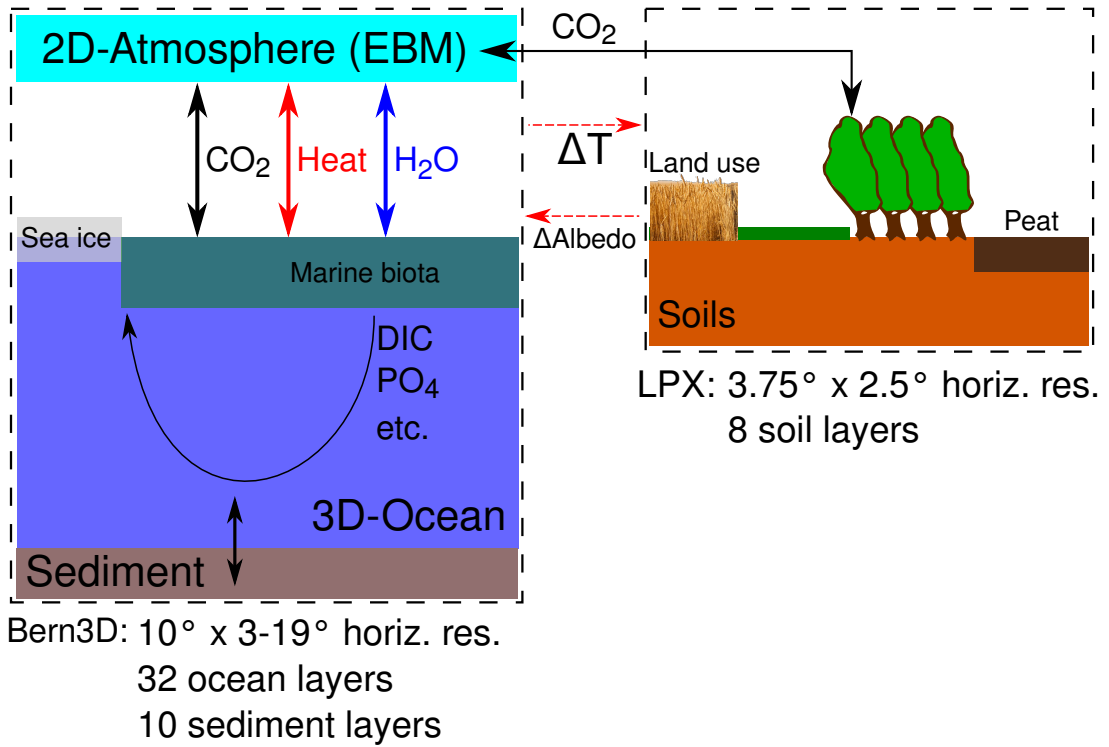


Figure 4.1: Schematic view of the main coupling mechanisms and model components of the Bern3D-LPX model. Carbon is exchanged between atmosphere, terrestrial vegetation, soils, oceans, and ocean sediments (black arrows). The LPX component is driven by global annual mean temperature anomalies with respect to the preindustrial state simulated by the Bern3D model. Changes in land surface albedo are fed back to the Bern3D atmosphere energy and moisture balance model (EBM).

4.2.1 Land surface albedo model

Calculation of surface albedo in LPX

The monthly land surface albedo is calculated within the LPX component from the simulated vegetation cover, vegetation type, and snow cover. Following Otto et al. (2011), the fractional cover by leaves (f_{leaf}) and by stems and branches (f_{stem}) is calculated for each grid cell, plant functional type (PFT), and month. The leaf cover is calculated from the grid cell foliar projective cover (FPC_{grid}) and daily phenology $\phi(d)$,

$$f_{\text{leaf}}(\text{pft}, m) = \frac{1}{N_{\text{days}}} \sum_{d=1}^{N_{\text{days}}} \text{FPC}_{\text{grid}}(\text{pft}) \cdot \phi(d, \text{pft}). \quad (4.1)$$

FPC_{grid} quantifies the potential grid cell area that is covered by leaves of one PFT and depends on the leaf area index of one individual, LAI_{ind} , the crown area, and the population density in that grid cell N_{ind} (Sitch et al., 2003). This potential cover, which is constant over one year, is then modified by the daily phenology which accounts for summer-green and rain-green PFTs that shed their leaves in winter or under water stress, respectively. N_{days} denotes the number of days in the corresponding month.

To calculate the fractional cover by stems and branches, a vegetation area index (including phenology) is defined as

$$\text{VAI}_{\text{ind}}(d, \text{pft}) = \text{LAI}_{\text{ind}}(\text{pft}) \cdot \phi(d) + \text{SAI}_{\text{ind}}(\text{pft}), \quad (4.2)$$

where the stem area index, SAI_{ind} , is a new PFT-dependent parameter. Currently, it is set to 0.5 for all tree PFTs, except for tropical evergreen trees (0.1), boreal summer-green needle trees (0.3), and boreal summer-green broadleaved trees (1.1). The concept of the vegetation index is the same as for the leaf area index, which relates the leaf surface to the ground surface area on which the vegetation grows, but it includes also the surface area of stems and branches. Without a stem area index, the vegetation cover would be zero in winter for summer-green trees, when $\phi(d)$ goes to zero. This is important for the albedo calculation because stems and branches mask the snow-covered ground to some extent (Otto et al., 2011). The grid cell vegetation cover (VPC_{grid} , including phenology) is then calculated analogously to FPC_{grid} (Eq. 7 and 8 in Sitch et al., 2003) as

$$\text{VPC}_{\text{grid}}(\text{pft}, m) = \text{crownarea}(\text{pft}) \cdot N_{\text{ind}}(\text{pft}) \frac{1}{N_{\text{days}}} \sum_{d=1}^{N_{\text{days}}} \left(1 - e^{-0.5 \cdot \text{VAI}_{\text{ind}}(\text{pft}, d)}\right). \quad (4.3)$$

The fractional cover by stems and branches is then the difference between the total vegetation cover and the area covered by leaves:

$$f_{\text{stem}}(\text{pft}, m) = \text{VPC}_{\text{grid}}(\text{pft}, m) - f_{\text{leaf}}(\text{pft}, m). \quad (4.4)$$

For PFTs other than trees, f_{stem} is zero.

From these grid cell cover fractions, the contribution of one PFT to the albedo is calculated as

$$\alpha_{\text{PFT}} = f_{\text{stem}} \left[(1 - f_{\text{veg}}^{\text{snow}}) \alpha_{\text{soil}} + f_{\text{veg}}^{\text{snow}} \alpha_{\text{veg}}^{\text{snow}} \right] + f_{\text{leaf}} \left[(1 - f_{\text{veg}}^{\text{snow}}) \alpha_{\text{leaf}} + f_{\text{veg}}^{\text{snow}} \alpha_{\text{veg}}^{\text{snow}} \right], \quad (4.5)$$

where $f_{\text{veg}}^{\text{snow}}$ is the fraction of the plant surface covered with snow (described below). $\alpha_{\text{soil}} = 0.16$, $\alpha_{\text{veg}}^{\text{snow}}$, and α_{leaf} are the albedo of stems and branches (here assumed to be equal to the albedo of bare soil), snow covered vegetation, and green leaves, respectively. The albedo of snow covered vegetation ($\alpha_{\text{veg}}^{\text{snow}}$) is fixed at 0.4 for trees. For other PFTs, it is assumed to be equal to the albedo of snow on bare soil ($\alpha_{\text{soil}}^{\text{snow}}$, see below). The canopy albedo $\alpha_{\text{leaf}}(\text{pft})$ is a new PFT-dependent parameter. The values for trees and grasses are from Otto et al. (2011) by assuming $\alpha = 0.67 \cdot \alpha_{\text{VIS}} + 0.33 \cdot \alpha_{\text{NIR}}$. The albedo of land-use PFTs are set to 0.15 for crops, 0.16 for pastures (Myhre et al., 2005; Tian et al., 2004), and to 0.12 for built-up areas. For the wetland PFTs graminoids and sphagnum, albedo of 0.16 (grass) and 0.14 (Berglund & Mace, 1972) are assumed, respectively.

The monthly average albedo in one grid cell can then be calculated by adding the contribution from the different PFTs and the remaining uncovered area, which is assumed to be unshaded bare soil:

$$\alpha(m) = \sum_{\text{pft}} \alpha_{\text{PFT}}(\text{pft}, m) + \left(1 - \sum_{\text{pft}} \text{VPC}_{\text{grid}}(\text{pft}, m)\right) \left[(1 - f_{\text{soil}}^{\text{snow}}) \alpha_{\text{soil}} + f_{\text{soil}}^{\text{snow}} \alpha_{\text{soil}}^{\text{snow}} \right], \quad (4.6)$$

where $f_{\text{soil}}^{\text{snow}}$ and $\alpha_{\text{soil}}^{\text{snow}}$ are the fraction and albedo of snow covered soil, respectively.

The snow albedo is calculated after Kubatzki (2000) (CLIMBER-2.1 model). Maximum values of $\alpha_{\text{max}}^{\text{VIS}} = 0.9$ and $\alpha_{\text{max}}^{\text{NIR}} = 0.6$ are assumed for visible and near-infrared light, respectively (Dickinson et al., 1986). The temperature dependency is parametrized by defining a function $\nu(T)$, with $\nu(T \leq -5^\circ\text{C}) = 0$ and $\nu(T \geq 5^\circ\text{C}) = 1$. Between -5°C and 5°C , $\nu(T)$ is cosine shaped. The snow albedo then is calculated as

$$\alpha_{\text{soil}}^{\text{snow}} = 0.67 \cdot \alpha_{\text{max}}^{\text{VIS}} [1 - 0.2(1 - \nu(T))] + 0.33 \cdot \alpha_{\text{max}}^{\text{NIR}} [1 - 0.5(1 - \nu(T))], \quad (4.7)$$

assuming a partitioning of 67% and 33% between visible and near-infrared light. The factors 0.2 and 0.5 account for the faster aging of snow with respect to the near-infrared radiation (Kubatzki, 2000).

To determine the snow cover fraction, three surface types with different roughness scales are considered, namely trees, grasses, and bare soil. For trees, the maximum snow cover fraction is a function of grid box snow height h_{snow} and temperature

$$f_{\text{tree,max}}^{\text{snow}} = \nu(T) \left(0.6 \cdot \frac{h_{\text{snow}}}{10 \text{ m}} + 0.4 \cdot \left(1 - \frac{h_{\text{snow}}}{10 \text{ m}} \right) \right), \quad (4.8)$$

which limits the maximum snow cover for trees to 60% and accounts for the fact that more snow falls off the trees at higher temperatures (Kubatzki, 2000). The maximum snow cover for grass and soil is set to 100%. The effective snow cover for each surface type is then given by

$$f^{\text{snow}} = f_{\text{max}}^{\text{snow}} \frac{h_{\text{snow}}/h_{\text{scale}}}{1 + h_{\text{snow}}/h_{\text{scale}}}, \quad (4.9)$$

where h_{scale} is a constant parameter that is related to the roughness scale of the surface (0.5 m for trees, 0.3 m for grass, and 0.15 m for bare soil). These snow cover fractions are used as $f_{\text{veg}}^{\text{snow}}$ and $f_{\text{soil}}^{\text{snow}}$ in the equations 4.5 and 4.6 according to the corresponding surface type (tree PFTs, grass PFTs, or bare soil).

The albedo model described here is validated and discussed in section 4.4.2.

Coupling LPX and Bern3D surface albedo

Monthly surface albedo fields calculated by LPX are passed to the Bern3D component, where they are mapped from the LPX to the coarser Bern3D grid (see Appendix A.2 for details). The surface albedo is used by the EBM to calculate the outgoing shortwave radiation (Ritz et al., 2011). A climatology obtained from MODIS satellite observations is used as a baseline ($\alpha_{\text{atm}}(i, j)$), on top of which changes in surface albedo simulated by LPX ($\Delta\alpha_{\text{LPX}}(i, j)$) are added:

$$\alpha_{\text{atm}}(i, j) = \alpha_{\text{atm}}(i, j) + \Delta\alpha_{\text{LPX}}(i, j) \quad (4.10)$$

This method eliminates some systematic errors such as the inappropriate soil albedo in deserts (see section 4.4.2). A more detailed technical description of the Bern3D-LPX coupling is given in Appendix A.

4.3 Experimental setup

Spin-up

The Bern3D ocean and atmosphere components are spun up to steady-state during 80'000 years under constant 850 AD conditions (CO_2 concentration of 279.3 ppm, no radiative forcing from other greenhouse gases, no volcanic or aerosol forcing, constant orbital parameters, constant land-use map), except for the atmospheric ^{14}C signature, which is prescribed during the last 10'250 years of the spin-up to include the signal from ^{14}C variations before 850 AD. Such a long spin-up time is required by the ocean sediment to reach equilibrium. The LPX component was initialized with last glacial maximum conditions and a subsequent transient simulation from 21 kyBP to 850 AD in order to account for the peat accumulation that is assumed not to be in equilibrium by 850 AD.

Historical simulations

The historical simulations over the last millennium (850-2005 AD) start from the spin-up and the following forcings are applied:

- CO₂: Reconstructed CO₂ concentrations from the Law Dome ice core record (Etheridge et al., 1996; MacFarling Meure et al., 2006), linearly blended into the RCP data set⁴ (Meinshausen et al., 2011) between 1765 and 1800.
- AGG: Reconstructed concentrations of the additional greenhouse gases CH₄ (Etheridge et al., 1996; MacFarling Meure et al., 2006) and N₂O (Flückiger et al., 2002, 1999; Machida et al., 1995; Battle et al., 1996), linearly blended into the RCP data set between 1765 and 1800, which also contains concentrations of fluorinated gases controlled under the Kyoto Protocol (HFCs, PFCs, and SF₆) and Montreal Protocol (CFCs, HCFCs, Halons, CCl₄, CH₃Br, CH₃Cl), respectively (Meinshausen et al., 2011).
- LND: Anthropogenic land cover changes (natural to crop and pasture) from 850 to 1699 reconstructed by Pongratz et al. (2008), linearly blended into the historical RCP land-use data (Hurtt et al., 2009) over the period 1500 to 1699.
- SUL: Optical depth calculated from historical RCP SO₄ concentrations⁴ (1855 to 2005). SO₄ concentrations are vertically integrated to determine the atmospheric sulphate aerosol burden, which is then multiplied by a constant specific extinction cross-section factor of 8 m² g⁻¹ to obtain the optical depth⁵.
- VOL: Radiative forcing due to volcanic aerosols. The radiative forcing is calculated with a simple linear conversion constant from a time series of aerosol optical depth⁵ (Crowley et al., 2008).
- ORB: Forcing by annual varying orbital parameters following Berger (1978).
- SOL: Changes in the total solar irradiance are prescribed using data from Delaygue & Bard (2009) for the period 850 to 1609 and from Lean (2000) and Wang et al. (2005) for the period 1610-2005.

Ozone, stratospheric H₂O, indirect aerosol effects, organic carbon, black carbon, and mineral dust are not considered in these simulations. There are relatively large uncertainties associated with the radiative forcing of these agents and their positive and negative contributions tend to cancel out. The present-day additional forcing is estimated to be -0.25 W m⁻² with a uncertainty that is significantly larger than that (Forster et al., 2007). Therefore it has been decided not to include those forcings in the EMIC AR5 simulations. Changes in ice sheets, topography, or coast lines are not considered either.

In addition to the standard simulation with all forcings (hist_TOT), one simulation is performed for each of the forcing components, in which all other forcings remain constant at their initial values used during the spin-up. Further, three simulations in which the atmospheric CO₂ is allowed to evolve freely are performed; one with the total forcing (histC_TOT), where fossil fuel CO₂ emissions (including cement manufacture and gas flaring) are prescribed (1765-2005; Marland et al., 2008; Meinshausen et al., 2011), one where only natural forcings (SOL, VOL, ORB) are applied (histC_NAT), and one where only land-use changes are prescribed (histC_LND). Two control runs over the historical period with constant forcings and either constant CO₂ concentrations (ctrl) or free CO₂ (ctrlC) and no anthropogenic emissions are used to check for model drifts.

⁴<http://www.iiasa.ac.at/web-apps/tnt/RcpDb>

⁵<http://climate.uvic.ca/EMICAR5/forcing>

Future projections

The historical simulation with all forcings (hist_TOT) is continued from year 2005 to 2300 for the four Representative Concentration Pathway scenarios RCP3-PD, RCP4.5, RCP6, and RCP8.5 (Taylor et al., 2009; Moss et al., 2010; van Vuuren et al., 2011), which specify the model forcing from 2005 to 2100, followed by their extensions (ECP) from 2100 to 2300 (Meinshausen et al., 2011). More specifically, CO₂ and additional greenhouse gas concentrations available from the RCP database⁴ are prescribed from 2005 to 2300 and projected land-use changes (Hurtt et al., 2009) and sulphate aerosol concentrations from the RCP database are applied for the period 2005 to 2100 and held fixed afterward. No volcanic forcing and no changes in the orbital forcing is applied after 2005. The last solar cycle with values from 1996 to 2008 is repeated to prescribe total solar irradiance throughout the simulations. The four simulations RCP3, RCP4, RCP6, and RCP8 are repeated with the same setup but with prescribed CO₂ emissions instead of concentrations (free atmospheric CO₂; simulations RCP3C, RCP4C, RCP6C and RCP8C).

The committed climate change by 2300 is quantified by extending the simulations under four different assumptions until the year 3000:

1. The CO₂ concentration and all other forcings remain constant at the 2300 level (CO₂ concentration commitment, default simulation).
2. Instead of CO₂ concentrations, CO₂ emissions remain constant at the 2300 level and all other forcings are kept constant at the 2300 level (CO₂ emission commitment, ec).
3. The CO₂ emissions are set instantaneously to preindustrial (1840-1850) levels, while all other forcings are kept constant at the 2300 level (CO₂ climate commitment, co2cc).
4. The CO₂ emissions and all other forcings except land-use changes are instantaneously reverted back to preindustrial levels (climate commitment, cc).

Please note that in the latter three cases the model forcing is switched from prescribed CO₂ concentrations to prescribed CO₂ emissions. The goal of these simulations is to examine the long-term response of the climate system to the human perturbation. By holding the model forcings constant after 2300, the subsequent response depends only on changes before 2300. Further, the four simulations allow the exploration of different types of commitments, which can be interpreted to define lower and upper bounds for the committed changes.

To study the irreversibility, the concentration commitment simulations are further extended from year 3000 to year 4000 in three different ways. In two simulations atmospheric CO₂ is decreased linearly to preindustrial levels in 100 years (irrA) and 1000 years (irrB), respectively. In the third simulation, CO₂ is allowed to evolve freely after 3000 with zero anthropogenic emissions.

In addition to the extended RCP scenarios, four temperature stabilization experiments from year 2005 to 2500 are conducted. In these simulations, the model is forced to follow a prescribed temperature profile by dynamically adjusting the CO₂ emissions (see Appendix B.4 for details). By using this technique, the allowable cumulative emissions that are compatible with a specified temperature stabilization target can be quantified (Zickfeld et al., 2009). The temperature profiles are generated using a cubic spline interpolation that matches the slope of the temperature at the end of the historical simulation and stabilizes at the targets of 1.5, 2.0, 3.0, and 4.0 °C above the simulated preindustrial global mean temperature. The radiative forcing from other greenhouse gases and aerosols is linearly decreased to zero from 2005 to 2300 in these simulations. All other forcings are held constant at their 2005 values.

Further, several idealized experiments ($2xCO_2$ and $4xCO_2$) are performed, which are not discussed in detail here. A complete list of simulations is given in table 4.1.

Table 4.1: Simulations overview.

<i>No.</i>	<i>Name</i>	<i>Start</i>	<i>End</i>	<i>Years</i>	<i>Start from</i>	<i>Description</i>
1	ctrl	850	2005	1156	(spin-up)	Control (standard)
2	ctrlC	850	2005	1156	(spin-up)	Control (free CO ₂)
3	hist_TOT	850	2005	1156	(spin-up)	Historical (TOT forcing)
4	hist_CO2	850	2005	1156	(spin-up)	Historical (CO ₂ forcing)
5	hist_AGG	850	2005	1156	(spin-up)	Historical (AGG forcing)
6	hist_LND	850	2005	1156	(spin-up)	Historical (LND forcing)
7	hist_SUL	850	2005	1156	(spin-up)	Historical (SUL forcing)
8	hist_SOL	850	2005	1156	(spin-up)	Historical (SOL forcing)
9	hist_VOL	850	2005	1156	(spin-up)	Historical (VOL forcing)
10	hist_ORB	850	2005	1156	(spin-up)	Historical (ORB forcing)
11	histC_TOT	850	2005	1156	(spin-up)	Historical (TOT forcing, free CO ₂)
12	histC_NAT	850	2005	1156	(spin-up)	Historical (NAT forcing, free CO ₂)
13	histC_LND	850	2005	1156	(spin-up)	Historical (LND forcing, free CO ₂)
14	RCP3	2006	2999	994	hist_TOT	RCP3PD (CO ₂ conc. commitment)
15	RCP4	2006	2999	994	hist_TOT	RCP4.5 (CO ₂ conc. commitment)
16	RCP6	2006	2999	994	hist_TOT	RCP6 (CO ₂ conc. commitment)
17	RCP8	2006	2999	994	hist_TOT	RCP8.5 (CO ₂ conc. commitment)
18	RCP3C	2006	2999	994	histC_TOT	RCP3PD (free CO ₂)
19	RCP4C	2006	2999	994	histC_TOT	RCP4.5 (free CO ₂)
20	RCP6C	2006	2999	994	histC_TOT	RCP6 (free CO ₂)
21	RCP8C	2006	2999	994	histC_TOT	RCP8.5 (free CO ₂)
22	RCP3ec	2300	2999	994	RCP3	RCP3PD (CO ₂ emis. commitment)
23	RCP3co2cc	2300	2999	994	RCP3	RCP3PD (CO ₂ climate commitment)
24	RCP3cc	2300	2999	994	RCP3	RCP3PD (climate commitment)
25	RCP4ec	2300	2999	994	RCP4	RCP4.5 (CO ₂ emis. commitment)
26	RCP4co2cc	2300	2999	994	RCP4	RCP4.5 (CO ₂ climate commitment)
27	RCP4cc	2300	2999	994	RCP4	RCP4.5 (climate commitment)
28	RCP6ec	2300	2999	994	RCP6	RCP6 (CO ₂ emis. commitment)
29	RCP6co2cc	2300	2999	994	RCP6	RCP6 (CO ₂ climate commitment)
30	RCP6cc	2300	2999	994	RCP6	RCP6 (climate commitment)
31	RCP8ec	2300	2999	994	RCP8	RCP85 (CO ₂ emis. commitment)
32	RCP8co2cc	2300	2999	994	RCP8	RCP85 (CO ₂ climate commitment)
33	RCP8cc	2300	2999	994	RCP8	RCP85 (climate commitment)
34	RCP3irrA	3000	3999	1000	RCP3	RCP3PD (irreversibility 100yr)
35	RCP3irrB	3000	3999	1000	RCP3	RCP3PD (irreversibility 1000yr)
36	RCP3irrC	3000	3999	1000	RCP3	RCP3PD (irreversibility free-CO ₂)
37	RCP4irrA	3000	3999	1000	RCP4	RCP4.5 (irreversibility 100yr)
38	RCP4irrB	3000	3999	1000	RCP4	RCP4.5 (irreversibility 1000yr)
39	RCP4irrC	3000	3999	1000	RCP4	RCP4.5 (irreversibility free-CO ₂)
40	RCP6irrA	3000	3999	1000	RCP6	RCP6 (irreversibility 100yr)
41	RCP6irrB	3000	3999	1000	RCP6	RCP6 (irreversibility 1000yr)
42	RCP6irrC	3000	3999	1000	RCP6	RCP6 (irreversibility free-CO ₂)
43	RCP8irrA	3000	3999	1000	RCP8	RCP85 (irreversibility 100yr)
44	RCP8irrB	3000	3999	1000	RCP8	RCP85 (irreversibility 1000yr)
45	RCP8irrC	3000	3999	1000	RCP8	RCP85 (irreversibility free-CO ₂)
46	Tstab1.5	2000	2499	500	hist_TOT	Temperature stabilization (1.5 °C)
47	Tstab2.0	2000	2499	500	hist_TOT	Temperature stabilization (2.0 °C)
48	Tstab3.0	2000	2499	500	hist_TOT	Temperature stabilization (3.0 °C)

Table 4.1: Simulations overview (*cont.*)

<i>No.</i>	<i>Name</i>	<i>Start</i>	<i>End</i>	<i>Years</i>	<i>Start from</i>	<i>Description</i>
49	Tstab4.0	2000	2499	500	hist_TOT	Temperature stabilization (4.0 °C)
50	CO2x2	1855	2854	1000	ctrl	2xCO ₂
51	CO2x4A	1855	2854	1000	ctrl	4xCO ₂ A (instant. fixed conc.)
52	CO2x4B	1855	2854	1000	ctrl	4xCO ₂ B (instant. freely evolving)
53	CO2x4C	1855	2854	1000	ctrl	4xCO ₂ C (1%/yr, const. afterwards)
54	CO2x4D	1855	2854	1000	ctrl	4xCO ₂ D (1%/yr, free afterwards)
55	CO2x4E	1855	2854	1000	ctrl	4xCO ₂ E (1%/yr, preind. rad. CO ₂)
56	CO2x4F	1855	2854	1000	ctrl	4xCO ₂ F (1%/yr, but only rad. CO ₂)
57	CO2x4G	1855	2854	1000	ctrl	4xCO ₂ G (1%/yr, fixed diag. emis.)

4.4 Results

4.4.1 Control simulations

Two control simulations over the historical period (850 – 2005) with prescribed and free atmospheric CO₂, respectively, are used to check for unintended model drifts. An increasing trend in soil carbon is expected and consistent with the model set up which assumes that peatland soil carbon pools are not in equilibrium at the start of the simulations in 850 AD. The continued peat accumulation leads to an increase in land carbon of about 10 GtC over 1000 years in both control simulations. Consequently, the terrestrial uptake reduces the carbon content of the atmosphere (-1 ppm) and ocean (-8 GtC) in the simulation with free atmospheric CO₂. This leads to a slight decreasing trend in the global mean surface temperature of about -0.02 °C over 1000 years. In the control simulation with constant atmospheric CO₂, no drifts in global mean temperature or ocean carbon content are found, which shows that the trends in the free-CO₂ simulation are only caused by the intended terrestrial carbon uptake.

4.4.2 Land surface albedo changes and their impact on the radiative forcing

Validation of the surface albedo model

To validate the albedo model described in section 4.2.1, the simulated surface albedo is compared with MODIS satellite observations for the period 2001-2010 (Moody et al., 2005; Strahler et al., 1999) obtained from NEO⁶. The MODIS data set is re-gridded to the LPX model grid and monthly climatologies are calculated for both, the MODIS data and the Bern3D-LPX simulation.

The annual mean albedo pattern and magnitude is reproduced reasonably by the model in most regions (Fig. 4.2a-c). The notable differences are the overestimation at latitudes 45°N-60°N and the systematically too low values in the Sahara desert area. Systematic discrepancies, such as those in deserts, are relatively unproblematic as long as only deviations from the LPX reference albedo are applied to the Bern3D baseline albedo map (and as long as these regions remain deserts). The timing and amplitude of the global mean annual cycle is also relatively well represented, when the Sahara desert is excluded (Fig. 4.2d-f). Global mean albedo values are overestimated by up to 10% in winter and slightly underestimated

⁶<http://neo.sci.gsfc.nasa.gov>

in summer. The overestimation is mostly due to regions at latitudes 45°N-60°N and the underestimation in summer stems mostly from high latitudes (Fig. 4.2f and 4.3).

The simulated albedo at mid- to high-latitudes depends critically on a realistic representation of snow cover and vegetation type. High albedo values of 0.5 or more are only reached where the snow is able to cover a large portion of the ground, i.e. on grass- and croplands or in forests with a large fraction of summer-green trees. The taiga, for example, which is dominated by coniferous forests, is clearly visible in the MODIS map as a band of reduced albedo around 60°N in February (Fig. 4.3). and it is also represented to some extent in the model results (Fig. 4.3). Thus, the differences found between model and observation-based data are most likely a combination of deficiencies in the albedo model as well as in the simulated vegetation pattern and timing and magnitude of snow cover.

There is certainly some potential to further reduce the errors in the simulated present-day albedo. The roughness scales and stem area indices, used in the albedo model, have been used mainly as tuning parameters to get a more or less realistic snow masking for the winter albedo. The choice of these parameters could likely be improved by using data assimilation techniques. Also, the calculation of the snow cover fraction for trees could probably be improved by including the leaf area index and interception capacity (Roesch & Roeckner, 2006; Roesch et al., 2001). Particularly, the albedo model should be improved if absolute values instead of anomalies are to be used in the shortwave radiation code of the Bern3D model at a later stage. For the current study, however, the current model is considered to simulate the surface albedo well enough.

Land use induced changes in surface albedo

The direct influence of land-use changes on the surface albedo is estimated by including or excluding the contribution of land-use areas when calculating the average albedo of a grid cell. Including land use generally leads to an increase in the simulated surface albedo. No decrease can be found in the decade 2001-2010, for which the model has been validated. The effect is most visible during winter at latitudes between 40°N and 60°N, where the albedo locally is up to 0.3 higher than when including just the natural vegetation (Fig. 4.4). This can mostly be attributed to an increased snow cover in winter resulting from the conversion of forests to pasture and croplands. Annual mean albedo values are increased by 0.04–0.1 in regions with extensive land use at those latitudes. While snow plays an important role with respect to albedo changes as a result of altered vegetation, the conversion of natural vegetation to agricultural land changes the surface albedo also directly because crops and pasture generally reflect more sunlight than forests. This can be seen, for example, at low latitudes where the extent of tropical forests, which have a very low albedo, has been reduced as a result of land use and annual mean albedo values are increased by up to 0.04 (Fig. 4.4e,f).

Impact of albedo changes on the radiative forcing

Changes in the surface albedo translate to a change in the radiative forcing because the fraction of the incoming solar radiation which is reflected back to space is different. Thereby internal and external forcing mechanisms can be distinguished. Please note that here the term ‘forcing’ is not used strictly for an external forcing, as it is usual in the feedback analysis terminology, but for the combined effect of external forcing and feedbacks on the radiative balance.

The change in surface albedo as a result of land-use change is considered an external anthropogenic forcing without feedback. For example, when boreal forests are converted to pasture or croplands, the winter albedo generally increases because these vegetation types allow a

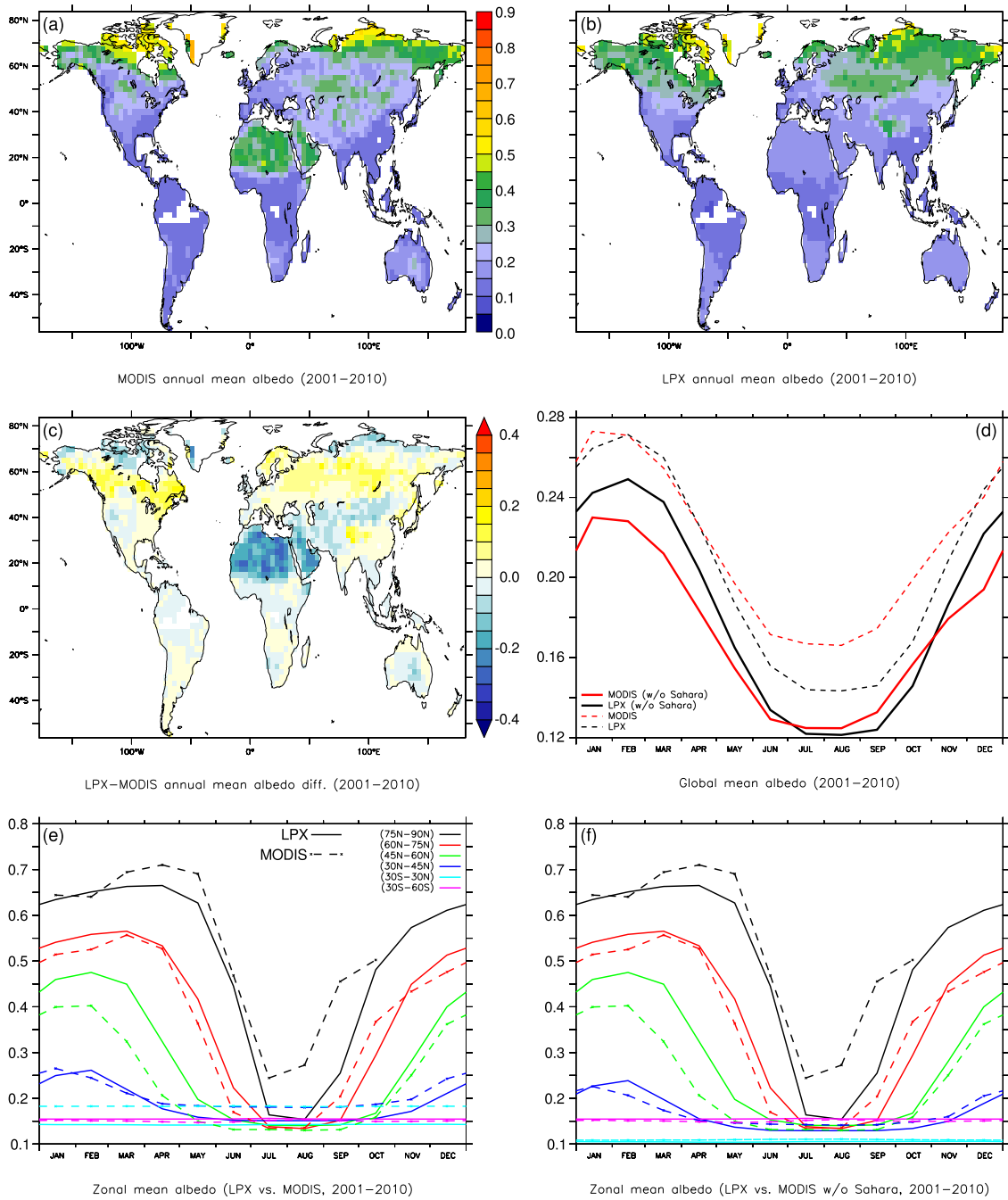


Figure 4.2: Maps of annual mean surface albedo from (a) MODIS, (b) simulated by LPX, and (c) the difference LPX-MODIS. (d) Annual cycle of global mean albedo with and without the Sahara desert. Annual cycle at different latitudes (e) including and (f) excluding the Sahara desert.

more extended snow cover. Climate change, on the other hand, can lead to 'natural' albedo changes which in turn affect the radiative forcing and the climate system. Those natural albedo changes therefore represent an internal feedback mechanism. Higher temperatures, for example, decrease the snow cover and thereby the albedo, which in turn leads to an increase in radiative forcing and an amplified warming. This is the most prominent internal feedback mechanism but climate change can also lead to shifts in vegetation, which may change the surface albedo.

The external radiative forcing directly caused by land-use induced surface albedo changes in

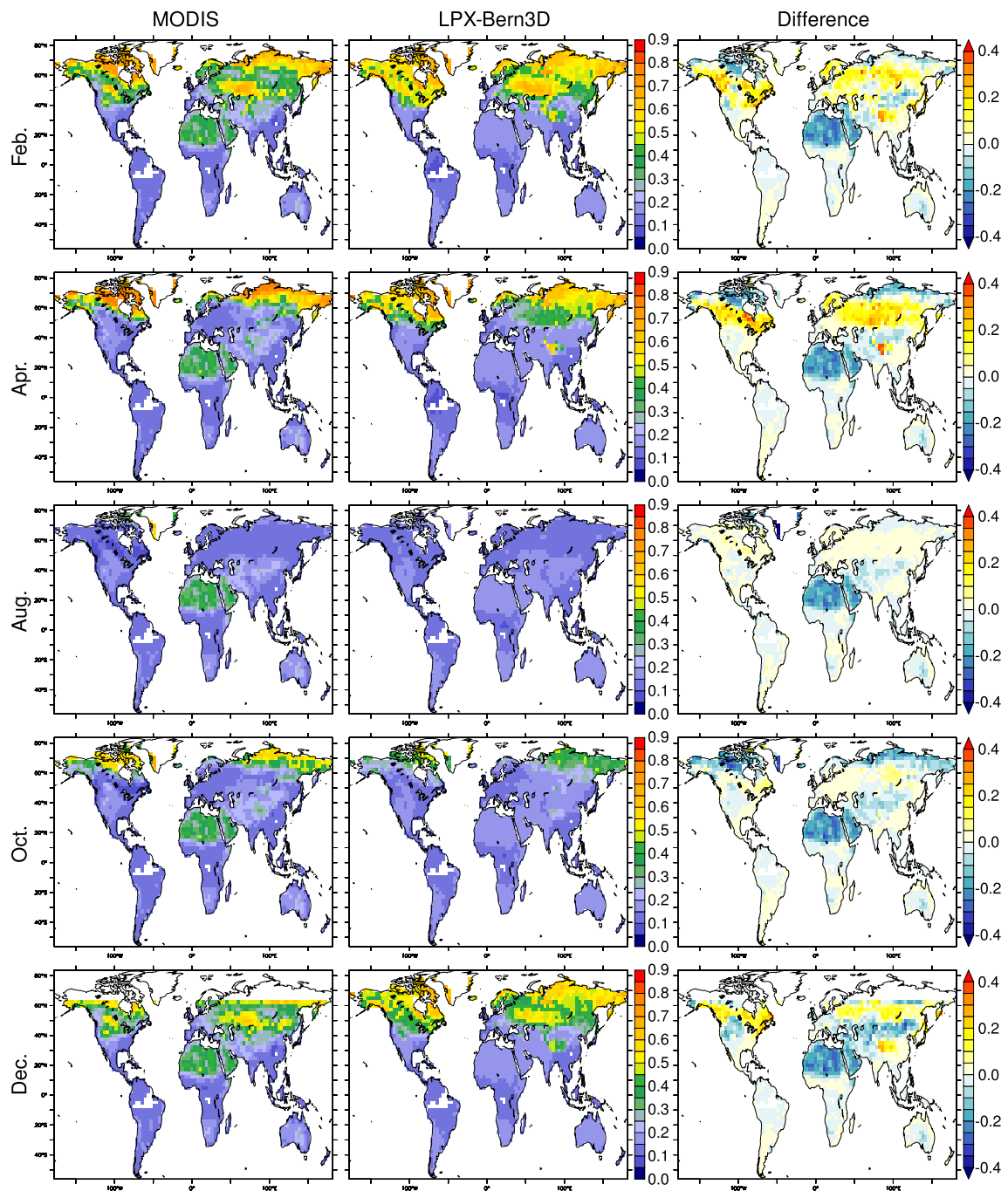


Figure 4.3: Maps of monthly mean surface albedo from MODIS (left), simulated by LPX (middle), and the difference LPX-MODIS (right) for the months Feb., Apr., Aug., Oct., and Dec. (top to bottom).

the historical simulation amounts to -0.25 W m^{-2} by the year 2005 (relative to 1750), which is well within the estimated range of $-0.20 \pm 0.20 \text{ W m}^{-2}$ given by Forster et al. (2007). By that time, the radiative influence from natural albedo changes is almost zero (Fig. 4.5a). Under projected global warming the internal forcing increases and acts as a positive feedback. In the RCP8.5 scenario, the internal forcing reaches the magnitude of the land-use induced forcing (-0.29 W m^{-2}) in the last quarter of the 21st century and both effects cancel out. With further increasing temperatures, the internal forcing dominates and the net effect changes from a negative to a positive forcing. By 2300, when the global mean temperatures have increased

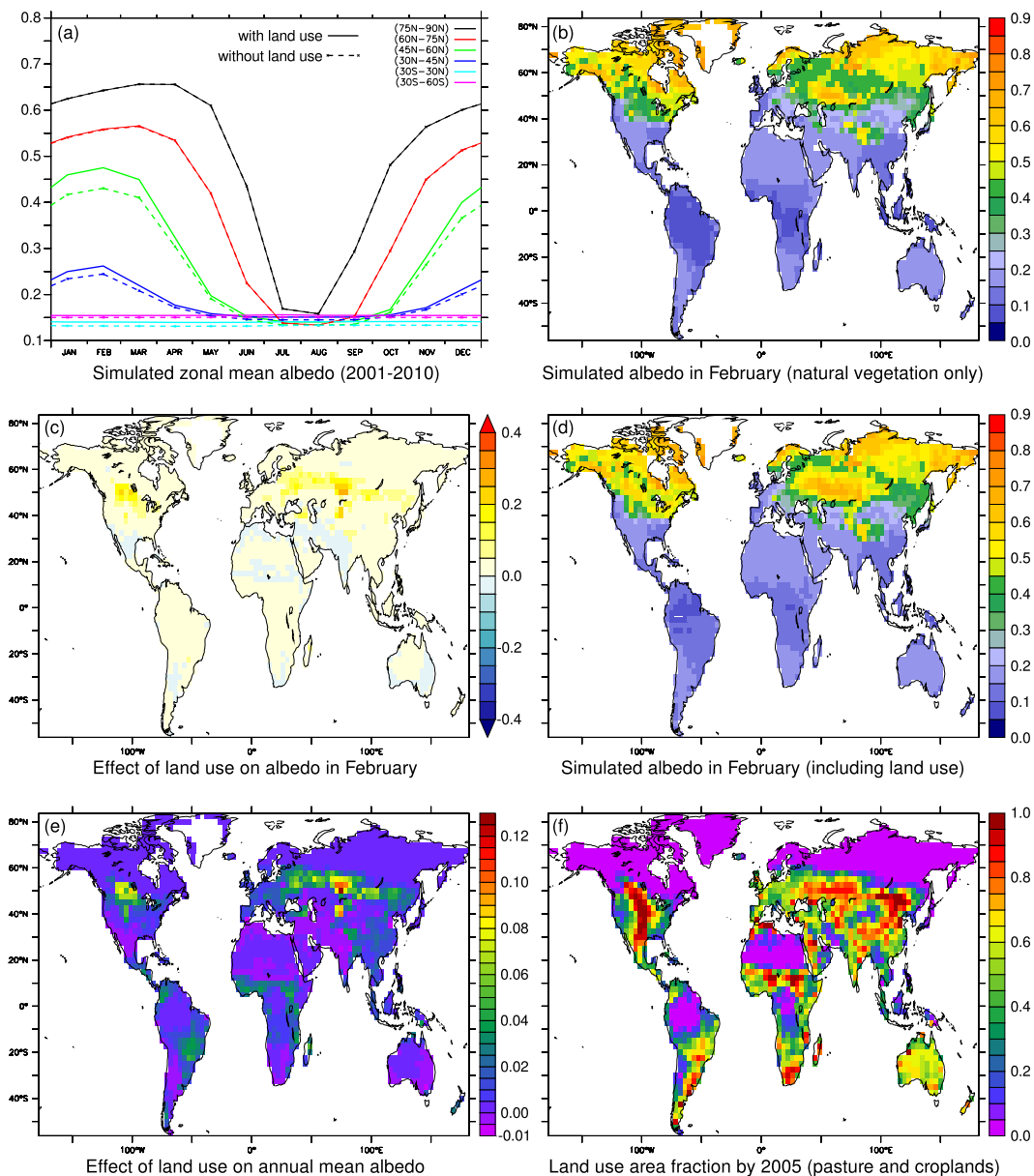


Figure 4.4: The effect of land-use changes on the simulated surface albedo (2001–2010). (a) Annual cycle of the zonally averaged albedo at different latitudes. Maps of the simulated albedo in February without (b) and with (d) land use. Change in February (c) and annual mean (e) surface albedo by including land-use areas. (f) Prescribed land-use area (crops and pasture) by 2005 expressed as grid cell area fraction.

by about 9°C in the RCP8.5 projection, the internal and external radiative forcings from albedo changes are 1.07 W m^{-2} and -0.37 W m^{-2} , respectively (Fig. 4.5a). The internal surface albedo feedback amplifies the total external forcing (from greenhouse gases, aerosols, land-use changes) by about 8% at that time.

Changes in land use not only lead to surface albedo changes but also to CO_2 emissions. The contribution of these two opposite effects to the radiative forcing is quantified with a simulation where only land-use changes are applied, atmospheric CO_2 is allowed to evolve freely, and all other forcings remain constant (histC_LND). During the first half of the last millennium, the net radiative forcing is mainly dominated by CO_2 emissions, yet both effects are relatively small (Fig. 4.5b). The relative importance of the albedo forcing increases over time. The reduction of the CO_2 forcing by the compensating albedo forcing increases from

about 10% to 50-60% by 1750. After that, both effects increase significantly in response to intensified land use during the industrial period and the relative contribution of the albedo forcing decreases again slightly. By the year 2000 the simulated CO_2 radiative forcing of 0.52 W m^{-2} is reduced by about 40% (0.21 W m^{-2}) to a net forcing of 0.31 W m^{-2} (Fig. 4.5b).

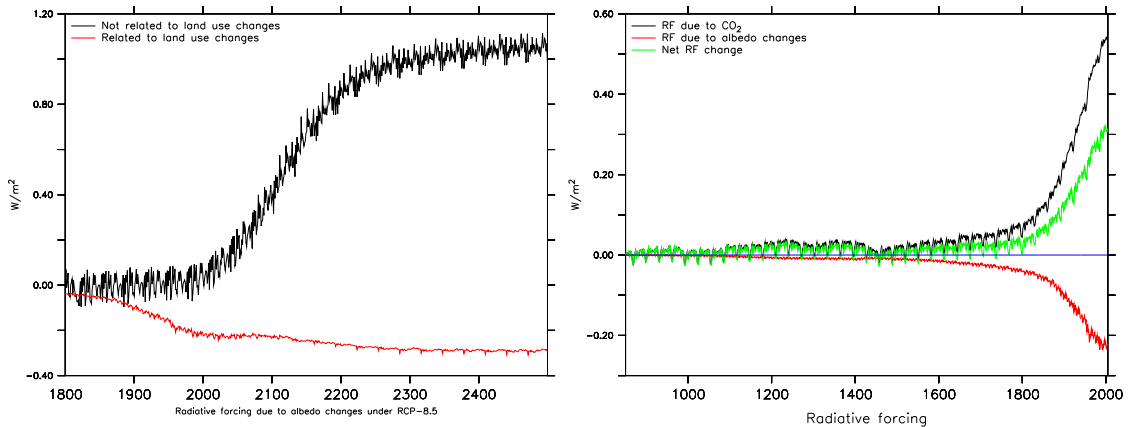


Figure 4.5: (a) Radiative forcing attributed to natural and land-use induced changes in surface albedo in the RCP8.5 scenario simulation. (b) Contribution of changes in atmospheric CO_2 concentrations and surface albedo to the net radiative forcing in a simulation over the last millennium in which only land-use changes and no other forcings were applied.

Equilibrium climate sensitivity of the coupled model

The albedo feedback increases the equilibrium climate sensitivity⁷ of the coupled Bern3D-LPX model by 0.2°C relative to the uncoupled Bern3D model, which has been tuned to a climate sensitivity of 3.0°C (Ritz et al., 2011). In order to re-adjust the climate sensitivity to this value, the feedback parameter of the Bern3D EBM must be reduced from -0.20 W m^{-2} to -0.25 W m^{-2} . For the simulation presented here, the feedback parameter is not adjusted, i.e. the climate sensitivity of the model is 3.2°C . A calibration curve was derived that relates the feedback parameter to the equilibrium climate sensitivity of the coupled Bern3D-LPX model (Table 4.2, Fig. 4.6). It can be used in upcoming studies to specifically modify the climate sensitivity of the model, e.g. to estimate uncertainties in projections.

In the prospect of simulations for which the climate sensitivity of the model might want to be changed, a calibration curve was derived that relates the feedback parameter to the equilibrium climate sensitivity of the coupled Bern3D-LPX model (Table 4.2, Fig. 4.6).

Table 4.2: Values of the Bern3D EBM feedback parameter (λ_{EBM}) corresponding to different climate sensitivities (CS) of the coupled Bern3D-LPX model.

CS (K)	0.5	1.0	2.0	3.0	4.0	5.0	6.0	8.0	10.0
$\lambda_{\text{EBM}} (\text{W m}^{-2})$	-4.01	-1.88	-0.55	-0.25	0.03	0.26	0.33	0.44	0.61

⁷The equilibrium climate sensitivity is the temperature change simulated for a doubling of the preindustrial atmospheric CO_2 concentration after reaching a new steady-state.

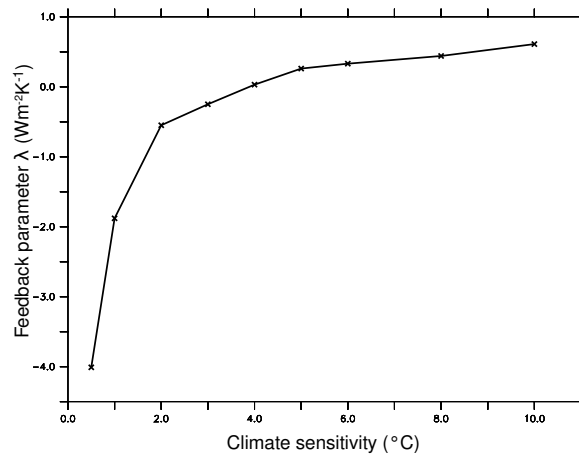


Figure 4.6: Calibration curve for the Bern3D EBM feedback parameter λ to attain different climate sensitivities from 0.5 K to 10 K with the coupled Bern3D-LPX model.

4.4.3 Projected warming, steric sea level rise, and ocean acidification

In this section, future projections of changes in global mean temperatures, steric sea level rise, and ocean acidification under the four RCP scenarios (2005–2100) and their extensions (ECP, 2100–2300) are presented. In these simulations, the prescribed CO_2 concentrations compass a range from 420 to 925 ppm by the year 2100 and stabilize later at 360 to 1960 ppm by 2300 (Fig. 4.7a). Together with other forcings, this leads to a total external radiative forcing of 7.7 W m^{-2} in 2100 with respect to 1800 for RCP8.5 (Fig. 4.7b), which is 9% lower than the specified target for that scenario (van Vuuren et al., 2011). After 2100, the radiative forcing continues to increase up to about 12 W m^{-2} in this scenario, which is a very high value compatible with the high concentration levels assumed in that scenario (Meinshausen et al., 2011). In RCP4.5, the simulated radiative forcing is also lower ($\sim 10\%$) than the target and stabilizes at 4.1 W m^{-2} . The targets for the other two scenarios are well matched; in RCP6 the radiative forcing stabilizes at 5.9 W m^{-2} without overshoot and in RCP3-PD it peaks at 2.9 W m^{-2} around 2050 and declines to 2.5 W m^{-2} by 2100. The RCP targets are specified as “approximate radiative forcing levels”, which are defined as $\pm 5\%$ of the stated levels (van Vuuren et al., 2011). This criterion is only matched by the RCP6 and RCP3-PD simulations.

Simulations with prescribed fossil-fuel CO_2 emissions instead of atmospheric concentrations lead to higher CO_2 and radiative forcing levels (dashed lines in Fig. 4.7). The reason for that is a different carbon cycle response in the Bern3D-LPX model than in the MAGICC6 model, which was used to calculate the concentrations prescribed in the standard RCP simulations (Meinshausen et al., 2011). This is further discussed in section 4.4.4. In the simulations with prescribed emissions, the simulated radiative forcing is generally higher than the RCP targets. The 8.5 W m^{-2} target specified in RCP8.5 by 2100 is well matched (8.7 W m^{-2}) but the radiative forcing in the other scenarios are 6% (RCP4.5) to 20% (RCP6) higher. In the following, only results from the standard simulations with prescribed CO_2 concentrations (as required by the EMIC AR5 protocol) are discussed. The projected warming and sea level rise for the emission-driven simulations are indicated as a reference in Fig. 4.7 and can be viewed to some degree as an indication of uncertainties in the response of the carbon cycle.

Global warming

Global mean surface air temperatures (SAT) are projected to increase by 1.8°C (RCP3-PD), 2.6°C (RCP4.5), 3.2°C (RCP6), and 4.6°C (RCP8.5) by 2100 relative to preindustrial levels

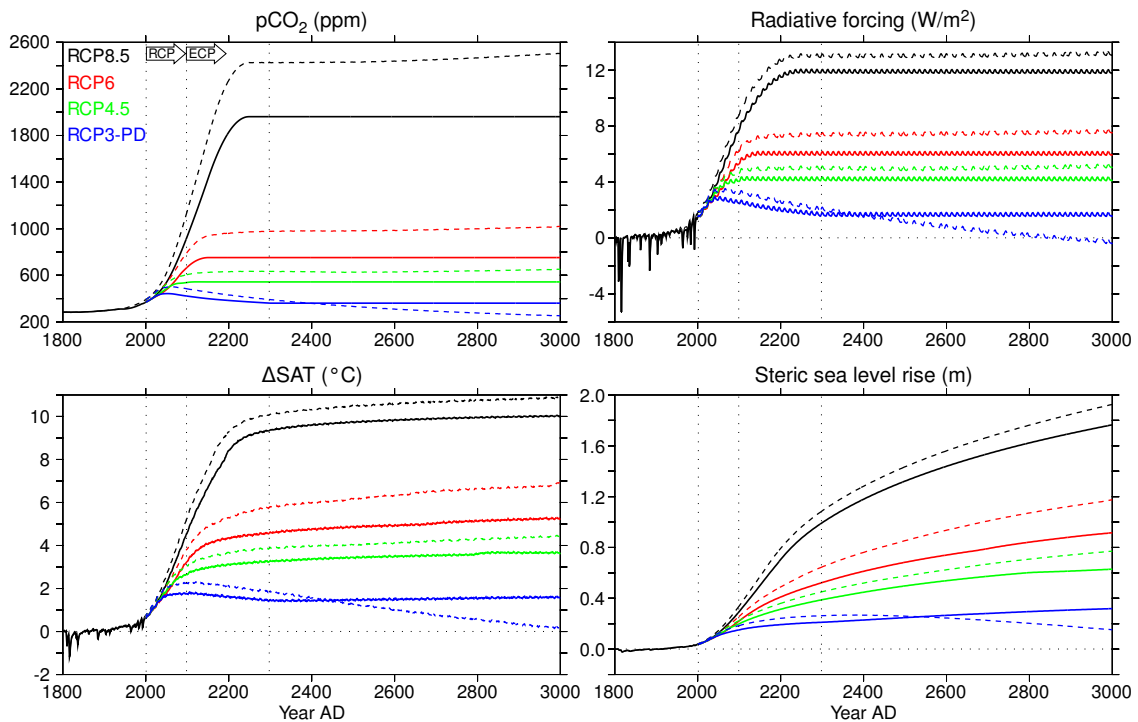


Figure 4.7: Atmospheric CO₂ concentrations, external radiative forcing, changes in global mean surface air temperature (SAT), and steric sea level rise over the historical period and for the four future scenarios RCP8.5 (black), RCP6 (red), RCP4.5 (green), and RCP3-PD (blue). Solid lines indicate results from the standard simulations with prescribed atmospheric CO₂ (shown in the first panel). The dashed lines indicate corresponding simulation results when fossil-fuel CO₂ emissions are prescribed instead and atmospheric CO₂ is allowed to evolve freely.

(Fig. 4.7). After 2100, the temperatures continue to increase in all scenarios except for RCP3-PD, where a decrease in atmospheric CO₂ is assumed. Due to the inertia of the ocean, temperatures continue to rise, even after the external radiative forcing is stabilized. By the year 2300, the projected SAT increases are 1.5, 3.3, 4.6, and 9.4 °C.

The committed warming by 2300 is quantified by extending the simulations under four different assumptions (Sect. 4.3). For the RCP8.5 scenario, the committed warming by the year 3000 ranges from 7.8 °C (cc; preind. CO₂ emissions and other forcings) to 10.4 °C (ec; sustained 2300 CO₂ emissions and other forcings). This relatively small range (compared to the absolute temperature increase) shows that the temperature response during the rest of the millennium and beyond is mostly determined by the high CO₂ emissions before 2300 in this scenario. With lower CO₂ emissions before 2300 in the other scenarios, the relative importance of non-CO₂ forcings and the assumptions for the evolution of CO₂ after 2300 (constant concentrations, constant emissions or preindustrial emissions) increases. In the low RCP3-PD scenario, the committed warming by 3000 is only 0.25 °C in the cc simulation, where all CO₂ emissions and all other forcings are set to preindustrial values by 2300, while it is 1.7 °C when the CO₂ concentration remains constant after 2300.

Steric sea level rise

The heat taken up by the ocean leads to thermal expansion of water masses. This increase in volume causes the sea level to rise. On global average, the projected steric sea level rise by 2100 is 14 cm (RCP3-PD) to 29 cm (RCP-8.5) by 2100 (Fig. 4.7). Due to the slow heat uptake of the deep ocean, the response in sea level rise is strongly delayed. Therefore, the sea level continues to rise for a long time, even after stabilizing the radiative forcing. By 2300,

the projected rise is 20 cm (RCP3-PD), 38 cm (RCP4.5), 52 cm (RCP6), and 99 cm (RCP8.5). Assuming a constant forcing after 2300, the sea level will rise by another 77 cm during the following 700 years in the high RCP8.5 scenario (Fig. 4.7), while the additional committed increase is limited to 39 cm in the cc simulation (not shown). In RCP6 and RCP4.5, the additional rise is 39 cm and 24 cm under constant CO₂ levels (5 cm and -2 cm in cc). Even in the low RCP3-PD scenario, where a stringent climate policy is assumed to strongly limit greenhouse gas emissions in the 21st century, the sea level is projected to rise by another 50% (10 cm) to 30 cm during 700 years after 2300 when assuming constant forcings. In contrast, the sea level immediately starts to decrease again and reaches 11 cm by 3000, when CO₂ emissions and other forcings are instantaneously set to preindustrial values in 2300 resulting in an abrupt reduction of the radiative forcing by about 50% (1 W m^{-2}) in the cc simulation.

Ocean acidification

A significant amount of the CO₂ emitted to the atmosphere is taken up by the ocean, which leads to ocean acidification (see section 1.4.2 and chapter 2 for an introduction and definition of terms). The simulated global mean surface aragonite saturation state (Ω_{arag}) decreases by about 0.4 from 3.2 to 2.8 during the historical period (1820-2000; Fig. 4.8a). The global mean surface pH decreases from 8.16 to 8.08 (Fig. 4.8b). These decreases are essentially the same as simulated with the NCAR CSM1.4 model (Chapter 2) but the absolute values of global mean surface Ω_{arag} are somewhat lower (0.2) in the simulation with the Bern3D-LPX model. This is mostly due to lower values in the Tropics and in the Arctic Ocean (Fig. 4.8c). In the Tropics, the Bern3D-LPX model is clearly biased low, while the NCAR CSM1.4 matches the observation based estimates quite well. At high latitudes both models tend to simulate lower surface Ω_{arag} than estimated from observations. Observations in the Arctic Ocean, however, are relatively scarce.

The projected decrease in global mean surface Ω_{arag} over the 21st century is -1.22, -0.83, -0.55 for the RCP8.5, RCP6, and RCP4.5 scenarios. In the RCP3-PD scenario, it decreases by about -0.28 in the first half of the century and then starts to increase slowly in response to the decreasing atmospheric CO₂ in the second half of the century (Fig. 4.8a). Surface pH shows a similar response and values of 7.73, 7.86, 7.93, and 8.02 are projected by 2100 for the RCP8.5, RCP6, RCP4.5, and RCP3-PD scenarios, respectively (Fig. 4.8b).

The response in surface Ω_{arag} in the RCP8.5 scenario is very similar to the response in SRES-A2 simulated with the NCAR CSM1.4 model (Ω_{arag} decrease of -1.20), while the decrease in pH is more pronounced in RCP8.5 with the Bern3D model. It has to be noted, however, that atmospheric CO₂ is about 10% higher in RCP8.5 (927 ppm) than in SRES-A2 (844 ppm) by 2100. The RCP4.5 scenario is comparable to the SRES-B1 simulation with NCAR CSM1.4 in terms of atmospheric CO₂ by 2100 (only 1 ppm difference) as well as in the pH decrease, but the simulated decrease in global mean surface Ω_{arag} is larger in SRES-B1 (-0.63; Fig. 4.8a). The projected surface Ω_{arag} by 2100 of 2.3, 2.0, and 1.6 for RCP4.5, RCP6, and RCP8.5 are at the lower end of the uncertainty ranges found with the Bern2.5CC model for different assumptions of carbon cycle parameters and climate sensitivity (cf. Fig. 14.2 in Chapter 5). In RCP3-PD, the projected value of 2.6 is lower than the uncertainty range obtained with Bern2.5CC (2.8–3.2). However, the values are compatible when correcting for the low bias in Bern3D-LPX of ~ 0.2 for present-day Ω_{arag} . After 2100, surface Ω_{arag} stabilizes relatively soon at about 1.9 and 2.3 in the RCP4.5 and RCP6 scenarios, respectively, as a result of stabilizing atmospheric CO₂ levels. In RCP3-PD, Ω_{arag} continues to increase to 2.9 by 2300, while in the high-emission scenario RCP8.5 it decreases to 1.0, which means that large parts of the global surface ocean would become undersaturated with respect to aragonite by 2300.

The Arctic Ocean was found to be very sensitive to ocean acidification and to show a more complex response to increasing CO₂ and climate change as most other regions in simulations

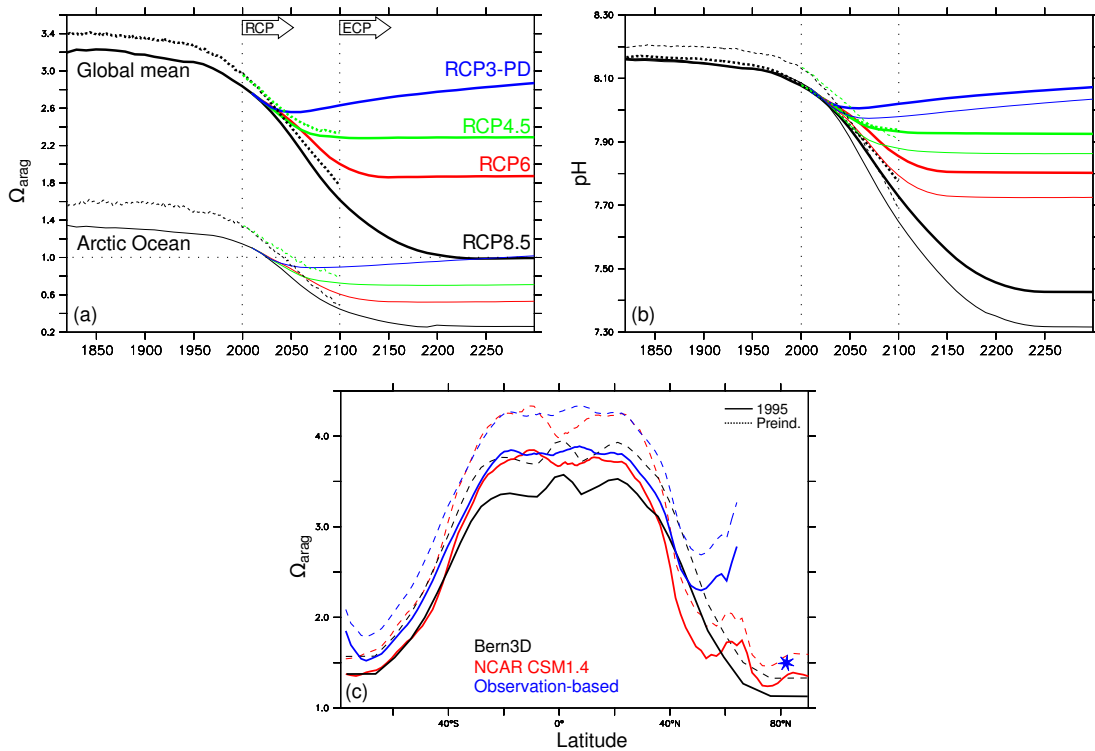


Figure 4.8: Simulated (a) surface Ω_{arag} and (b) pH, globally averaged (bold lines) and in the Arctic Ocean (thin lines). Solid lines are results from Bern3D-LPX under the RCP3-PD (blue), RCP4.5 (green), RCP6 (red), and RCP3-PD (black) scenarios and their extensions to 2300; dashed lines indicate results from NCAR CSM1.4-carbon under the SRES A2 (black) and B1 (green) scenarios (cf. Chapter 2). (c) Zonally averaged surface Ω_{arag} simulated with Bern3D-LPX (black) and NCAR CSM1.4-carbon (red) under preindustrial (dashed) and 1995 (solid) conditions. Blue lines indicate annual mean estimates based on observational data from WOA01 (Conkright et al., 2002) and GLODAP (Key et al., 2004). The blue star indicates an estimate for surface Ω_{arag} in the Arctic based on data from three cruises during summer (cf. Chapter 2).

with the NCAR CSM1.4-model (Chapter 2; Frölicher & Joos, 2010). In the RCP8.5 and RCP4.5 simulations with the Bern3D-LPX model, the decreases in Ω_{arag} , and particularly in pH, projected for the Arctic Ocean are less pronounced (Fig. 4.8a,b) and the response in the Arctic is similar to the global average. This, however, is likely related to the simpler representation of processes (e.g. sea ice dynamics or the hydrological cycle) and to the very coarse resolution at high latitudes (only 1.5 boxes in latitude in the Arctic) in the Bern3D model. It illustrates the limitations of a model of intermediate complexity.

In contrast to the surface ocean, where Ω_{arag} follows closely the evolution of atmospheric CO_2 , the pattern and timing at depth is more complex as it depends on the transport of anthropogenic carbon from the surface to the deep ocean. The simulated saturation horizon by the year 2000 is somewhat too deep in the Atlantic (Fig. 4.9), when compared to observation-based estimates (Fig. 4 in Chapter 2). In the Pacific, the decreasing depth of the saturation horizon towards the north is represented well (not shown), particularly in comparison with the results from the NCAR CSM1.4 model, which lacks this feature in the North Pacific (Chapter 2). By 2100, the saturation horizon is projected to rise significantly in the Southern Atlantic in all four RCP scenarios (Fig. 4.9). It reaches the surface in RCP4.5, RCP6, and RCP8.5 at about 65°S, 55°S, and 48°S, respectively. In RCP3-PD the South Atlantic remains slightly oversaturated by 2100. Interestingly, the depth of the saturation horizon between 40°S and 40°N by 2100 depends only relatively weakly on the scenario. It remains at 2500-3000 m, while the 'bubble' of undersaturated waters at about 500 m depth

increases by a slightly different degree in the four scenarios.

In the North Atlantic and Arctic Ocean, the differences between the scenarios are again more pronounced. Undersaturation of the Arctic surface ocean by 2100 is projected in all scenarios, with increasing severity. In the RCP3-PD scenario, however, most of the subsurface waters to a depth of 2500 m remains supersaturated. With higher atmospheric CO₂ levels in the other scenarios, more of these waters become undersaturated and in RCP8.5, large parts of the North Atlantic are undersaturated from surface to depth (Fig. 4.9). From 2100 to 2300, anthropogenic CO₂ continues to invade the ocean, even if atmospheric CO₂ is stabilized (RCP4.5 and RCP6) or decreased (RCP3-PD). Consequently, the total amount of carbon released to the atmosphere becomes more relevant by 2300 than by 2100 as can be seen by the differences between scenarios in the projected aragonite saturation state by 2300 (Fig. 4.9).

4.4.4 Carbon cycle changes in the RCP scenarios

In this section, the simulated response of the carbon cycle in the RCP scenarios is discussed. Figure 4.10 shows the simulated changes in the different carbon reservoirs over the industrial period and for the four RCP scenarios. They represent all changes in the closed carbon cycle system, i.e. all changes add up to zero at any time. In the standard simulations shown here, the atmospheric carbon content (cyan) is prescribed and the ocean (blue), sediment (red), and land (green) carbon stock changes are simulated by the model. The change in terrestrial carbon also includes fluxes related to anthropogenic land use. The budget is then closed by the change in fossil fuel reserves or other carbon storage (black). The flux causing the changes in this reservoir is termed 'implied fossil-fuel emissions', but it can also include fluxes from other sources or sinks not simulated by the model. Particularly, it includes also the removal of carbon from the simulated atmosphere-land-ocean-sediment system, e.g. by removing CO₂ from the atmosphere by carbon capture and storage techniques. This is required for example in the RCP3-PD scenario after 2050 to attain the prescribed atmospheric CO₂ levels (Fig. 4.10). The ocean acts as a carbon sink and by 2300 has taken up 25% (RCP8.5), 45% (RCP6), 50% (RCP4.5), and 70% (RCP3-PD) of the carbon released from land and fossil fuels. The response of the land carbon pools is more complex due to the interaction of land use and natural vegetation and the release of carbon from soils. Generally, the land (including land-use change) acts as a net source in all scenarios. The changes in carbon stored in sediments (ocean sediment compartment plus net changes from burial and weathering fluxes) are very small compared to other changes and on minor importance on these timescales (Fig. 4.10). In the following, implied CO₂ emissions and changes in terrestrial carbon stocks are discussed in more detail.

CO₂ emissions

The RCP scenarios are defined by radiative forcing targets and therefore the primary forcing mechanism for climate models are the atmospheric greenhouse gas concentrations and not the emissions (Hibbard et al., 2007; van Vuuren et al., 2011, Chapter 1). The approach for coupled carbon cycle-climate models is to calculate the corresponding fossil-fuel CO₂ emissions compatible with the concentration scenario. These emissions can then be compared to other carbon cycle-climate models and to emissions from IAMs⁸ for different socio-economic scenarios and mitigation strategies (Moss et al., 2010). The RCP greenhouse gas concentrations used to force the models have been calculated with the MAGICC6 model based on the emissions calculated by the IAMs for the selected pathways (Meinshausen et al., 2011). By comparing the implied emissions of a model with these emissions, the carbon cycle dynamics

⁸Integrated Assessment Models

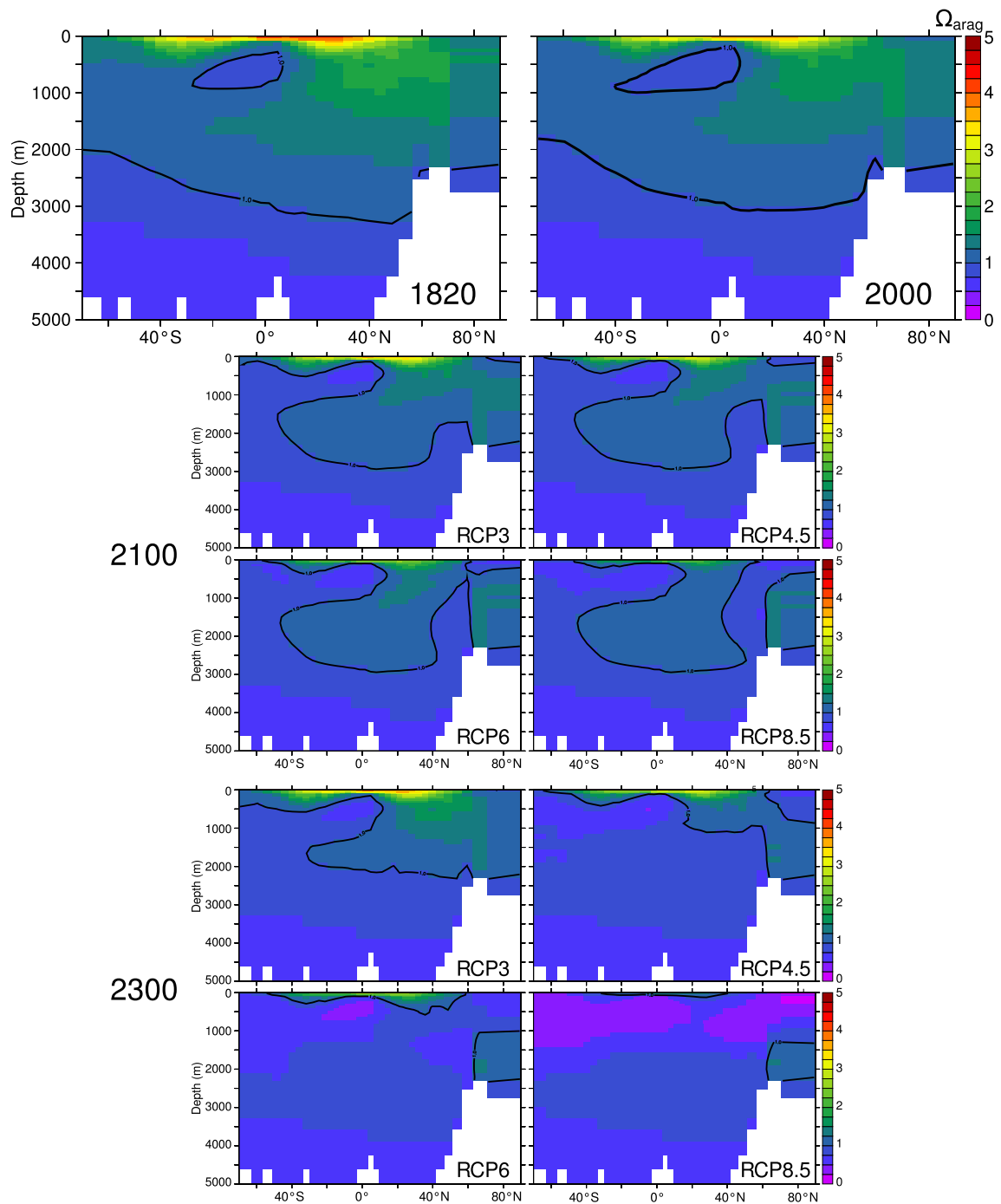


Figure 4.9: Zonally averaged Ω_{arag} in the Atlantic and Arctic Ocean by 1820, 2000, 2100, and 2300 simulated with Bern3D-LPX under the extended RCP3-PD, RCP4.5, RCP6, and RCP8.5 scenarios. The black line indicates the saturation horizon (where $\Omega_{\text{arag}} = 1$).

and feedbacks of that model are implicitly compared with those of the MAGICC model. In the same way, implied historical emissions by prescribing historical CO_2 concentrations can be compared with the reconstructed emissions.

Over the historical period (1800 to 2005), the implied cumulative fossil-fuel (FF) emissions simulated with the Bern3D-LPX model are 77 GtC lower than the reconstructed emissions (Fig. 4.11a). Consequently, in a simulation with specified historical FF emissions and free atmospheric CO_2 (histC-TOT), the simulated CO_2 concentrations are higher than observed

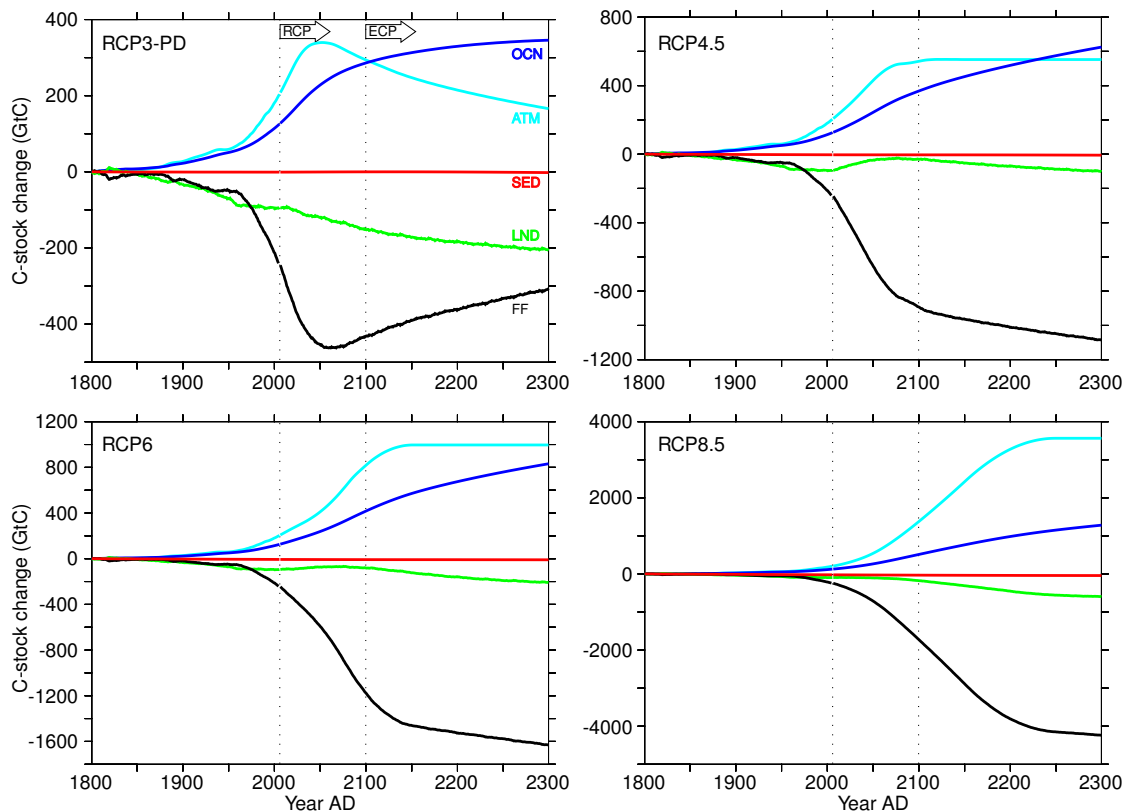


Figure 4.10: Changes in the carbon content of atmosphere (cyan), ocean (blue), sediments (red; ocean sediment compartment plus net changes from burial and weathering fluxes), terrestrial vegetation and soils (green), and fossil fuel reserves or other carbon storage (black) simulated with the Bern3D-LPX model under the four extended RCP scenarios. Please note the different scale of the vertical axes in the panels.

(24 ppm by 2005, Fig. 4.11e). The concentrations match the historical record closely from 1800 to 1940. Around 1940 the observed CO_2 remains almost constant for about a decade, while in histC.TOT pCO_2 continues to rise during that period. This issue was also found in an earlier study with the BernCC-LPJ model (Fig. 3 in Strassmann et al., 2008). Accordingly, the implied FF CO_2 emissions are lower during that period than the reconstructed emissions when prescribing CO_2 (Fig. 4.11c). From 1950 to 2005 the discrepancy is somewhat smaller but the implied emissions are still lower as reconstructed, and CO_2 levels rise faster than in the simulation with prescribed emissions (histC.TOT). This suggests that the simulated CO_2 uptake by ocean and land is too weak and/or the emissions from land-use change are too high during the historical period. Uncertainties in the reconstructed emissions (0.3 GtC/yr; Canadell et al., 2007) can potentially explain about 25% of the difference between 1940 and 2005. The ocean uptake of 1.5 GtC/yr for the period 1959 to 2005 is at the lower end of the range of 1.9 ± 0.4 GtC/yr estimated by Canadell et al. (2007). Given this uncertainty range, the relatively weak oceanic sink can potentially explain up to 68% of the deviation from reconstructed emissions between 1940 and 2005. Accordingly, 7% to 100% of the difference can be attributed to a too low net uptake by the land (including land use), which is only weakly constrained by observations. In the future projections, the simulated implied FF emissions remain for the most part smaller than specified in the scenarios (Fig. 4.11c). The simulated cumulative FF emissions (2000 to 2300) are 19% (RCP4.5) to 44% (RCP3-PD) smaller. Consequently, atmospheric CO_2 concentrations are higher in simulations where FF CO_2 emissions are prescribed (Fig. 4.7).

Similar to the FF CO_2 emissions, the simulated land-use fluxes can be compared to the

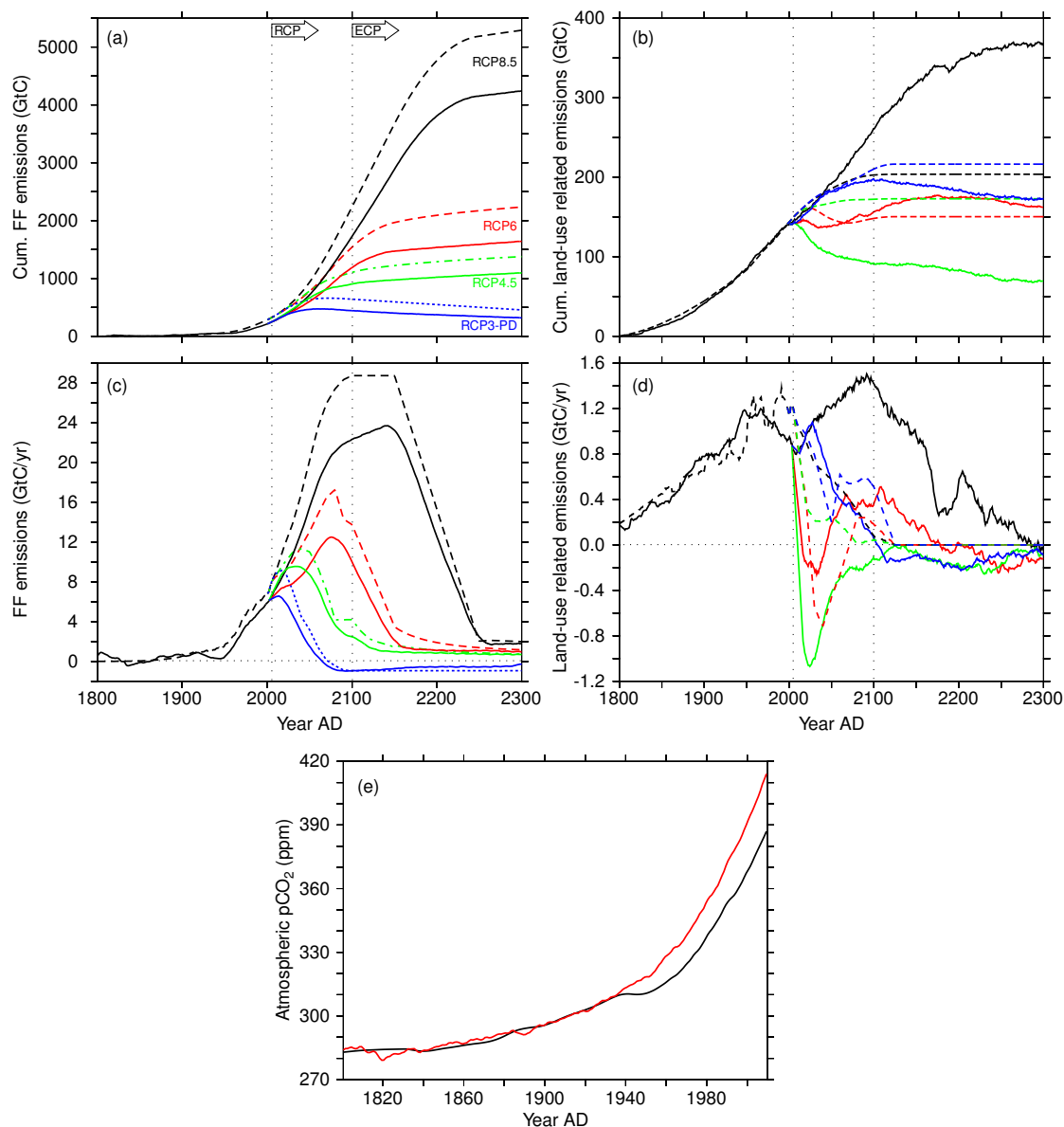


Figure 4.11: (a) Diagnosed cumulative fossil-fuel CO_2 emissions from simulations with the Bern3D-LPX model with prescribed CO_2 concentrations from the four extended RCP scenarios (solid lines). Dashed lines indicate reconstructed historical emissions (1800-2005) and the emissions corresponding to the four RCP scenarios (which have been used to calculate the prescribed CO_2 concentrations). (b) Diagnosed cumulative net CO_2 emissions related to land-use change including all feedbacks and indirect effects (estimated from the difference of simulations with and without land-use changes and prescribed atmospheric CO_2). Dashed lines indicate land-use emissions assumed for the RCPs. (c,d) Same as (a) and (b) but for annual emissions. The diagnosed emissions from Bern3D-LPX (solid lines) have been smoothed (31-year running mean). (e) Reconstructed historic atmospheric CO_2 concentrations (1800-2005) prescribed in the standard simulations (black) and diagnosed in a simulation with prescribed CO_2 emissions (red).

land-use emissions provided by the RCP scenario community. Land use fluxes consist of the direct carbon release from land-use change ('book-keeping' fluxes) and indirect fluxes due to a fertilization feedback and 'lost sinks', because converted areas are less efficient as a CO_2 -fertilized carbon sink (Strassmann et al., 2008). The net land-use flux, including all feedbacks and indirect effects, is estimated from simulations with and without land-use change, while keeping all other forcings identical. Over the historical period, the simulated net land-use flux is largely compatible with the harmonized emissions from the RCP database (Fig. 4.11d). In

the future projections, however, this picture changes. In the RCP8.5 scenario, the simulated net land-use flux continues to increase, while the RCP land-use emissions decrease almost to zero by 2100. The additional land-use fluxes can probably be attributed mostly to lost sinks (Strassmann et al., 2008). As a result, the simulated cumulative net land-use flux is about 165 GtC larger than assumed in the RCP8.5 scenario. In contrast, the simulated cumulative net flux is about 100 GtC lower by 2300 for the RCP4.5 than specified (Fig. 4.11b). This can be explained by the fact that in this scenario the land-use area is reduced shortly after 2005 (Fig. 4.12d). The conversion of land-use areas back to natural vegetation and the effect of ‘gained sinks’ leads to a negative net land-use flux in this simulation, which is not present in the specified land-use emissions for RCP4.5.

An important caveat has to be mentioned here: Unfortunately, an error was found in the LPX model implementation at the time of writing this chapter. Due to this error, water limitation was not in effect when simulating vegetation growth on land-use areas, probably resulting in too low land-use emissions. The simulations will be redone with a corrected model version but this was not possible within the time frame of this thesis.

Changes in terrestrial carbon stocks

Over the historical period, a reduction in vegetation carbon of about 120 GtC is simulated, while soil and litter carbon stocks gain about 25 GtC (Fig. 4.12a). The loss in vegetation carbon is due to land-use change. The integrated net ecosystem production (NEP) is positive over that period but this increase is superimposed by a larger removal of vegetation by land use (Fig. 4.12b), which makes the land to a net source of carbon. In a simulation without land-use change, all land carbon pools increase (Fig. 4.12c) and the land acts as a carbon sink during the historical period.

The projected changes in vegetation carbon in the four RCP scenarios can be divided in two groups with respect to the prescribed change in land-use area. In the RCP4.5 and RCP6 scenarios the land-use area decreases after the year 2005, whereas in the RCP8.5 and RCP3-PD it continues to increase (Fig. 4.12d). In the first group (RCP4.5 and RCP6), the vegetation carbon stocks start to increase again and most of the vegetation carbon lost during the historical period is regained by 2100 (Fig. 4.12a). From 2100 to 2300, where the land-use area is kept constant, the increase in vegetation carbon continues and by 2300 25 to 40 GtC more carbon is stored in vegetation than at preindustrial times in these scenarios. The vegetation carbon increase is driven by fertilization due to higher atmospheric CO₂ levels, climate change, and by the conversion of used land area back to natural vegetation, which acts as a more efficient CO₂ sink. The latter seems to play an important role, as can be seen in the significantly higher productivity independent of lower or higher atmospheric CO₂ levels and temperatures than in the RCP8.5 and RCP3-PD scenarios, where the land-use area continues to increase in the 21st century (Fig. 4.12b). In contrast to the first group, the RCP8.5 and RCP3-PD scenarios show almost no change in vegetation carbon during the 21st century (Fig. 4.12a). This means, that in both scenarios the carbon lost from increased land use is compensated by increased productivity due to CO₂ fertilization and climate change. The CO₂ levels, however, are very different in the two scenarios, while an about equal amount of carbon is lost directly because of land-use change (Fig. 4.12c). This can only be explained with the effect of lost sinks, which scales with the CO₂ level (Strassmann et al., 2008). In the RCP3-PD scenario, the land-use emissions are only slightly amplified by feedbacks and lost sinks so that a relatively small CO₂ fertilization effect is required to compensate the net land-use flux. In the RCP8.5, on the other hand, both the CO₂-fertilized productivity and the effect of lost sinks is high due to higher CO₂, which leads to a net compensation as in the low RCP3-PD scenario. From 2100 to 2300, the vegetation carbon decreases slightly in RCP3-PD owing to constant land use and a small reduction in CO₂ levels, whereas it

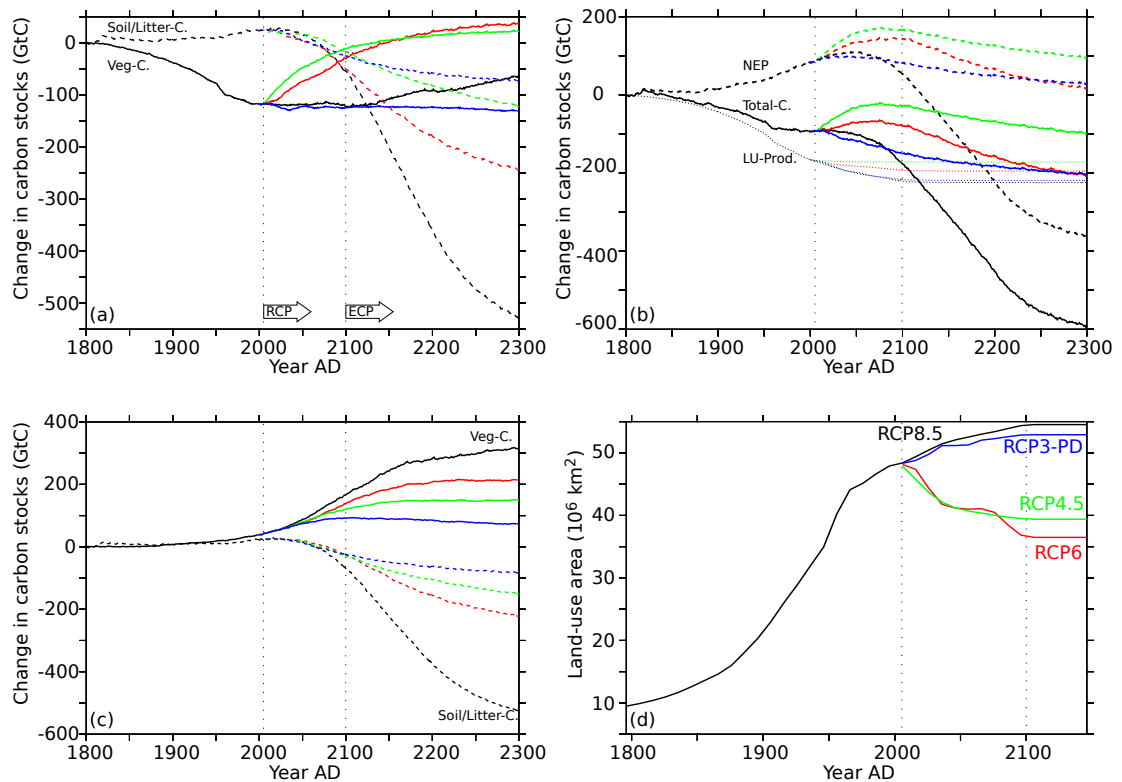


Figure 4.12: (a) Changes in terrestrial carbon stocks simulated with Bern3D-LPX under the extended RCP8.5 (black), RCP6 (red), RCP4.5 (green), and RCP3-PD (blue) scenarios. Solid lines indicate vegetation carbon (including land-use changes), dashed lines indicate the carbon content of soils and litter. (b) Changes in carbon stocks from changes in the net ecosystem production (NEP, i.e. net changes in productivity and heterotrophic respiration; dashed lines) and direct land-use changes (product pools; dotted lines). Both, NEP and direct land-use changes as well as vegetation and soil/litter carbon in (a) add up to the total change in terrestrial carbon stocks (solid lines). (c) Same as (a) but for a simulation without land-use change. (d) Land-use area changes in the four RCP scenarios prescribed in the standard simulations (constant after 2100).

increases in RCP8.5 due to the continued increase in CO_2 that stimulates productivity. In simulations without land-use change, vegetation carbon stocks increase in all scenarios (Fig. 4.12c). The increase scales approximately with the CO_2 level, with saturation at very high levels in the RCP8.5 scenario, and reaches 75 GtC (RCP3-PD) to 310 GtC (RCP8.5) by 2300. This illustrates the importance of land-use changes in terms of direct but also indirect fluxes.

After the increase over the historic period, the amount of carbon stored in soils and litter starts to decrease in the first half of the 21st century in all scenarios (Fig. 4.12a). By 2100, soil and litter carbon stocks are projected to be about 20 GtC (RCP4.5) to 50 GtC (RCP8.5) smaller than at preindustrial times and thereby contributing to the atmospheric CO_2 increase. However, this potential contribution of 9–24 ppm (neglecting feedbacks and ocean uptake) is small compared to the total increase in atmospheric CO_2 of 140–645 ppm by 2100. In the long term, the decrease in soil and litter carbon is approximately proportional to the temperature increase. The strong temperature increase in the RCP8.5 scenario leads to a large soil carbon release of about 500 GtC by 2300 (Fig. 4.12a), which dominates the total change in land carbon (Fig. 4.12b). The decrease of 250 GtC in RCP6 is also relatively large, while the decreases in RCP3-PD and RCP4.5 are of the same order of magnitude as the changes in vegetation carbon. To relate this losses of carbon from soils to the atmosphere they are compared to the corresponding cumulative fossil-fuel CO_2 emissions in the scenarios (Table 4.3). The amount of carbon lost from soils (2000–2300) correspond to 12–14% of the

FF emissions in the RCP4.5, RCP6, and RCP8.5 scenarios, and to 78% in the RCP3-PD scenarios, where negative FF emissions are assumed after 2050. Land use changes have some effect on changes in soil and litter carbon. During the 21st century, land-use change tends to enhance the loss of carbon from soil and litter pools, particularly in the RCP6 simulation. From 2100 to 2300, where land-use areas are kept constant, the decrease in soil and litter carbon is slower in the RCP3-PD and RCP4.5 simulations when applying land-use changes than in simulations without land use. In the RCP6 scenario, however, the decrease is still faster with land use like in the 21st century. In the RCP8.5 scenario land use has only a very limited effect on the large change in soil carbon (Fig. 4.12a,c).

The large amount of carbon released in the RCP8.5 scenario by 2300 (~ 500 GtC, which is about a third of the initial stock) stems mostly from mineral soils at high northern latitudes (Fig. 4.13, Table 4.3). The contribution of carbon released from northern peatlands is relatively small (~ 30 GtC). Mineral soils store up to 60 kg m^{-2} carbon in a cold climate which can be released when temperatures rise, soils thaw, and respiration is enhanced. By 2300, most of this carbon is projected to be lost and the high soil carbon contents have mostly decreased to $5\text{-}15 \text{ kg m}^{-2}$, which corresponds to values also found in many temperate and tropical regions (Fig. 4.13). The amount of carbon released depends largely on the initial stock. In a simulation without sublayer hydrology (i.e. soils are not able to freeze), the simulated present-day soil carbon content is about 30% lower (~ 1100 GtC) than in the standard simulation. Consequently, the amount of carbon released is also smaller. This demonstrates the importance of a realistic representation of the carbon storage in soils with respect to both, the amount of carbon stored and the mechanisms related to the carbon release (e.g. thawing of permafrost soils). This is particularly true for the high emission scenarios and on longer time scales.

4.4.5 Temperature stabilization

Four temperature stabilization simulations are performed to quantify the allowable CO_2 emissions compatible with temperature targets of 1.5, 2.0, 3.0, and 4.0 °C above preindustrial global mean temperatures. Following (Zickfeld et al., 2009) CO_2 emissions are adjusted by a temperature tracking method (described in Appendix B.4) to follow the prescribed temperature profiles (Fig. 4.14a). The temperature profiles are generated using a cubic spline interpolation that matches the slope of the temperature at the end of the historical simulation.

To stabilize global mean surface temperatures at 1.5 °C above preindustrial, atmospheric CO_2 has to be stabilized shortly after 2020 at about 415 ppm (Fig. 4.14b). Accordingly, CO_2 emissions must be sharply reduced to less than 1 GtC/yr in the first half of the 21st century (Fig. 4.14c). The corresponding allowable cumulative emissions (2005-2300) are 390 GtC (Fig. 4.14d). Higher CO_2 levels of 460 ppm, 600 ppm, and 770 ppm by 2300 lead to a stabilization at the higher temperature targets. In those cases, CO_2 emission reductions

Table 4.3: Simulated changes (GtC; 2000 to 2300) in the amount of carbon stored in northern peatlands (Peat), natural mineral soils (Nat.), and soils of used land (LU). The total change is related to the cumulative fossil-fuel emissions ($\%E_{FF}$) of the same period.

<i>Scenario</i>	<i>Peat</i>	<i>Nat.</i>	<i>LU</i>	<i>Total</i>	$\%E_{FF}$
RCP3-PD	+3	-82	-4	-83	78%
RCP4.5	-1	-43	-77	-121	14%
RCP6	-6	-110	-108	-224	16%
RCP8.5	-34	-384	-71	-483	12%

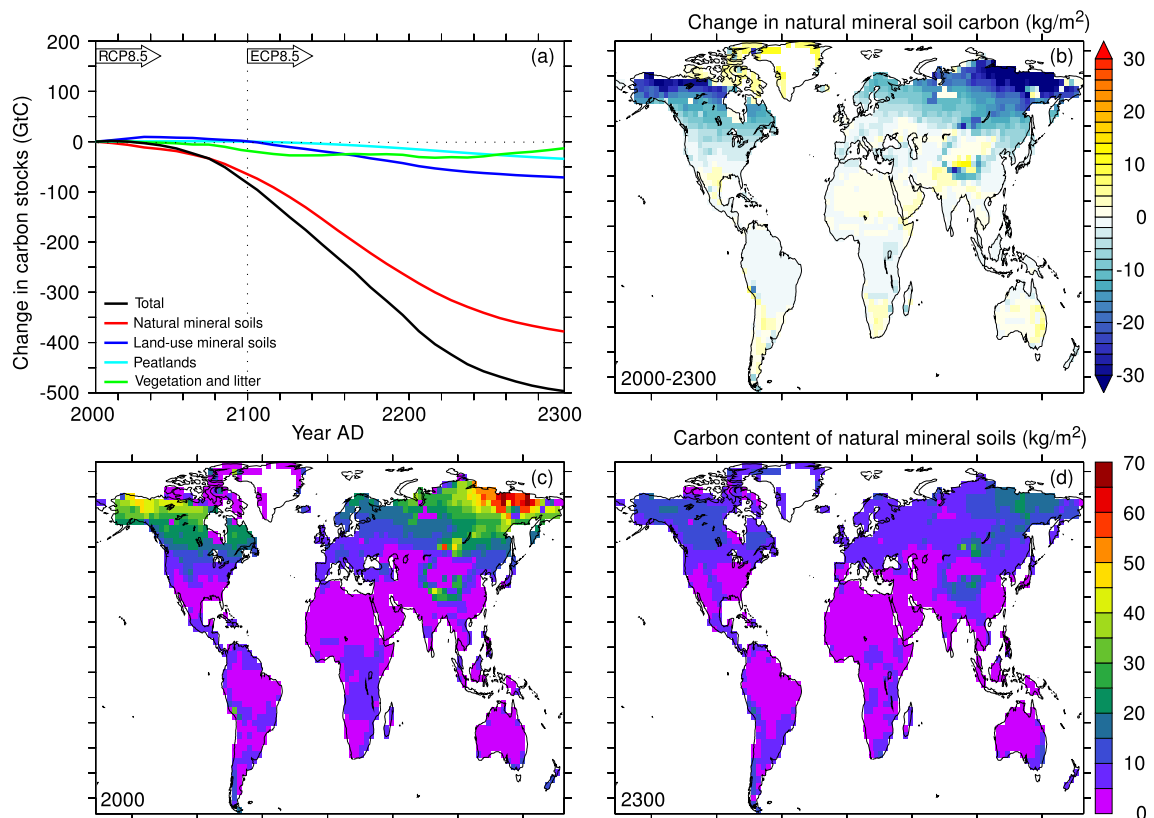


Figure 4.13: Changes in terrestrial carbon stocks from 2000 to 2300 simulated with Bern3D-LPX under the extended RCP8.5 scenario. (a) Global changes in total land carbon (black), carbon stored in natural mineral soils (red), in soils of land-use areas (blue), in northern peatlands (cyan), and in vegetation/litter (green). Maps of changes (b) in the carbon content of natural mineral soils from 2000 (c) to 2300 (d)

are allowed to occur later and at a slower rate. For the high 4°C target, emissions of about 10 GtC/yr during a large part of the 21st century are compatible with the target but must be reduced at a relatively fast rate in the following century. The allowable cumulative emissions by 2300 for the 2, 3, and 4°C targets are 580 GtC , 1030 GtC , and 1520 GtC , respectively (Fig. 4.14d).

In these simulations, the land-use area is kept constant after 2005. Therefore, the diagnosed allowable emissions also include potential emissions after 2005 related to land-use change. This is different than in the RCP simulations where land-use changes occur in the 21st century and the associated emissions are not included in the diagnosed implied fossil-fuel emissions. Further, the radiative forcing from other greenhouse gases and aerosols is reduced to zero by 2300 in the temperature stabilization simulations. Thus, any radiative forcing from these agents is also implicitly included in the CO_2 forcing and the allowable CO_2 emissions diagnosed here should be viewed as total CO_2 -equivalent emissions.

Zickfeld et al. (2009) reported a median estimate of allowable emissions of 590 GtC for the 2° temperature stabilization target, which is only slightly higher than found here. They have quantified the cumulative emissions for the 2, 3, and 4°C targets with the University of Victoria Earth System Climate Model (UVic ESCM) for different assumptions of climate sensitivity and the strength of the climate-carbon cycle feedback. The results presented here are largely compatible with their simulations where a climate sensitivity of 4°C with a medium feedback or a climate sensitivity of 3.6°C with a strong feedback was assumed. 3.6°C is the standard climate sensitivity of the UVic ESCM, which is slightly higher than the

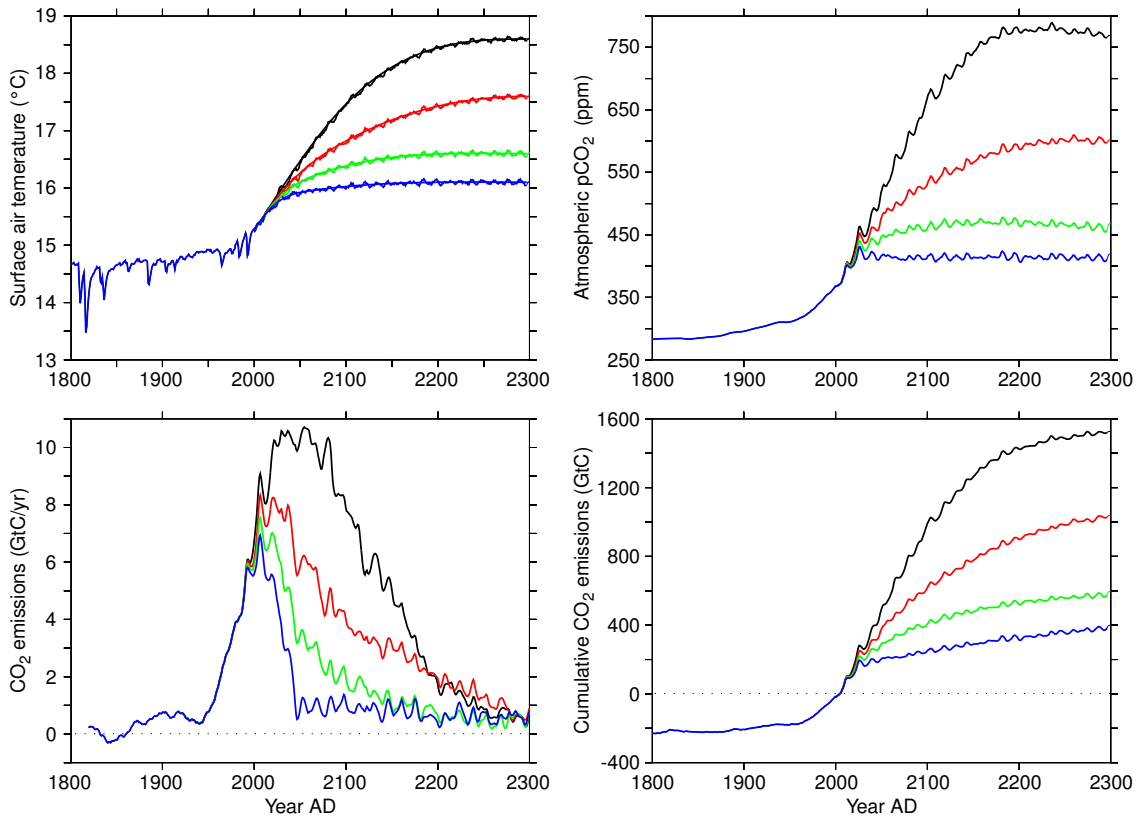


Figure 4.14: Global mean surface air temperatures, atmospheric CO_2 , and CO_2 emissions simulated over the historical period and for four temperature stabilization profiles from 2000 to 2300. The prescribed temperature profiles which stabilize at 1.5, 2.0, 3.0, and 4.0 °C above preindustrial temperatures are also shown in the first panel (smooth lines). The temperature tracking method leads to large fluctuations in annual CO_2 emissions, which have been smoothed out with a 40-year running mean filter. The other panels show annual mean values.

sensitivity of the Bern3D-LPX model used here (3.2°C).

4.5 Summary & Conclusions

The Bern3D-LPX model has been applied to perform a large set of coupled climate-carbon cycle simulations over the last millennium and into the future under different scenarios. It is the first application of this model with a fully coupled carbon cycle. Also, a new land surface albedo has been implemented and verified with present-day observations. A radiative forcing of -0.25 W m^{-2} from land-use induced surface albedo changes is simulated for the year 2005. This negative forcing counteracts the positive radiative forcing caused by CO_2 emissions from land-use changes and the resulting net forcing is about 40% smaller when including both effects. With increasing temperatures in future scenarios, the average snow cover is reduced and the climate-albedo feedback becomes relevant. In the high baseline scenario RCP8.5, albedo changes from natural vegetation areas contribute about 8% ($+1.1 \text{ W m}^{-2}$) to the total radiative forcing by 2300. This forcing is offset by -0.4 W m^{-2} from land-use induced albedo changes. The surface albedo feedback increases the climate sensitivity of the model by 0.2°C.

Future temperatures, steric sea level rise, and ocean acidification are projected for the four RCP scenarios and their extensions. Projected changes in the global mean temperature by 2100 range from 1.8°C in the low mitigation scenario (RCP3-PD) to 4.6°C in the high

baseline scenario (RCP8.5). By 2300, a warming of 1.5 °C to 9.4 °C is projected. Changes in sea level due to thermal expansion are delayed with respect to the surface warming because of the large heat capacity of the ocean. The projected sea level rise is 14 cm to 29 cm by 2100 and 20 cm to 99 cm by 2300 for the four scenarios. Committed changes by 2300 are quantified by extending the simulations to the year 3000 under different assumptions. Further, simulated carbonate saturation (Ω_{arag}) and pH in the ocean are compared with observation-based estimates as well as with the results from the NCAR CSM1.4 and Bern2.5CC models presented in chapters 2 and 5. Generally, the simulated changes are similar to those found with the NCAR CSM1.4 and Bern2.5CC models, but absolute values of the surface aragonite saturation state in Bern3D-LPX are somewhat too low. Projected global mean surface Ω_{arag} range from 1.6 to 2.6 by 2100. Undersaturation of surface waters is projected in all scenarios for the Arctic Ocean and in all scenarios except RCP3-PD for the Southern Ocean. By 2300, the projected global mean Ω_{arag} range from 2.9 in RCP-3PD to 1.0 in the RCP8.5 scenario, which means a widespread undersaturation of the global oceans in the high baseline scenario.

Implied fossil fuel (FF) CO₂ emissions diagnosed in the standard simulations with prescribed atmospheric CO₂ are lower than reconstructed for the historical period (after 1940) and also lower than the emissions assumed in the four RCP scenarios, which have been used to calculate the prescribed concentrations with the MAGICC6 model. Consequently, simulated CO₂ concentrations are higher in the emission-driven simulations. This implies relatively weak terrestrial and oceanic carbon sinks and/or large land-use CO₂ emissions simulated by the Bern3D-LPX model. The simulated ocean uptake is at the lower end of observation-based estimates and therefore likely to cause some of the differences. Land use related CO₂ emissions (including feedbacks and indirect effects) are largely compatible with reconstructed emissions over the historical period. In the future scenarios, simulated CO₂ emissions that can be attributed to land-use changes differ from the emissions assumed in the RCP scenarios. This is most likely due to the effect of lost sinks (Strassmann et al., 2008) and may contribute to the differences in implied future FF CO₂ emissions. With rising global temperatures, a significant amount of carbon is lost from soils in the long-term. The losses from 2000–2300 amount to 12–16% of the corresponding FF CO₂ emissions in the same period for the RCP4.5, RCP6, and RCP8.5 scenarios, and to 78% in the RCP3-PD low mitigation scenario. The different responses of the carbon cycle in the MAGICC6 and Bern3D-LPX models under future scenarios is likely a combination of the different effects mentioned above. In the high RCP8.5 scenario, for example, indirect land-use effects and carbon lost from soils can potentially explain about 60% of the difference in cumulative emissions between 2000 and 2300. The remaining part would be attributed to a weaker oceanic carbon sink. Some care has to be taken when interpreting these results because the simulated land-use emissions are likely too low as mentioned earlier in section 4.4.4.

Allowable emissions are quantified for four temperature stabilization pathways from 2000 to 2300 by using a temperature-tracking method. The simulated allowable cumulative CO₂ emissions are 390 GtC (stabilization at 1.5 °C), 580 GtC (2 °C), 1030 GtC (3 °C), and 1520 GtC (4 °C). The radiative forcing associated with these emissions also include the forcing from non-CO₂ greenhouse gases and aerosols.

The results presented here provide an overview of the main characteristics of the coupled model and newly implemented features. There are many possibilities for further, more detailed analyses. These could cover a detailed carbon cycle-climate feedback analysis, an extended assessment of land-use related fluxes, or a closer look at the numerous commitment and irreversibility simulations. Also, the simulations over the last millennium are just mentioned briefly here and provide a resource for additional work (e.g. on volcanic eruptions that seem to have a relatively large impact on ocean circulation and global temperatures in this model). Further, the analyses could be extended with a more regional view of changes by exploring the two- and three-dimensional output fields of the model. Some of this will be

done within the EMIC AR5 project, also including results from other participating groups. Moreover, the simulations presented here are also performed within a probabilistic framework. In this ongoing study, uncertainties in climate sensitivity, carbon cycle, and radiative forcing parameters are considered by using a Monte Carlo based approach and observational data constraints to provide probabilistic projections (see outlook in Chapter 7).

Bibliography

- Battle, M., Bender, M., Sowers, T., Tans, P. P., Butler, J. H., Elkins, J. W., Ellis, J. T., Conway, T., Zhang, N., Lang, P., & Clarke, A. D., 1996. Atmospheric gas concentrations over the past century measured in air from firn at the South Pole, *Nature*, 383(6597), 231–235.
- Berger, A. L., 1978. Long-term variations of daily insolation and quaternary climatic changes, *J. Atmos. Sci.*, 35(12), 2362–2367.
- Berglund, E. R. & Mace, A. C., 1972. Seasonal albedo variation of black spruce and sphagnum-sedge bog cover types, *J. Appl. Meteorol.*, 11(5), 806–812.
- Bintanja, R., 1996. The parameterization of shortwave and longwave radiative fluxes for use in zonally averaged climate models, *J. Climate*, 9(2), 439–454.
- Canadell, J. G., Le Quere, C., Raupach, M. R., Field, C. B., Buitenhuis, E. T., Ciais, P., Conway, T. J., Gillett, N. P., Houghton, R. A., & Marland, G., 2007. Contributions to accelerating atmospheric CO₂ growth from economic activity, carbon intensity, and efficiency of natural sinks, *Proc. Nat. Acad. Sci. USA*, 104(47), 18866–18870.
- Conkright, M. E., Antonov, J. I., Boyer, T. P., Locarnini, R. A., O'Brien, T. D., Stephens, C., & Garcia, H. E., 2002. *World Ocean Atlas 2001*, vol. 49-52 of NOAA Atlas NEDIS, US Govt. Printing Office, Washington, D. C.
- Crowley et al., T., 2008. Volcanism and the Little Ice Age, *PAGES Newsletter*, (16), 22–23.
- Delaygue, G. & Bard, E., 2009. Solar forcing based on Be-10 in Antarctica ice over the past millennium and beyond, *EGU 2009 General Assembly*, (#EGU2009-6943).
- Dickinson, R., Henderson-Sellers, A., Kennedy, P., & Wilson, M., 1986. Biosphere atmosphere transfer scheme (BATS) for the NCAR community climate model, NCAR Tech. Note NCAR/TN-275+STR, National Center for Atmospheric Research, Boulder, Colorado, USA.
- Edwards, N. R., Willmott, A. J., & Killworth, P. D., 1998. On the role of topography and wind stress on the stability of the thermohaline circulation, *J. Phys. Oceanogr.*, 28(5), 756–778.
- Etheridge, D. M., Steele, L. P., Langenfelds, R. L., Francey, R. J., Barnola, J. M., & Morgan, V. I., 1996. Natural and anthropogenic changes in atmospheric CO₂ over the last 1000 years from air in antarctic ice and firn, *J. Geophys. Res.-Atmos.*, 101(D2), 4115–4128.
- Farquhar, G. D., Caemmerer, S. V., & Berry, J. A., 1980. A biochemical-model of photosynthetic CO₂ assimilation in leaves of C-3 species, *Planta*, 149(1), 78–90.
- Flückiger, J., Dallenbach, A., Blunier, T., Stauffer, B., Stocker, T. F., Raynaud, D., & Barnola, J. M., 1999. Variations in atmospheric N₂O concentration during abrupt climatic changes, *Science*, 285(5425), 227–230.
- Flückiger, J., Monnin, E., Stauffer, B., Schwander, J., Stocker, T. F., Chappellaz, J., Raynaud, D., & Barnola, J. M., 2002. High-resolution Holocene N₂O ice core record and its relationship with CH₄ and CO₂, *Global Biogeochem. Cy.*, 16(1010).
- Forster, P., Ramaswamy, V., Artaxo, P., Berntsen, T., Betts, R., Fahey, D. W., Haywood, J., Lean, J., Lowe, D. C., Myhre, G., Nganga, J., Prinn, R., Raga, G., Schulz, M., & Dorland, R. V., 2007. *Climate Change 2007: The Physical Science Basis. Contribution of Working Group I to the Fourth Assessment Report of the Intergovernmental Panel on Climate Change*, chap. 2: Changes in Atmospheric Constituents and in Radiative Forcing, pp. 129–234, Cambridge University Press, Cambridge, United Kingdom and New York, NY, USA.
- Frölicher, T. L. & Joos, F., 2010. Reversible and irreversible impacts of greenhouse gas emissions in multi-century projections with the NCAR global coupled carbon cycle-climate model, *Clim. Dynam.*, 34(Published online: 12 January 2010).
- Gehlen, M., Bopp, L., Emprin, N., Aumont, O., Heinze, C., & Ragueneau, O., 2006. Reconciling surface ocean productivity, export fluxes and sediment composition in a global biogeochemical ocean model, *Biogeochemistry*, 3, 521–537.
- Gerber, S., Joos, F., Brugger, P., Stocker, T. F., Mann, M. E., Sitch, S., & Scholze, M., 2003. Constraining temperature variations over the last millennium by comparing simulated and observed atmospheric CO₂, *Clim. Dynam.*, 20(2-3), 281–299.

- Gerten, D., Schaphoff, S., Haberlandt, U., Lucht, W., & Sitch, S., 2004. Terrestrial vegetation and water balance - hydrological evaluation of a dynamic global vegetation model, *J. Hydrol.*, 286(1-4), 249–270.
- Heinze, C., Maier-Reimer, E., Winguth, A. M. E., & Archer, D., 1999. A global oceanic sediment model for long-term climate studies, *Global Biogeochem. Cy.*, 13(1), 221–250.
- Hibbard, K. A., Meehl, G. A., Cox, P., & Friedlingstein, P., 2007. A strategy for climate change stabilization experiments, *EOS*, 88(20), 217–221.
- Hurtt, G., Chini, L., Frolking, S., Betts, R., Feddema, J., Fischer, G., Goldewijk, K., Hibbard, K., Janetos, A., Jones, C., Kinderman, G., Kinoshita, T., Riahi, K., Shevliakova, E., Smith, S., Stehfest, E., Thomson, A., Thornton, P., vanVuuren, D., & Wang, Y., 2009. Harmonization of global land-use scenarios for the period 1500-2100 for IPCC-AR5, *iLEAPS Newsletter*, (7), 6–8.
- Joos, F., Prentice, I. C., Sitch, S., Meyer, R., Hooss, G., Plattner, G.-K., Gerber, S., & Hasselmann, K., 2001. Global warming feedbacks on terrestrial carbon uptake under the Intergovernmental Panel on Climate Change (IPCC) emission scenarios, *Global Biogeochem. Cy.*, 15(4), 891–907.
- Key, R. M., Kozyr, A., Sabine, C. L., Lee, K., Wanninkhof, R., Bullister, J., Feely, R. A., Millero, F., Mordy, C., & Peng, T.-H., 2004. A global ocean carbon climatology: Results from Global Data Analysis Project (GLODAP), *Global Biogeochem. Cy.*, 18(GB4031+).
- Kubatzki, C., 2000. *Wechselwirkungen zwischen Klima und Landoberfläche im Holozän - Modellstudien*, Ph.D. thesis, FU Berlin, Berlin, Germany.
- Lean, J., 2000. Evolution of the sun's spectral irradiance since the Maunder Minimum, *Geophys. Res. Lett.*, 27(16), 2425–2428.
- MacFarling Meure, C., Etheridge, D., Trudinger, C., Steele, P., Langenfelds, R., van Ommen, T., Smith, A., & Elkins, J., 2006. Law dome CO₂, CH₄ and N₂O ice core records extended to 2000 years BP, *Geophys. Res. Lett.*, 33(L14810).
- Machida, T., Nakazawa, T., Fujii, Y., Aoki, S., & Watanabe, O., 1995. Increase in the atmospheric nitrous-oxide concentration during the last 250 years, *Geophys. Res. Lett.*, 22(21), 2921–2924.
- Marland, G., Boden, T. A., & Andres, R. J., 2008. *Global, Regional, and National Fossil Fuel CO₂ Emissions*, In Trends: A Compendium of Data on Global Change, Carbon Dioxide Information Analysis Center, Oak Ridge National Laboratory, U.S. Department of Energy, Oak Ridge, Tenn., U.S.A.
- Meinshausen, M., Smith, S. J., Calvin, K. V., Daniel, J. S., Kainuma, M., Lamarque, J.-F., Matsumoto, K., Montzka, S. A., Raper, S. C. B., Riahi, K., Thomson, A. M., Velders, G. J. M., & van Vuuren, D., 2011. The RCP greenhouse gas concentrations and their extension from 1765 to 2300, *Clim. Change*, 109, 213–241.
- Moody, E. G., King, M. D., Platnick, S., Schaaf, C. B., & Gao, F., 2005. Spatially complete global spectral surface albedos: Value-added datasets derived from terra MODIS land products, *IEEE Trans. Geosci. Remote Sens.*, 43(1), 144–158.
- Moss, R. H., Edmonds, J. A., Hibbard, K. A., Manning, M. R., Rose, S. K., van Vuuren, D. P., Carter, T. R., Emori, S., Kainuma, M., Kram, T., Meehl, G. A., Mitchell, J. F. B., Nakicenovic, N., Riahi, K., Smith, S. J., Stouffer, R. J., Thomson, A. M., Weyant, J. P., & Wilbanks, T. J., 2010. The next generation of scenarios for climate change research and assessment, *Nature*, 463(7282), 747–756.
- Müller, S. A., Joos, F., Edwards, N. R., & Stocker, T. F., 2006. Water mass distribution and ventilation time scales in a cost-efficient, three-dimensional ocean model, *J. Climate*, 19(21), 5479–5499.
- Myhre, G., Highwood, E. J., Shine, K. P., & Stordal, F., 1998. New estimates of radiative forcing due to well mixed greenhouse gases, *Geophys. Res. Lett.*, 25(14), 2715–2718.
- Myhre, G., Kvalevag, M. M., & Schaaf, C. B., 2005. Radiative forcing due to anthropogenic vegetation change based on modis surface albedo data, *Geophys. Res. Lett.*, 32(21).
- Najjar, R. G., Orr, J., Sabine, C. L., & Joos, F., 1999. Biotic-HOWTO. internal OCMIP report, Tech. rep., LSCE/CEA Saclay, Gif-sur-Yvette, France.
- Orr, J. & Najjar, R. G., 1999. Abiotic-HOWTO. internal OCMIP report, Tech. rep., LSCE/CEA Saclay, Gif-sur-Yvette, France.

- Otto, J., Raddatz, T., & Claussen, M., 2011. Strength of forest-albedo feedback in mid-Holocene climate simulations, *Clim. Past*, 7, 1027–1039.
- Parekh, P., Joos, F., & Müller, S. A., 2008. A modeling assessment of the interplay between aeolian iron fluxes and iron-binding ligands in controlling carbon dioxide fluctuations during antarctic warm events, *Paleoceanography*, 23(4).
- Pongratz, J., Reick, C., Raddatz, T., & Claussen, M., 2008. A reconstruction of global agricultural areas and land cover for the last millennium, *Global Biogeochem. Cy.*, 22(3).
- Reader, M. C. & Boer, G. J., 1998. The modification of greenhouse gas warming by the direct effect of sulphate aerosols, *Clim. Dynam.*, 14(7-8), 593–607.
- Ritz, S. P., Stocker, T. F., & Joos, F., 2011. A coupled dynamical ocean-energy balance atmosphere model for paleoclimate studies, *J. Climate*, 24(2), 349–375.
- Roesch, A. & Roeckner, E., 2006. Assessment of snow cover and surface albedo in the echam5 general circulation model, *J. Climate*, 19(16), 3828–3843.
- Roesch, A., Wild, M., Gilgen, H., & Ohmura, A., 2001. A new snow cover fraction parametrization for the ECHAM4 GCM, *Clim. Dynam.*, 17(12), 933–946.
- Schmidt, G. A., Jungclaus, J. H., Ammann, C. M., Bard, E., Braconnot, P., Crowley, T. J., Delaygue, G., Joos, F., Krivova, N. A., Muscheler, R., Otto-Bliesner, B. L., Pongratz, J., Shindell, D. T., Solanki, S. K., Steinhilber, F., & Vieira, L. E. A., 2011. Climate forcing reconstructions for use in PMIP simulations of the last millennium (v1.0), *Geosci. Model Dev.*, 4(1), 33–45.
- Sitch, S., Smith, B., Prentice, I. C., Arneth, A., Bondeau, A., Cramer, W., Kaplan, J. O., Levis, S., Lucht, W., Sykes, M. T., Thonicke, K., & Venevsky, S., 2003. Evaluation of ecosystem dynamics, plant geography and terrestrial carbon cycling in the LPJ dynamic global vegetation model, *Glob. Change Biol.*, 9(2), 161–185.
- Spahni et al., R., in prep.
- Stocker, B. D., Strassmann, K., & Joos, F., 2011. Sensitivity of Holocene atmospheric CO₂ and the modern carbon budget to early human land use: analyses with a process-based model, *Biogeosciences*, 8(1), 69–88.
- Strahler, A. H., Muller, J.-P., & MODIS Science Team Members, 1999. MODIS BRDF/albedo product: Algorithm theoretical basis document, version 5.0, Tech. Rep. MOD43.
- Strassmann, K. M., Joos, F., & Fischer, G., 2008. Simulating effects of land use changes on carbon fluxes: past contributions to atmospheric CO₂ increases and future commitments due to losses of terrestrial sink capacity, *Tellus B*, 60(4), 583–603.
- Strassmann, K. M., Plattner, G.-K., & Joos, F., 2009. CO₂ and non-CO₂ radiative forcings in climate projections for twenty-first century mitigation scenarios, *Clim. Dynam.*, 33(6), 737–749, published online 20 Dec 2008.
- Taylor, K. E., Stouffer, R. J., & Meehl, G. A., 2009. A summary of the CMIP5 experiment design, Tech. rep., available from http://cmip-pcmdi.llnl.gov/cmip5/experiment_design.html.
- Thompson, S. L. & Warren, S. G., 1982. Parameterization of outgoing infrared radiation derived from detailed radiative calculations, *J. Atmos. Sci.*, 39(12), 2667–2680.
- Tian, Y., Dickinson, R. E., Zhou, L., Myneni, R. B., Friedl, M., Schaaf, C. B., Carroll, M., & Gao, F., 2004. Land boundary conditions from MODIS data and consequences for the albedo of a climate model, *Geophys. Res. Lett.*, 31(5), 5 pp.
- Tschumi, T., Joos, F., & Parekh, P., 2008. How important are southern hemisphere wind changes for low glacial carbon dioxide? A model study, *Paleoceanography*, 23(4).
- Tschumi, T., Joos, F., Gehlen, M., & Heinze, C., 2011. Deep ocean ventilation, carbon isotopes, marine sedimentation and the deglacial CO₂ rise, *Clim. Past*, 7(3), 771–800.
- van Vuuren, D. P., Edmonds, J., Kainuma, M. L. T., Riahi, K., Thomson, A., Matsui, T., Hurtt, G., Lamarque, J.-F., Meinshausen, M., Smith, S., Grainer, C., Rose, Hibbard, K. A., Nakicenovic, N., Krey, V., & Kram, T., 2011. Representative concentration pathways: an overview, *Clim. Change*.

- Wang, Y. M., Lean, J. L., & Sheeley, N. R., 2005. Modeling the sun's magnetic field and irradiance since 1713, *Astrophys. J.*, 625, 522–538.
- Wania, R., Ross, I., & Prentice, I. C., 2009a. Integrating peatlands and permafrost into a dynamic global vegetation model: 1. evaluation and sensitivity of physical land surface processes, *Global Biogeochem. Cy.*, 23.
- Wania, R., Ross, I., & Prentice, I. C., 2009b. Integrating peatlands and permafrost into a dynamic global vegetation model: 2. evaluation and sensitivity of vegetation and carbon cycle processes, *Global Biogeochem. Cy.*, 23.
- Weaver, A. J., Eby, M., Wiebe, E. C., Bitz, C. M., Duffy, P. B., Ewen, T. L., Fanning, A. F., Holland, M. M., MacFadyen, A., Matthews, H. D., Meissner, K. J., Saenko, O., Schmittner, A., Wang, H. X., & Yoshimori, M., 2001. The UVic Earth system climate model: Model description, climatology, and applications to past, present and future climates, *Atmos. Ocean*, 39(4), 361–428.
- Zickfeld, K., Eby, M., Matthews, H. D., & Weaver, A. J., 2009. Setting cumulative emissions targets to reduce the risk of dangerous climate change, *Proc. Nat. Acad. Sci. USA*, 106(38), 16129–16134.

Chapter 5

Impact of climate change mitigation on ocean acidification projections

Fortunat Joos, Thomas L. Frölicher, Marco Steinacher, and Gian-Kasper Plattner

Published as chapter 14 in: *Ocean Acidification*, edited by J.-P. Gattuso and L. Hansson, Oxford Univ. Press, pp. 272–290, 2011.

CHAPTER 14

Impact of climate change mitigation on ocean acidification projections

Fortunat Joos, Thomas L. Frölicher, Marco Steinacher, and Gian-Kasper Plattner

14.1 Introduction

Ocean acidification caused by the uptake of carbon dioxide (CO₂) by the ocean is an important global change problem (Kleypas *et al.* 1999; Caldeira and Wickett 2003; Doney *et al.* 2009). Ongoing ocean acidification is closely linked to global warming, as acidification and warming are primarily caused by continued anthropogenic emissions of CO₂ from fossil fuel burning (Marland *et al.* 2008), land use, and land-use change (Strassmann *et al.* 2007). Future ocean acidification will be determined by past and future emissions of CO₂ and their redistribution within the earth system and the ocean. Calculation of the potential range of ocean acidification requires consideration of both a plausible range of emissions scenarios and uncertainties in earth system responses, preferably by using results from multiple scenarios and models.

The goal of this chapter is to map out the spatio-temporal evolution of ocean acidification for different metrics and for a wide range of multigas climate change emissions scenarios from the integrated assessment models (Nakićenović 2000; Van Vuuren *et al.* 2008b). By including emissions reduction scenarios that are among the most stringent in the current literature, this chapter explores the potential benefits of climate mitigation actions in terms of how much ocean acidification can be avoided and how much is likely to remain as a result of inertia within the energy and climate systems. The long-term impacts of carbon emissions are addressed using so-called zero-emissions commitment scenarios and pathways leading to stabilization of atmospheric CO₂. Discussion will primarily rely on results from the cost-efficient Bern2.5CC model (Plattner

et al. 2008) and the comprehensive carbon cycle–climate model of the National Centre for Atmospheric Research (NCAR), CSM1.4-carbon (Steinacher *et al.* 2009; Frölicher and Joos 2010).

The magnitude of the human perturbation of the climate system is well documented by observations (Solomon *et al.* 2007). Carbon emissions from human activities force the atmospheric composition, climate, and the geochemical state of the ocean towards conditions that are unique for at least the last million years (see Chapter 2). The current atmospheric CO₂ concentration of 390 ppmv is well above the natural range of 172 to 300 ppmv of the past 800 000 years (Lüthi *et al.* 2008). The rate of increase in CO₂ and in the radiative forcing from the combination of the well-mixed greenhouse gases CO₂, methane (CH₄), and nitrous oxide (N₂O) is larger during the Industrial Era than during any comparable period of at least the past 16 000 years (Joos and Spahni 2008). Ocean measurements over recent decades show that the increase in surface-ocean CO₂ is being paralleled by a decrease in pH (Doney *et al.* 2009). Ongoing global warming is unequivocal (Solomon *et al.* 2007): observational data show that global-mean sea level is rising, ocean heat content increasing, Arctic sea ice retreating, atmospheric water vapour content increasing, and precipitation patterns changing. The last decade (2000 to 2009) was, on a global average, the warmest in the instrumental record (<http://data.giss.nasa.gov/gistemp/>). Proxy reconstructions suggest that recent anthropogenic influences have widened the last-millennium multi-decadal temperature range by 75% and that late 20th century warmth exceeded peak temperatures over the past millennium by 0.3°C (Frank *et al.* 2010).

The range of plausible 21st century emissions pathways leads to further global warming and ocean acidification (Van Vuuren *et al.* 2008b; Strassmann *et al.* 2009). Projections based on the scenarios of the Special Report on Emissions Scenarios (SRES) of the Intergovernmental Panel on Climate Change (IPCC) give reductions in average global surface pH of between 0.14 and 0.35 units over the 21st century, adding to the present decrease of 0.1 units since pre-industrial time (Orr *et al.* 2005; see also Chapters 1 and 3). Comprehensive earth system model simulations show that continued carbon emissions over the 21st century will cause irreversible climate change on centennial to millennial timescales in most regions, and impacts related to ocean acidification and sea level rise will continue to aggravate for centuries even if emissions are stopped by the year 2100 (Frölicher and Joos 2010). In contrast, in the absence of future anthropogenic emissions of CO₂ and other radiative agents, forced changes in surface temperature and precipitation will become smaller in the next centuries than internal variability for most land and ocean grid cells and ocean acidification will remain limited. This demonstrates that effective measures to reduce anthropogenic emissions can make a difference. However, continued carbon emissions will affect climate and the ocean over the next millennium and beyond (Archer *et al.* 1999; Plattner *et al.* 2008) and related climate and biogeochemical impacts pose a substantial threat to human society.

Thirty years ago, with their box-diffusion carbon cycle model, Siegenthaler and Oeschger (1978) demonstrated the long lifetime of an atmospheric CO₂ perturbation and pointed out that carbon emissions must be reduced ‘if the atmospheric radiation balance is not to be disturbed in a dangerous way’. The United Nations Framework Convention on Climate Change (UNFCCC) that came into force in 1994 has the ultimate objective (article 2) ‘to achieve . . . stabilization of greenhouse gas concentrations in the atmosphere at a level that would prevent dangerous anthropogenic interference with the climate system. Such a level should be achieved within a time frame sufficient to allow ecosystems to adapt naturally to climate change...’ (UN 1992). Scenarios provide a useful framework for establishing policy-relevant information related to the UNFCCC. Here, the link

between atmospheric CO₂ level and ocean acidification, and the timescales of change, are addressed.

The outline of this chapter is as follows. In the next section, we will discuss different classes of scenarios, their underlying assumptions, and how these scenarios are used. Metrics for assessing ocean acidification are also introduced. In Section 14.3, the evolution over this century of atmospheric CO₂, global-mean surface air temperature, and global-mean surface ocean acidification for the recent range of baseline and mitigation scenarios from integrated assessment models is presented. In Section 14.4, the minimum commitment, as a result of past and 21st century emissions, to long-term climate change and ocean acidification arising from inertia in the earth system alone is addressed. In Section 14.5, regional changes in surface ocean chemistry are discussed. In Section 14.6, delayed responses, irreversibility, and changes in the deep ocean are addressed using results from the comprehensive NCAR CSM1.4-carbon model. Finally, in Section 14.7, idealized profiles leading to CO₂ stabilization are discussed to further highlight the link between greenhouse gas stabilization, climate change, and ocean acidification. The overarching logic is to use the cost-efficient Bern2.5CC model to explore the scenario space and uncertainties for global-mean values and the NCAR CSM1.4-carbon model to investigate regional details for a limited set of scenarios. The set of baseline and emissions scenarios and associated changes in CO₂ and global-mean surface temperature have been previously discussed (Van Vuuren *et al.* 2008b; Strassmann *et al.* 2009). We also refer to the literature for a more detailed discussion of the NCAR CSM1.4-carbon ocean acidification results (Steinacher *et al.* 2009; Frölicher and Joos 2010).

14.2 Scenarios and metrics

Scenario-based projections are a scientific tool kit for investigating alternative evolutions of anthropogenic emissions and their influence on climate, the earth system, and the socio-economic system. Scenario-based projections are not to be misunderstood as predictions of the future, and as the time horizon increases the basis for the underlying assumptions becomes increasingly uncertain.

One class of scenarios includes idealized emissions or concentration pathways to investigate processes, feedbacks, timescales, and inertia in the climate system. These scenarios are usually developed from a natural science perspective and used for their illustrative power. Examples are a complete instantaneous reduction of emissions at a given year or idealized pathways leading to stabilization of greenhouse gas concentrations (Schimel *et al.* 1997). Another class of emissions scenarios has been developed using integrated assessment frameworks and integrated assessment models (IAMs) by considering plausible future demographic, social, economic, technological, and environmental developments. Examples include the scenarios of the IPCC SRES (Nakićenović *et al.* 2000) and the more recently developed representative concentration pathways (RCPs; Moss *et al.* 2008, 2010; Van Vuuren *et al.* 2008a).

The SRES emissions scenarios do not include explicit climate change mitigation actions. Such scenarios are usually called baseline or reference scenarios. In this chapter, results based on the two illustrative SRES scenarios B1 and A2, a low- and a high-emissions baseline scenario, are discussed (Fig. 14.1). The SRES scenarios have been widely

used in the literature and in the IPCC Fourth Assessment Report. They are internally consistent scenarios in the sense that each is based on a 'narrative storyline' that describes the relationships between the forces driving emissions. The 21st century emissions of the major anthropogenic greenhouse gases [CO_2 , CH_4 , N_2O , halocarbons, and sulphur hexafluoride (SF_6)], aerosols and tropospheric ozone precursors [sulphur dioxide (SO_2), carbon monoxide (CO), NO_x , and volatile organic compounds (VOCs)] are quantified with IAMs. The extent of the technological improvements contained in the SRES scenarios is not always appreciated. The SRES scenarios include already large and important improvements in energy intensity (energy used per unit of gross domestic product) and the deployment of non-carbon-emitting energy supply technologies compared with the present (Edmonds *et al.* 2004). By the year 2100, the primary energy demand in the SRES scenarios ranges from 55% to more than 90% lower than had no improvement in energy intensity occurred. In addition, in many of the SRES scenarios the deployment of non-carbon-emitting energy supply systems (solar, wind, nuclear, and biomass) exceeds the size of the global energy system in 1990.

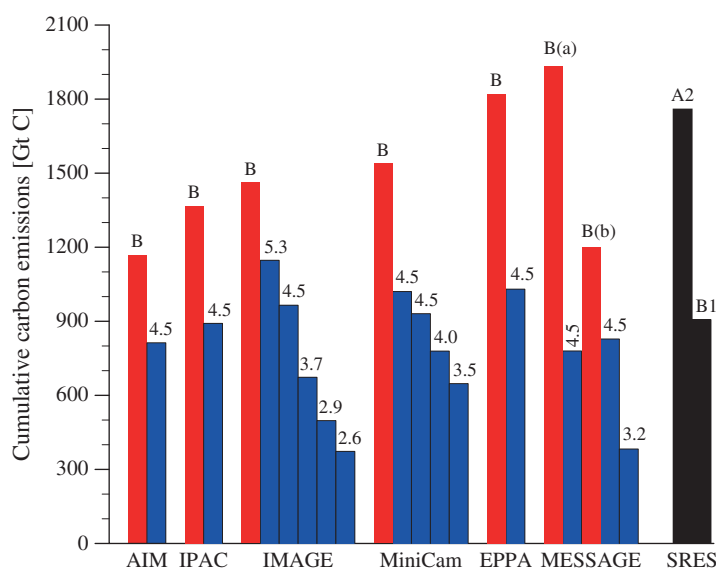


Figure 14.1 Cumulative CO_2 emissions in gigatonnes of carbon (Gt C) over the 21st century for a range of baseline (B; red), climate mitigation (blue), and the SRES A2 and B1 (black) scenarios. The numbers related to the mitigation scenarios indicate the radiative forcing targets in W m^{-2} imposed in the IAMs. The labels below the columns refer to the IAMs used to quantify the scenarios (Weyant *et al.* 2006) and to the SRES scenarios (Nakićenović 2000), respectively.

However, by design they do not include explicit policies to mitigate greenhouse gas emissions, which would lower the extent of climate change experienced over the 21st century.

Progress in developing multigas mitigation scenarios after the SRES report now allows for a comparison between consequences for the earth system of climate mitigation versus baseline scenarios. Figure 14.1 illustrates the relationship between scenarios and individual IAMs and how individual mitigation scenarios are linked to a specific baseline scenario for the post-SRES set of scenarios. Many mitigation scenarios were generated with several IAMs as part of the Energy Modeling Forum Project 21 (EMF-21; Weyant *et al.* 2006). The IAMs feature representations of the energy system and other parts of the economy, such as trade and agriculture, with varying levels of spatial and process detail. They also include formulations to translate emissions into concentrations and the associated radiative forcing (RF). The latter is a metric for the perturbation of the radiative balance of the lower atmosphere–surface system. Scenarios are generated by minimizing the total costs under the constraints set by societal drivers (e.g. population, welfare, and technological innovation) and most are related to SRES ‘storylines’. Adding a constraint on RF in a baseline scenario leads to a scenario with policies specifically aimed at mitigation. The mitigation scenarios analysed here are constrained by stabilization of total RF in the period 2100 to 2150 with RF targets ranging from 2.6 to 5.3 W m⁻². From the wider set of baseline and mitigation scenarios described in the literature, four have been specifically selected and termed representative concentration pathways (RCPs). These include two mitigation scenarios with a RF target of 2.6 and 4.5 W m⁻² and two baseline scenarios with a RF of around 6 and 8.5 W m⁻² by the end of this century.

Two metrics appear particularly well suited for characterizing the outcome of a scenario in terms of ocean acidification. These are changes in pH and changes in the saturation state of water with respect to aragonite, a mineral form of calcium carbonate (CaCO₃) secreted by marine organisms. Ocean uptake of the weak acid CO₂ from the atmosphere causes a reduction in pH and in turn alters the CaCO₃ precipitation equilibrium (see Chapter 1).

Recent studies indicate that ocean acidification due to the uptake of CO₂ has adverse consequences for many marine organisms as a result of decreased CaCO₃ saturation, affecting calcification rates, and via disturbance to acid–base physiology (see Chapters 6–8). Vulnerable organisms that build shells and other structures of CaCO₃ in the relatively soluble form of aragonite or high-magnesian calcite, but also organisms that form CaCO₃ in the more stable form of calcite may be affected. Undersaturation as projected for the high-latitude ocean (Orr *et al.* 2005; Steinacher *et al.* 2009) has been found to affect pteropods for example, an abundant group of species forming aragonite shells (Orr *et al.* 2005; Comeau *et al.* 2009). Changes in CaCO₃ saturation are also thought to affect coral reefs (Kleypas *et al.* 1999; Langdon and Atkinson 2005; Hoegh-Guldberg *et al.* 2007; Cohen and Holcomb 2009). The impacts are probably not restricted to ecosystems at the ocean surface, but potentially also affect life in the deep ocean such as the extended deep-water coral systems and ecosystems at the ocean floor. The degree of sensitivity varies among species (Langer *et al.* 2006; Müller *et al.* 2010) and there is a debate about whether some taxa may show enhanced calcification at the levels of CO₂ projected to occur over the 21st century (Iglesias-Rodriguez *et al.* 2008). This wide range of different responses is expected to affect competition among species, ecosystem structure, and overall community production of organic material and CaCO₃. On the other hand, the impact of plausible changes in CaCO₃ production and export (Gangstø *et al.* 2008) on atmospheric CO₂ is estimated to be small (Heinze 2004; Gehlen *et al.* 2007). Other impacts of ocean acidification with potential influences on marine ecosystems include alteration in the speciation of trace metals as well as an increase in the transparency of the ocean to sound (Hester *et al.* 2008). The changes in the chemical composition of seawater such as higher concentrations of dissolved CO₂ are also likely to affect the coupled carbon and nitrogen cycle and the food web in profound ways (Hutchins *et al.* 2009), and the volume of water with a ratio of oxygen to CO₂ below the threshold for aerobic life is likely to expand (Brewer and Peltzer 2009).

The saturation state with respect to aragonite, Ω_a , is defined by:

$$\Omega_a = \frac{[\text{Ca}^{2+}][\text{CO}_3^{2-}]}{K_{sp}^*}$$

where brackets denote concentrations in seawater, here for calcium ions and carbonate ions, and K_{sp}^* is the apparent solubility product defined by the equilibrium relationship for the dissolution reaction of aragonite. Similarly, saturation can be defined with respect to calcite which is less soluble than aragonite. Uptake of CO_2 causes an increase in total dissolved inorganic carbon (C_T) and a decrease in the carbonate ion concentration and in saturation (see Chapter 1). Shells or other structures start to dissolve in the absence of protective mechanisms when saturation falls below 1 for the appropriate mineral phase. A value of Ω greater than 1 corresponds to supersaturation. Supersaturated conditions are possible, as the activation energy for forming aragonite or calcite is high.

The pH describes the concentration or, more precisely, the activity of the hydrogen ion in water, a_{H^+} , by a logarithmic function:

$$\text{pH}_T = -\log_{10} a_{\text{H}^+}.$$

The activity of hydrogen ion is important for all acid–base reactions. In this chapter, the total pH scale is used as indicated by the subscript T.

14.3 Baseline and mitigation emissions scenarios for the 21st century: how much acidification can be avoided?

Figure 14.1 shows the cumulative carbon emissions over this century for the recent set of baseline and mitigation scenarios (Van Vuuren *et al.* 2008b) and Fig. 14.2 their temporal evolution. Cumulative CO_2 emissions are in the range of 1170 to 1930 Gt C for the seven baseline scenarios and between 370 and 1140 Gt C for the mitigation scenarios, with the highest emissions associated with a high forcing and a weak mitigation target. In the baseline (no climate policy) scenarios, the range of increase in greenhouse gas emissions by 2100 is from 70 to almost 250% compared with the year 2000 (here, emissions are measured in CO_2 -equivalent— CO_2 -equivalent emissions of a forcing agent denote the

amount of CO_2 emissions that would cause the same radiative forcing over a time period of 100 years; IPCC 2007). Emissions growth slows down in the second half of the century in all baseline scenarios, because of a combination of stabilizing global population levels and continued technological change. The mitigation scenarios necessarily follow a different path, with a peak in global emissions between 2020 and 2040 at a maximum value of 50% above current emissions.

The projected CO_2 concentrations for the baseline cases calculated with the Bern2.5CC model (Plattner *et al.* 2008) range from 650 to 960 ppmv in 2100 using best-estimate model parameters (Fig. 14.2C). The CO_2 concentrations in the mitigation scenarios range from 400 to 620 ppmv in 2100. Uncertainties in the carbon cycle and climate sensitivity increase the overall range to 370 to 1310 ppmv (bars in Fig. 14.2C; Plattner *et al.* 2008). Uncertainties are particularly large for the high end. The two scenario sets, baseline and mitigation, are also distinct with respect to their trends. All baseline scenarios show an increasing trend in atmospheric CO_2 , implying rising concentrations beyond 2100. In contrast, the mitigation scenarios show little growth or even a declining trend in CO_2 by 2100.

Projected global-mean surface air temperature changes by the year 2100 (relative to 2000) are 2.4 to 4.2°C (Fig. 14.2D) for the baseline scenarios and best-estimate Bern2.5CC model parameters. Uncertainties in the carbon cycle and climate sensitivity more than double the ranges associated with emissions. For the mitigation scenarios, the projected temperature changes by 2100 are 1.1 to 2.1°C using central model parameters. The mitigation scenarios bring down the overall range of CO_2 and temperature change substantially relative to the baseline range. As for CO_2 , the greatest difference compared with the baseline is seen during the second part of the century, when the rate of temperature change slows considerably in all mitigation scenarios in contrast to the baseline scenarios. In several mitigation scenarios, surface air temperature has more or less stabilized by year 2100 (Van Vuuren *et al.* 2008b; Strassmann *et al.* 2009).

The evolution of the global-mean saturation state of aragonite (Fig. 14.2E) and pH_T (Fig. 14.2F) in the surface ocean mirrors the evolution of atmospheric

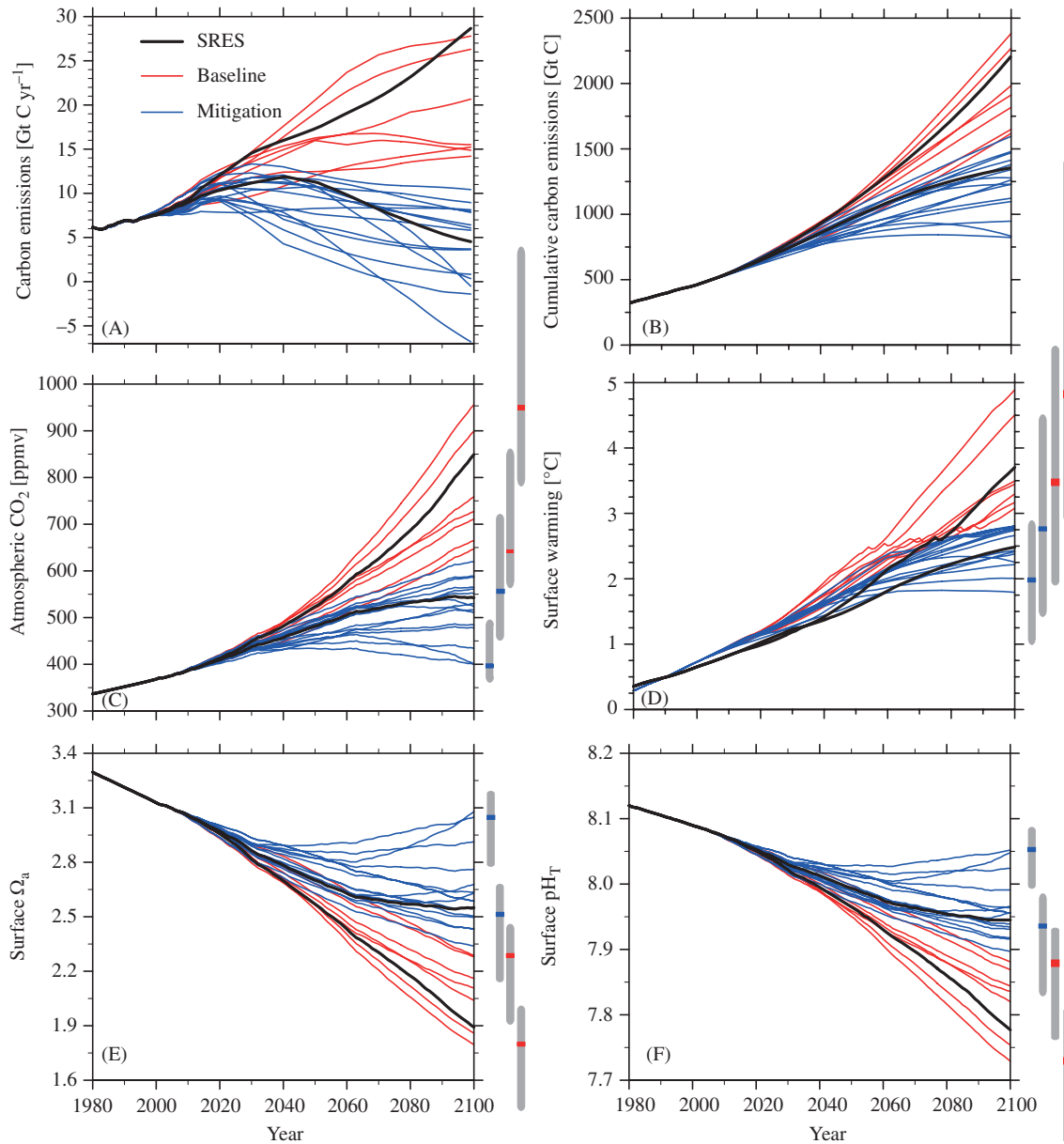


Figure 14.2 (A) Annual and (B) cumulative CO₂ emissions prescribed in the Bern2.5CC model and projected (C) atmospheric CO₂, (D) changes in global-mean surface air temperature, (E) global average surface saturation with respect to CaCO₃ in the form of aragonite, and (F) global average surface pH on the total pH scale (pH_T). Baseline scenarios are shown by red lines and mitigation scenarios by blue dotted lines. The SRES high-emissions A2 and low-emissions B1 marker scenarios are given by black lines. Bars indicate uncertainty ranges for the year 2100 and for the four representative concentration pathways (RCPs), marked for evaluation by climate modellers in preparation for the IPCC Fifth Assessment Report. The ranges were obtained by combining different assumptions about the behaviour of the CO₂ fertilization effect on land, the response of soil heterotrophic respiration to temperature, and the turnover time of the ocean, thus approaching an upper boundary of uncertainties in the carbon cycle, and additionally accounting for the effect of varying climate sensitivity from 1.5 to 4.5°C (Joos *et al.* 2001).

CSM1.4-carbon model have been selected to illustrate the long-term influence of anthropogenic carbon emissions on ocean acidification and climate (Fig. 14.4). In the first scenario ('Hist' case), emissions are hypothetically set to zero in 2000. In the other two scenarios, emissions follow the SRES B1 (low 'B1_c' case) and SRES A2 (high 'A2_c' case) path until 2100, when emissions are instantaneously set to zero. Setting emissions immediately to zero in 2000 or 2100 is not realistic, but it allows the quantification of the long-term impact of previous greenhouse gas emissions. The three scenarios roughly span the

range of 21st century carbon emissions from baseline and mitigation scenarios (Fig. 14.2A). The 'Hist' case obviously features lower emissions (397 Gt C) than any of the mitigation scenarios. Cumulative emissions in the 'B1_c' case (1360 Gt C) are somewhat smaller than those from the highest mitigation scenario and the lowest baseline scenario shown in Figs 14.1 and 14.2 and emissions in the 'A2_c' case (2210 Gt C) are close to those of the most extreme baseline scenario.

While projected atmospheric CO_2 and surface saturation in 2100 is similar for the Bern2.5CC

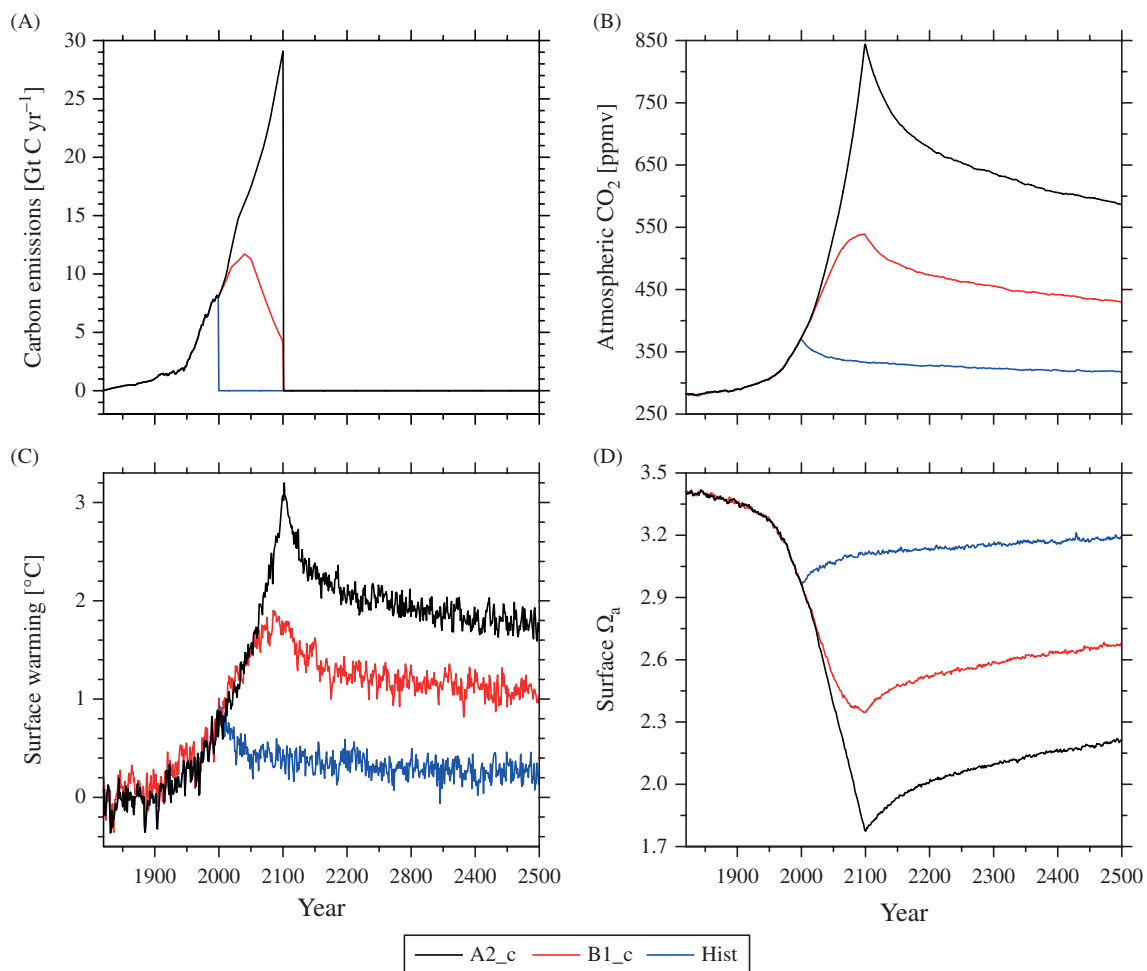


Figure 14.4 Long-term impact of 21st century carbon emissions. (A) Carbon emissions, (B) atmospheric CO_2 , (C) global-mean surface air-temperature change, and (D) global average saturation state of surface waters with respect to aragonite (Ω_a) for three illustrative emissions commitment scenarios evaluated with the NCAR CSM1.4-carbon model (Frölicher and Joos 2010). In the high 'A2_c' case and the low 'B1_c' case, 21st century emissions follow the SRES A2 and SRES B1 business-as-usual scenario, respectively. Emissions are set to zero in both cases after 2100. In the 'Hist' case, emissions are stopped in the year 2000.

model (Fig. 14.2C) and the CSM1.4-carbon (Fig. 14.4B), projected 21st century warming is lower in CSM1.4-carbon than in the Bern2.5CC model. This difference is primarily related to the difference in climate sensitivity; 2°C for a nominal doubling of CO₂ in the CSM1.4 versus 3.2°C for the Bern2.5CC best estimate.

Atmospheric CO₂ concentration increases by 300% and by 190% over this century in the high 'A2_c' and low 'B1_c' case, respectively (Fig. 14.4B). Thereafter, atmospheric CO₂ decreases only very slowly, although carbon emissions are (unrealistically) reduced to zero in 2100. Atmospheric CO₂ concentration is still twice as high by 2500 than in pre-industrial times in the 'A2_c' case. On the other hand, CO₂ falls below 350 ppmv within a few decades in the 'Hist' case. The global-mean surface temperature anomaly peaks at 3°C in the 'A2_c' case and at 1.7°C in the 'B1_c' case and remains elevated for centuries (Fig. 14.4C). In the 'Hist' case, global-mean surface temperature remains only slightly perturbed (0.2°C warming) by 2500. The global average saturation state of aragonite in the surface ocean closely follows the evolution of atmospheric CO₂. Mean surface Ω_a is reduced by about half in 2100 for the 'A2_c' case and remains reduced over the next centuries.

The long perturbation lifetime of CO₂ is a consequence of the centennial to millennial timescales of overturning of various carbon reservoirs. Most of the excess carbon is taken up by the ocean and slowly (on a multicentury to millennial timescale) mixed down to the abyss. Ultimately, interaction with ocean sediments and the weathering cycle will remove the anthropogenic carbon perturbation from the atmosphere on timescales of millennia to hundreds of millennia (Archer *et al.* 1999; see Chapter 2).

In conclusion, the results from the commitment scenarios show that the magnitude of 21st century CO₂ emissions pre-determines the range of atmospheric CO₂ concentrations, temperature, and ocean acidification for the coming centuries, at least in the absence of the large-scale deployment of a technology to remove excess CO₂ from the atmosphere. In other words, the CO₂ emitted in the next decades will perturb the physical climate system, biogeochemical cycle, and ecosystems for centuries.

14.5 Regional changes in surface ocean acidification: undersaturation in the Arctic is imminent

The impacts of climate change and ocean acidification on natural and socio-economic systems depend on local and regional changes in climate and acidification rather than on global average metrics. It is important to recognize that the global-mean metrics discussed in the previous sections lead to different changes regionally (Fig. 14.5). Fortunately, the spatial patterns of change in pH_T and surface Ω_a scale closely with atmospheric CO₂ (Figs 14.6 and 14.7). This eases the discussion of local changes for the scenario range and enables us to make inferences for local and regional changes from projected atmospheric CO₂. This section presents regional changes in the saturation state of aragonite, Ω_a , and pH_T for the three commitment scenarios introduced in the previous section and as evaluated in the NCAR CSM1.4-carbon model.

There are large regional differences in the surface saturation state for pre-industrial conditions and in its change over time (Figs 14.5 and 14.6). The surface ocean was saturated with respect to aragonite in all regions under pre-industrial conditions (Kleypas *et al.* 1999; Key *et al.* 2004; Steinacher *et al.* 2009); the lowest saturation levels are simulated in the Arctic and in the Southern Ocean, whereas surface water with saturation values above 4 can be found in the tropics.

Surface-water saturation is projected to decrease rapidly in all regions until 2100 and remains reduced for centuries for all three zero-emission commitment scenarios (Fig. 14.6). The largest ocean-surface changes are found in the tropics and subtropics for Ω_a . In the high 'A2_c' case, Ω_a in the tropics and subtropics decreases from a saturation state of more than 4 in pre-industrial times to saturation below 2.5 at the end of the 21st century. The saturation of tropical and subtropical surface waters remains below 3 until 2500. Although experimental evidence remains scarce, these projected low saturation states in combination with other stress factors such as increased temperature pose the risk of the irreversible destruction of warm-water coral reefs (Kleypas *et al.* 1999; Hoegh-Guldberg *et al.* 2007).

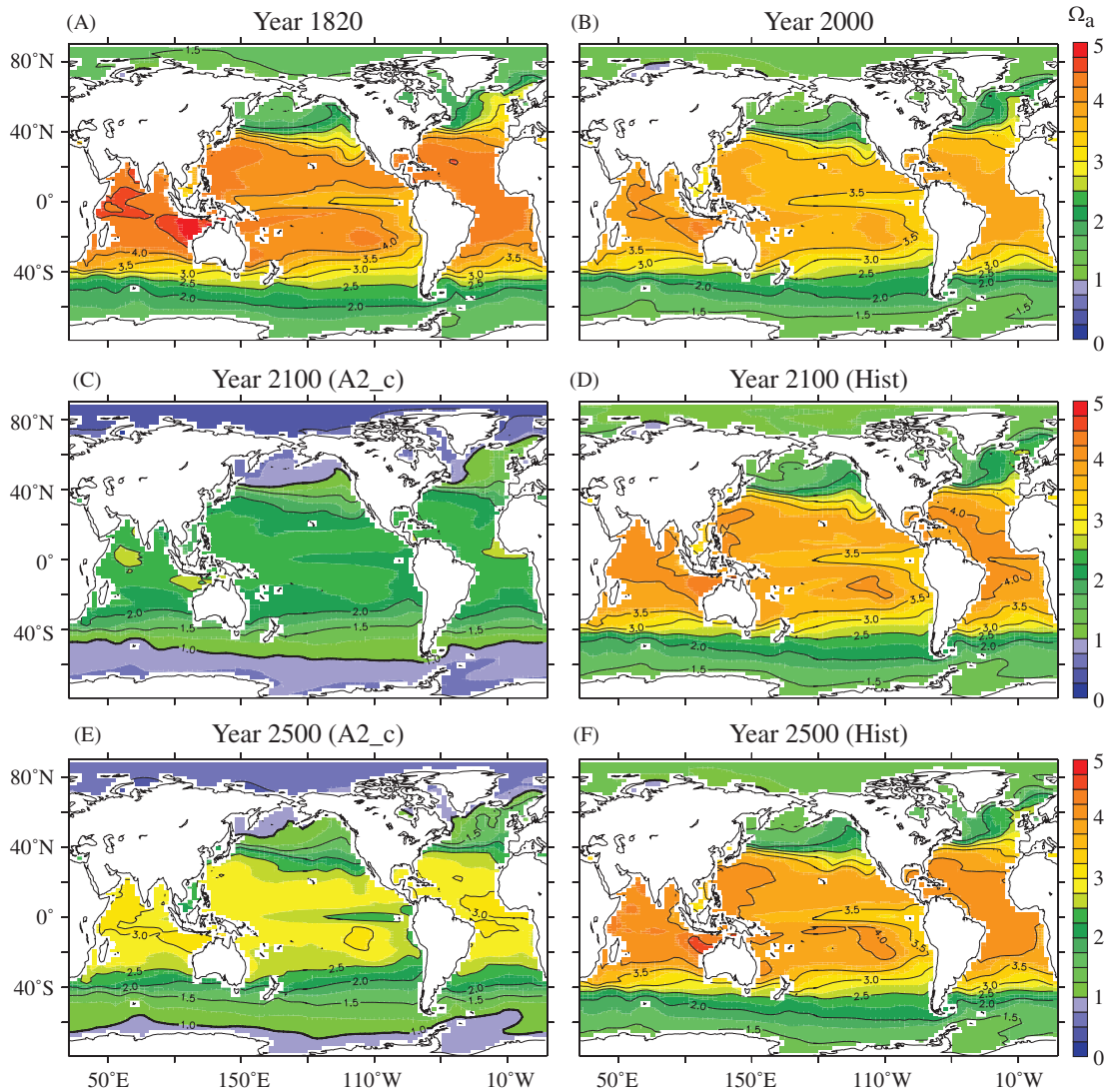


Figure 14.5 Regional distribution of the annual-mean saturation state with respect to aragonite (Ω_a) in the surface ocean for (A) pre-industrial conditions (here 1820), (B) by the year 2000, (C, D) by the end of the century, and (E, F) by 2500. The NCAR CSM1.4-carbon model was forced with reconstructed CO_2 emissions up to 2000. Emissions were set to zero after 2100 in the high 'A2_c' case (C, E) and after 2000 in the 'Hist' case (D, F). Blue colours indicate undersaturation and green to red colours supersaturation.

Undersaturation in the Arctic is imminent (Fig. 14.6C). By the time atmospheric CO_2 exceeds 490 ppmv (in 2040 in the 'A2_c' case), more than half of the Arctic Ocean will be undersaturated (annual mean; Steinacher *et al.* 2009). Undersaturation with respect to aragonite remains widespread in the Arctic Ocean for centuries even after cutting emissions in 2100 for both the 'A2_c' and the 'B1_c' cases (Frölicher and Joos 2010). The Southern Ocean

becomes undersaturated on average when atmospheric CO_2 exceeds 580 ppmv (Orr *et al.* 2005) and remains undersaturated for centuries for the 'A2_c' commitment case. Large-scale undersaturation in the Southern Ocean is avoided in the 'B1_c' and 'Hist' cases.

The main reason for the vulnerability of the Arctic Ocean is its naturally low saturation state. In addition, climate change amplifies ocean acidification in

282 OCEAN ACIDIFICATION

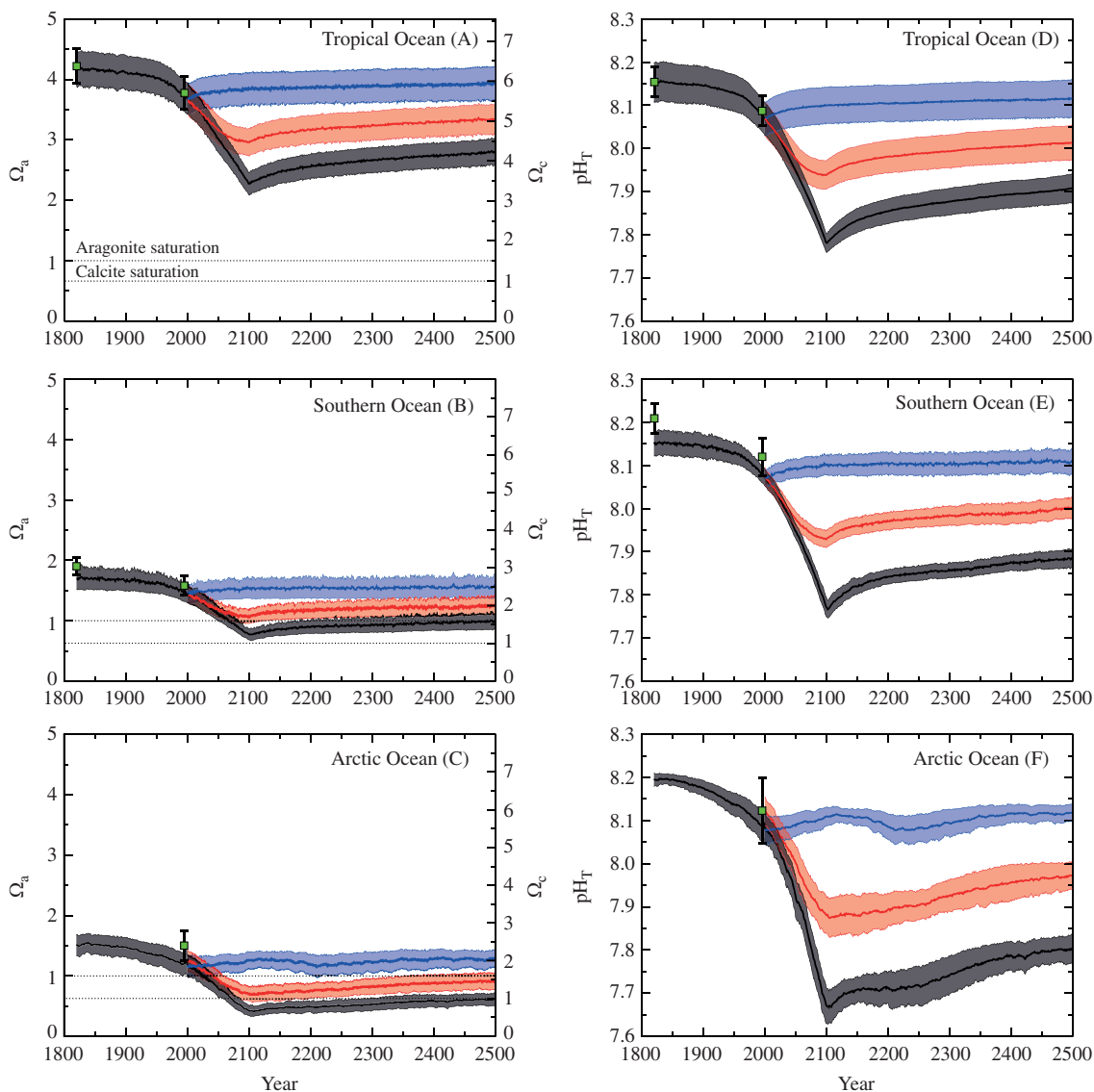


Figure 14.6 Projected evolution of CaCO_3 saturation states (left) and total pH (right) in the surface of the tropical ocean (30°N – 30°S), Southern Ocean (60°S – 90°S), and Arctic Ocean (65°N – 90°N , except the Labrador and Greenland–Iceland–Norwegian seas) and for emissions commitment scenarios with no ('Hist' case, blue line, blue shading), low ('B1_c' case, red line, red shading) and high ('A2_c' case, black line, grey shading) emissions in the 21st century. Saturation with respect to aragonite, Ω_a , is indicated on the left y-axis and with respect to calcite, Ω_c , on the right y-axis. Shown are modelled annual means as well as the combined spatial and interannual variability of annual-mean values within each region (shading, ± 1 SD). Observation-based estimates are shown by squares for the Southern Ocean and the tropics (GLODAP and World Ocean Atlas 2001, annual mean) and for summer conditions in the Arctic Ocean (CARINA database) with bars indicating the spatial variability. Model results are from the NCAR CSM1.4-carbon model. The level of $\Omega = 1$ separating supersaturated and undersaturated conditions for aragonite and calcite is shown by dashed, horizontal lines.

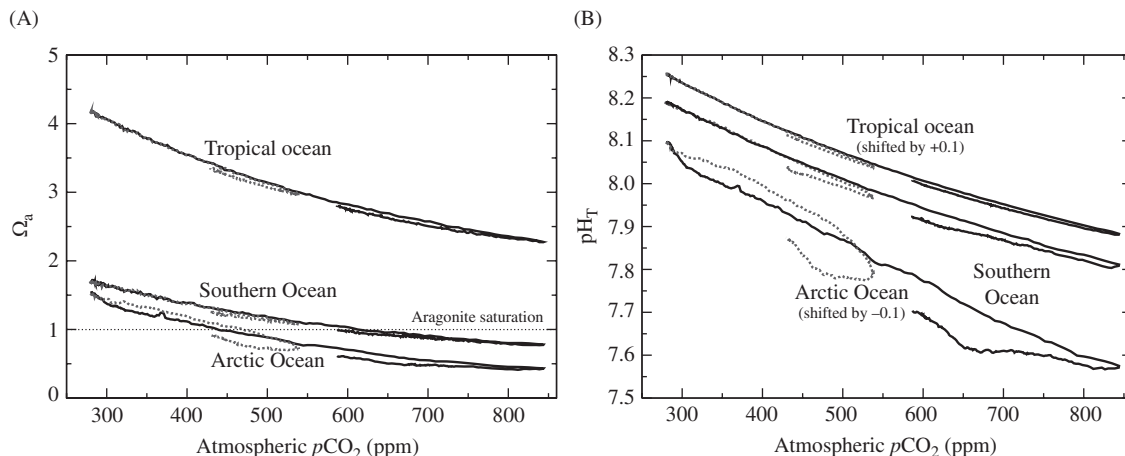


Figure 14.7 Saturation state (Ω_a) and total pH (pH_T) in surface water of three regions as a function of atmospheric CO_2 . Results are from the low 'B1_c' (dashed) and high 'A2_c' (solid) commitment scenarios. The relation between atmospheric CO_2 and saturation state and pH_T shows almost no path dependency in the tropical ocean and Southern Ocean. Some path dependency is found in the Arctic Ocean, with lower values in surface saturation and pH_T for a given CO_2 concentration simulated after the peak in atmospheric CO_2 . Note that the pH_T - CO_2 curves are shifted by +0.1 pH units for the tropical region and by -0.1 pH units for the Arctic region for clarity.

the Arctic, in contrast to other regions such as the Southern Ocean and the low-latitude oceans, where climate change has almost no effect on the saturation state in our simulations. Climate change amplifies the projected decrease in annual-mean Ω_a in the Arctic Ocean by 22% mainly due to surface freshening in response to the retreat of sea ice, causing local alkalinity to decrease and the uptake of anthropogenic carbon to increase (see also Chapter 3).

In summary, regional changes in the saturation state and pH_T of surface waters are distinct. The largest decrease in pH_T is simulated in the Arctic Ocean, where the lowest saturation is also found. Undersaturation is imminent in Arctic surface water (Figs 14.6 and 14.7) and remains widespread over centuries for 21st century carbon emissions of the order of 1000 Gt C or more.

14.6 Delayed responses in the deep ocean

Ocean acidification also affects the ocean interior as anthropogenic carbon continues to invade the ocean. Figure 14.8 displays how the saturation state and pH_T changes along the transect from Antarctica, through the Atlantic Ocean to the North Pole for the 'A2_c' commitment scenario. The saturation

horizon separating supersaturated from undersaturated water rises from a depth between ~2000 and 3000 m all the way up to the surface at high latitudes. The volume of water that is supersaturated with respect to aragonite strongly decreases with time. In parallel, the volume of water with low pH_T expands.

A general decrease in CaCO_3 saturation corresponds to a loss of volume providing habitat for many species that produce CaCO_3 structures. Following Steinacher *et al.* (2009), five classes of aragonite saturation levels are defined: (1) Ω_a above 4, considered optimal for the growth of warm-water corals, (2) Ω_a of 3 to 4, considered as adequate for coral growth, (3) Ω_a of 2 to 3, (4) Ω_a of 1 to 2, considered marginal to inadequate for coral growth, though experimental evidence is scarce, and finally (5) undersaturated water considered to be unsuitable for aragonite producers. Figure 14.9 shows the evolution of the ocean volume occupied by these five classes for the three commitment simulations. In the 'A2_c' case, water masses with saturation above 3 vanish by 2070 ($\text{CO}_2 \sim 630$ ppmv). Overall, the volume occupied by supersaturated water decreases from 40% in pre-industrial times to 25% in 2100 and 10% in 2300, and the volume of undersaturated water

284 OCEAN ACIDIFICATION

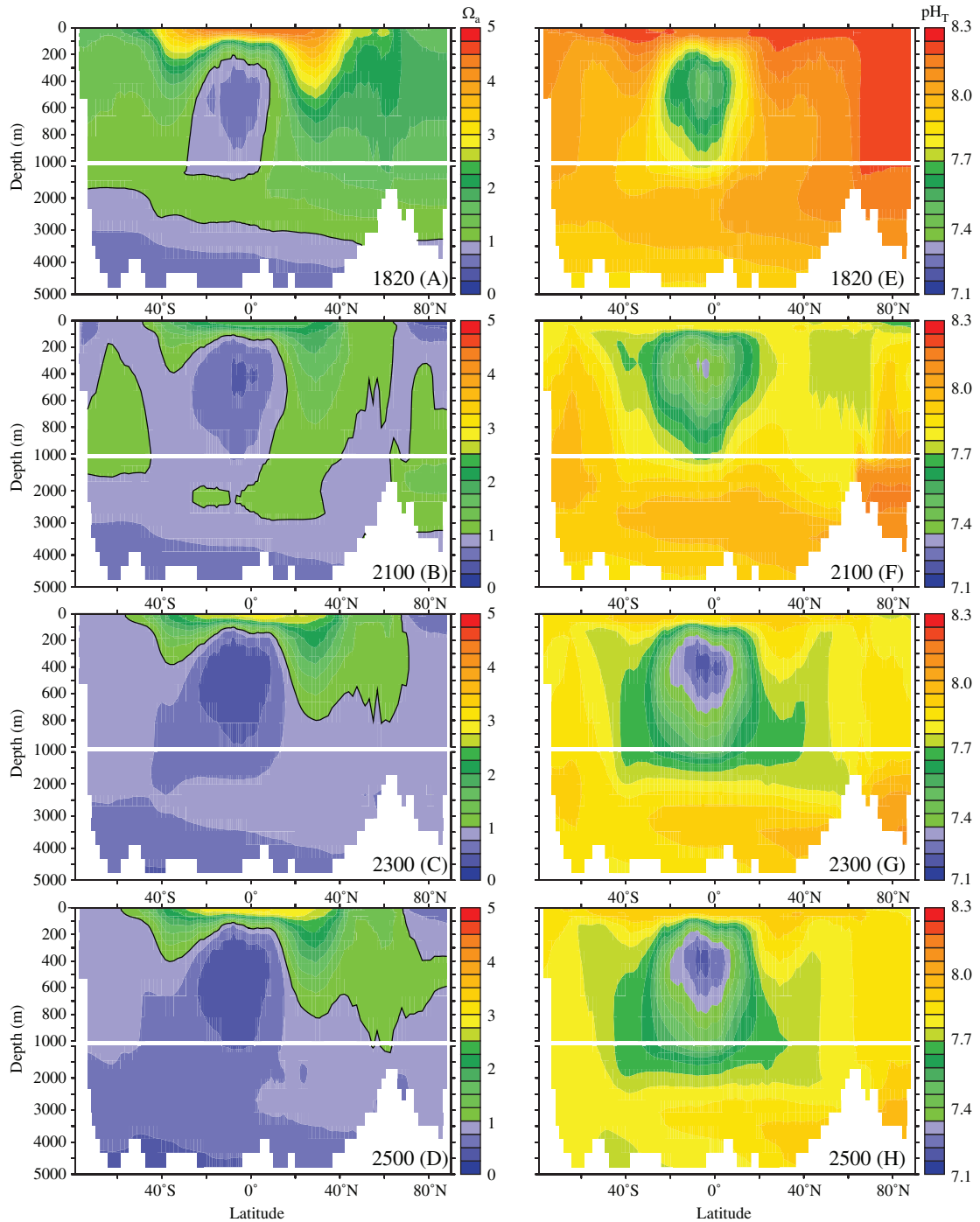


Figure 14.8 Saturation state with respect to aragonite (Ω_a , left) and total pH (pH_T , right) in the Atlantic and Arctic Oceans (zonal mean) for the high 'A2_c' commitment scenario by the year 1820 (A, E), 2100 (B, F), 2300 (C, G), and 2500 (D, H). Blue colours in the left panels indicate undersaturation. Note the different depth scales for the upper and the deep ocean, separated by the white horizontal line.

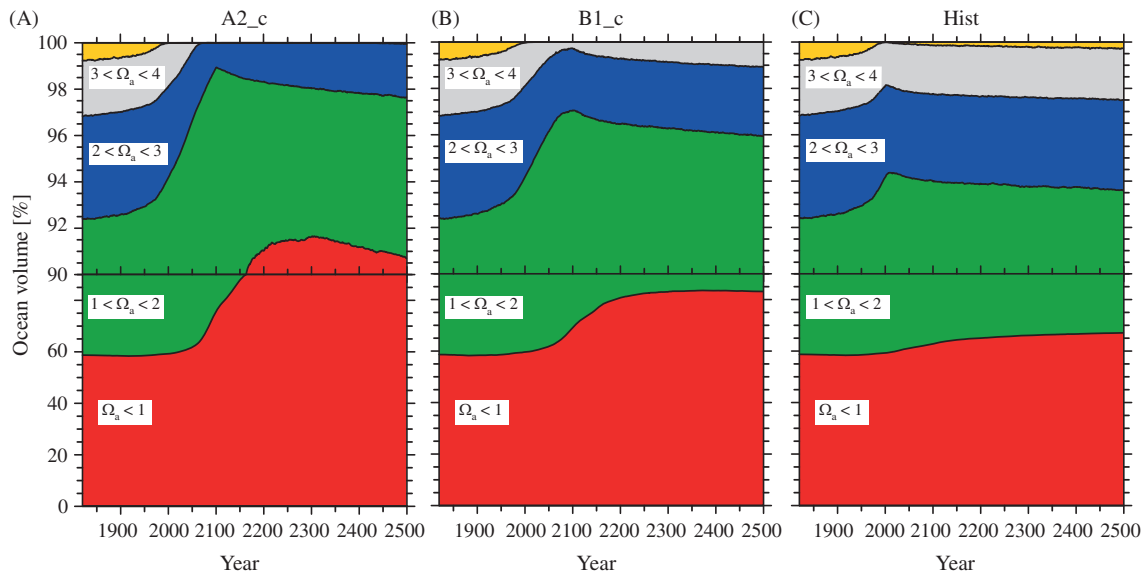


Figure 14.9 Evolution of the volume of water occupied by five classes of saturation with respect to aragonite (Ω_a) for the three illustrative emissions commitment scenarios. In the high 'A2_c' case and the low 'B1_c' case, 21st century emissions follow the SRES A2 and SRES B1 business-as-usual scenario, respectively. Emissions are set to zero in both cases after 2100. In the 'Hist' case, emissions are stopped in the year 2000. Note that the y-axis is stretched above 90%.

increases accordingly. The low 'B1_c' case also exhibits a large expansion of undersaturated water from 59 to 83% of ocean volume. In the 'Hist' case, the perturbations in volume fractions are much more modest and trends are largely reversed in the well-saturated upper ocean over the next few centuries.

The response of the saturation state is delayed in the ocean interior. This delay reflects the centennial timescales of the surface-to-deep transport of the anthropogenic carbon perturbation (Fig. 14.8). In the 'A2_c' case, the volume of undersaturated water reaches its maximum around 2300, 200 years after emissions have been stopped (Fig. 14.9). Even in the 'Hist' case, the volume fraction of supersaturated water continues to decrease. The fact that the volume fraction continues to change significantly after 2100 in the 'A2_c' and 'B1_c' cases demonstrates that some impacts of 21st century fossil fuel carbon emissions are strongly delayed and cause problems for centuries even for the extreme case of an immediate stop to emissions, i.e. the long-term commitment is substantial.

14.7 Pathways leading to stabilization of atmospheric CO_2

In this section, illustrative pathways leading to stabilization in atmospheric CO_2 are discussed in terms of their implications for projected ocean acidification and carbon emissions from the Bern2.5CC model (Fig. 14.10). The idea behind prescribing the CO_2 pathway is to illustrate how anthropogenic emissions have to develop if atmospheric CO_2 is to be stabilized as called for by the UNFCCC (UN 1992) and to illustrate the link between changes to the earth system and CO_2 stabilization levels.

Atmospheric CO_2 is prescribed to stabilize at levels ranging from 350 to 1000 ppmv. This causes surface-ocean saturation, Ω_a , to stabilize between 3.3 and 1.7 compared to a pre-industrial mean of 3.7. Surface-ocean pH_T stabilizes at 8.1 to 7.7 (pre-industrial 8.2). This corresponds to an increase in the hydrogen ion concentration of 20 to 300% relative to pre-industrial times. Global-mean change of temperature of the surface ocean is between 1°C for the 350 ppmv stabilization level and 5°C for the 1000 ppmv stabilization level when the climate

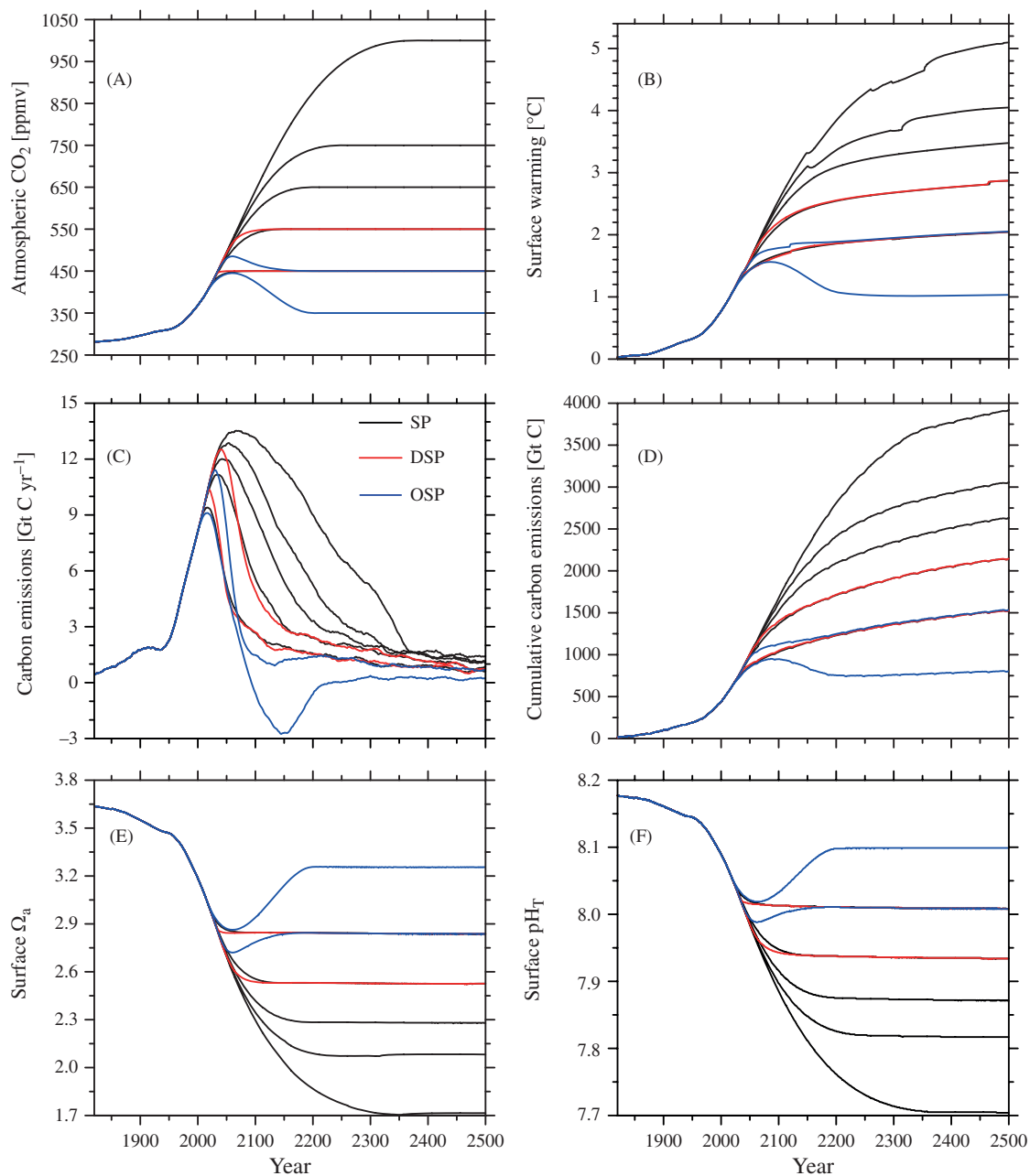


Figure 14.10 (A) Prescribed atmospheric CO₂ for pathways leading to stabilization and Bern2.5CC model projected (B) global-mean surface air temperature change, (C) annual and (D) cumulative carbon emissions, (E) global-mean surface saturation with respect to aragonite (Ω_a), and (F) global-mean surface total pH (pH_T). Pathways where atmospheric CO₂ overshoots the stabilization concentration are shown as blue lines and pathways with a delayed approach to stabilization as red lines; the different pathways to the same stabilization target illustrate how results depend on the specifics of the stabilization pathway. The label SP refers to stabilization profile, DSP to delayed stabilization profile, and OSP to overshoot stabilization profile.

sensitivity in the Bern2.5CC model is set to 3.2°C for a nominal doubling of CO₂.

Carbon emissions must drop if CO₂ is to be stabilized. Carbon emissions are allowed to increase for a few years to a few decades, depending on the pathway, but then have to drop in all cases and eventually become as low as the long-term geological carbon sink of a few tenths of a Gt C only. This is a consequence of the long lifetime of the anthropogenic perturbation. Atmospheric CO₂ thus reflects the sum of past emissions rather than current emissions. Cumulative emissions by 2500 for the Bern2.5CC model are in the range of 750 to 4000 Gt C for a stabilization between 350 and 1000 ppmv. Conventional fossil resources, mainly in the form of coal, are estimated to be about 5000 Gt C.

If emission reductions are delayed (DSP and OSP pathways in Fig. 14.10), more stringent reductions have to be implemented later in order to meet a certain stabilization target. This is illustrated by the two overshoot scenarios in which atmospheric CO₂ is prescribed to increase above the final stabilization levels and by the delayed scenarios where CO₂ is allowed to further increase initially.

The higher the emissions the larger the fraction of CO₂ emissions that stays airborne on timescales up to a few thousand years. This fraction is 20% for the 350 ppmv target and 40% for the 1000 ppmv target by the year 2500. The higher airborne fraction for high relative to low stabilization levels is primarily a consequence of the non-linearity of the seawater carbonate chemistry. The higher the partial pressure of CO₂, the smaller is the relative change in dissolved inorganic carbon for a given change in $p\text{CO}_2$. Thus, the partitioning of carbon between the atmosphere and the ocean shifts towards a higher fraction remaining airborne the greater the amount of carbon added to the ocean–atmosphere system.

14.8 Conclusions

We have examined a large set of projections for 21st century emissions for CO₂ and for a suite of non-CO₂ greenhouse and other air pollutant gases from the recent scenario literature (Van Vuuren *et al.* 2008b). Emissions scenarios provide an indication of the potential effects of mitigation policies. Most of the IAMs used to generate the set of baseline and

mitigation scenarios are idealized in many ways. New technologies and policies are assumed to be globally applicable and are often introduced over relatively short periods of time. Especially in the lowest mitigation scenarios, it is assumed that global climate policies can be implemented in the next few years to allow emissions to peak by 2020. These scenarios do not deal with the question of political feasibility and assume mitigation policies are implemented globally.

Physical impacts in terms of ocean acidification and climate change are lower in mitigation than baseline scenarios. Global average surface saturation with respect to aragonite is reduced to 3.1–2.4 by year 2100 in the mitigation compared to 2.3–1.8 in the baseline scenarios. The lowest scenarios result in a decrease in saturation state of 0.6 by 2100 compared with pre-industrial values and show only a small difference of 0.1 between current and end of century saturation conditions. These scenarios provide a guide to the range of global-mean surface acidification that may occur, assuming an ambitious climate policy. These low scenarios with forcing targets below 3 W m⁻² depart from the corresponding no-climate policy baseline by 2015–2020 and incorporate the widespread development and deployment of existing carbon-neutral technologies. They require socio-political and technical conditions very different from those now existing.

Global emissions in the scenarios with a 4.5 W m⁻² forcing target begin to diverge from baseline values by about 2020 to 2030, with emissions dropping to approximately present levels by 2100. CO₂, temperature, and ocean acidification start to diverge from the baseline projections later than emissions. This emphasizes the importance of early decisions to meet specific climate change mitigation targets.

Trends can be persistent and impacts of carbon emissions may continue for decades and centuries, long after carbon emissions have been reduced, due to the inertia in the climate–carbon system. This is exemplified by emissions commitment scenarios where carbon and other emissions are hypothetically set to zero and subsequent changes can be investigated. The projected global changes will affect different regions differently depending on their vulnerability to these changes. Widespread year-round undersaturation of surface waters in the

Arctic Ocean with respect to aragonite is likely to become reality in only a few years (Steinacher *et al.* 2009) and ocean acidification and Arctic undersaturation from baseline 21st century carbon emissions is irreversible on human timescales (Frölicher and Joos 2010). Globally, the volume of supersaturated water decreases for another two centuries after carbon emissions stop; the fraction of the ocean volume occupied by supersaturated water is as low as 8% in 2300 with the 'A2_c' case compared with 42% for pre-industrial conditions.

The focus of the analysis above is mainly on the magnitude of change. However, it should be stressed that rates of change are important. The rates of change of climate and ocean acidification co-determine the impacts on natural and socio-economic systems and their capabilities to adapt. Earlier analyses of the ice core and atmospheric records show that the 20th-century increase in CO₂ and its radiative forcing occurred more than an order of magnitude faster than any sustained change during at least the past 22 000 years (Joos and Spahni 2008). This implies that global climate change and ocean acidification, which are anthropogenic in origin, are progressing at high speed. It is evident from Fig. 14.2 that rates of change in surface-ocean pH_T and in Ω_a are much lower for the range of mitigation scenarios than for the range of baseline emissions scenarios.

A range of geoengineering options have been discussed to limit potential impacts of anthropogenic carbon emissions and climate change. Here, we summarize a few conclusions from a recent report (The Royal Society 2009). CO₂ removal techniques address the root cause of climate change by removing CO₂ from the atmosphere. Solar radiation management techniques attempt to offset the effects of increased greenhouse gas concentrations by causing the earth to absorb less solar radiation. Obviously, solar radiation management techniques do not contribute in a relevant way to mitigation of ocean acidification. Of the CO₂ removal methods assessed, none has yet been demonstrated to be effective at an affordable cost and with acceptable side-effects (The Royal Society 2009). If safe and low-cost methods can be deployed at an appropriate scale they could make an important contribution to reducing CO₂ concentrations and could provide a useful comple-

ment to conventional emissions reductions. Methods that remove CO₂ from the atmosphere without perturbing natural systems, and without requirements for large-scale land-use changes, such as CO₂ capture from air (IPCC 2005) and possibly also enhanced weathering, are likely to have fewer side-effects. Geoengineering techniques are currently not ready for application, in contrast to low-carbon technologies.

Experimental evidence has emerged in the past years that ocean acidification has negative impacts on many organisms and may severely affect cold- and warm-water corals or high-latitude species such as aragonite-producing pteropods. Considering the precautionary principle mentioned in the UNFCCC, our results may imply that atmospheric CO₂ should be stabilized somewhere around 450 ppmv or below in order to avoid the risk of large-scale disruptions in marine ecosystems. A stabilization of atmospheric CO₂ at or below 450 ppmv requires a stringent reduction in carbon emissions over the coming decades. The results from the IAMs suggest that such a low stabilization target is economically feasible.

14.9 Acknowledgements

This chapter is a contribution to the European Project on Ocean Acidification, EPOCA (FP7/2007–2013; no. 211384). We acknowledge support by the Swiss National Science Foundation and by the EU projects CARBOOCEAN (511176) and EUR-OCEANS (511106–2). Simulations with the NCAR CSM1.4-carbon model were carried out at the Swiss National Computing Center in Manno, Switzerland. We thank S. C. Doney, I. Fung, K. Lindsay, J. John, and colleagues for providing the CSM1.4-carbon code and J.-P. Gattuso, L. Hansson, and A. Oschlies for helpful comments.

References

- Archer, D., Kheshgi, H., and Maier-Reimer, E. (1999). Dynamics of fossil fuel CO₂ neutralization by marine CaCO₃. *Global Biogeochemical Cycles*, **12**, 259–76.
- Brewer, P.G. and Peltzer, E.T. (2009). Limits to marine life. *Science*, **324**, 347–8.
- Caldeira, K. and Wickett, M.E. (2003). Anthropogenic carbon and ocean pH. *Nature*, **425**, 365.

- Cohen, A.L. and Holcomb, M. (2009). Why corals care about ocean acidification: uncovering the mechanism. *Oceanography*, **2009**, 118–27.
- Comeau, S., Gorsky, G., Jeffree, R., Teyssié, J.-L., and Gattuso, J.-P. (2009). Impact of ocean acidification on a key Arctic pelagic mollusc (*Limacina helicina*). *Biogeosciences*, **6**, 1877–82.
- Doney, S.C., Fabry, V.J., Feely, R.A., and Kleypas, J.A. (2009). Ocean acidification: the other CO₂ problem. *Annual Review of Marine Science*, **1**, 169–92.
- Edmonds, J., Joos, F., Nakićenović, N., Richels, R.G., and Sarmiento, J.L. (2004). Scenarios, targets, gaps and costs. In: C.B. Field and M.R. Raupach (eds), *The global carbon cycle: integrating humans, climate and the natural world*, pp. 77–102. Island Press, Washington, DC.
- Frank, D.C., Esper, J., Raible, C.C. *et al.* (2010). Ensemble reconstruction constraints of the global carbon cycle sensitivity to climate. *Nature*, **463**, 527–30.
- Frölicher, T.L. and Joos, F. (2010). Reversible and irreversible impacts of greenhouse gas emissions in multi-century projections with the NCAR global coupled carbon cycle-climate model. *Climate Dynamics*, **35**, 1439–59.
- Gangstø, R., Gehlen, M., Schneider, B., Bopp, L., Aumont, O., and Joos, F. (2008). Modeling the marine aragonite cycle: changes under rising carbon dioxide and its role in shallow water CaCO₃ dissolution. *Biogeosciences*, **5**, 1057–72.
- Gehlen, M., Gangstø, R., Schneider, B., Bopp, L., Aumont, O., and Ethe, C. (2007). The fate of pelagic CaCO₃ production in a high CO₂ ocean: a model study. *Biogeosciences*, **4**, 505–19.
- Heinze, C. (2004). Simulating oceanic CaCO₃ export production in the greenhouse. *Geophysical Research Letters*, **31**, L16308, doi:10.1029/2004GL020613.
- Hester, K.C., Peltzer, E.T., Kirkwood, W.J., and Brewer, P.G. (2008). Unanticipated consequences of ocean acidification: a noisier ocean at lower pH. *Geophysical Research Letters*, **35**, L19601, doi:10.1029/2008GL034913.
- Hoegh-Guldberg, O., Mumby, P.J., Hooten, A.J. *et al.* (2007). Coral reefs under rapid climate change and ocean acidification. *Science*, **318**, 1737–42.
- Hutchins, D.A., Mulholland, M.R., and Fu, F. (2009). Nutrient cycles and marine microbes in a CO₂-enriched ocean. *Oceanography*, **22**, 128–45.
- Iglesias-Rodríguez, M.D., Halloran, P.R., Rickaby, R.E.M. *et al.* (2008). Phytoplankton calcification in a high-CO₂ world. *Science*, **320**, 336–40.
- IPCC (2005). IPCC Special Report on Carbon Dioxide Capture and Storage. Prepared by Working Group III of the Intergovernmental Panel on Climate Change (eds Metz, B., O. Davidson, H. C. de Coninck, M. Loos, and L. A. Meyer). Cambridge University Press, Cambridge.
- IPCC (2007). Climate Change 2007: Mitigation. Contribution of Working Group III to the Fourth Assessment Report of the Intergovernmental Panel on Climate Change (eds B. Metz, O.R. Davidson, P.R. Bosch, R. Dave, L.A. Meyer). Cambridge University Press, Cambridge.
- Joos, F. and Spahni, R. (2008). Rates of change in natural and anthropogenic radiative forcing over the past 20,000 years. *Proceedings of the National Academy of Sciences USA*, **105**, 1425–30.
- Joos, F., Prentice, I.C., Sitch, S. *et al.* (2001). Global warming feedbacks on terrestrial carbon uptake under the Intergovernmental Panel on Climate Change (IPCC) emission scenarios. *Global Biogeochemical Cycles*, **15**, 891–908.
- Key, R.M., Kozyr, A., Sabine, C.L. *et al.* (2004). A global ocean carbon climatology: results from Global Data Analysis Project (GLODAP). *Global Biogeochemical Cycles*, **18**, GB4031, doi:10.1029/2004GB002247.
- Kleypas, J.A., Buddemeier, R.W., Archer, D., Gattuso, J.P., Langdon, C., and Opdyke, B.N. (1999). Geochemical consequences of increased atmospheric carbon dioxide on coral reefs. *Science*, **284**, 118–20.
- Langdon, C. and Atkinson, M.J. (2005). Effect of elevated pCO₂ on photosynthesis and calcification of corals and interactions with seasonal change in temperature/irradiance and nutrient enrichment. *Journal of Geophysical Research – Oceans*, **110**, C09S07, doi:10.1029/2004JC002576.
- Langer, G., Geisen, M., Baumann, K. *et al.* (2006). Species-specific responses of calcifying algae to changing seawater carbonate chemistry. *Geochemistry, Geophysics, Geosystems*, **7**, Q09006, doi:10.1029/2005GC001227.
- Lüthi, D., Floch, M.L., Bereiter, B. *et al.* (2008). High-resolution carbon dioxide concentration record 650,000–800,000 years before present. *Science*, **453**, 379–82.
- Marland, G., Boden, T.A., and Andres, R.J. (2008). *Global, regional, and national CO₂ emissions*. Carbon Dioxide Information Analysis Center, Oak Ridge National Laboratory, US Department of Energy, Oak Ridge, TN.
- Moss, R.H., Babiker, M., Brinkman, S. *et al.* (2008). *Towards new scenarios for analysis of emissions, climate change, impacts, and response strategies*, 132 pp. Intergovernmental Panel on Climate Change, Geneva.
- Moss, R.H., Edmonds, J.A., Hibbard, K.A. *et al.* (2010). The next generation of scenarios for climate change research and assessment. *Nature*, **463**, 747–56.
- Müller, M.N., Schulz, K.G., and Riebesell, U. (2010). Effects of long-term high CO₂ exposure on two species of coccolithophores. *Biogeosciences*, **7**, 1109–16.
- Nakićenović, N., Alcamo, J., Davis, G. *et al.* (2000). *Special report on emissions scenarios*. Intergovernmental Panel on Climate Change, Cambridge University Press, New York.
- Orr, J.C., Fabry, V.J., Aumont, O. *et al.* (2005). Anthropogenic ocean acidification over the twenty-first century and its impact on calcifying organisms. *Nature*, **437**, 681–6.

- Plattner, G.-K., Knutti, R., Joos, F. *et al.* (2008). Long-term climate commitments projected with climate - carbon cycle models. *Journal of Climate*, **21**, 2721–51.
- Schimel, D., Grubb, M., Joos, F. *et al.* (1997). *IPCC technical paper III. Stabilisation of atmospheric greenhouse gases: physical, biological, and socio-economic implications*. Intergovernmental Panel on Climate Change, Geneva.
- Siegenthaler, U. and Oeschger, H. (1978). Predicting future atmospheric carbon dioxide levels. *Science*, **199**, 388–95.
- Solomon, S., Qin, D., Manning, M. *et al.* (2007). Technical summary. In: S. Solomon, D. Qin, M. Manning, Z. Chen, M. Marquis, K.B. Averyt, M. Tignor, and H.L. Miller (eds), *Climate change 2007: the physical science basis. Contribution of Working Group I to the Fourth Assessment Report of the Intergovernmental Panel on Climate Change*, pp. 19–91. Cambridge University Press, Cambridge.
- Steinacher, M., Joos, F., Frölicher, T.L., Plattner, G.-K., and Doney, S.C. (2009). Imminent ocean acidification in the Arctic projected with the NCAR global coupled carbon cycle-climate model. *Biogeosciences*, **6**, 515–33.
- Strassmann, K.M., Joos, F., and Fischer, G. (2007). Simulating effects of land use changes on carbon fluxes: past contributions to atmospheric CO₂ increases and future commitments due to losses of terrestrial sink capacity. *Tellus B*, **60B**, 583–603.
- Strassmann, K.M., Plattner, G.K., and Joos, F. (2009). CO₂ and non-CO₂ radiative forcing agents in twenty-first century climate change mitigation scenarios. *Climate Dynamics*, **33**, 737–49.
- The Royal Society (2009). *Geoengineering the climate: science, governance and uncertainty*. The Royal Society, London.
- UN (1992). *United Nations Framework Convention on Climate Change*. United Nations, New York.
- Van Vuuren, D.P., Feddema, J., Lamarque, J.-F. *et al.* (2008a). *Work plan for data exchange between the integrated assessment and climate modeling community in support of phase-0 of scenario analysis for climate change assessment (representative community pathways)*. http://cmip-pcmdi.llnl.gov/cmip5/docs/RCP_handshake.pdf
- Van Vuuren, D.P., Meinshausen, M., Plattner, G.-K. *et al.* (2008b). Temperature increase of 21st century mitigation scenarios. *Proceedings of the National Academy of Sciences USA*, **105**, 15258–62.
- Weyant, J.R., de la Chesnaye, F.C., and Blanford, G.J. (2006). Overview of EMF-21: multigas mitigation and climate policy. *Energy Journal*, **27**, 1–32.

Chapter 6

Fingerprints of changes in the terrestrial carbon cycle in response to large reorganizations in ocean circulation

Anil Bozbiyik, Marco Steinacher, Fortunat Joos, Thomas F. Stocker, and Laurie Menviel
Published in *Climate of the Past*, Volume 7, pp. 319–338, 2011.

Fingerprints of changes in the terrestrial carbon cycle in response to large reorganizations in ocean circulation

A. Bozbiyik^{1,2}, M. Steinacher^{1,2}, F. Joos^{1,2}, T. F. Stocker^{1,2}, and L. Menviel^{1,2}

¹Climate and Environmental Physics, University of Bern, Bern, Switzerland

²Oeschger Center for Climate Change Research, University of Bern, Bern, Switzerland

Received: 27 August 2010 – Published in Clim. Past Discuss.: 23 September 2010

Revised: 28 February 2011 – Accepted: 1 March 2011 – Published: 28 March 2011

Abstract. CO₂ and carbon cycle changes in the land, ocean and atmosphere are investigated using the comprehensive carbon cycle-climate model NCAR CSM1.4-carbon. Ensemble simulations are forced with freshwater perturbations applied at the North Atlantic and Southern Ocean deep water formation sites under pre-industrial climate conditions. As a result, the Atlantic Meridional Overturning Circulation reduces in each experiment to varying degrees. The physical climate fields show changes qualitatively in agreement with results documented in the literature, but there is a clear distinction between northern and southern perturbations. Changes in the physical variables, in turn, affect the land and ocean biogeochemical cycles and cause a reduction, or an increase, in the atmospheric CO₂ concentration by up to 20 ppmv, depending on the location of the perturbation. In the case of a North Atlantic perturbation, the land biosphere reacts with a strong reduction in carbon stocks in some tropical locations and in high northern latitudes. In contrast, land carbon stocks tend to increase in response to a southern perturbation. The ocean is generally a sink of carbon although large reorganizations occur throughout various basins. The response of the land biosphere is strongest in the tropical regions due to a shift of the Intertropical Convergence Zone. The carbon fingerprints of this shift, either to the south or to the north depending on where the freshwater is applied, can be found most clearly in South America. For this reason, a compilation of various paleoclimate proxy records of Younger Dryas precipitation changes are compared with our model results. The proxy records, in general, show good agreement with the model's response to a North Atlantic freshwater perturbation.

1 Introduction

Records from various climate proxies, especially Greenland ice cores and sediments from the North Atlantic, suggest that there have been large and abrupt changes in the climate during the last glacial period (Stocker, 2000; Rahmstorf, 2002; Clement and Peterson, 2008). Those transitions occurred on the time scale of a few decades to as little as a few years. The Greenland ice core from North GRIP contains 26 such abrupt warming events with amplitudes locally of up to 16 °C (NorthGRIP Members, 2004; Huber et al., 2006; Steffensen et al., 2008). These are known as *Dansgaard-Oeschger (D-O) events* (Dansgaard et al., 1984; Oeschger et al., 1984). There are also accompanying intense cold periods preceding these events which have a corresponding signal in the sediment cores from the northern Atlantic that are marked by distinct layers of ice rafted debris (Heinrich, 1988; Bond et al., 1993; Hemming, 2004). These surges of large amounts of ice into the sea, known as *Heinrich events*, are associated with some of the coldest temperatures in Greenland. Moreover, high-resolution measurements on Antarctic ice cores indicate that each of the D-O events has a less abrupt counterpart in the south (EPICA Community Members, 2006), likely due to the operation of the bipolar seesaw (Stocker and Johnsen, 2003). The last event in this sequence was the Younger Dryas cold event (12.7–11.6 cal kyr BP) and its termination with an abrupt warming (D-O 0). Signatures of those climate events have also been found in other climate archives, such as the isotopic and pollen records in the lake and marine sediments (Eicher et al., 1981; Ruddiman and McIntyre, 1981; Bond et al., 1993; Yu and Eicher, 1998; Ammann et al., 2000; Baker et al., 2001; Prokopenko et al., 2001; Voelker, 2002; Hughen et al., 2004; Barker et al., 2009) and European and Asian loess records (Ding et al., 1999; Porter, 2001; Rousseau et al., 2002) with a geographic distribution from Europe to Asia and beyond.



Correspondence to: A. Bozbiyik
 (bozbiyik@climate.unibe.ch)

Many of the characteristics of an abrupt climate change event can be simulated by coupled climate models that are perturbed by anomalous freshwater fluxes applied in the North Atlantic (Bryan, 1986; Mikolajewicz, 1996; Schiller et al., 1997; Manabe and Stouffer, 1999; Marchal et al., 1998; Timmermann et al., 2003; Knutti et al., 2004; Zhang and Delworth, 2005; Stocker and Marchal, 2000; Stouffer et al., 2006), which can cause the collapse of the Atlantic Meridional Overturning Circulation (AMOC).

The purpose of this paper is to determine the dependence of the climate and carbon cycle to the freshwater perturbations of different origins and identify fingerprints of these responses, by using a comprehensive atmosphere-ocean global circulation model coupled with a land surface model. Moreover, we quantify the changes in the carbon cycle during a collapse of the AMOC under pre-industrial conditions, considering both northern and southern possible origins. In this respect, both ocean response and the response of the land biosphere have been investigated with a special focus on a region of South America, where the model simulates particularly strong responses.

The reasons behind these abrupt changes found in the paleoclimate records have been surmised already in 1984 as a result of the nonlinear nature of the ocean-climate system (Oeschger et al., 1984). One such nonlinearity in the system is the existence of different modes of the thermo-haline circulation. At least some of the past abrupt climate changes, including the Younger Dryas event which caused intense cooling around the northern Atlantic and had climatic impacts over the globe, are considered to be a result of such rapid reorganizations (Boyle and Keigwin, 1987; Duplessy et al., 1988; Broecker, 1997; Clark et al., 2002). It is also documented in the records of ^{14}C and ^{10}Be that the ocean's ventilation in the North Atlantic was slowed during these cold periods (Hughen et al., 2000; Muscheler et al., 2000).

Any interruption in this ocean-wide circulation would have climatic effects both on regional and global scales. Those effects include intense cooling in the Northern Hemisphere, centred around Northern Europe and Greenland spreading to the northern Pacific (Okumura et al., 2009); changes in the marine ecosystem in the Atlantic (Schmittner, 2005) and sea level in the North Atlantic (Levermann et al., 2005); changes in precipitation patterns over the tropics due to the shift of the Inter-tropical Convergence Zone (ITCZ) (Vellinga and Wood, 2002; Dahl et al., 2005) and changes in the El Niño-Southern Oscillation phenomenon (Timmermann et al., 2005, 2007). The tropics have an important role in the abrupt climate change events, that is globalizing the Northern Hemispheric phenomenon of the AMOC shutdown through reorganizations in the ocean and the atmosphere (Chiang, 2009).

Understanding the response of the global carbon cycle to a large freshwater input into the ocean is necessary in order to explain the changes in the CO_2 concentration in the atmosphere during those abrupt events. During the intense cooling

events in Greenland and the more gradual Antarctic warm events, atmospheric CO_2 records show small but significant variations. Antarctic warm events A1 to A4 had seen atmospheric concentrations of CO_2 rise by about 20 ppmv (Stauffer et al., 1998; Indermühle et al., 2000), and by about the same amount during the much shorter Younger Dryas cold event (Monnin et al., 2001).

There are two different ideas regarding the source of this increase, that is either the ocean or the change of vegetation cover on land. While some modelling experiments have suggested that this atmospheric CO_2 increase was due to an oceanic release of carbon (Marchal et al., 1999; Schmittner and Galbraith, 2008), others suggest that it was due to a land carbon release (Köhler et al., 2005; Obata, 2007; Menviel et al., 2008). Ocean outgassing, for instance, can explain the increasing atmospheric CO_2 levels if the cooling of the sea surface is constrained to the high northern latitudes, the warming in the Southern Ocean is more pronounced and the contribution from land is not taken into account (Marchal et al., 1999). Schmittner and Galbraith (2008) also identified the ocean as the source of the atmospheric CO_2 increase during abrupt climate change events. Due to the absence of a complex atmospheric component, however, their model is probably limited in representing tropical precipitation changes that have a potentially large impact on the land biosphere.

The other possible contributor to the carbon cycle changes during abrupt climate change events is the land biosphere. Köhler et al. (2005) have found that under both pre-industrial and pre-Younger Dryas conditions, atmospheric CO_2 concentration rises due to the release of carbon from land, with the rise in the latter being slightly less pronounced.

More recently, Obata (2007) employed a general circulation model coupled with a simple land surface model to simulate an AMOC shutdown which caused a release of carbon from land resulting in an atmospheric CO_2 increase. In another study, using an earth system model of intermediate complexity (LOVECLIM), Menviel et al. (2008) suggested that in the event of an AMOC shutdown, the ocean acted as a carbon sink and the land as a carbon source under both pre-industrial and LGM (Last Glacial Maximum) conditions. Our results support their conclusions in many ways and extend it further by offering a clearer picture of the reaction of the land biosphere. An alternative location for applying freshwater perturbations is also a feature of our study which gives insight as to which hemisphere might have triggered such events in the past. The fingerprints of each trigger (northern or southern) are evident in the South American continent, which is the centre of action for carbon cycle changes on land. A comparison of our model results with paleo-records in that region is also provided.

The paper is organised as follows; in Sect. 2 a brief description of the model and the experiments is given, in Sect. 3 the results of our experiments are explained, which is followed by the discussion and conclusions in Sect. 4.

2 Methods

2.1 Model description

The model used in this study is a modified version of the CSM1.4-carbon climate model developed by the National Centre for Atmospheric Research (NCAR) in Boulder, USA. It is a fully coupled 3-D climate model that consists of land, ocean, atmosphere and sea ice components integrated via a flux coupler without flux adjustments (Boville and Gent, 1999).

The CSM 1.4-carbon source code is available electronically on the CCSM website (http://www.cesm.ucar.edu/working_groups/Biogeo/csm1_bgc/). The detailed description of the model is given by Doney et al. (2006) and Fung et al. (2005). Further information on the sensitivity of the model to external forcing can be found in the literature (Fung et al., 2005; Frölicher et al., 2009; Frölicher and Joos, 2010; Steinacher et al., 2009, 2010).

The atmospheric component CCM3 of the model has a spectral truncation resolution of approximately 3.75° (T31 Grid) and 18 vertical levels with 10 in the troposphere and 8 in the stratosphere (Kiehl et al., 1998).

The ocean component is called the NCAR CSM Ocean Model (NCOM) and has 25 vertical levels with longitudinal resolution of 3.6° and latitudinal resolution between 0.8° to 1.8° (T31x3 Grid) (Gent et al., 1998). Since the original version of CSM1.0, modifications have been made on horizontal and vertical diffusivity and viscosity to improve the equatorial ocean circulation and inter-annual variability.

The sea-ice component has the same resolution as the ocean component and the land component has the resolution of the atmosphere component. The overall water cycle is closed through a river runoff scheme.

In the fully coupled carbon-climate model, atmospheric CO₂ is a prognostic variable whose balance is determined by exchange fluxes with the land and ocean (Fung et al., 2005). The carbon-cycle in the ocean is based on the OCMIP-2 biotic carbon model (Najjar et al., 1992). The main differences between the original OCMIP-2 model and this model are that the biological source-sink term has been changed from a restoring formulation to a prognostic formulation and iron has been added as a limiting nutrient together with a parametrization for the iron-cycle (Doney et al., 2006).

The land biogeochemistry in the CSM1.4-carbon model is a combination of the NCAR Land Surface Model (LSM) (Bonan, 1996) and the Carnegie-Ames-Stanford Approach (CASA) biogeochemical model (Randerson et al., 1997), both of which are very well documented in the literature. Carbon is recycled in the CASA model following the life cycles of plant functional types (PFTs) through carbon assimilation via photosynthesis and carbon release via mortality, decomposition and microbial respiration (Fung et al., 2005). There are 3 soil texture types and 14 PFTs with fractional coverage of up to four PFTs within each model

grid-box. Carbon assimilation is calculated by the LSM by estimating stomatal conductance of CO₂ and water vapour in the leaves that are in shaded or directly lit conditions (Sellers et al., 1996). The net primary productivity (NPP) is fixed as 50% of the gross primary productivity (GPP) and is calculated by LSM to be allocated to three alive biomass pools of leaf, wood and roots. The allocation of NPP to these biomass pools is climate dependent, i.e., more of the NPP is allocated to the roots under water-limited conditions, while under light-limited conditions leaves are the preferred choice of biomass pool (Friedlingstein et al., 1999). In addition to three alive biomass pools, there are 9 dead biomass pools with leaf mortality contributing to the surface litter pool, root mortality contributing to the soil litter pool and wood mortality contributing to the coarse woody debris pool. The rest of the 9 dead biomass classes includes dead surface and soil microbial pools and slow and passive pools. The rate of transfer between different carbon pools is climate sensitive, determined by soil temperature and soil moisture saturation.

The carbon cycle is fully coupled to the water and energy cycles such that changes in the temperature and soil moisture calculated by LSM affect the NPP, allocation and decomposition rates and changes in the leaf area fraction calculated by CASA affect GPP transpiration and albedo. A terrestrial CO₂ fertilization effect is inherent to the model because carbon assimilation via the Rubisco enzyme is limited by the internal leaf CO₂ concentration that is dependent on the atmospheric CO₂ concentration. Thus, the productivity increases with the atmospheric CO₂ concentration, eventually saturating at high CO₂ levels (Doney et al., 2006).

Other land surface processes that can affect atmosphere-biosphere interactions, but are not implemented in this study include: explicit nitrogen cycle, fires, volcanic eruptions, dynamic vegetation change and anthropogenic land cover change.

2.2 Experimental setup

The model used in this study was brought to steady state with the 1000-year spin-up procedure undertaken by Doney et al. (2006). The 1000-yr integration is nearly stable with a minimal drift in the deep ocean. There are known biases in this spin-up, which include a cold bias in the surface air temperature (SAT) over the continental interior in the Northern Hemisphere, precipitation anomalies in the tropics such as the formation of the ITCZ over the Pacific as two bands of excess precipitation, and too much or too little precipitation over land in some tropical regions of South America, Central Africa and Southeastern Asia. These biases in the physical climate also lead to corresponding anomalies of NPP and carbon storage on land that include an underestimation of NPP in higher latitudes and an overestimation in lower latitudes. Nevertheless, overall global NPP compares well with the reconstructed pre-industrial levels of NPP. The simulated climatologies in carbon inventory and fluxes resemble those

determined from available observations. Atmospheric CO₂ excursions are small, 4 ppm over several centuries, and no abrupt changes are found during the integration. The spin-up stops at the 1820 AD atmospheric CO₂ levels and our experiments start at this point in time. Additional runs with two of the freshwater settings have been performed starting from a slightly different point in time at the steady state in order to account for the effects of short term variability in the climate system. The starting points for those additional runs are chosen with a different ENSO state than the original runs.

The freshwater hosing experiments (Table 1) are designed to investigate the response of the ocean and climate system to a freshening of the surface water around the key deep water formation sites in the Northern and Southern Hemispheres under pre-industrial conditions of atmospheric CO₂ (278 ppm). Perturbations applied simulate a change in the freshwater budget of the high-latitude ocean as a result of a surge in glacial melt-water from Greenland, Antarctica, or other pre-industrial continental glacial formations such as the Laurentide icesheet, which is responsible for the abrupt climate events of Younger Dryas 12.7–11.6 cal kyr BP and another smaller one during Holocene around 8200 yr BP (Barber et al., 1999).

It is important to note here that even though we compare our results with paleoclimate reconstructions, the boundary conditions used in our experiments are not glacial boundary conditions which had significantly different levels of atmospheric CO₂, as well as differences in temperature, precipitation and biome distribution, especially in mid- and high-latitudes. In the Discussion section, we address this issue by comparing it to a previous study by Menviel et al. (2008).

For each perturbation the freshwater input was assumed to be a rectangular pulse uniform over 100 years. The duration of each run is 300 years including the duration of the perturbations. The three different sites where the freshwater is applied are the northern Atlantic Ocean between the latitudes of 50° N and 70° N (including the Labrador Sea) and the Weddell Sea and Ross Sea in the Southern Ocean.

The perturbation, which is actually a negative salinity flux as there is no actual water volume in the parametrization of the model, is set to correspond to a freshwater flux of 1.0 Sv (in two of the experiments smaller perturbations of 0.5 Sv and 0.3 Sv are applied) distributed uniformly across the area of the perturbation. There has been no salt compensation performed (Stocker et al., 2007). The amounts of the freshwater fluxes are highly idealized and do not directly correspond to the recorded events in the past.

3 Results

3.1 Global average

The most direct response of the climate system to a freshwater perturbation is a reduction in the maximum strength

Table 1. List of experiments given together with the region where freshwater is applied and the size of the perturbation. Different starting years for perturbations in the ensemble experiments refer to the date in the Control and are chosen according to the ENSO index in order to account for the effect of natural variability in the system. In addition to the ensemble experiments, three sensitivity simulations have been performed to investigate the effect of a different perturbation size and/or freshwater input region.

Experiment	Freshwater Input	Freshwater Flux (Sv)	Start Year
Control	–	–	0
Ensemble Experiments			
1.0 NA-1	North Atlantic	1.0	0
1.0 NA-2	~	1.0	30
1.0 NA-3	~	1.0	126
1.0 NA-4	~	1.0	263
1.0 NA-5	~	1.0	295
1.0 Ros-1	Ross Sea	1.0	0
1.0 Ros-2	~	1.0	30
1.0 Ros-3	~	1.0	126
1.0 Ros-4	~	1.0	263
1.0 Ros-5	~	1.0	295
Sensitivity Experiments			
1.0 Wed	Weddell Sea	1.0	0
0.3 NA	North Atlantic	0.3	0
0.5 NA	~	0.5	0

of the North Atlantic Meridional Overturning Circulation (Fig. 1a). By the end of the perturbation, the maximum North Atlantic MOC strength is reduced from around 24 Sv to 2 Sv for experiment 1.0 NA and to 4 Sv and 6 Sv for experiments 0.5 NA and 0.3 NA, respectively. Along with this reduction in the North Atlantic Deep Water, the Antarctic Bottom Water penetrates further into the Atlantic. For the 1.0 NA experiment, the circulation does not recover during our simulations, whereas in the 0.5 NA and 0.3 NA experiments it regains its original strength by the end of the experiments.

In response to a freshwater flux from near Antarctica (1.0 Wed and 1.0 Ros), the strength of the North Atlantic MOC slightly increases in the beginning, which is followed by a reduction of smaller magnitude than in the 1.0 NA experiment. The mechanism behind this is explained by Stouffer et al. (2007) as the *dilution effect*, i.e., freshwater input from the Southern Ocean, does not stay there but is rather transported to the other parts of the ocean. This is evidenced by the time evolution of salinity. The result of the freshwater perturbation is a decrease in the global mean surface air temperature (SAT) in all experiments (Fig. 1b). Together with the changes in the precipitation fields, these two climatic variables cause the atmospheric CO₂ concentration to increase by up to 20 ppmv in the 1.0 NA experiments and to decrease by up to 10 ppmv in the Southern Ocean experiments (Fig. 1c).

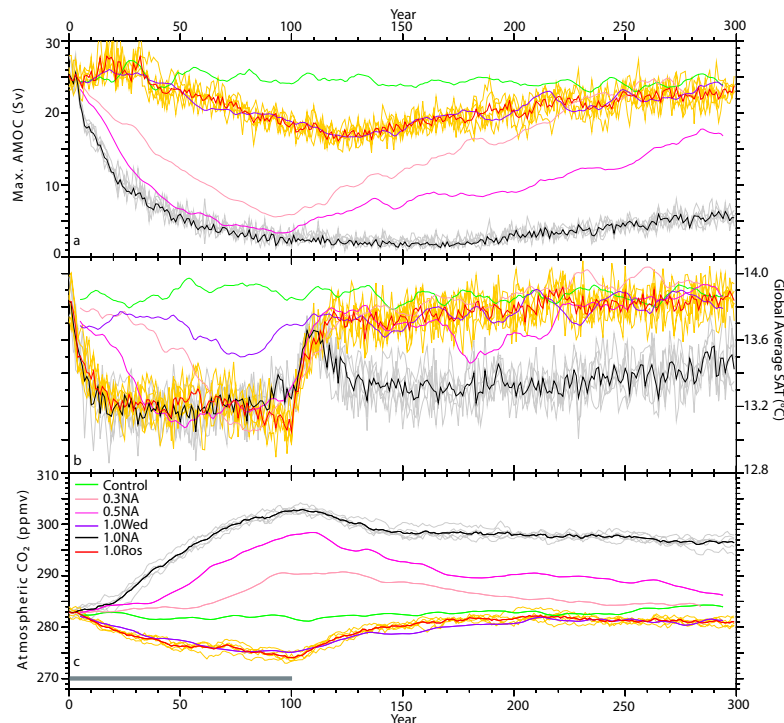


Fig. 1. Time series of: (a) Maximum North Atlantic MOC strength (Sv), (b) Global Annual Mean SAT ($^{\circ}\text{C}$) and (c) surface atmospheric CO_2 concentration (ppmv). The green curve represents the Control; pink and magenta represent the smaller perturbations from the NA of 0.3 and 0.5 Sv, respectively, and violet represent the 1.0 Wed perturbation. The other two perturbations of 1.0 NA (black) and 1.0 Ros (red) are given as the averages of five ensemble members and the grey and orange curves in the background are the five individual runs in each ensemble, intended to show the spread of the anomalies. The values are 10-year box averages. The grey bar at the bottom marks the duration of the freshwater input.

3.2 Physical response

Because temperature and precipitation changes impact the carbon cycle, we first present changes in these two variables.

In the 1.0 NA experiment annual mean surface air temperature in the Northern Atlantic region decreases drastically (Fig. 2, left column) with reduced heat input from lower latitudes, as a result of the shutdown of the MOC in the Atlantic. Anomalies of up to -15°C are observed over the North Atlantic between Iceland and Scandinavia. The cooling is not confined to the North Atlantic region but further extends to the high latitudes over North America and Asia. In line with the idea of inter-hemispheric redistribution of heat, the Southern Hemisphere exhibits warm anomalies of up to 3°C over the Southern Pacific, Atlantic and Indian oceans and up to 6°C over South America. In 1.0 NA, this general pattern stays roughly the same even 200 years after the end of the freshwater input, except for a temporary spike in the SAT coinciding with the end of the perturbation. The reason for that warming lies in the subsurface warming in the North Atlantic

as a result of the increased stratification. A resumption of the vertical mixing, once the freshwater perturbation is switched off, brings up water to the surface from the subsurface warm pool which was created during the AMOC shut-down. By that time, this subsurface warm pool is mixed with the surface water and, subsequently, the atmosphere. However, this mixing is insufficient to restart the AMOC because of the diluted state of the surface water. Even though there is a slight increase in the salinity during this exchange, it is not enough to bring it to the original values. To a lesser extent, the warming is also caused by the delayed warming in the Southern Hemisphere, as it takes time for the warming to penetrate towards Antarctica.

Generally, the duration and severity of the atmospheric cooling (and warming) is dependent on the size of the freshwater flux. However, South America remains the region where the strongest warming occurs in all the North Atlantic experiments.

In the 1.0 Ros and 1.0 Wed experiments the strongest cooling in surface temperatures is observed in the Southern

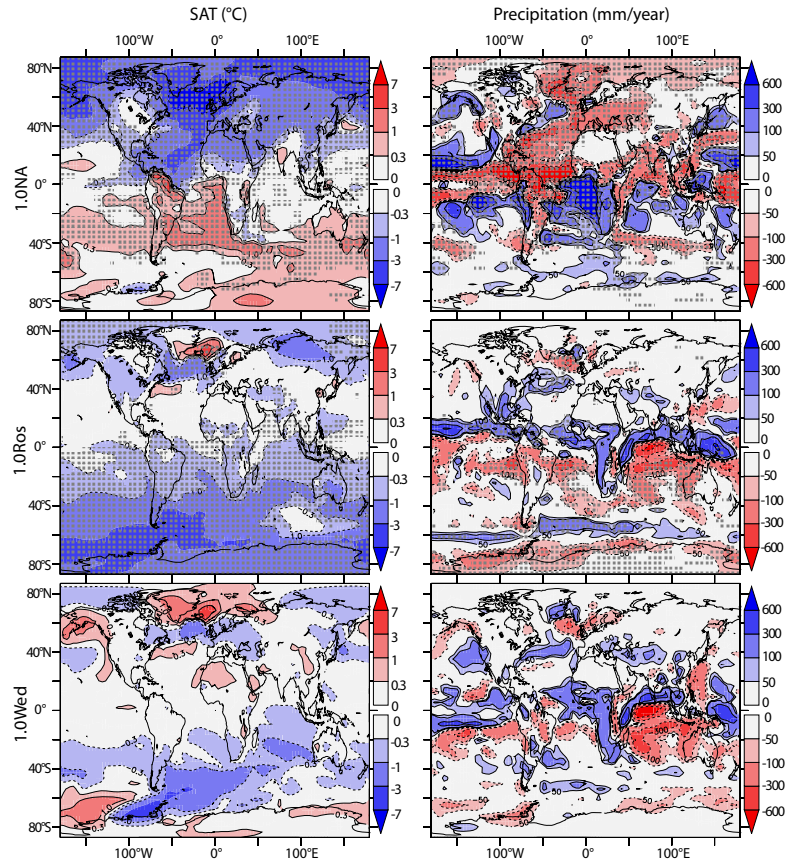


Fig. 2. The left column shows the SAT anomalies ($^{\circ}\text{C}$) with respect to the Control by the end of the 100-year perturbation (decadal average of the model years 97–106) for the experiments 1.0NA (top), 1.0Ros (middle), and 1.0Wed (bottom). The right column shows the precipitation anomalies (mm yr^{-1}). Stippled areas indicate where the ensemble mean anomaly is significantly different from zero at the 67% level (Student's t-Test). Confidence level of the 1.0Wed experiment results is not quantified since there is only one simulation available.

Hemisphere near Antarctica and the strongest warming is in the Northern Hemisphere near Greenland. But in the 1.0Ros experiment, partial cold anomalies can also be seen in the Northern Hemisphere high latitudes. Because of this more widespread cooling in the 1.0Ros experiment, the range of global average SAT anomaly is comparable to the 1.0NA experiment, even though local anomalies are not as severe.

Overall, the regional amplitudes of the anomalies are smaller for the Southern Ocean perturbations. This is in line with the fact that there is a smaller reduction in the AMOC strength, as mentioned in the previous section. This can be due to the fact that freshwater is diluted in the larger volume of the Southern Ocean. Thus, a larger freshwater input is needed in order to achieve a response similar in magnitude to the 1.0NA experiment.

As air temperature and sea surface temperature play a great role in the determination of the precipitation patterns, a change in those fields also cause a change in the amount and distribution of precipitation over the globe (Fig. 2, right column). The largest precipitation anomalies occur mainly at low latitudes and over the oceans, where water vapour availability is the greatest. But for the following analysis of the land biosphere, the most important changes are in South America and Africa. In the 1.0NA experiment, total annual precipitation anomalies of up to 1.6 m are recorded in those locations.

The distribution of the most severe precipitation anomalies near the equator is consistent with what is expected from a shift of the ITCZ. Northern Atlantic perturbations cause a southward shift of the ITCZ as a result of the cooling in the Northern Hemisphere, whereas perturbations from the Southern Ocean cause a northward shift. This northward

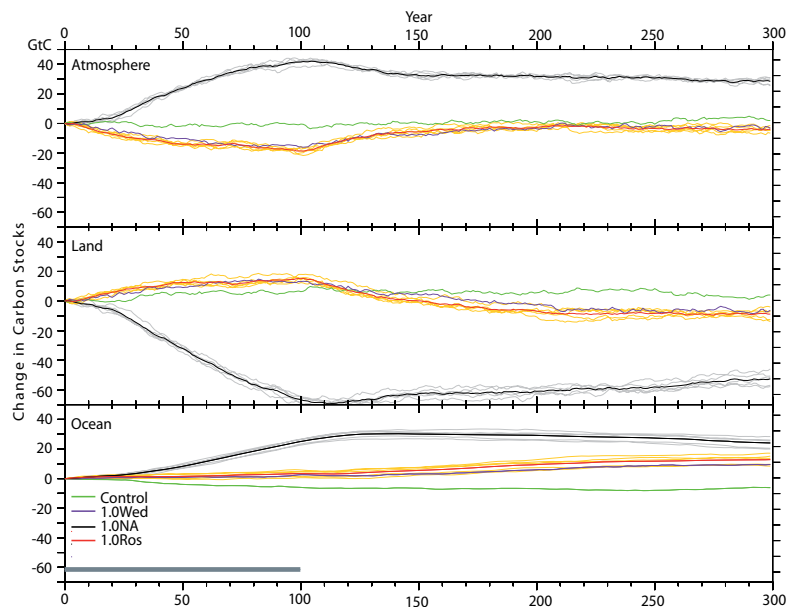


Fig. 3. Responses to freshwater perturbations of different carbon inventories: atmosphere (top), land (middle), and ocean (bottom). The values are the anomalies with respect to the 100-year average of the Control and given in GtC. Values are 10-year box averages. The two perturbations of 1.0NA (black) and 1.0Ros (red) are given as the averages of five ensemble members and the grey and orange curves in the background are the five individual runs in each ensemble. The grey bar at the bottom marks the duration of the freshwater input.

migration of the ITCZ was also simulated in a study by Menviel et al. (2010). In that study, freshwater was applied uniformly over the Southern Ocean leading to similar changes in the ocean circulation and deep water formation. A decrease in the SST and SAT values in the Southern Hemisphere accompanied by subsurface warming in the Southern Ocean is also one of the commonalities.

3.3 Response of the carbon cycle

3.3.1 Changes in the global carbon inventories

Climatic change, as a result of a freshwater perturbation as in our experiments, affects the distribution of carbon in the three main reservoirs of land, ocean and atmosphere. The freshwater perturbations from the northern deep water formation site cause an increase in the atmospheric carbon inventory, while the southern perturbations cause a decrease and associated changes in each carbon inventory (Fig. 3).

The response of the land carbon stocks to the three perturbations from the North Atlantic amounts to a decrease by several tens of GtC. The magnitude of this decrease is proportional to the strength of the freshwater perturbation. It is also important to note here that in the control run a drift of about -6 GtC over 300 years is recorded in the ocean. This does not invalidate our experiments as the magnitude is relatively small. The negative carbon drift in the ocean is

slightly masking the carbon uptake by the ocean in all experiments.

Changes in the land carbon stocks immediately affect the atmosphere, while the time required for this perturbation to reach the much larger inventory of the ocean is longer. The land carbon stocks decline as a response to the 1.0NA perturbation causing the atmospheric CO_2 to increase, which, in time, is partially taken up by the ocean. Yet, in the time frame of our simulations a larger than expected portion of the carbon emitted from land remains in the atmosphere. This indicates that the ocean does not behave like a passive carbon sink, in which case it would be expected to take up a much larger proportion of the carbon emitted to the atmosphere. Instead, after the initial increase, total carbon in the ocean stays quite stable until the end of the experiment. This points to a reorganization of the ocean carbon cycle, which leads to a new equilibrium with the atmosphere.

For the 1.0NA experiment, emissions from the land biosphere exceed 60 GtC by the end of the perturbation, and yet only about 20 GtC are taken up by the ocean by the end of the experiment. This amount corresponds to less than one third of the total emitted carbon by the land biosphere. At this time, some 30 GtC are still in the atmosphere and about 15 GtC go back to the land due to the recovery of the land biosphere. The changes in carbon stocks scale with the size of the freshwater perturbations.

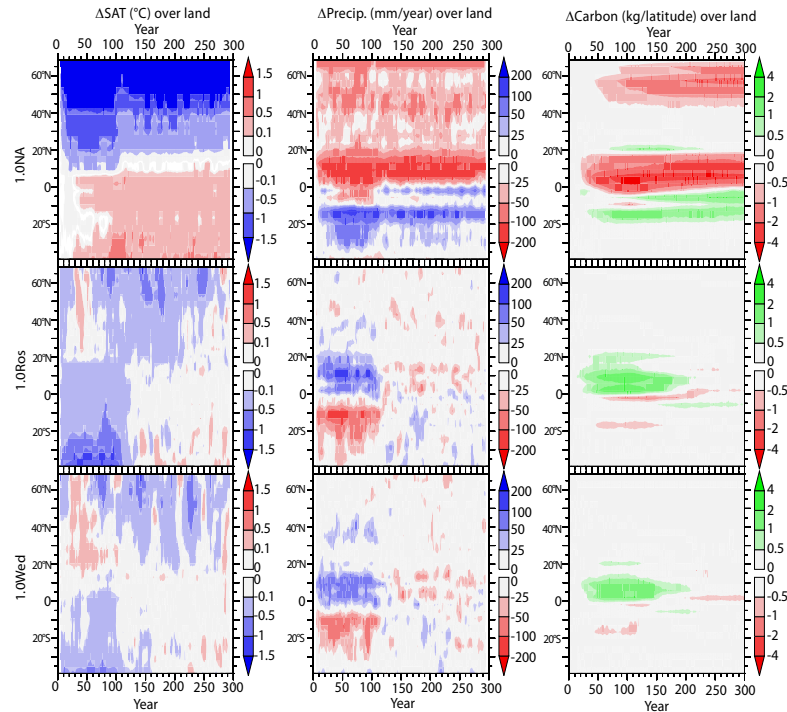


Fig. 4. From top to bottom, each row represents the experiments 1.0NA, 1.0Ros, and 1.0Wed, respectively. Given in each column are zonal mean changes of temperature (left), precipitation (middle) and total carbon per latitude (right) on land. The precipitation and the SAT values are averaged over 10 years.

In the experiments with a freshwater input from Antarctica, the change in the land carbon stocks is an increase. The peak values of the increase in the land carbon pools are about 20 GtC for experiment 1.0Ros and about 12 GtC for 1.0Wed, resulting in a reduced atmospheric CO_2 concentration. However, these changes are not permanent and return to their original values soon after the perturbations stop. Changes in the ocean carbon inventory are smaller, reaching about 10 GtC by the end of the experiments and cannot be easily distinguished from the variations in the control. It is safe to assume that a southern perturbation on a scale comparable to our experiments (that is to say less intense than a northern perturbation) creates changes in the land biosphere that are relatively short-lived. The response of the ocean to decreasing atmospheric CO_2 concentrations would be releasing carbon to balance it. Whereas, the slight increase in the oceanic carbon instead of an expected decrease leads us to believe that the changes in the carbon cycle in the ocean play a role in this experiment, too. Hence, the stable behaviour of the ocean carbon inventory during the first 140 years of the 1.0Ros experiment is probably due to the fact that the competing effects of the reorganization of the carbon cycle and the decrease of the atmospheric CO_2 concentrations due to land uptake cancel each other out.

A similar experiment performed with the LOVECLIM climate model did not lead to any significant changes in atmospheric CO_2 (Menviel et al., 2010).

3.3.2 A more regional look

The response of the land biosphere shows clear latitudinal dependencies accompanied by the strong latitudinal coupling of the climate parameters, temperature and precipitation. Figure 4 shows the zonal averages of the changes in the temperature and precipitation fields over land, and total land carbon stocks per latitude. Changes in the carbon stocks closely follow the changes in the precipitation in lower latitudes, while in higher latitudes temperature anomalies become more dominant. This is not surprising given the fact that, as a result of an MOC shutdown, in the higher latitudes temperature anomalies are larger than precipitation anomalies and the lower latitudes experience substantial changes in precipitation due to the shift of the ITCZ and the exponential dependence of saturated water vapour pressure to temperature. Hence, small temperature changes translate into large differences in precipitation in the tropics where the ambient temperature is higher (Bard, 2002). Nevertheless, globally, precipitation anomalies are responsible for most of the change

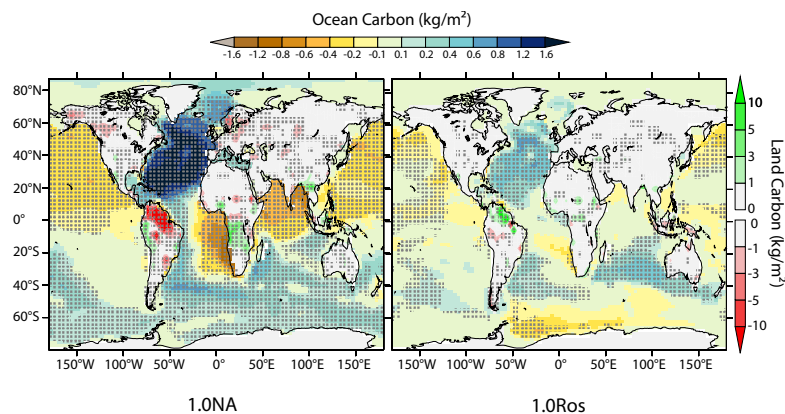


Fig. 5. Changes in the carbon stocks (kg m^{-2}) in the ocean and on land (note the different colour bars) for 1.0NA and 1.0Ros experiments, by the end of the perturbation (decadal average of model years 97–106). Stippled areas indicate where the ensemble mean anomaly is significantly different from zero at the 67% level (Student's t-Test).

in the carbon stocks on land as most of the carbon emissions stem from the large vegetation pool of the low latitudes.

However, Fig. 4 cannot capture the inhomogeneous distribution of changes within those climatic zones. Therefore, we consider a snapshot of the distribution of the changes in the carbon stocks both on land and in the ocean (Fig. 5). In the ocean, most of the carbon ends up in the Atlantic Ocean. However, this does not necessarily mean an increased air-sea gas exchange in this region. The main reason for the carbon build-up in the Atlantic is the increased transport of DIC-rich Antarctic Bottom Water and a smaller amount comes from the air-sea gas exchange. The decreased primary production makes a small negative contribution. This reorganization also causes the reduction of total carbon in the other oceans, especially in the northern part of the Pacific and Indian Oceans. The contribution from the air-sea gas exchange is positive in the Pacific and Indian oceans, whereas in the Southern Ocean outgassing prevails. The carbon stocks in the North Pacific are influenced negatively by the increased circulation at depth due to the onset of deep water formation in this region. The initiation of North Pacific meridional overturning as a result of the AMOC shutdown has also been reported in previous modelling and reconstruction studies (Mikolajewicz et al., 1997; Okazaki et al., 2010; Menviel et al., 2011). This is an interesting feature which requires further investigation with regards to the underlying mechanisms. However, this is beyond the scope of the present study.

On land, the biggest changes occur in the tropical regions of South America, Africa and southeastern Asia, with the high latitudes contributing to anomalies smaller in magnitude but more widespread. As has been shown in Fig. 4, the regions near the equator exhibit large precipitation anomalies due to the shift of the ITCZ, either positive or negative.

In order to account for the life-cycle of the land vegetation and different cycling time-scales of carbon, the model includes various carbon pools, as mentioned in the methods section. The biggest change occurs in the vegetation pool (Fig. 6). Carbon inventories in the vegetation decrease in northern latitudes and in northern South America. The response of the soil carbon is determined by the competing influences of the input from the vegetation pool as well as the microbial overturning in the soil, which is reduced due to the lower temperatures. The sum of these two influences at high latitudes, where bigger proportions of carbon are stored in the soil, is a small increase in soil carbon. Where the temperature change is positive, as is the case in parts of South America, the proportion of the soil carbon compared to the carbon stored in the vegetation cover is small. In northern South America soil carbon content amounts to about 8 kg m^{-2} on average, whereas average carbon stored in the vegetation cover is more than 20 kg m^{-2} . Because of these factors, the contribution of the soil carbon pool to the changes in the atmospheric CO_2 concentration remains small.

In order to quantify the correlation between the anomalies in various climatic variables and the changes in the carbon stocks on land, a linear regression analysis has been performed. As the vegetation carbon pool is the biggest contributor to those changes and it is directly affected by the changes in the net primary production (NPP), which in turn is determined by the climate, NPP is chosen as the variable of interest for this comparison. Figure 7 shows the sensitivity of the NPP to those variables, given here with the colour shading. This reveals the latitudinal dependency of the sensitivity of NPP, especially to temperature anomalies; there is a positive dependence in the colder climates of high latitudes, whereas it is negative in the warmer tropical regions. Also shown in the figure is the correlation between NPP and three

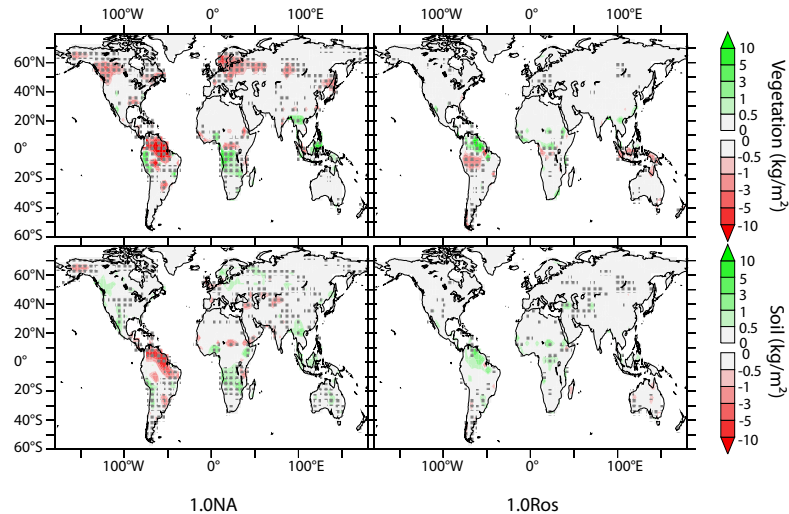


Fig. 6. Changes in the vegetation and soil (including litter) carbon (kg m^{-2}) by the end of the perturbation (decadal average) for the experiments 1.0NA (left) and 1.0Ros (middle). Stippled areas indicate where the ensemble mean anomaly is significantly different from zero at the 67% level (Student's t-Test).

climatic variables, temperature, precipitation and soil moisture. Soil moisture shows the highest correlation with NPP, as it is a composite variable that is determined by both precipitation and temperature. Correlation is generally higher in low latitudes for precipitation and soil moisture, while temperature shows a better correlation in the high latitudes. Nevertheless, South America stands out as a region of high correlation for each of the variables mentioned, including temperature.

3.3.3 South America – a more detailed analysis

In our model simulations, the contribution of the South American continent to the global atmospheric CO_2 rise (or fall, in the case of southern perturbations) is disproportionately high compared to the rest of the world. About half of all the losses in the land carbon pool is from the northern part of South America in the 1.0NA experiment, as well as a comparable fraction of the gains in the 1.0Ros experiment (Table 2).

The net change in the total carbon stocks in the northern part of South America (the region marked in Fig. 8 top left) is more than 40 GtC by the end of the 100-year perturbation. The driving factors of this substantial change are the increasing temperature and reduced precipitation, the combined effect of which is the transformation of one of the wettest climates on land into an arid desert-like climate unable to sustain the carbon-rich rain-forest type vegetation.

Precipitation decreases by about 400 mm yr^{-1} and the surface air temperature rises by 1.4°C on average (Fig. 9). Soil

carbon also decreases significantly, but this amounts to only half of the change in the vegetation carbon pool.

The response in the northern South America is a combination of changes in the precipitation and the air temperature, which is influenced by the prevailing winds. Over the ocean, where water vapour availability is primarily governed by the sea surface temperature, a positive correlation between the SAT and precipitation is apparent in most places. Over land, on the other hand, wind-driven transport of moisture from the sea is crucial. The north-easterlies that carry moist air to northern South America are weakened (Fig. 10) and, due to the colder SST in the northern equatorial Atlantic, their moisture content is reduced, which makes the region drier. This, in turn, results in a substantial drop in the latent heat flux (Fig. 9 last panel), most of which is due to reduced canopy transpiration as a result of the decrease in rain-forest vegetation. Consequently, a larger portion of the heat is transferred as sensible heat, raising the SAT. Removal of the rain-forest type vegetation, therefore, creates a very important feedback which further reduces the evapotranspiration and the latent heat flux.

The dramatic change in the northern part of South America also persists in the 1.0Ros experiment, though with an opposite sign. As in the 1.0NA experiment, a greater portion of the total anomaly in this experiment is in the vegetation carbon pool and it follows the changes in the climate field; higher precipitation and lower SAT values that lead to higher soil moisture.

The rest of the continent is also affected significantly by the changes in the climate system. Among them are the

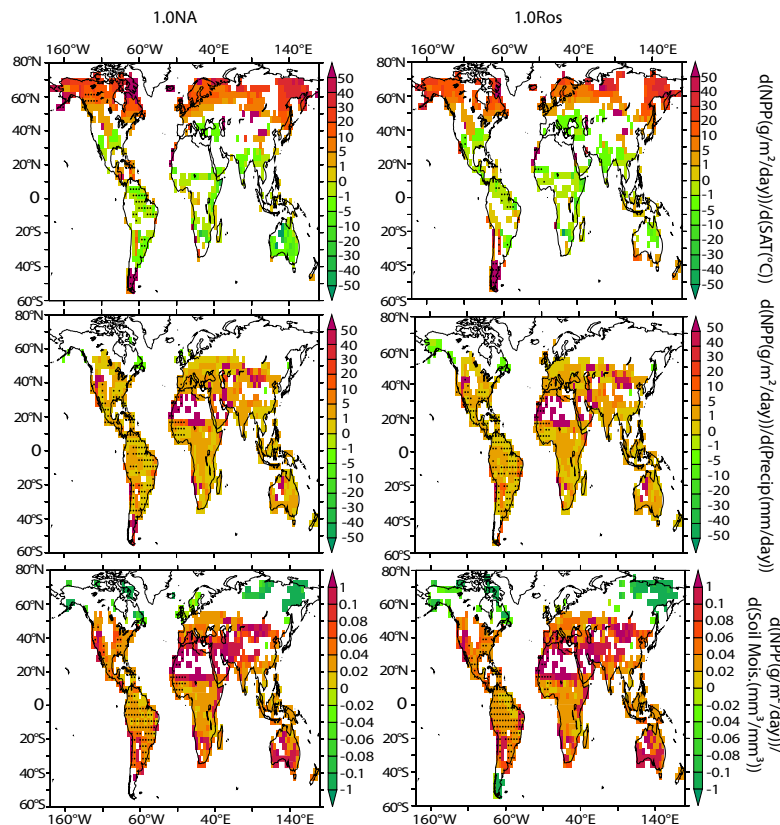


Fig. 7. Results of a linear regression analysis between NPP ($\text{g m}^{-2} \text{day}^{-1}$) and the climatic variables of SAT ($^{\circ}\text{C}$, top), precipitation (mm day^{-1} , middle), and soil moisture ($\text{mm}^3 \text{mm}^{-3}$, bottom). Colour shading represents the sensitivity of NPP to the changes of these variables (slope of the linear regression). Only the grid cells with a value of the square of the correlation coefficient greater than 0.1 ($R^2 > 0.1$) are coloured and the cells with $R^2 > 0.5$ are both coloured and stippled. The 1.0NA experiment is given on the left column and 1.0Ros on the right.

western part of the continent and northeastern Brazil, both of which respond oppositely relative to the northern part of the continent such that, NPP increases in the 1.0NA experiment and decreases in the 1.0Ros experiment. Those changes, basically, follow the shift of the ITCZ. The opposite impact (relative to the northern South America) of the ITCZ displacement on the climate and vegetation of the northeastern Brazil during the Younger Dryas (Wang et al., 2004) and Heinrich events (Dupont et al., 2010) is also evident in the records of the past climate.

The high-latitude regions of South America do not play an important role, in general. Although the southern parts of South America show a decrease in the carbon stocks in 1.0Ros experiment due to the lower temperatures, compared to the other regions, it does not add up to significant values. This is simply because of the initially small size of the carbon pool in that region.

Figures 8 and 9 reveal the characteristic property of a South American response to a reduction in the thermohaline circulation, which is a distinct and opposite reaction at the two different locations of the freshwater perturbation. 1.0NA and 1.0Ros experiments produce opposite responses not only in the north of the continent, but also in the rest of the continent (central/northeastern Brazil and possibly the western part of the continent) that form a dipole relationship with the north. Currently, the ITCZ over South America is located northward of the continent, and northeastern Brazil has a semi-arid climate. During reduced AMOC, the north end of this continental dipole responds in a positive way to a North Atlantic perturbation while the other end responds negatively, and vice-versa in the case of a southern perturbation. This kind of a decoupling of the precipitation response within the continent is also documented in other studies (Cruz et al., 2009).

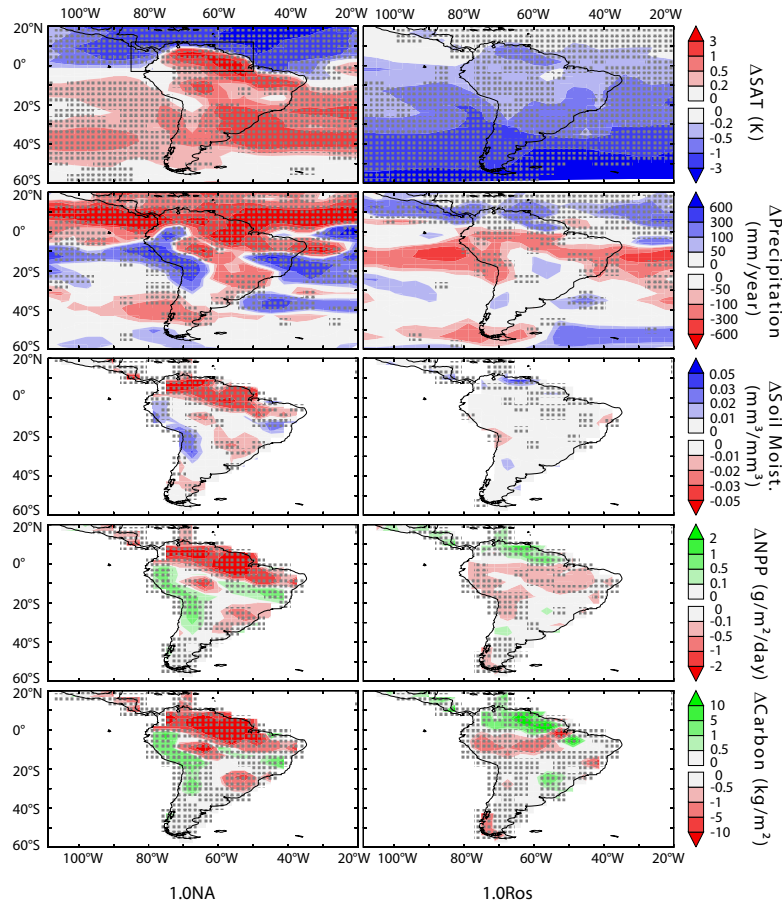


Fig. 8. Snapshots of the anomalies of various climatic variables and terrestrial carbon by the end of the perturbation (decadal average) for the experiments 1.0NA (left column) and 1.0Ros (right column). Anomalies are calculated as the 97–106 years of experiments minus the 100-year averaged Control. The variables shown from top to bottom are as follows, SAT ($^{\circ}\text{C}$), precipitation (mm year^{-1}), soil moisture ($\text{mm}^3 \text{mm}^{-3}$), NPP ($\text{g m}^{-2} \text{day}^{-1}$) and Total Carbon (kg m^{-2}). Stippled areas indicate where the ensemble mean anomaly is significantly different from zero at the 67% level (Student's t-Test).

3.4 Comparison of South American paleoclimate reconstructions with the model results

A comparison of several paleoclimate reconstructions of precipitation anomalies during the Younger Dryas period (Table 3) with our model results shows a good agreement between proxy records and the 1.0NA experiment responses in most locations (Fig. 11), which supports the robustness of the ITCZ-shift hypothesis and the existence of a dipole relation between the north of the continent and eastern and southern Brazil, as suggested by Wang et al. (2007). Such a dipole seems to exist between the north and the west of the continent too (Martin et al., 1997). This increase in precipitation in the west of the continent is also apparent in the

proxy records. Differences in the boundaries of the precipitation increase and decrease exist, yet it should be kept in mind that the ability of the model to make regional predictions is limited by its resolution.

Overall, the difference in behaviour of the global carbon cycle, together with the site-specific responses in South America give us a way to interpret the origin of the freshwater input. Thus, for future reconstruction studies considering the anti-phase relationship between different parts of the continent and also the opposite responses to the origin of the freshwater input should help us obtain a clearer picture of what has actually happened during such events.

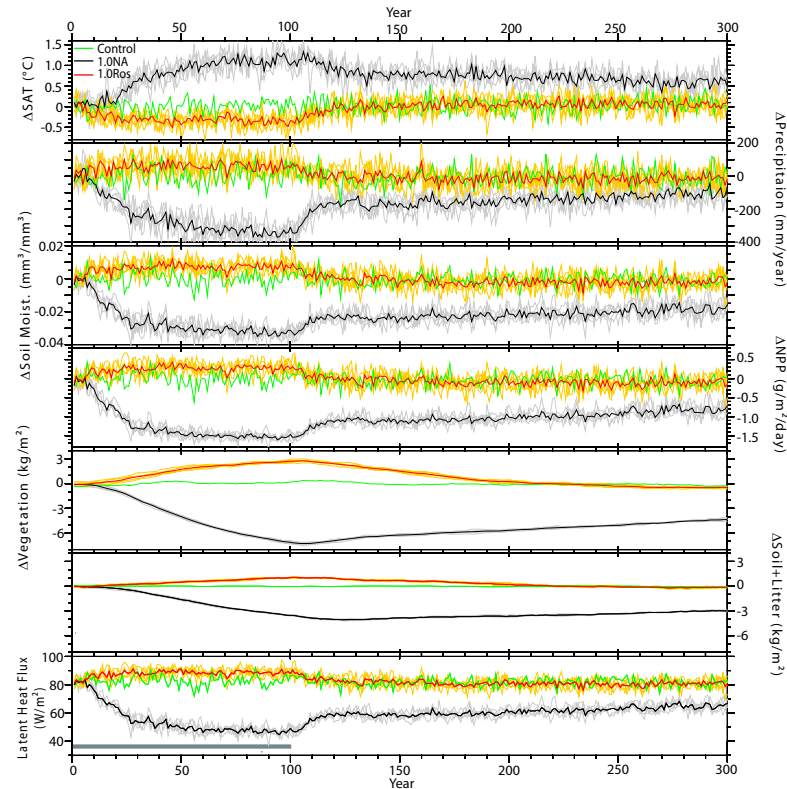


Fig. 9. Time evolution of the changes in the northern part of South America (the region marked in Fig. 8, top left panel). From top to bottom are shown the anomalies in SAT ($^{\circ}\text{C}$), precipitation (mm yr^{-1}), soil moisture ($\text{mm}^3 \text{mm}^{-3}$), NPP ($\text{g m}^{-2} \text{day}^{-1}$), Vegetation Carbon (kg m^{-2}), Soil and Litter Carbon (kg m^{-2}), and Latent Heat Flux (W m^{-2}). The green curve is the Control and the black and red curves are the ensemble averages of the 1.0NA the 1.0Ros experiments, respectively. The thin grey and orange curves are the individual ensemble members of the respective experiment. The grey bar at the bottom marks the duration of the freshwater input.

4 Discussion and conclusions

In our model simulations the response of the climate and the land biosphere to a collapse or a reduction in the AMOC can be divided into two categories according to where the freshwater perturbation is applied. All the perturbations from the North Atlantic Deep Water formation region cause similar responses, which are opposite to those caused by the perturbations from the Weddell Sea and the Ross Sea. Weddell Sea and Ross Sea responses are also different from each other, Ross Sea creating a much more widespread cooling and a clearer precipitation signal. That seems to be because the Ross Sea is a more important player in the creation of the AABW in our model than the Weddell Sea and, therefore, the perturbation in the Ross Sea has a stronger effect on the global climate. We note, however, that the specific locations of deep water formation are model dependent.

The most significant changes in precipitation occur around the tropics near the ITCZ, whose position is sensitive to shifts in SST. This, in turn, creates large changes in the carbon stocks in these locations. Additionally, the fact that large amounts of carbon are stored in low latitudes causes these precipitation anomalies to amplify changes in carbon stocks. Köhler et al. (2005) forced the Lund-Potsdam-Jena (LPJ) model with an output from freshwater experiments with the ECBILT-CLIO model. They found large changes in carbon stocks in the boreal zone and relatively small carbon stock changes in the tropics in contrast to our results. There are a variety of differences between the two studies. Vegetation dynamics is explicitly simulated in the LPJ, whereas vegetation distribution is prescribed in the NCAR CSM1.4-carbon model. On the other hand, interactions and feedbacks between vegetation and climate, such as those related to albedo and the water cycle, are represented in the coupled NCAR model, but not in the forced runs with LPJ. The

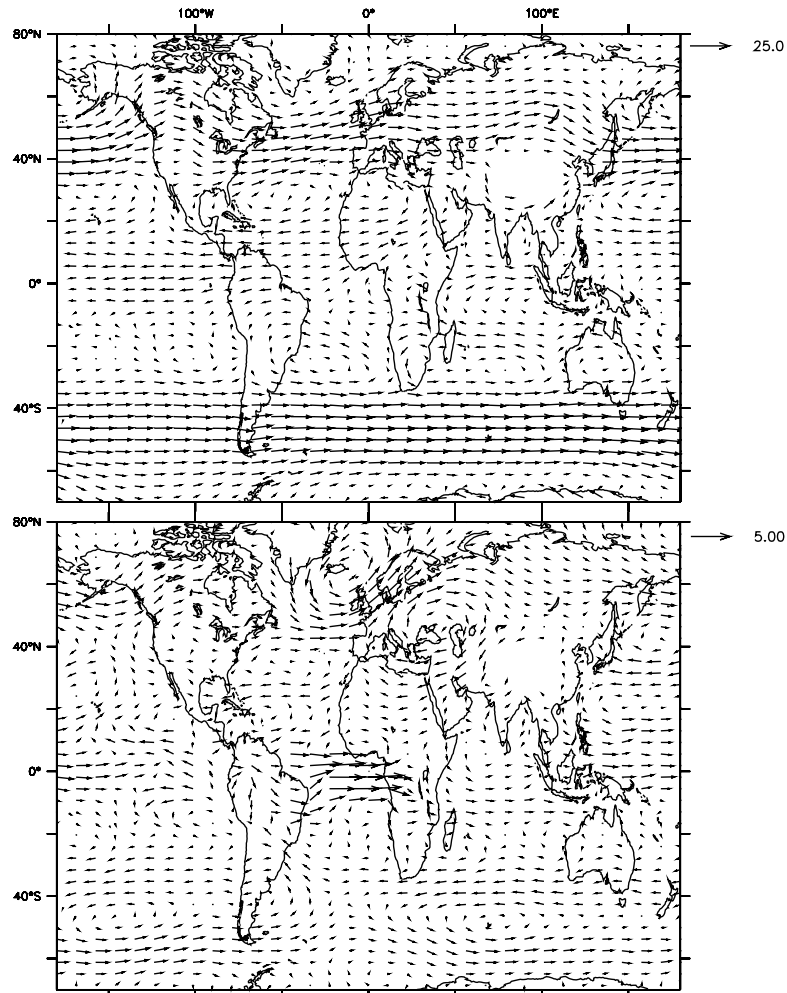


Fig. 10. Wind velocity (m s^{-1}) at 800 mbar for the Control (100-year average, top) and the anomaly at years 97–106 in 1.0NA (bottom). The reference vector is 25 m s^{-1} for Control and 5 m s^{-1} for the 1.0NA anomaly.

atmospheric dynamics in the cost-efficient ECBILT-CLIO is represented in a simplified manner which limits its ability to simulate dynamics in the tropics.

While the southward shift of the ITCZ after the northern perturbations is well studied with climate models and supported by paleoclimate records (Leduc et al., 2009), we show that the opposite is also true, that is to say, the northward shift of the ITCZ in response to a southern perturbation. Moreover, this has direct consequences for the tropical rain-forest type of vegetation in that region. The very direction of this shift determines the direction of the change in the atmospheric CO_2 concentration through its effects on the land carbon pool in the low latitudes.

The magnitude of CO_2 increase during the Heinrich events and also during the Younger Dryas event was around 20 ppmv, as recorded in ice-cores (Indermühle et al., 2000; Monnin et al., 2001). According to our results, all of this amplitude can be explained by the carbon release from the land biosphere while the ocean acts as a carbon sink. The isotopic signature of the CO_2 from the ice cores also points to a land origin for the increase during Younger Dryas (Smith et al., 1999). Moreover, in a recent comprehensive simulation of the last deglaciation, covering the Heinrich Event 1 (H1), with a coupled atmosphere-ocean general circulation model, Liu et al. (2009) successfully reproduced the major features of this cooling event. They found strong cooling

Table 2. A selection of regions that have recorded considerable changes given with their land area, the limits defined and the change of total carbon stocks in that area by the year 101 (end of the perturbation). 0.5 NA and 0.3 NA experiments are also included in the list for the purpose of comparison.

Regions	Area	Size (10 ⁶ km ²)	Change of Total Carbon (GtC)				
			1.0 NA	0.5 NA	0.3 NA	1.0 Ros	1.0 Wed
Northern Europe	13° W–28° E 50° N–65° N	2.04	–3.34	–3.35	–2.58	–0.16	–0.27
Northern North America	51° W–160° W 50° N–65° N	7.02	–4.58	–4.00	–2.92	–0.68	–0.40
Northern South America	50° W–84° W 1° S–10° N	3.14	–42.86	–29.16	–13.75	15.20	10.10
Africa	15° W–30° E 18° S–18° N	12.26	10.05	6.17	1.16	5.54	7.43
Southeast Asia	90° E–150° E 14° S–22° N	5.88	9.44	5.73	2.76	–0.31	–1.78
Other		119.26	–37.35	–21.27	–7.28	–5.45	–2.22
Total land		149.6	–68.64	–45.88	–22.61	14.14	12.86

Table 3. List of the paleoclimate reconstruction studies of precipitation change in and around South America during the Younger Dryas event, as used in the compilation given in Fig. 11. Reconstructed anomalies during Younger Dryas are given in comparison with our model results from the experiment 1.0 NA. A wide range of climate proxies are used in these reconstructions including, marine sediments, lake sediments, ice cores and speleothems. Pollen records as written in parenthesis are indicative of a change in the vegetation. These are shown in the figure as squares to distinguish from the rest of the proxies (circles).

#	Location	Proxy	Model	Proxy Type	Reference
1	Ceara Rise, Brazil	wet	dry	Marine sediment (Ti/Ca, Fe/Ca)	Arz et al. (1998)
2	Lake Titicaca, Bolivia and Peru	wet	wet	Lake sediment	Baker et al. (2001)
3	Atacama Desert, Chile	wet	wet	Fossil rodent middens	Betancourt et al. (2000)
4	La Yeguada, Panama	dry	dry	Lake sediment (charcoal)	Bush et al. (1992)
5	Laguna de Chochos, Peru	dry	wet	Lake sediment (pollen)	Bush et al. (2005)
6	Botuverá Cave, Brazil	wet	dry	Speleothem	Cruz et al. (2005)
7	Laguna Baja, Peru	dry	wet	Lake sediment (pollen)	Hansen and Rodbell (1995)
8	Cariaco Basin, Venezuela	dry	dry	Marine sediment (Ti/Ca, Fe/Ca)	Haug et al. (2001)
9	Cariaco Basin, Venezuela	dry	dry	Marine sediment (bio-markers)	Hughen et al. (2004)
10	NE Brazil	wet	dry	Marine sediment	Jennerjahn et al. (2004)
11	Lagoa do Caçó, Brazil	dry	dry	Lake sediment (pollen)	Ledru et al. (2002)
12	Amazon Basin	dry	dry	Marine sediment (planktonic $\delta^{18}\text{O}$)	Maslin and Burns (2000)
13	Heulmo mire, Chile	dry	dry	Lake sediment (pollen)	Massaferro et al. (2009)
14	Lago Condorito, Chile	dry	dry	Lake sediment (pollen)	Moreno (2000)
15	Offshore-Lima, Peru	wet	wet	Marine sediment	Rein et al. (2005)
16	Serra dos Carajas, Brazil	wet	dry	Lake sediment (pollen)	Servant et al. (1999)
17	Salitre, Brazil	dry	dry	Lake sediment (pollen)	Servant et al. (1999)
18	Colombia	dry	dry	Lake sediment (pollen)	van't Veer et al. (2000)
19	Lapa dos Brejões and Toca da Barriguda caves, Brazil	wet	wet	Speleothem	Wang et al. (2004)
20	Caverna Botuverá, Brazil	wet	dry	Speleothem	Wang et al. (2007)

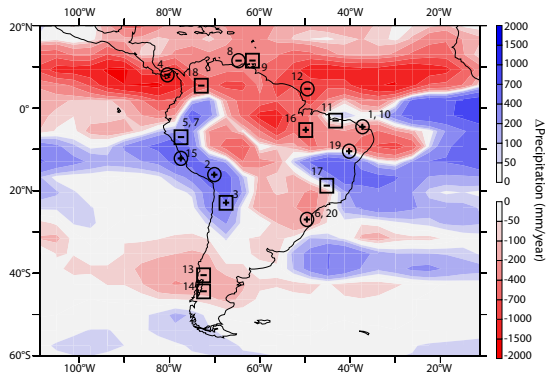


Fig. 11. Compilation of different reconstructions showing precipitation and vegetation changes in South America during the Younger Dryas event (ca. 12 kyr BP). Plus (+) sign indicates dryer conditions during the event and minus (–) sign wetter. Square frames around the signs are used for vegetation proxies, whereas circle frames are for precipitation proxies in general. The colour shading in the background shows the 10-year average annual precipitation anomaly by the end of the perturbation in the experiment 1.0NA. The numbering of the studies is as follows: 1. Arz et al. (1998), 2. Baker et al. (2001), 3. Betancourt et al. (2000), 4. Bush et al. (1992), 5. Bush et al. (2005), 6. Cruz et al. (2005), 7. Hansen and Rodbell (1995), 8. Haug et al. (2001), 9. Hughen et al. (2004), 10. Jennerjahn et al. (2004), 11. Ledru et al. (2002), 12. Maslin and Burns (2000), 13. Massafiero et al. (2009), 14. Moreno (2000), 15. Rein et al. (2005), 16–17. Servant et al. (1999), 18. van't Veer et al. (2000), 19. Wang et al. (2004), 20. Wang et al. (2007).

in the Northern Hemisphere with a milder warming in the south, and reduced precipitation in the Cariaco basin (northern South America). The good agreement of the general patterns of change indicates that a comparison of a paleoclimate event under glacial conditions (H1) and our simulations under pre-industrial conditions is reasonable.

The net atmospheric CO_2 increase in our experiments is comparable to, but more than, that of Obata (2007) with similar initial conditions. Even though the changes in the climatic variables and the NPP show a strong resemblance, their magnitudes differ in some areas. These include a more wide-spread cooling in the Northern Hemisphere in our experiments, and a smaller land biosphere response to the precipitation anomalies in eastern Asia. Additionally, a larger negative anomaly is recorded in northern part of South America in our study. Yet, the general effect of the ITCZ-shift is robust in both studies. The differences may be attributed to the more limited representation of the land biosphere in the model used by Obata (2007).

The exact amount of the contribution of the land biosphere to this atmospheric CO_2 increase, however, should be taken with caution since the glacial vegetation cover on land was different than that implemented here. Our experiments are done under pre-industrial conditions with a larger vegetation

carbon pool than during the glacial times. In a previous study (Menviel et al., 2008), in which the experiments were done under both pre-industrial and glacial boundary conditions, it has been shown that the differences in the amplitudes of the individual contributions from the land and ocean carbon pools may lead to an opposite net effect on the atmospheric CO_2 , even though the nature of each contribution is qualitatively the same. In their study, irrespective of the initial state, the roles of the ocean as a carbon sink and of the land as a carbon source remain unchanged. Also, the changes on land are very similar in both cases, that is, a reduction in the carbon stocks in the high and mid-latitudes of the Northern Hemisphere and in the tropics north of the equator and an increase to the south. Yet, the emissions from land under glacial conditions are weaker than under the pre-industrial conditions. That is probably due to the lower moisture content of the glacial atmosphere, which leads to the dampening effects of the ITCZ shift (Menviel et al., 2008), and relatively large gains in primary production in some regions such as eastern Asia and southern North America. Compared to our experiments, the main differences are the larger increases in carbon stocks in the Southern Hemisphere and the above-mentioned regions in the north, which might be due to some model specific differences as well as the initial conditions.

Nevertheless, as the patterns of the anomalies are very similar in both studies, it is safe to assume that our results are relevant for paleo-reconstructions as a possible indirect way to distinguish between the sources of freshwater discharge in abrupt cooling events, because the northern Atlantic and Antarctic perturbations have distinct implications for the land biosphere. Globally, the atmospheric CO_2 signal is different; an increase for the North Atlantic case and a decrease for the Antarctic case. Regionally, the South American continent proves to be in a particularly suitable position to record such past events, as the movement of the ITCZ – either to the south or to the north – would create distinguishable and, at some places, opposite responses.

In addition to what has been presented in the results section, there are some other notable features that are observed in response to the freshwater perturbations, such as the North Pacific Deep Water formation, or the strengthening of Southern Hemispheric westerlies (Fig. 10). A more detailed investigation of those responses may be undertaken in a future study.

The results of this study have also implications for future anthropogenic climate change which, as many modelling studies show, is to cause a reduction in the AMOC (Meehl et al., 2007). The effects of such a reduction can be substantial for climate and for low latitude ecosystems including, but not limited to, the rain-forests. It is also important to note that, the changes in the carbon cycle during such an event would possibly contribute to the increase in the atmospheric carbon and hence, operate as a weak positive feedback to the global warming, in addition to that associated with outgassing from a warmer ocean (Joos et al., 1999).

Acknowledgements. This study was funded by the Swiss National Science Foundation and the support by the project Past4Future is also acknowledged. Simulations were carried out at the Swiss National Supercomputing Centre in Manno, Switzerland. We thank S. C. Doney, I. Fung, K. Lindsay, J. John and colleagues for providing the CSM1.4-carbon code and M. Grosjean for advice on the South American paleo-records. We also thank the two anonymous reviewers and H. Hooghiemstra for their constructive comments.

Edited by: A. Sluijs

References

- Ammann, B., Birks, H. J. B., Brooks, S. J., Eicher, U., von Grafenstein, U., Hofmann, W., Lemdahl, G., Schwander, J., Tobolski, K., and Wick, L.: Quantification of biotic responses to rapid Climatic Changes around the Younger Dryas: A synthesis, *Palaeogeogr. Palaeoclimatol.*, 159, 313–347, 2000.
- Arz, H. W., Patzold, J., and Wefer, G.: Correlated millennial-scale changes in surface hydrography and terrigenous sediment yield inferred from last-glacial marine deposits off northeastern Brazil, *Quaternary Res.*, 50, 157–166, 1998.
- Baker, P. A., Seltzer, G. O., Fritz, S. C., Dunbar, R. B., Grove, M. J., Tapia, P. M., Cross, S. L., Rowe, H. D., and Broda, J. P.: The History of South American Tropical Precipitation for the Past 25 000 Years, *Nature*, 291, 640–643, 2001.
- Barber, D. C., Dyke, A., Hillaire-Marcel, C., Jenning, A. E., Andrews, J. T., Kerwin, M. W., Bilodeau, G., McNeely, R., Southon, J., Morehead, M. D., and Gagnon, J.-M.: Forcing of the cold event of 8200 years ago by catastrophic drainage of Laurentide lakes, *Nature*, 400, 344–348, 1999.
- Bard, E.: Climate Shock: Abrupt Changes over Millennial Time Scales, *Phys. Today*, 55, 32–39, 2002.
- Barker, S., Diz, P., Vautravers, M. J., Knorr, J. P. G., Hall, I. R., and Broecker, W. S.: Interhemispheric Atlantic seesaw response during the last deglaciation, *Nature*, 457, 1097–1102, 2009.
- Betancourt, J. L., Latorre, C., Rech, J. A., Quade, J., and Rylander, K. A.: A 22,000-Year Record of Monsoonal Precipitation from Northern Chile's Atacama Desert, *Science*, 289, 1542–1546, 2000.
- Bonan, G. B.: The NCAR land surface model (LSM version 1.0) coupled to the NCAR Community Climate Model, Tech. rep., 1996.
- Bond, G., Broecker, W., Johnsen, S., McManus, J., Labeyrie, L., Jouzel, J., and Bonani, G.: Correlations between climate records from North Atlantic sediments and Greenland ice, *Nature*, 365, 143–147, 1993.
- Boville, B. A. and Gent, P. R.: The NCAR Climate System Model, Version One, *J. Climate*, 11, 1115–1130, 1999.
- Boyle, E. A. and Keigwin, L. D.: North Atlantic thermohaline circulation during the past 20 000 years linked to high latitude surface temperature, *Nature*, 330, 35–40, 1987.
- Broecker, W. S.: Thermohaline Circulation, the Achilles Heel of Our Climate System: Will Man-Made CO₂ Upset the Current Balance?, *Science*, 278, 1582–1588, 1997.
- Bryan, F.: High-latitude salinity effects and interhemispheric thermohaline circulations, *Nature*, 323, 301–304, 1986.
- Bush, M. B., Piperno, D. R., Colinvaux, P. A., Oliveira, P. E. D., Krissek, L. A., Miller, M. C., and Rowe, W. E.: A 14 300-Yr Paleocological Profile of a Lowland Tropical Lake in Panama, *Ecol. Monogr.*, 62, 251–275, 1992.
- Bush, M. B., Hansen, B. C. S., Rodbell, D. T., Seltzer, G. O., Young, K. R., León, B., Abbott, M. B., Silman, M. R., and Gosling, W. D.: A 17 000-year history of Andean climate and vegetation change from Laguna de Chochos, Peru, *J. Quaternary Sci.*, 20, 703–714, 2005.
- Chiang, J. C. H.: The Tropics in Paleoclimate, *Annu. Rev. Earth Pl. Sc.*, 37, 263–297, 2009.
- Clark, P. U., Pisias, N. G., Stocker, T. F., and Weaver, A. J.: The role of the thermohaline circulation in abrupt climate change, *Nature*, 415, 863–869, 2002.
- Clement, A. C. and Peterson, L. C.: Mechanisms of abrupt climate change of the last glacial period, *Rev. Geophys.*, 46, RG4002, doi:10.1029/2006RG000204, 2008.
- Cruz, F. W., Burns, S. J., Karmann, I., Sharp, W. D., Vuille, M., Cardoso, A. O., Ferrari, J. A., Silva Dias, P. L., and Viana, O.: Insolation-driven changes in atmospheric circulation over the past 116 000 years in subtropical Brazil, *Nature*, 434, 63–65, 2005.
- Cruz, F. W., Vuille, M., Burns, S. J., Wang, X., Cheng, H., Werner, M., Edwards, R. L., Karmann, I., Auler, A. S., and Nguyen, H.: Orbitally driven east-west antiphasing of South American precipitation, *Nat. Geosci.*, 2, 210–214, 2009.
- Dahl, K. A., Broccoli, A. J., and Stouffer, R. J.: Assessing the role of North Atlantic freshwater forcing in millennial scale climate variability: a tropical Atlantic perspective, *Clim. Dynam.*, 24, 325–346, 2005.
- Dansgaard, W., Johnson, S. J., Clausen, H. B., Dahl-Jensen, D., Gundestrup, N., Hammer, C. H., and Oeschger, H.: North Atlantic oscillations revealed by deep Greenland ice cores, *Climate Processes and Climate Sensitivity*, *Geophys. Monogr.*, 29, 288–298, 1984.
- Ding, Z. L., Ren, J. Z., Yang, S. L., and Liu, T. S.: Climate instability during the penultimate glaciation: evidence from two high-resolution loess records, China, *J. Geophys. Res.*, 104, 20123–20132, 1999.
- Doney, S. C., Lindsay, K., Fung, I., and John, J.: Natural Variability in a Stable, 1000-Yr Global Coupled Climate-Carbon Cycle Simulation, *J. Climate*, 19, 3033–3054, 2006.
- Duplessy, J. C., Shackleton, N. J., Fairbanks, R. G., Labeyrie, L., and Oppo, D. W.: Deepwater source variations during the last climatic cycle and their impact on the global deepwater circulation, *Paleoceanography*, 3, 343–360, 1988.
- Dupont, L. M., Schlutz, F., Ewah, C. T., Jennerjahn, T. C., Paul, A., and Behling, H.: Two-step vegetation response to enhanced precipitation in Northeast Brazil during Heinrich event 1, *Global Change Biol.*, 16, 1647–1660, 2010.
- Eicher, U., Siegenthaler, U., and Wegmueller, S.: Pollen and isotope analysis on late and post-glacial sediments of the Tourbiere de Chirens (Dauphine, France), *Quaternary Res.*, 15, 160–170, 1981.
- EPICA Community Members: One-to-one coupling of glacial climate variability in Greenland and Antarctica, *Nature*, 444, 195–198, 2006.

- Friedlingstein, P., Joel, G., Field, C. B., and Fung, I. Y.: Toward an allocation scheme for global terrestrial carbon models, *GlobAL Change Biol.*, 5, 755–770, 1999.
- Frölicher, T. L. and Joos, F.: Reversible and irreversible impacts of greenhouse gas emissions in multi-century projections with the NCAR global coupled carbon cycle-climate model, *Clim. Dynam.*, 1–21, 2010.
- Frölicher, T. L., Joos, F., Plattner, G.-K., Steinacher, M., and Doney, S. C.: Natural variability and anthropogenic trends in oceanic oxygen in a coupled carbon cycle-climate model ensemble, *Global Biogeochem. Cy.*, 23, GB1003, doi:10.1029/2008GB003316, 2009.
- Fung, I., Doney, S. C., Lindsay, K., and John, J.: Evolution of carbon sinks in a changing climate, *P. Natl. Acad. Sci. USA*, 102, 11201–11206, 2005.
- Gent, P. R., Bryan, F. O., Danabasoglu, G., Doney, S. C., Holland, W. R., Large, W. G., and McWilliams, J. C.: The NCAR Climate System Model Global Ocean Component, *J. Climate*, 11, 1287–1306, 1998.
- Hansen, B. C. S. and Rodbell, D. T.: A Late-Glacial/Holocene Pollen Record from the Eastern Andes of Northern Peru, *Quaternary Res.*, 44, 216–227, 1995.
- Haug, G. H., Hughen, K. A., Sigman, D. M., Peterson, L. C., and Rohl, U.: Southward migration of the intertropical convergence zone through Holocene, *Science*, 293, 1304–1308, 2001.
- Heinrich, H.: Origin and consequences of cyclic ice rafting in the northeast Atlantic ocean during the past 130 000 years, *Quaternary Res.*, 29, 142–152, 1988.
- Hemming, R. S.: Heinrich events: Massive late Pleistocene detritus layers of the North Atlantic and their global climate imprint, *Rev. Geophys.*, 42, RG1005, doi:10.1029/2003RG000128, 2004.
- Huber, C., Leuenberger, M., Spahni, R., Fluckiger, J., Schwander, J., Stocker, T. F., Johnsen, S., Landals, A., and Jouzel, J.: Isotope calibrated Greenland temperature record over Marine Isotope Stage 3 and its relation to CH₄, *Earth Planet. Sc. Lett.*, 243, 504–519, 2006.
- Hughen, K. A., Southon, J. R., Lehman, S. J., and Overpeck, J. T.: Synchronous radiocarbon and climate shifts during the last deglaciation, *Science*, 290, 1951–1954, 2000.
- Hughen, K. A., Eglinton, T. I., Xu, L., and Makou, M.: Abrupt tropical vegetation response to rapid climate changes, *Science*, 304, 1955–1959, 2004.
- Indermühle, A., Monnin, E., Stauffer, B., Stocker, T. F., and Wahlen, M.: Atmospheric CO₂ concentration from 60 to 20 kyr BP from the Taylor Dome Ice Core, Antarctica, *Geophys. Res. Lett.*, 27, 735–738, 2000.
- Jennerjahn, T. C., Ittekkot, V., Arz, H. W., Behling, H., Patzold, J., and Wefer, G.: Asynchronous Terrestrial and Marine Signals of Climate Change During Heinrich Events, *Science*, 306, 2236–2239, 2004.
- Joos, F., Plattner, G.-K., Stocker, T. F., Marchal, O., and Schmittner, A.: Global warming and marine carbon cycle feedbacks on future atmospheric CO₂, *Science*, 284, 464–467, 1999.
- Kiehl, J. T., Hack, J. J., Bonan, G. B., Boville, B. A., Williamson, D. L., and Rasch, P. J.: The National Center for Atmospheric Research Community Climate Model: CCM3, *J. Climate*, 11, 1131–1149, 1998.
- Knutti, R., Flueckiger, J., Stocker, T. F., and Timmermann, A.: Strong hemispheric coupling of glacial climate through freshwater discharge and ocean circulation, *Nature*, 430, 851–856, 2004.
- Köhler, P., Joos, F., Gerber, S., and Knutti, R.: Simulated changes in vegetation distribution, land carbon storage, and atmospheric CO₂ in response to a collapse of the North Atlantic thermohaline circulation, *Clim. Dynam.*, 25, 689–708, 2005.
- Ledru, M.-P., Mourguiart, P., Ceccantini, G., Turcq, B., and Sifeddine, A.: Tropical climates in the game of two hemispheres revealed by abrupt Climatic Change, *Geology*, 30, 275–278, 2002.
- Leduc, G., Vidal, L., Tachikawa, K., and Bard, E.: ITCZ rather than ENSO signature for abrupt climate changes across the tropical Pacific?, *Quaternary Res.*, 72, 123–131, 2009.
- Levermann, A., Griesel, A., Hofmann, M., Montoya, M., and Rahmstorf, S.: Dynamic sea level changes following changes in the thermohaline circulation, *Clim. Dynam.*, 24, 347–354, 2005.
- Liu, Z., Otto-Bliesner, B. L., He, F., Brady, E. C., Tomas, R., Clark, P. U., Carlson, A. E., Lynch-Stieglitz, J., Curry, W., Brook, E., Erickson, D., Jacob, R., Kutzbach, J., and Cheng, J.: Transient Simulation of Last Deglaciation with a New Mechanism for Bölling-Allerød Warming, *Science*, 325, 310–314, 2009.
- Manabe, S. and Stouffer, R. J.: The role of thermohaline circulation in climate, *Tellus A*, 51, 91–109, 1999.
- Marchal, O., Stocker, T. F., and Joos, F.: Impact of Oceanic Reorganizations on the Ocean Carbon Cycle and Atmospheric Carbon Dioxide Content, *Paleoceanography*, 15, 341–354, 1998.
- Marchal, O., Stocker, T. F., Joos, F., Indermühle, A., Blunier, T., and Tschumi, J.: Modeling the concentration of atmospheric CO₂ during the Younger Dryas climate event, *Clim. Dynam.*, 15, 341–354, 1999.
- Martin, L., Bertaux, J., Corrège, T., Ledru, M.-P., Mourguiart, P., Sifeddine, A., Soubiès, F., Wirmann, D., Suguio, K., and Turcq, B.: Astronomical Forcing of Contrasting Rainfall Changes in Tropical South America between 12,400 and 8800 cal yr B.P., *Quaternary Res.*, 47, 117–122, 1997.
- Maslin, M. A. and Burns, S. J.: Reconstruction of the Amazon Basin effective moisture availability over the past 14 000 years, *Science*, 290, 2285–2287, 2000.
- Massaferro, J., Moreno, P., Denton, G., Vandergoes, M., and Dieffenbacher-Krall, A.: Chironomid and pollen evidence for climate fluctuations during the Last Glacial Termination in NW Patagonia, *Quaternary Sci. Rev.*, 28, 517–525, 2009.
- Meehl, G. A., Stocker, T. F., Collins, W. D., Friedlingstein, P., Gaye, A. T., Gregory, J. M., Kitoh, A., Knutti, R., Murphy, J. M., Noda, A., Raper, S. C. B., Watterson, I. G., Weaver, A. J., and Zhao, Z.-C.: Global Climate Projections, in: *Climate Change 2007: The Physical Science Basis. Contribution of Working Group I to the Fourth Assessment Report of the Intergovernmental Panel on Climate Change*, Cambridge University Press, Cambridge, UK and New York, NY, USA, 2007.
- Menviel, L., Timmermann, A., Mouchet, A., and Timm, O.: Meridional reorganizations of marine and terrestrial productivity during Heinrich events, *Paleoceanography*, 23, PA1203, doi:10.1029/2007PA001445, 2008.
- Menviel, L., Timmermann, A., Timm, O., and Mouchet, A.: Climate and biogeochemical response to a rapid melting of the West Antarctic Ice Sheet during interglacials and implications for future climate, *Paleoceanography*, 25, PA4231, doi:10.1029/2009PA001892, 2010.

- Menziel, L., Timmermann, A., Timm, O., and Mouchet, A.: Deconstructing the last Glacial Termination: the role of millennial and orbital-scale forcings, *Quaternary Sci. Rev.*, JQSR2995, doi:10.1016/j.quascirev.2011.02.005, in press, 2011.
- Mikolajewicz, U.: A meltwater-induced collapse of the “conveyor belt” thermohaline circulation and its influence on the distribution of $\Delta^{14}\text{C}$ and $\delta^{18}\text{O}$ in the oceans, vol. 189 of Technical Report, Tech. rep., Hamburg, Germany, 1996.
- Mikolajewicz, U., Crowley, J. C., Schiller, J. C., and Voss, R.: Modeling teleconnections between the North Atlantic and North Pacific during the Younger Dryas, *Nature*, 387, 384–387, 1997.
- Monnin, E., Indermuhle, A., Daellenbach, A., Flueckiger, J., Stauffer, B., Stocker, T. F., Raynaud, D., and Barnola, J.-M.: Atmospheric CO_2 Concentrations over the Last Glacial Termination, *Science*, 291, 112–114, 2001.
- Moreno, P. I.: Climate, Fire, and Vegetation between About 13,000 and 9200 ^{14}C yr B.P. in the Chilean Lake District, *Quaternary Res.*, 54, 81–89, 2000.
- Muscheler, R., Beer, J., Wagner, G., and Finkel, R. C.: Changes in deep-water formation during the Younger Dryas event inferred from ^{10}Be and ^{14}C records, *Nature*, 408, 567–570, 2000.
- Najjar, R. G., Sarmiento, J. L., and Toggweiler, J. R.: Downward Transport and Fate of Organic Matter in the Ocean: Simulations with a General Circulation Model, *Global Biogeochem. Cy.*, 6, 45–76, 1992.
- NorthGRIP Members: High-resolution climate record of the Northern Hemisphere back into the last glacial interglacial period, *Nature*, 431, 147–151, 2004.
- Obata, A.: Climate-Carbon Cycle Model Response to Freshwater Discharge into the North Atlantic, *J. Climate*, 20, 5962–5976, 2007.
- Oeschger, H., Beer, J., Siegenthaler, U., and Stauffer, B.: Late glacial climate history from ice cores, in: *Geophysical Monograph*, edited by: Hansen, J. E. and Takahashi, T., American Geophysical Union, Washington, DC, 29, 299–306, 1984.
- Okazaki, Y., Timmermann, A., Menziel, L., Harada, N., Abeuchi, A., Chikamoto, M., Mouchet, A., and Asahi, H.: Deep water formation in the North Pacific during the Last Glacial termination, *Science*, 329, 200–204, 2010.
- Okumura, Y. M., Deser, C., Hu, A., Timmermann, A., and Xie, S.-P.: North Pacific Climate Response to Freshwater Forcing in the Subarctic North Atlantic: Oceanic and Atmospheric Pathways, *J. Climate*, 22, 1424–1445, 2009.
- Porter, S. C.: Chinese loess record of monsoon climate during the last glacial-interglacial cycle, *Earth Sci. Rev.*, 54, 115–128, 2001.
- Prokopenko, A. A., Williams, D. F., Karabanov, E. B., and Khursevich, G. K.: Continental response to Heinrich events and Bond cycles in sedimentary record of Lake Baikal, Siberia, *Global Planet. Change*, 28, 217–226, 2001.
- Rahmstorf, S.: Ocean circulation and climate during the past 120 000 years, *Nature*, 419, 207–214, 2002.
- Randerson, J., Thompson, M., Conway, T., Fung, I., and Field, C.: The Contribution of Terrestrial Sources and Sinks to Trends in the Seasonal Cycle of Atmospheric Carbon Dioxide, *Global Biogeochem. Cy.*, 11, 535–560, 1997.
- Rein, B., Lückge, A., Reinhardt, L., Sirocco, F., Wolf, A., and Dullo, W.-C.: El Niño variability off Peru during the last 20 000 years, *Paleoceanography*, 20, PA4003, doi:10.1029/2004PA001099, 2005.
- Rousseau, D. D., Antoine, P., Hatte, C., Lang, A., Zoller, L., Fontugne, M., Othman, D. B., Luck, J. M., Moine, O., Labonne, M., Bentaleb, I., and Jolly, D.: Abrupt millennial Climatic Changes from Nussloch (Germany) upper Weichselian eolian records during the last glaciation, *Quaternary Sci. Rev.*, 21, 1577–1582, 2002.
- Ruddiman, W. F. and McIntyre, A.: The North Atlantic Ocean during the last glaciation, *Palaeogeogr. Palaeoclimatol.*, 35, 145–214, 1981.
- Schiller, A., Mikolajewicz, U., and Voss, R.: The stability of the North Atlantic thermohaline circulation in a coupled ocean-atmosphere general circulation model, *Clim. Dynam.*, 13, 325–357, 1997.
- Schmittner, A.: Decline of the marine ecosystem caused by a reduction in the Atlantic overturning circulation, *Nature*, 434, 628–633, 2005.
- Schmittner, A. and Galbraith, E. D.: Glacial greenhouse-gas fluctuations controlled by ocean circulation changes, *Nature*, 456, 373–376, 2008.
- Sellers, P., Randall, D., Collatz, G., Berry, J., Field, C., Dazlich, D., Zhang, C., Collelo, G., and Bounoua, L.: A Revised Land Surface Parametrization (SiB2) for Atmospheric GCMs, Part I: Model Formulation, *J. Climate*, 9, 676–705, 1996.
- Servant, M., Maley, J., Turcq, B., Absy, M.-L., Brenac, P., Fournier, M., and Ledru, M.-P.: Tropical forest changes during the Late Quaternary in African and South American lowlands, *Global Planet. Change*, 7, 25–40, 1999.
- Smith, H. J., Fischer, H., Wahlen, M., Mastroianni, D., and Deck, B.: Dual modes of the carbon cycle since the Last Glacial Maximum, *Nature*, 400, 248–250, 1999.
- Stauffer, B., Blunier, T., Dallenbach, A., Indermühle, A., Schwander, J., Stocker, T. F., Tschumi, J., Chappellaz, J., Raynaud, D., Hammer, C. U., and Clausen, H. B.: Atmospheric CO_2 concentration and millennial-scale climate change during the last glacial period, *Nature*, 392, 59–62, 1998.
- Steffensen, J. P., Andersen, K. K., Bigler, M., Clausen, H. B., Dahl-Jensen, D., Fischer, H., Goto-Azuma, K., Hansson, M., Johnsen, S. J., Jouzel, J., Masson-Delmotte, V., Popp, T., Rasmussen, S. O., Rothlisberger, R., Ruth, U., Stauffer, B., Siggaard-Andersen, M.-L., Sveinbjornsdottir, A. E., Svensson, A., and White, J. W. C.: High-Resolution Greenland Ice Core Data Show Abrupt Climate Change Happens in Few Years, *Science*, 321, 680–684, 2008.
- Steinacher, M., Joos, F., Frölicher, T. L., Plattner, G.-K., and Doney, S. C.: Imminent ocean acidification in the Arctic projected with the NCAR global coupled carbon cycle-climate model, *Biogeosciences*, 6, 515–533, doi:10.5194/bg-6-515-2009, 2009.
- Steinacher, M., Joos, F., Frölicher, T. L., Bopp, L., Cadule, P., Cocco, V., Doney, S. C., Gehlen, M., Lindsay, K., Moore, J. K., Schneider, B., and Segsneider, J.: Projected 21st century decrease in marine productivity: a multi-model analysis, *Biogeosciences*, 7, 979–1005, doi:10.5194/bg-7-979-2010, 2010.
- Stocker, T. F.: Past and future reorganizations in the climate system, *Quaternary Sci. Rev.*, 19, 301–319, 2000.
- Stocker, T. F. and Johnsen, S. J.: A minimum thermodynamic model for the bipolar seesaw, *Paleoceanography*, 18, 1620–1635, 2003.
- Stocker, T. F. and Marchal, O.: Abrupt climate change in the computer: Is it real?, *P. Natl. Acad. Sci. USA*, 97, 1362–1365, 2000.

- Stocker, T. F., Timmermann, A., Renold, M., and Timm, O.: Effects of Salt Compensation on the Climate Model Response in Simulations of Large Changes of the Atlantic Meridional Overturning Circulation, *J. Climate*, 20, 5912–5928, 2007.
- Stouffer, R. J., Yin, J., Gregory, J. M., Dixon, K. W., Spelman, M. J., Hurlin, W., Weaver, A. J., Eby, M., Flato, G. M., and Hasumi, H.: Investigating the Causes of the Response of the Thermohaline Circulation to Past and Future Climate Changes, *J. Climate*, 19, 1365–1387, 2006.
- Stouffer, R. J., Seidov, D., and Haupt, B. J.: Climate Response to External Sources of Freshwater: North Atlantic versus the Southern Ocean, *J. Climate*, 20, 436–448, 2007.
- Timmermann, A., Gildor, H., Schulz, M., and Tziperman, E.: Coherent Resonant Millennial-Scale Climate Oscillations Triggered by Massive Meltwater Pulses, *J. Climate*, 16, 2569–2585, 2003.
- Timmermann, A., An, S. I., Krebs, U., and Goosse, H.: ENSO Suppression due to Weakening of the North Atlantic Thermohaline Circulation, *J. Climate*, 18, 3122–3139, 2005.
- Timmermann, A., Okumura, Y., An, S. I., Clement, A., Dong, B., Guilyardi, E., Hu, A., Jungclaus, J. H., Renold, M., Stocker, T. F., Stouffer, R. J., Sutton, R., Xie, S. P., and Yin, J.: The influence of a weakening of the Atlantic meridional overturning circulation on ENSO, *J. Climate*, 20, 4899–4919, 2007.
- van't Veer, R., Islebe, G. A., and Hooghiemstra, H.: Climatic Change during the Younger Dryas chron in northern South America: a test of the evidence, *Quaternary Sci. Rev.*, 19, 1821–1835, 2000.
- Vellinga, M. and Wood, R. A.: Global Climatic Impacts of a Collapse of the Atlantic Thermohaline Circulation, *Climatic Change*, 54, 251–267, 2002.
- Voelker, A. H. L.: Global distribution of centennial-scale records for Marine Isotope Stage (MIS)3: a database, *Quaternary Sci. Rev.*, 21, 1185–1212, 2002.
- Wang, X., Auler, A. S., Edwards, R. L., Cheng, H., Cristalli, P. S., Smart, P. L., Richards, D. A., and Shen, C.: Wet periods in northeastern Brazil over the past 210 kyr linked to distant climate anomalies, *Nature*, 432, 740–743, 2004.
- Wang, X., Auler, A. S., Edwards, R. L., Cheng, H., Ito, E., Wang, Y., Kong, X., and Solheid, M.: Millennial-scale precipitation changes in southern Brazil over the past 90 000 years, *Geophys. Res. Lett.*, 34, L05708, doi:10.1029/2007GL031149, 2007.
- Yu, Z. and Eicher, U.: Abrupt climate oscillations during the last deglaciation in Central North America, *Science*, 282, 2235–2238, 1998.
- Zhang, R. and Delworth, T. L.: Simulated Tropical Response to a Substantial Weakening of the Atlantic Thermohaline Circulation, *J. Climate*, 18, 1853–1860, 2005.

Chapter 7

Outlook

The work presented in this thesis can be continued and extended in several ways. Some of them have already been mentioned in previous chapters, such as a more in-depth analysis of feedbacks, climate change commitment, or irreversibility in the large set of simulations with the Bern3D-LPX model presented in chapter 4. Here, three main approaches are highlighted.

First, models can be developed further by including additional processes and feedbacks, which have not been considered previously. Ocean biogeochemical models, for example, are still limited in simulating the interaction of species in pelagic ecosystems and how these systems and food webs will change in the coming decades. Shifts between species within a given functional type or acclimatisation and adaptation is often not considered. Such interactions might be included in a new generation of ecosystem models (e.g. Barton et al., 2010). Also, interactions between the elemental cycles and ocean acidification such as the mediation of the organic matter export by CaCO_3 production (Hofmann & Schellnhuber, 2009) could be explored further. Another possibility is to include feedbacks not only between climate and atmospheric CO_2 but also between climate and other substances that influence the radiative balance, such as marine emissions of dimethyl sulphide (DMS) or N_2O . The LPX model has been extended recently to be able to simulate CH_4 (Wania et al., 2010; Spahni et al., 2011) and N_2O emissions from terrestrial ecosystems. Those features will allow interactive simulations with all three major greenhouse gases (CO_2 , CH_4 , and N_2O) in Bern3D-LPX to quantify the joint feedbacks between climate and those greenhouse gases, which are currently largely unknown.

Secondly, existing models can be improved by optimizing their parametrization and/or resolution. Data assimilation techniques can be helpful for this task (e.g. Gerber & Joos, 2010). More specifically, the low bias in the carbonate saturation simulated by the Bern3D-LPX model (see Chap. 4) could probably be reduced by adjusting model parameters to generate a more realistic alkalinity distribution. Additionally, an increase of the currently very low horizontal resolution at high latitudes in the Bern3D model might help to improve the simulated response in the Arctic Ocean. Similarly, the vertical ocean diffusivity parameter could possibly be modified for a better match between observed and simulated historical CO_2 concentrations (Chap. 4).

The third important issue that is highlighted here is the quantification of uncertainties. The causal chain from human activities to global impacts on climate or ecosystems involve uncertainties at each step. Uncertainties in the response of the carbon cycle to climate change, for example, introduce a considerable uncertainty when translating CO_2 emissions to changes in atmospheric CO_2 concentrations. Uncertainties in the climate sensitivity complicate the prediction of temperature changes for a given change in CO_2 concentrations in a similar way. The association of a quantified uncertainty with the projection of a variable makes it a much

stronger statement and would be helpful for taking decisions based on that projection (Allen et al., 2000; Knutti et al., 2002; Meinshausen et al., 2009; Tomassini et al., 2010).

One way to address this problem is to provide an ensemble of simulations which explores the model parameter space within its range of uncertainty. Observational data can then be used to constrain the uncertainty range by assigning probabilities to individual ensemble members based on a metric that quantifies the compatibility of this specific parameter setting with observations. This approach typically requires a large number of simulations which is often not feasible with complex models because of computational constraints. Therefore reduced complexity models, such as the Bern3D-LPX, are ideal tools for this task.

The goal of an ongoing study is to extend the results presented in chapter 4 to provide probabilistic projections with a Monte Carlo based approach. In a first explorative phase, 26 model parameters have been selected which affect the carbon cycle and climate response of the model. These parameters control, for example, the photosynthesis of the terrestrial biosphere, the climate sensitivity of the model, the air-sea gas exchange and ocean mixing, or the radiative forcing from aerosols. The defined parameter space is sampled using a Latin Hypercube Sampling method (McKay et al., 1979) to generate a model ensemble of 1000 members. With each model in this ensemble, the historical simulation (1800-2010) described in chapter 4 is performed.

A collection of observational data sets is used to calculate a likelihood for each model configuration that quantifies its compatibility with the observational data. Following a Bayesian approach, posterior probability density functions (PDF) can then be calculated for the individual parameters and for projected quantities (Rougier, 2007). This method is illustrated in Fig. 7.1 by constraining a parameter governing terrestrial photosynthesis with observational estimates of the fraction of absorbed photosynthetically active radiation (fAPAR) based on satellite data.

A major challenge regarding this probabilistic approach is the definition of a meaningful likelihood function to constrain the parameter space. The likelihood function should represent a proper probabilistic measure to be able to make valid conclusions with respect to the probability of future projections (Rougier, 2007). A common approach is to compare the data-model difference to a normal distribution with a variance that combines the observational and model error. Specifying those errors, however, is often not straightforward. Further, errors can be correlated in time, space, and/or between different variables. This is particularly true for variables for which a large amount of measurements is available, such as three-dimensional ocean tracer fields. In those cases, a proper probabilistic treatment requires the specification of a covariance matrix, which is often unknown or difficult to estimate (e.g. Schmittner et al., 2009). Thus, several methodical problems need to be solved in the continuation of this study.

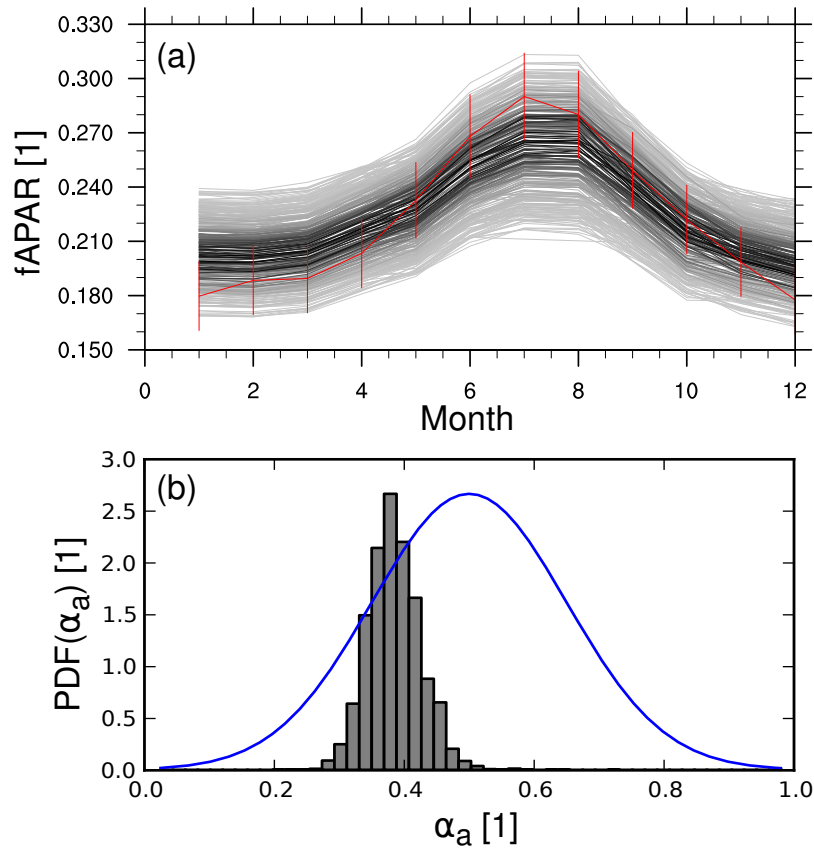


Figure 7.1: Illustration of constraining the model parameter space by observational data in a probabilistic approach. Panel (a) shows the annual cycle of the fraction of absorbed photosynthetically active radiation (fAPAR) estimated from satellite observations (red; Gobron et al., 2006) and for an ensemble of model simulations with Bern3D-LPX (black/gray). The darkness of the lines indicates the likelihood of the model results to be compatible with the observations. Please note that only results from the 300 simulations with the highest likelihoods are shown. The whole ensemble (1000 members) spans a much wider range from flat annual cycles around 0.07 to maximum values of about 0.45. The model ensemble has been generated by sampling 26 parameters from defined prior distributions. The prior PDF for one of these parameter (α_a) is shown by the blue line in panel (b). α_a is a parameter in the LPX model that primarily accounts for the photosynthetically active radiation absorbed by non-photosynthetic structures (such as branches) and thus controls the amount of radiation available for photosynthesis (Sitch et al., 2003; Zaehle et al., 2005). By using the likelihoods indicated in panel (a) as weights, the plausible parameter range assumed for the prior distribution (blue) is reduced significantly in the posterior distribution (gray bars). Moreover, the most probable value for α_a is shifted from 0.5 to about 0.38 in the posterior PDF. Please note the the posterior PDF is scaled to the maximum value of the prior for visibility, and thus the values on the y-axis only apply to the prior distribution.

Bibliography

- Allen, M. R., Stott, P. A., Mitchell, J. F. B., Schnur, R., & Delworth, T. L., 2000. Quantifying the uncertainty in forecasts of anthropogenic climate change, *Nature*, 407(6804), 617–620.
- Barton, A. D., Dutkiewicz, S., Flierl, G., Bragg, J., & Follows, M. J., 2010. Patterns of diversity in marine phytoplankton, *Science*, 327(5972), 1509–1511.
- Gerber, M. & Joos, F., 2010. Carbon sources and sinks from an Ensemble Kalman Filter ocean data assimilation, *Global Biogeochem. Cy.*, 24.
- Gobron, N., Pinty, B., Auzan, O., Chen, J. M., Cohen, W. B., Fensholt, R., Gond, V., Huemmrich, K. F., Lavergne, T., Melin, F., Privette, J. L., Sandholt, I., Taberner, M., Turner, D. P., Verstraete, M. M., & Widlowski, J.-L., 2006. Evaluation of fraction of absorbed photosynthetically active radiation products for different canopy radiation transfer regimes: Methodology and results using Joint Research Center products derived from SeaWiFS against ground-based estimations, *J. Geophys. Res.-Atmos.*, 111(D13110).
- Hofmann, M. & Schellnhuber, H.-J., 2009. Oceanic acidification affects marine carbon pump and triggers extended marine oxygen holes, *Proc. Nat. Acad. Sci. USA*, 106(9), 3017–3022.
- Knutti, R., Stocker, T. F., Joos, F., & Plattner, G. K., 2002. Constraints on radiative forcing and future climate change from observations and climate model ensembles, *Nature*, 416(6882), 719–723.
- McKay, M. D., Beckman, R. J., & Conover, W. J., 1979. A comparison of three methods for selecting values of input variables in the analysis of output from a computer code, *Technometrics*, 21(2), 239–245.
- Meinshausen, M., Meinshausen, N., Hare, W., Raper, S. C. B., Frieler, K., Knutti, R., Frame, D. J., & Allen, M. R., 2009. Greenhouse-gas emission targets for limiting global warming to 2 degrees c, *Nature*, 458(7242), 1158–U96.
- Rougier, J., 2007. Probabilistic inference for future climate using an ensemble of climate model evaluations, *Clim. Change*, 81(3-4), 247–264.
- Schmittner, A., Urban, N. M., Keller, K., & Matthews, D., 2009. Using tracer observations to reduce the uncertainty of ocean diapycnal mixing and climate-carbon cycle projections, *Global Biogeochem. Cy.*, 23(GB4009).
- Sitch, S., Smith, B., Prentice, I. C., Arneth, A., Bondeau, A., Cramer, W., Kaplan, J. O., Levis, S., Lucht, W., Sykes, M. T., Thonicke, K., & Venevsky, S., 2003. Evaluation of ecosystem dynamics, plant geography and terrestrial carbon cycling in the LPJ dynamic global vegetation model, *Glob. Change Biol.*, 9(2), 161–185.
- Spahni, R., Wania, R., Neef, L., van Weele, M., Pison, I., Bousquet, P., Frankenberg, C., Foster, P. N., Joos, F., Prentice, I. C., & van Velthoven, P., 2011. Constraining global methane emissions and uptake by ecosystems, *Biogeosciences*, 8(6), 1643–1665.
- Tomassini, L., Knutti, R., Plattner, G.-K., van Vuuren, D. P., Stocker, T. F., Howarth, R. B., & Borsuk, M. E., 2010. Uncertainty and risk in climate projections for the 21st century: comparing mitigation to non-intervention scenarios, *Clim. Change*, 103(3-4), 399–422.
- Wania, R., Ross, I., & Prentice, I. C., 2010. Implementation and evaluation of a new methane model within a dynamic global vegetation model: LPJ-WHyMe v1.3.1, *Geosci. Model Dev.*, 3(2), 565–584.
- Zaehle, S., Sitch, S., Smith, B., & Hatterman, F., 2005. Effects of parameter uncertainties on the modeling of terrestrial biosphere dynamics, *Global Biogeochem. Cy.*, 19(3).

Appendix A

Coupling of the Bern3D and LPX models

A.1 Method

This appendix provides a technical overview of the coupling mechanism used to combine the Bern3D and LPX models. The coupler routine of the Bern3D model, calculates the change in atmospheric CO₂ given different fluxes at each time step of the integration:

$$\frac{d\text{CO}_2(t)}{dt} = E_{\text{FF}}(t) + E_{\text{LU}}(t) - F_{\text{Ind}}(t) - F_{\text{ocn}}(t) \quad (\text{A.1})$$

E_{FF} and E_{LU} denote fossil fuel (FF) and land use emissions. F_{Ind} and F_{ocn} are the simulated fluxes from the atmosphere to the land and ocean, respectively. CO₂ concentrations, E_{FF} , E_{LU} , and F_{Ind} can be prescribed with time series. F_{Ind} will be calculated by the LPX model if a missing value is prescribed, F_{ocn} is always calculated by the Bern3D model. E_{LU} can be used to prescribe land use CO₂ emissions explicitly. It should be zero if land use emissions are calculated interactively by the LPX model. In that case CO₂ fluxes from land use are included in F_{Ind} . Either the prescribed CO₂ or E_{FF} must be a missing value in order to be able to solve the budget. If CO₂ concentrations are prescribed the implied emissions are calculated and vice versa. Which of them is prescribed may change during a simulation. E.g. historical CO₂ concentrations can be prescribed and for future scenarios the model can switch to prescribed emissions and simulate the concentrations interactively. When carbon isotopes are enabled, the ¹³C-signature of FF emissions must be prescribed additionally.

As mentioned above, if the prescribed value for $F_{\text{Ind}}(t)$ is a missing value, the Bern3D model will obtain the carbon flux from the LPX model. This will be done only once in a model year because of the design of the LPX model. The LPX main routine is called in the first Bern3D time step of each year. Input data are the global mean atmospheric CO₂ concentration, the isotopic signatures for ¹³C and ¹⁴C (if enabled), and ΔT_{glob} , the global annual mean temperature deviation from the previous year with respect to the preindustrial steady state. ΔT_{glob} is used by the LPX model to scale anomaly patterns for temperature, precipitation and cloud cover that have been obtained in a global warming simulation with the NCAR model, which will then be added on top of the 31-year baseline climatology, in order to emulate the spatial response of the NCAR model to changing global mean temperatures. Given this input, LPX simulates one annual cycle and returns the total atmosphere-land flux for that year including the isotopic signatures. This flux is saved and applied uniformly as F_{Ind} at each Bern3D time step of the year. In addition to the carbon fluxes, two-dimensional fields of simulated surface albedo are returned from LPX, which are mapped to the Bern3D

grid and applied as described in the next two sections. Figure A.1 provides an overview of the interactions between model components. Please note, that there is no coupling of the hydrological cycle between the LPX and Bern3D model components.

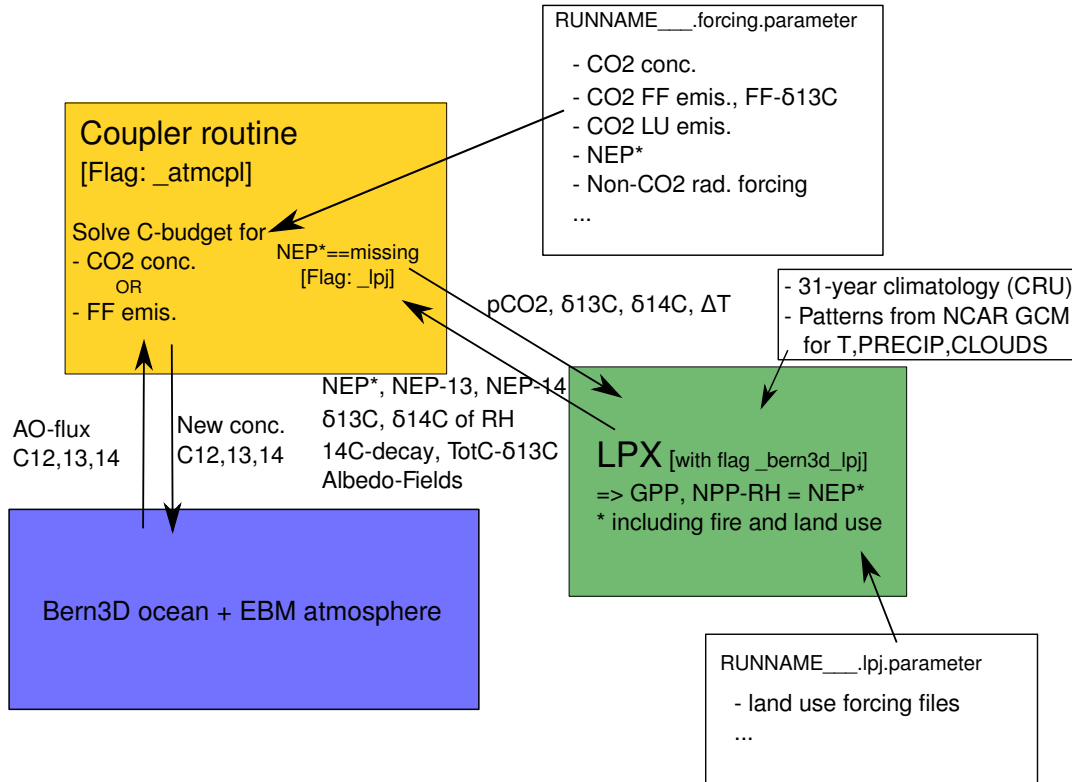


Figure A.1: Basic overview of interactions between Bern3D and LPX model components. The coupler routine (yellow) solves the carbon budget given the fluxes/concentrations from the Bern3D ocean and atmosphere (blue), the fluxes from LPX (green), and the prescribed forcings (white). LPX is driven by atmospheric CO₂ and global temperature anomalies from Bern3D to scale patterns for temperature, precipitation, and cloud anomalies, which are added on top of a baseline climatology.

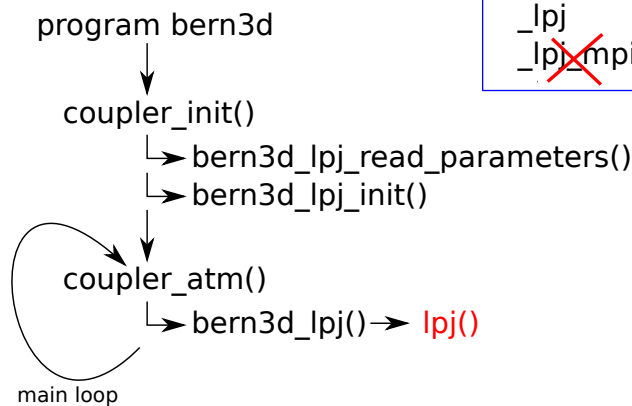
Technically, the LPX model can be executed as a subroutine within the Bern3D model (serial mode) or it can be executed as a separate process on the same or on another host (parallel mode). For the parallel mode, MPI is used for the communication between processes. In this mode, the LPX model can be parallelized further internally to increase the performance (see Appendix C). The maximal performance is reached when the LPX component requires the same amount of time to simulate one model year as the Bern3D component on a single node. The differences in the program flow between the serial and parallel modes are depicted in Figure A.2.

A.2 Mass-conserving mapping between LPX and Bern3D grids

The Bern3D and the LPX model components run on grids with different resolutions. A spatially resolved coupling of the model components requires the exchange of two-dimensional fields such as albedo maps, mass fluxes, or temperature fields. To translate those fields between the two different grids, a mapping matrix is calculated. The matrix elements are weights $w(i_{LPX}, j_{LPX}, i_{B3D}, j_{B3D})$ that are proportional to the overlapping area of grid-cell pairs $\{(i_{LPX}, j_{LPX}), (i_{B3D}, j_{B3D})\}$. The matrix needs to be calculated only once for a specific

Bern3D - LPX coupling modes

A) Serial mode (1 task)



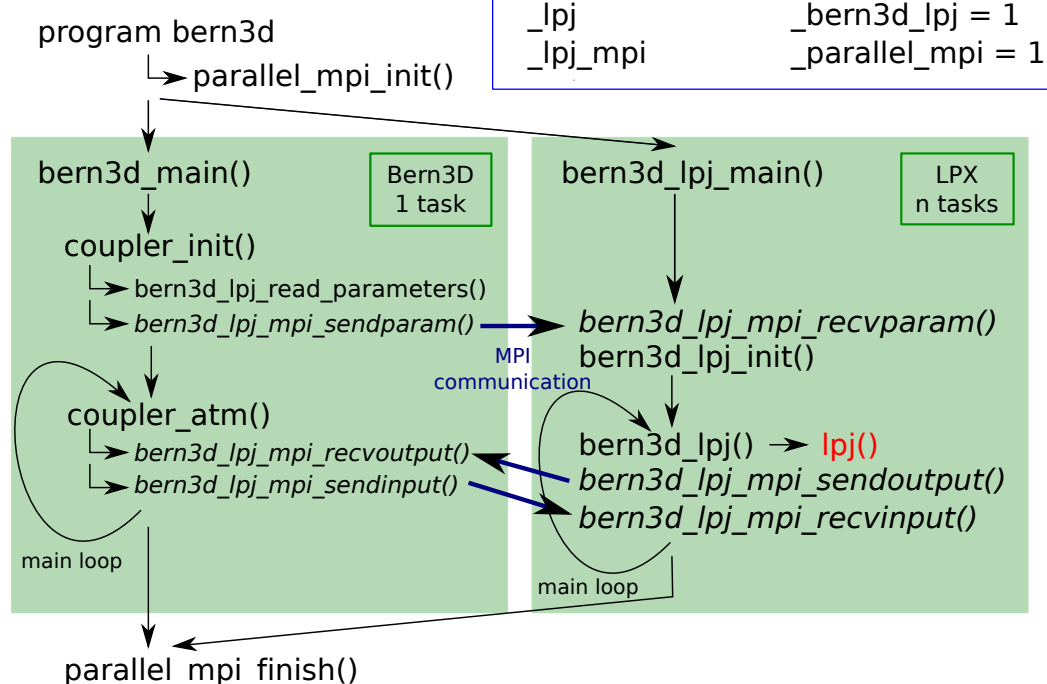
Bern3D flags:

`_lpj`
~~`_lpj_mpi`~~

LPX flags:

`_bern3d_lpj = 1`
`_parallel_mpi = 0`

B) Parallel mode (1+n tasks)



Bern3D flags:

`_lpj`
`_lpj_mpi`

LPX flags:

`_bern3d_lpj = 1`
`_parallel_mpi = 1`

Figure A.2: There are two ways to attach the LPX model to Bern3D. In the serial mode (A), only one process is executed and the LPX main routine (`lpj()`) is simply called from the Bern3D coupler routine. In the parallel mode (B), the setting is a bit more complex as Bern3D and LPX are executed as separate, parallel processes in order to improve performance. The program flow is basically the same, but additional routines (in italic) are required to communicate between the processes using the MPI framework. The processes can be executed on different hosts connected via a network and the LPX task can be parallelized further as described in Appendix C to increase the performance.

grid specification. This is done by the `bern3d_lpj_calcmmap()` routine which is called from the initialization routine `bern3d_lpj_initmap()` [`bern3d_lpj_map.F`].

The implemented algorithm is based on the assumption that the LPX grid resolution is higher than the Bern3D resolution at all points, i.e. one LPX grid cell may overlap with up to four Bern3D grid cells, but not more. This simplifies the problem significantly. For

each LPX grid cell $(i_{\text{LPX}}, j_{\text{LPX}})$ four factors f_k with $\sum f_k = 1$ are calculated that correspond to the overlapping area fractions of the adjacent Bern3D grid cells $(i_{\text{B3D}} - 1, j_{\text{B3D}} - 1)$, $(i_{\text{B3D}}, j_{\text{B3D}} - 1)$, $(i_{\text{B3D}} - 1, j_{\text{B3D}})$, and $(i_{\text{B3D}}, j_{\text{B3D}})$, respectively (Fig. A.3). The factors f_2 , f_3 , and f_4 can be zero if there is no overlap with the corresponding adjacent Bern3D grid cell. The indices $(i_{\text{B3D}}, j_{\text{B3D}})$ of the adjacent Bern3D grid cells for a given LPX grid cell are determined by searching the smallest lower-left corner coordinates (lon., lat.) that both are greater than the lower-left corner coordinates of the LPX grid cell $(i_{\text{LPX}}, j_{\text{LPX}})$. With these factors the following weights are calculated:

$$\begin{aligned}
 w(i_{\text{LPX}}, j_{\text{LPX}}, i_{\text{B3D}} - 1, j_{\text{B3D}} - 1) &= f_1 \frac{A_{\text{LPX}}(i_{\text{LPX}}, j_{\text{LPX}})}{A_{\text{B3D}}(i_{\text{B3D}} - 1, j_{\text{B3D}} - 1)} \\
 w(i_{\text{LPX}}, j_{\text{LPX}}, i_{\text{B3D}}, j_{\text{B3D}} - 1) &= f_2 \frac{A_{\text{LPX}}(i_{\text{LPX}}, j_{\text{LPX}})}{A_{\text{B3D}}(i_{\text{B3D}}, j_{\text{B3D}} - 1)} \\
 w(i_{\text{LPX}}, j_{\text{LPX}}, i_{\text{B3D}} - 1, j_{\text{B3D}}) &= f_3 \frac{A_{\text{LPX}}(i_{\text{LPX}}, j_{\text{LPX}})}{A_{\text{B3D}}(i_{\text{B3D}} - 1, j_{\text{B3D}})} \\
 w(i_{\text{LPX}}, j_{\text{LPX}}, i_{\text{B3D}}, j_{\text{B3D}}) &= f_4 \frac{A_{\text{LPX}}(i_{\text{LPX}}, j_{\text{LPX}})}{A_{\text{B3D}}(i_{\text{B3D}}, j_{\text{B3D}})},
 \end{aligned} \tag{A.2}$$

where A_{LPX} and A_{B3D} denote the corresponding grid cell areas. All other elements for a given LPX grid cell $(i_{\text{LPX}}, j_{\text{LPX}})$ are zero and $\sum_{i_{\text{B3D}}, j_{\text{B3D}}} w(i_{\text{LPX}}, j_{\text{LPX}}, i_{\text{B3D}}, j_{\text{B3D}}) = 1$ for all $i_{\text{B3D}}, j_{\text{B3D}}$.

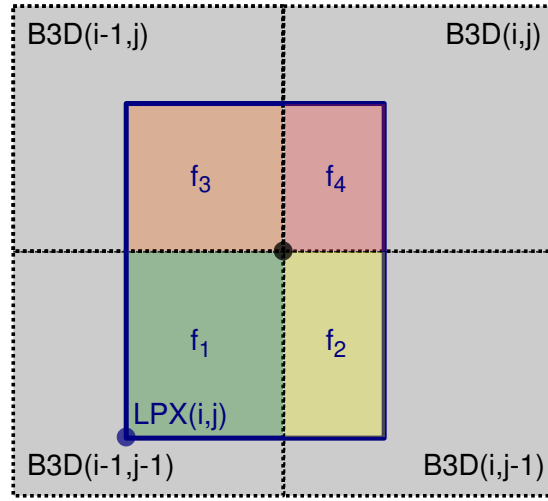


Figure A.3: LPX and Bern3D grid area fractions used to calculate mapping weights.

With the weights calculated during model initialization, LPX fields X_{LPX} can be translated to Bern3D fields at any time by

$$X_{\text{B3D}}(i_{\text{B3D}}, j_{\text{B3D}}) = \sum_{i_{\text{LPX}}, j_{\text{LPX}}} w(i_{\text{LPX}}, j_{\text{LPX}}, i_{\text{B3D}}, j_{\text{B3D}}) X_{\text{LPX}}(i_{\text{LPX}}, j_{\text{LPX}}), \tag{A.3}$$

while conserving the global integral. This is done by the subroutine `bern3d_lpj_map()`. The matrix multiplication is optimized by storing the minimum and maximum index of non-zero elements in the sparse matrix w for a given LPX grid cell.

Some care has to be taken when the field X contains missing values, which is usually the case (e.g. ocean boxes). The `bern3d_lpj_map()` routine offers three options to handle missing values:

1. None: Don't handle missing values at all. No checking for missing values is performed during the matrix multiplication

$$X_{\text{out}} = \sum_i w_i X_{\text{LPX},i}. \quad (\text{A.4})$$

2. Mixing: Use the default values of a given field (X_{in}) for the areas where LPX values are missing

$$X_{\text{out}} = \sum_i w_i^{\text{nomiss}} X_{\text{LPX},i} + (1 - \sum_i w_i^{\text{nomiss}}) X_{\text{in}}, \quad (\text{A.5})$$

where w_i^{nomiss} stands for the weights that correspond to non-missing LPX grid cells. This can be used, for example, to combine ocean and land fluxes, weighted by their area fractions. Note that if X_{in} is initialized with zero, the total mass is conserved by reducing concentrations in grid boxes that map to missing and non-missing values.

3. Up-scaling: Use the average non-missing data for the entire grid cell. Note that this option does **not** conserve mass anymore, but concentrations:

$$X_{\text{out}} = \frac{1}{\sum_i w_i^{\text{nomiss}}} \sum_i w_i^{\text{nomiss}} X_{\text{LPX},i}. \quad (\text{A.6})$$

There is a test program `bern3d_lpj_map_testprog.F`, which can be used to test the mapping routines. The mapping in the other direction, from the Bern3D grid to the LPX grid, is not yet implemented, but this should be straightforward by using the same weights and by adding a routine similar to `bern3d_lpj_map()`.

A.3 Coupling LPX and Bern3D surface albedo

The coupling of the albedo calculated by LPX with the albedo used in the shortwave radiation code of the Bern3D EBM module can be enabled with the flag `_lpj_albedo` in the Bern3D code. Monthly surface albedo fields are passed to the Bern3D coupler [`coupler.F`] along with the other output needed for interacting with the atmosphere, such as the global annual mean NEP. In order to be able to estimate changes in radiative forcing that are directly caused by land use changes, two fields are transferred. One is the total albedo (weighted average of all land use classes) and the other is the 'natural' albedo only (excluding anthropogenic land use classes). Note that the natural albedo can only be calculated as long as the natural land use area is greater than zero. If a grid box is entirely occupied by anthropogenic land use, the natural albedo will be a missing value.

In the Bern3D coupler routine, the fields are mapped to the Bern3D grid. Missing values are treated according to the up-scaling method (section A.2) with the default values being the albedo from the previous year if available, or the missing value otherwise. That means that when the natural land use area goes to zero in one grid cell, the natural albedo is kept at the value of the last year with non-zero natural area (CAVEAT: as long as the model is not restarted!). This has some implications for the radiative forcing diagnostics but not for the effective radiative forcing itself (section B.2).

In the atmospheric shortwave code [`atmcalcsw.F`], changes in the LPX albedo are added to the constant albedo climatology used by the Bern3D EBM. First, a reference annual cycle $\alpha_{\text{LPX}}^{\text{ref}}$ is determined by averaging the albedo field from LPX during a calibration period, which can be specified with the parameter `albedo_ref_years`. If the 31-years CRU climatology is used

for the LPX climate forcing, 31 years is a good choice for that period. After the calibration period, the EBM surface albedo α_{atm} is modified with

$$\alpha_{\text{atm}}(i, j) = \alpha_{\text{atm}}(i, j) + (\alpha_{\text{LPX}}(i, j) - \alpha_{\text{LPX}}^{\text{ref}}(i, j)) \quad (\text{A.7})$$

at each time step. Only Bern3D land grid cells (i, j) are considered, i.e. the albedo of ocean grid cells is not changed even if there are some LPX land grid cells that map to them. For Bern3d land grid cells which are partially ocean grid cells on the LPX grid, the average albedo of the LPX land cells is used for the entire cell (this is done automatically by using the up-scaling method when remapping the fields). To exclude potentially unrealistic values, the resulting albedo is limited to a maximum of 0.85 and a minimum of 0.01.

Appendix B

Implementation of new forcings and diagnostics in Bern3D

B.1 Sulphate aerosol forcing

Sulphate aerosols are taken into account by changing the surface albedo locally according to the parametrization by Reader & Boer (1998). This forcing is enabled by the `_ebm_aerosol_od` flag and the corresponding options in the forcing parameter file. A time-varying 2D field of aerosol optical depth $\delta(i, j, t)$ is read in at model start-up. The aerosol optical depth can be derived from the mass aerosol loading $B(\text{SO}_4^{2-})$. In the shortwave radiation code, the albedo is then modified as follows:

$$\alpha_{\text{atm}}(i, j, t) = \alpha_{\text{atm}}(i, j, t) + \frac{\beta \delta(i, j, t) (1 - \alpha_{\text{atm}}(i, j, t))^2}{\cos(\theta)}, \quad (\text{B.1})$$

where $\beta = 0.29$ and θ are the upward scattering parameter (Reader & Boer, 1998) and zenith angle, respectively. Because the parametrization does not work for zenith angles close to 90° , it is only applied if $\cos(\theta) > 0.001$ ($\theta \lesssim 89.9^\circ$). The contribution from diffuse radiation due to clouds is neglected.

B.2 Radiative forcing diagnostics

The EMIC AR5 simulation protocol requires to diagnose the total external radiative forcing (i.e. solar, orbital, greenhouse gases, aerosols, and land use change). These diagnostics can be enabled with the `_ebm_radforc_diag` flag. The radiative forcing due to changes in total solar irradiance and orbital parameters can simply be derived from the incoming shortwave flux at the top of the atmosphere (Ritz et al., 2011):

$$\text{RF}_{\text{sol,orb}}(t) = F_{\text{sw}}^{\text{TOA}}(t) - F_{\text{sw}}^{\text{TOA}}(t_0), \quad (\text{B.2})$$

where t_0 is the reference time. The radiative forcing due to greenhouse gases and volcanic aerosols (and possibly other external forcings) applied in the long wave radiation code [`atmplanetarylw.F`] is also straightforward because it is already specified in terms of a global radiative forcing RF_{glob} (GHGs other than CO_2 and volcanic aerosols) or can be translated directly (CO_2):

$$\text{RF}_{\text{ext.lw}}(t) = \text{RF}_{\text{glob}}(t) + 5.35 \text{ W m}^{-2} \cdot \log \left(\frac{p\text{CO}_{2,\text{atm}}(t)}{278 \text{ ppm}} \right) \quad (\text{B.3})$$

Diagnosing the radiative forcing due to changes in surface albedo is less trivial because it affects the calculation of the shortwave fluxes in a more complex way [`atmcalcsw.F`]. Technically, this is solved by calling the shortwave routine multiple times. First no additional forcings are applied, then the shortwave fluxes are calculated once with only the sulphate aerosol forcing enabled and once with only the ‘natural’ (i.e. not land use related, see section A.3 for a description and caveats) LPX albedo forcing. In the final step, all forcings are applied and this result is then also used for the actual model integration. The previous steps are just for diagnostic purposes and they are skipped if `_ebm_radforc_diag` is not enabled. Note that all changes in surface albedo simulated by LPX are considered as additional forcing in this step, although albedo changes that are not directly related to land use changes are an internal feedback and not considered an external forcing. By comparing the outgoing shortwave fluxes at the top of the atmosphere ($F_{\text{sw}}^{\text{up}}$ in Ritz et al. (2011)), the contributions of the different forcings can be estimated:

$$\begin{aligned} \text{RF}_{\text{aerosol}} &= F_{\text{sw,aerosol}}^{\text{up}} - F_{\text{sw},0}^{\text{up}} \\ \text{RF}_{\text{albedo.nat}} &= F_{\text{sw,albedo.nat}}^{\text{up}} - F_{\text{sw},0}^{\text{up}} \\ \text{RF}_{\text{albedo.LU}} &= F_{\text{sw,total}}^{\text{up}} - \text{RF}_{\text{aerosol}} - \text{RF}_{\text{albedo.nat}} - F_{\text{sw},0}^{\text{up}} \end{aligned} \quad (\text{B.4})$$

$F_{\text{sw},0}^{\text{up}}$, $F_{\text{sw,aerosol}}^{\text{up}}$, $F_{\text{sw,albedo.nat}}^{\text{up}}$, and $F_{\text{sw,total}}^{\text{up}}$ denote the diagnosed shortwave fluxes when applying no additional forcings, only sulphate aerosols, only LPX albedo changes without land use, or all forcings, respectively. For this estimation, a linear relationship between changes in surface albedo and the resulting radiative forcing is assumed.

The total external radiative forcing according to the EMIC AR5 protocol is then calculated as

$$\text{RF}_{\text{ext,total}} = \text{RF}_{\text{sol,orb}} + \text{RF}_{\text{ext.lw}} + \text{RF}_{\text{aerosol}} + \text{RF}_{\text{albedo.LU}}. \quad (\text{B.5})$$

B.3 Sea level rise and ocean heat content

Steric sea level rise (SSLR) and ocean heat content (OHC) are diagnosed when the flag `_diag_heatuptake` is set. The ocean heat content is calculated as follows for the total ocean volume as well as for the top 700 m, a depth level often found in observation based data-sets:

$$\text{OHC} = \sum_{i,j,k} c_p \rho(i,j,k) V(k) (T(i,j,k) + 273.15 \text{ K}), \quad (\text{B.6})$$

where $c_p = 3981.1 \text{ J kg}^{-1} \text{ K}^{-1}$ is the heat capacity of sea water, ρ the water density, V the grid cell volume, and T the temperature in $^{\circ}\text{C}$.

The global mean steric sea level rise is calculated as

$$\text{SSLR} = \frac{1}{A_{\text{oc}}} \sum_{i,j,k} d_z(k) \left(\frac{\rho_0(i,j,k)}{\rho(i,j,k)} - 1 \right), \quad (\text{B.7})$$

where A_{oc} is the total ocean area, $d_z(k)$ the grid cell height, and $\rho_0(i,j,k)$ the reference density, which is diagnosed at the first time step of the model integration.

The density ρ used to calculate SSLR and OHC needs to be converted from model units (ρ_{mod}) to real units with

$$\rho(i,j,k) = \rho_{\text{mod}}(i,j,k) \rho_{\text{sc}} + 0.7968 \text{ kg m}^{-2} \text{ psu}^{-1} \cdot S_0 + \rho_{\text{sc},0}, \quad (\text{B.8})$$

where $S_0 = 34.78$ psu is the reference salinity and $\rho_{sc,0} = 1000 \text{ kg m}^{-2}$ and

$$\begin{aligned}\rho_{sc} &= \rho_{sc,0} f_{sc} u_{sc} r_{sc} (g_{sc} d_{sc})^{-1} \\ &= 1000 \text{ kg m}^{-2} \cdot 0.5 \text{ m s}^{-1} \cdot 2 \cdot 7.2921^{-5} \text{ s}^{-1} \cdot 6.37 \cdot 10^6 \text{ m} \cdot (9.81 \text{ m s}^{-2} \cdot 5000 \text{ m})^{-1} \quad (\text{B.9}) \\ &= 0.9470 \text{ kg m}^{-2}\end{aligned}$$

are dimensional scale values, probably related to the following fundamental scales: water density, frequency corresponding to a timescale of $\approx 1.9 \text{ h}$ (?), ocean currents speed, Earth radius, gravity, and ocean depth.

B.4 Temperature tracking

Following Zickfeld et al. (2009), a temperature tracking mechanism has been implemented that allows it to force the model with a global mean surface temperature profile. During the simulation, CO₂ emissions required to follow the temperature profile are diagnosed interactively.

The temperature tracking can be switched on with the `_atmcpl.temptrack` flag. In this mode, the temperature profile $T_{in}(t)$, instead of CO₂ concentrations or emissions, is read according to the settings in the forcing parameter file `[coupler.F]`. At each time step, the CO₂ emissions are calculated as

$$E(t) = k_{conv} k_{damp} (T_{in}(t) - T_{rave}(t)), \quad (\text{B.10})$$

where $T_{rave}(t)$ is a running average of the simulated global mean temperature. The current averaging period is one year. $k_{conv} = \frac{300 \text{ ppm}}{3^\circ\text{C} \cdot \Delta t}$ is a conversion factor that relates CO₂ emissions to changes in temperature. This relation can be estimated with the climate sensitivity and the integration time step Δt of the model. A damping factor k_{damp} has to be included to ensure an over-damped system. The choice of this factor is crucial and not trivial. If the damping is too weak, strong oscillations in the simulated temperature may occur and it likely overshoots the prescribed profile significantly when the temperature trend changes rapidly. If it is too strong, the model is not able to follow the profile where the rate of change is too high (Fig. B.1). After some testing the following adaptive damping factor was introduced

$$\begin{aligned}k_{damp} &= f \cdot 0.05 + (1 - f) \cdot 0.005 \quad (\text{B.11}) \\ f &= \frac{\min(t - t_{cs}, 15 \text{ yr})}{15 \text{ yr}},\end{aligned}$$

where t_{cs} is the time at which the last change of sign in the emissions E occurred. That means that the damping is allowed to relax up to the maximum value of 0.05 with a timescale of 15 years. If a change of sign occurs, the damping factor is reset to the minimum value of 0.005. This method avoids oscillations and overshooting when the prescribed temperature profile changes rapidly, while it allows to follow steep continuing slopes. This has been validated with historical and projected (RCP-8.5) temperature profiles (Fig. B.1).

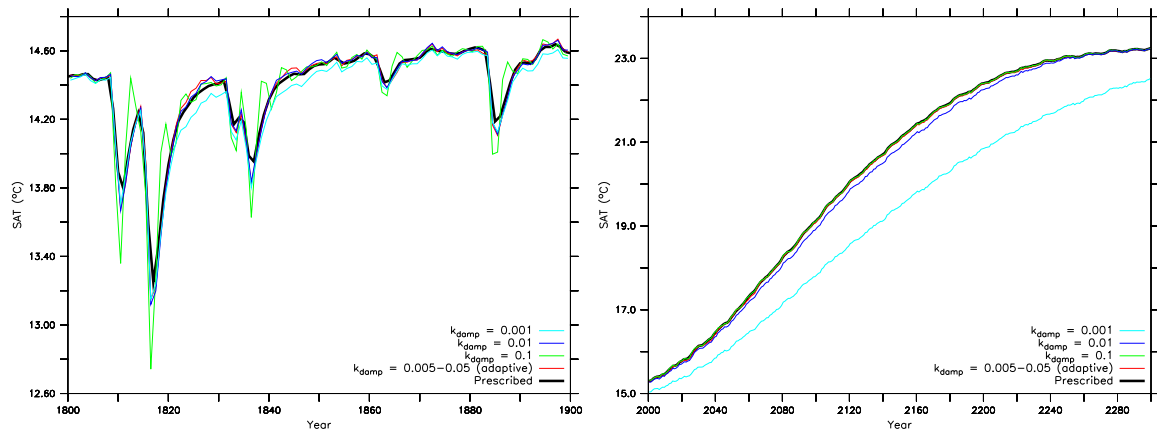


Figure B.1: Influence of different damping factors k_{damp} on the ability to track a prescribed temperature profile (black) for a historic (left) and projected future period (right). The red line shows the result with the adaptive damping factor that has finally been implemented.

Bibliography

- Reader, M. C. & Boer, G. J., 1998. The modification of greenhouse gas warming by the direct effect of sulphate aerosols, *Clim. Dynam.*, 14(7-8), 593–607.
- Ritz, S. P., Stocker, T. F., & Joos, F., 2011. A coupled dynamical ocean-energy balance atmosphere model for paleoclimate studies, *J. Climate*, 24(2), 349–375.
- Zickfeld, K., Eby, M., Matthews, H. D., & Weaver, A. J., 2009. Setting cumulative emissions targets to reduce the risk of dangerous climate change, *Proc. Nat. Acad. Sci. USA*, 106(38), 16129–16134.

Appendix C

Parallelization of the LPX model

The LPX model poses an ideal parallelization problem because the calculations for individual grid cells are independent from each other. Only the computation of global mean values and the coordinated input and output to files or other model components (e.g. when LPX is coupled to the Bern3D model) require communication between the parallel processes (tasks). The MPI (Message Passing Interface) framework¹ is used for the communication between the tasks. MPI allows the parallel computation on separate nodes that are interconnected via a network.

Due to the independence of individual grid cells, the domain (all grid cells) can be divided arbitrarily for the parallel processing by N tasks, where N can be any number between 2 and the number of grid cells. Because the slowest tasks limits the processing time of the whole domain, the challenge is to distribute the workload equally among the tasks. This is not easy because the processing time of each grid cell depends on the type of vegetation, number of land use classes etc. that are present in that cell. To optimize the distribution, computation costs for different grid cell types can be defined. An algorithm at the initialization of the model uses those weights to divide the domain into N parts that all have about the same computational costs ($1/N$ of the sum of costs of all grid cells). Currently, only ‘normal’ and peatland grid cells are distinguished, which eliminates the largest disproportions in computational costs because peatland cells are much more expensive. The equal distribution of the workload is crucial, especially when a large number of tasks are used. If, for example, the domain is distributed among 100 tasks and the distribution is ideal for 99 tasks (equal costs) and just one task is 30% slower than the others, then the computation time for the whole process is about 30% longer because 99% of the CPUs are wasting 30% of their time waiting for the slower process. To further optimize this, the computational cost of each grid cell could be measured with a calibration run, which could then be used to find an optimal partitioning of the domain.

After the distribution of the grid cells among the tasks, each task runs the LPX model for the grid cells that have been assigned to it. For simplicity, all tasks currently initialize all grid cells and read the input and restart data for the whole domain, although they operate only on a smaller set of grid cells. This could be optimized and would reduce the memory consumption and model initialization or input/output time. Most of the processing is done as if the individual tasks were independent model runs with a reduced number of grid cells, with the following exceptions: (i) At the end of one year all tasks send the data needed to calculate global values to the master task which then computes the required quantities. (ii) At time steps where a restart or output file is written, all tasks send their part of the required fields to the master task, which then writes the data to the output files.

¹<http://www.mcs.anl.gov/research/projects/mpi/>

C.1 Technical notes

1. To enable the parallelization code the flag ‘_parallel_mpi’ must be set to 1 in `lpj_feature_control.inc`. To compile the code, OpenMPI flags must be added to Makefiles:

```
COMPFLAGS += $(shell mpif90 --showme:compile)
DEBUGFLAGS += $(shell mpif90 --showme:compile)
LIBS      += $(shell mpif90 --showme:link)
```

2. To run the parallelized code the main program must be submitted with the option ‘#\$ -pe orte *NTASKS*’ in the submission file (see `submitjob_lpx_openmpi.sub` for an example), where *NTASKS* is the number of tasks that should be started. Each task has a different ‘`mpi_rank`’, which is used to trigger different behavior of the tasks. The global domain (`minline:maxline`) is divided into parts (`minline_task:maxline_task`) that will be processed by a specific task. Some parts of the code are executed only by some tasks (e.g. only the master task writes output files).

3. Most of the parallelization code is in ‘`parallel_mpi.F/.inc`’. Important changes in the LPX code, that should also be considered for future development, are:

1. `minline_task/maxline_task` should now be used to refer to the domain that is processed by ONE task. `minline/maxline` should only be used when really referring to the WHOLE domain, i.e. the global domain that has been processed by all tasks together and that has been merged by the master task.
2. All output data has to be gathered and merged by the master task before it is written to files. Therefore, new output variables have to be added to the following routines in `parallel_mpi.F`:

```
parallel_mpi_gather_restart    (restart file variables)
parallel_mpi_gather_cdfoutput (netcdf output variables)
parallel_mpi_gather_global    (global data -> ASCII output)
```

3. Code that should only be executed by the master task must be enclosed by if-statements:

```
if (mpi_rank.eq.mpi_lpjmaster) then
  ...
endif
```

4. The main program that drives the `lpj` routine must call ‘`parallel_mpi_init`’ once before calling the `lpj` routine for the first time. After the last call of the `lpj` routine ‘`parallel_mpi_finish`’ must be executed. Remember that the code in the main program will be executed by ALL tasks simultaneously unless you use ‘`mpi_rank`’ to select specific tasks. Typically, the main program looks similar to this:

```
program main
include 'lpj/lpj/parallel_mpi.inc'
...
call parallel_mpi_init
...
do year = 1,maxyears
  call lpj(year,...)
```

```
end do
...
if (mpi_rank.eq.mpi_lpmaster) then
  <some stuff that is only done by the master task>
endif
...
call parallel_mpi_finish
end program
```


Appendix D

Parallelization of the PISCES model

The marine ecosystem model PISCES can be used to replace the relative simple representation of the marine biota the Bern3D model. However, switching from the standard model setup to PISCES increases the computational costs significantly. Therefore, a shared-memory parallelization technique (OpenMP¹) has been applied in order to increase the computing performance. This appendix summarizes this attempt from a technical point of view.

D.1 Code changes

A bunch of depth/lat/lon loops in the PISCES code have been parallelized using OpenMP. This was done by adding `!$OMP PARALLEL DO` directives² before the loops. These directives are not FORTRAN code, but special comment lines that serve as instructions for the compiler. For example:

```
!$OMP PARALLEL DO PRIVATE(jk,jj,ji,[other local vars used in loop])
DO jk = 1,jpkk
. DO jj = 1,jpjj
. DO ji = 1,jpii
. (code that depends only on data at depth jk)
. END DO
. END DO
END DO
```

In this case the outermost loop (over `jk`) will be split up and executed in parallel (i.e. in separate threads). This implies that the code inside the loop must depend only on data at `jk` and not on data at other depth-slices (e.g. `jk-1`). This does not apply to `jj` and `ji`, because these loops will be executed completely by one thread. However, these variables must be declared as private in the `!$OMP PARALLEL DO` statement, along with other variables in the loop that need to be used independently by the parallel threads. This is crucial, because if you don't do this, the threads will use and modify the **same** variables and data in parallel.

For some loops it was necessary to change the order of the loops (i.e. switch depth with lat or lon), because the code inside the loop depends on data at other depths, but not on data at other lat/lon.

¹<http://openmp.org>

²PGI User's Guide, Chapter 5, p.135ff

D.2 Compiling and running

A program that has been parallelized using OpenMP (shared-memory) can only be executed in parallel on multi-CPU or multi-core machines by using multiple CPUs at the same time. It cannot be used to distribute the work on multiple nodes as it can be done with MPI (message-passing).

To compile the code with OpenMP support you simply have to add the `-mp` PGI compiler option. With this switch the compiler will interpret the `!$OMP` directives and parallelize the code. Without this option, these directives are ignored.

To run the program the stacksize limit of the shell has to be increased sometimes³. If you don't do this it is likely to get an 'Segmentation fault' error. You can do this with `ulimit -s unlimited` (bash, sh, ksh) or with `limit stacksize unlimited` (csh).

The parallelized program can be used like normal. In that case it will usually use only one CPU by default. You can set the number of CPUs (parallel threads) that should be used with the `OMP_NUM_THREADS` environment variable⁴. For example:

```
echo "test_____" | OMP_NUM_THREADS=2 ./bern3d
```

This will execute the Bern3D model on two CPUs (if available). Please note that you can set any number of threads, but it will be very slow if you specify more threads than actually available CPUs. You can view information about the CPU(s) of a machine with the command `cat /proc/cpuinfo`.

D.3 Results

With the code changes described above the performance was improved by about 19% by using two CPUs instead of one (20.8 sec/timestep to 16.8 sec/timestep on node beta022). This improvement is only moderate, possibly because relatively large memory data transfers limit the performance. On newer hardware with larger memory transfer bandwidth, the relative improvement of the parallelization is probably better. Also, this outcome suggests to address optimizations in the data management before further parallelizing the model. Large data amounts are copied between variables at each time step. This could probably be improved by using pointers and a double buffering approach.

The performance was also tested on the IBM p5 system (blanc) at CSCS in Manno. There, the improvement was 30%, 49%, 56%, and 58% when using 2, 3, 4, and 6 CPUs instead of one (20.1 sec/timestep (1 CPU) to 8.5 sec/timestep (6 CPUs)). Using more than 6 CPUs did not increase the performance. However, because of the different system another compiler was used in this test and the results have not been verified.

³PGI User's Guide, Section 1.5.2, p.29f

⁴PGI User's Guide, Section 5.19, p.154

Appendix E

The Bern3D NetCDF Module

E.1 Introduction

NetCDF (Network Common Data Form) is a data format commonly used to store array-oriented scientific data, and in particular gridded data in geosciences. More information about NetCDF can be found at <http://www.unidata.ucar.edu/software/netcdf/>. NetCDF files can be processed easily with command line tools like **nco**¹ or **cdo**² to perform standard operations (e.g. concatenating files, averaging, extracting variables etc.).

NetCDF is natively supported by many powerful data analysis and plotting tools such as FERRET³ or the NCAR Command Language (NCL)⁴. Further, NetCDF libraries or modules exist for many programming languages (e.g. FORTRAN, C, Perl⁵, Matlab⁶), which provide functions to access, create, and modify NetCDF data easily.

This appendix describes how NetCDF input/output was implemented in Bern3D replacing the old ASCII output. A modular approach is taken to encapsulate the technical details in generic routines. The goal is to minimize changes required in the existing model code, to facilitate the addition of new output variables or grid definitions, and to avoid duplication of code.

E.2 Bern3D NetCDF output

E.2.1 New source code files

NetCDF output is mainly implemented in the following files:

1. `netcdf_output.F`: Main routines that represent the interface to the rest of the model code. Time-dependent variables are defined here.
2. `netcdf_write.F`: Routines that define and write variables and header data to the NetCDF files (mostly generic code). Time-independent variables and global attributes are defined here.

¹<http://nco.sourceforge.net/>

²<http://www.mpimet.mpg.de/fileadmin/software/cdo/>

³<http://ferret.wrc.noaa.gov/Ferret/>

⁴<http://www.ncl.ucar.edu/>

⁵Module NetCDF (use `Netcdf;`), <http://www.unidata.ucar.edu/software/netcdf-perl/>

⁶NetCDF Toolbox (`help netcdf`), <http://mexcdf.sourceforge.net/>

3. `netcdf_util.F`: Low-level utility routines that are mainly used in `netcdf_write.F`. Most calls to NetCDF library routines are done here.
4. `netcdf_var.cmn.F`: Global variables used by the NetCDF module. Variable ID variables are declared here.

E.2.2 Output file types

Four different output types are currently implemented:

1. Full output, instantaneous (`cdf_type = 1`)
Filename: `RUNNAME_YYYYYYY_full_inst.nc`
2. Full output, averaged (`cdf_type = 2`)
Filename: `RUNNAME_YYYYYYY_full_ave.nc`
3. Time series output, instantaneous (`cdf_type = 3`)
Filename: `RUNNAME_YYYYYYY_timeseries_inst.nc`
4. Time series output, averaged (`cdf_type = 4`)
Filename: `RUNNAME_YYYYYYY_timeseries_ave.nc`

‘Full output’ refers to the low-frequency comprehensive output (usually full 2D or 3D fields) and ‘time series output’ refers to the high-frequency output (usually global averages) of some variables. Instantaneous output files contain the values at the end of the output interval (e.g. 31-DEC 23:59) and can be used to restart the model. Averaged output contain the values averaged over the output interval (e.g. annual mean). The full output files contain the same set of variables for both time representations, whereas for the time series output independent lists of variables are used. All files also contain the same set of time-independent variables and global attributes (model version, run description, date, grid, masks etc.). In the file names listed above `RUNNAME` is replaced by the name of the run and `YYYYYYY` by the base year `t0` (including leading zeroes) of the output period. Currently, the base year is limited to seven digits. The base year can be negative, in that case `YYYYYYY` is replaced by the minus sign plus six digits. (Note for FERRET users: When using dates where `year < 2` or `year > 9999`, the calendar feature must be disabled with the command ‘cancel mode calendar’.)

E.2.3 Choosing the output method

ASCII and NetCDF file output can be enabled and disabled independently using the preprocessor macros `-D_ascii` and `-D_netcdf`, respectively. If both flags are present, ASCII and NetCDF output will be created simultaneously.

NetCDF verbose messages to stdout can be enabled using the `-D_netcdf_debug` preprocessor switch.

E.2.4 Main concept

At model start-up `netcdf_init()` initializes the NetCDF output module. This includes the definition of output variable sets (incl. names, units etc.). To each variable an ID is assigned (e.g. `cdf_vid_2Dh_PSI` for full output of the barotropic stream function), which is used in the diagnostics code to store the data. For tracers which are stored in `ts(1:ntr, :, :, :)` the array `cdf_vid_3D_tr(1:ntr)` is used to store variable IDs.

During model integration `netcdf_output()` is called at the corresponding frequency for the different output types, which will create the NetCDF files and write out data. At the end of the run `netcdf_finish()` is called to do the cleanup.

In the diagnostics code of the model the output data is written to ASCII files as previously and/or stored to a `cdf_var_*` data structure using the variable ID. Typically for the full output variables this will look like this:

```

subroutine outputXY(unit)

include 'var.cmn'
include 'netcdf_var.cmn'

[...]

do i=1,imax
  do j=1,jmax
    do k=1,kmax
#ifdef _ascii
      !--- ASCII output
      if (not_missing)
        write(unit,*) varXY(i,j,k)/ndtyear
      else
        write(unit,*) 0.0
      endif
#endif
#ifdef _netcdf
      !--- NetCDF output
      if (not_missing)
        cdf_var_ave_3D(cdf_vid_3D_XY,i,j,k) = varXY(i,j,k)/ndtyear
      endif
#endif
    enddo
  enddo
enddo

[...]

```

Here `cdf_var_ave_3D` is the data structure for averaged 3D full output variables and `cdf_vid_3D_XY` is the ID of this variable defined in `netcdf_init()`.

E.2.5 Adding new time-dependent variables

Step 1: Defining the new variable in the NetCDF module

First you have to know the type of your new variable. Currently the following types are supported:

1. 3D full output: `VAR(time,depth,lat,lon)`
Suffix: 3D
2. 2D horizontal full output: `VAR(time,lat,lon)`
Suffix: 2Dh

3. 2D meridional full output: VAR(time,depth,lat)
Suffix: 2Dm
4. 2D horizontal ocean seasonal full output: VAR(time,yearstep_oc,lat,lon)
Suffix: 2Ds_oc
5. 2D horizontal ocean climatology full output: VAR(yearstep_oc,lat,lon)
Suffix: 2Dc_oc
6. 2D horizontal atm. climatology full output: VAR(yearstep_atm,lat,lon)
Suffix: 2Dc_atm
7. 2D horizontal monthly climatology full output: VAR(month,lat,lon)
Suffix: 2Dc_mon
8. 1D full output: VAR(time,lat/lon/depth)
Suffix: 1D
9. 0D (scalar) full output: VAR(time)
Suffix: 0D
10. 0D (scalar) atm. climatology full output: VAR(yearstep_atm)
Suffix: 0Dc_atm
11. Instantaneous time series: VAR(time)
Suffix: tim_inst
12. Averaged time series: VAR(time)
Suffix: tim_ave

All variables are defined in the subroutine `netcdf_init()` in `netcdf_output.F`. To define a new variable add the following lines to the corresponding block of definitions for this variable type (after the comment `Define output variables`):

```

cdf_nvars_SUFFIX = cdf_nvars_SUFFIX + 1
cdf_vid_SUFFIX_VAR = cdf_nvars_SUFFIX
cdf_var_name_SUFFIX(cdf_nvars_SUFFIX) = 'VAR'
cdf_var_lname_SUFFIX(cdf_nvars_SUFFIX) = 'Variable description'
cdf_var_units_SUFFIX(cdf_nvars_SUFFIX) = 'Units'
cdf_var_grid_SUFFIX(cdf_nvars_SUFFIX) = cdf_grid_GRIDSUFFIX

```

SUFFIX must be replaced by the suffix of the corresponding variable type (e.g. 2Dh, see list above) and VAR by the variable name (e.g. PSI, max. 16 characters). The variable description and units can be any strings with up to 80 characters (e.g. 'Barotropic Transport Streamfunction', 'm/s'). If the variable has no units the units string should be empty ('').

If the new variable is a standard tracer stored in the variable `ts(1:ntr, :, :, :)`, the predefined variable ID array should be used and the second line must then read

```

cdf_vid_3D_tr(tr_VAR) = cdf_nvars_3D

```

where `tr_VAR` is the variable that contains the tracer index. For all other variables the new variable `cdf_vid_SUFFIX_VAR`, which will contain the variable ID, must be newly declared in `netcdf_var.cmn.F`. Simply add the new variable name to the corresponding `Variable IDs` block (integer variable definition **and** common block).

The grid definition (last line) must only be present when defining full output variables. Time series variable definitions do not contain this line. The currently defined grids (`GRIDSUFFIX`) are listed in Table E.1.

If the output of a variable can be switched on and off with a preprocessor flag (e.g. `-D.tr_dic` or `-D.diagomaxA`), you should enclose your changes in `netcdf_output.F` and `netcdf_var.cmn.F` with the corresponding `#ifdef` and `#endif` directives.

Step 2: Storing the data in the model's diagnostics code

Once the new NetCDF output variable is defined as described in step one, the NetCDF module will take care of all NetCDF related operations. The only thing left to do is to store the data in the `cdf_var_STORAGESUFFIX` data structures. Like the ASCII output, this should be done in the diagnostics code of the model. `STORAGESUFFIX` is similar to the the suffixes described in step one, but the full output variable types are additionally divided into instantaneous (`cdf_var_inst_*`) and averaged (`cdf_var_ave_*`) variables. All available data structures and their common use are listed in Table E.2.

All output variables are of the type 'double' (`REAL*8`). Where no data is available (e.g. because of the topography), the value must be set to the missing value. To do this, the pre-defined constant `cdf_missing_val` should be used (the current value is `+1D30`). The NetCDF module automatically resets all values of the `cdf_var_STORAGESUFFIX` data structures to this value after each output timestep. Therefore it is sufficient to copy all non-missing values to these data structures; there is no need to set the missing values explicitly.

All code related to ASCII file output (i.e. `open()`, `write()`, and `close()` statements) should be enclosed by `#ifdef _ascii` and `#endif`. Correspondingly the statements which store the data to the `cdf_var_STORAGESUFFIX` structures must be enclosed by `#ifdef _netcdf` and `#endif` (see also example in section E.2.4).

E.2.6 Adding new time-independent variables and attributes

All time-independent variables (e.g. masks, constants etc.) and global attributes (e.g. run description, date, model version etc.) are defined and written to the NetCDF file in the subroutine `netcdf_header()` in `netcdf_write.F`. Global attributes are defined in section 1 using `n_dglob()`:

```
call n_dglob(fid,attribute_name,attribute_string)
```

`fid` is the ID of the current file and must not be changed. `attribute_name` and `attribute_string` can be any strings.

Time-independent variables are defined in section 3 of the subroutine `netcdf_header()`. Example for a scalar constant:

```
lname = 'Constant description'
call n_dscalar(fid,constant_name,lname,units)
```

`constant_name`, `lname`, and `units` can be any strings. Beneath, in section 5, the data is written to the file. Example for a scalar constant:

```
call n_pvar_v(fid,'constant_name',variable)
```

<i>Grid name</i>	<i>Description</i>	<i>Dimensions</i>
<code>cdf_grid_3D_t</code>	3D tracer	<code>VAR(time,z_t,lat_t,lon_t)</code>
<code>cdf_grid_3D_u</code>	3D U velocity	<code>VAR(time,z_t,lat_t,lon_u)</code>
<code>cdf_grid_3D_v</code>	3D V velocity	<code>VAR(time,z_t,lat_u,lon_t)</code>
<code>cdf_grid_3D_w</code>	3D W velocity	<code>VAR(time,z_w,lat_t,lon_t)</code>
<code>cdf_grid_2Dh_t</code>	2D horizontal tracer	<code>VAR(time,lat_t,lon_t)</code>
<code>cdf_grid_2Dh_u</code>	2D horizontal velocity	<code>VAR(time,lat_u,lon_u)</code>
<code>cdf_grid_2Dm_u</code>	2D meridional velocity	<code>VAR(time,z_w,lat_u)</code>
<code>cdf_grid_2Ds_oc</code>	2D horiz. seasonal ocean field	<code>VAR(time,yearstep_oc,lat_t,lon_t)</code>
<code>cdf_grid_2Dc_oc</code>	2D horiz. ocean climatology	<code>VAR(yearstep_oc,lat_t,lon_t)</code>
<code>cdf_grid_2Dc_atm</code>	2D horiz. atm. climatology	<code>VAR(yearstep_atm,lat_t,lon_t)</code>
<code>cdf_grid_2Dc_mon</code>	2D horiz. monthly climatology	<code>VAR(month,lat_t,lon_t)</code>
<code>cdf_grid_1Dy_t</code>	1D (lat) tracer	<code>VAR(time,lat_t)</code>
<code>cdf_grid_0D</code>	0D (scalar) value	<code>VAR(time)</code>
<code>cdf_grid_0Dc_atm</code>	0D (scalar) seasonal atm. value	<code>VAR(yearstep_atm)</code>

Table E.1: Currently available grid types (`cdf_grid_GRIDSUFFIX`) in the Bern3D NetCDF output module. Dimensions with the suffix `_t` refer to tracer grid coordinates (centers of grid cells), those with the suffix `_u` or `_w` refer to velocity grid coordinates (edges of grid cells). The `yearstep_oc` and `yearstep_atm` dimensions are the model timestep of the year for the ocean (`1-ndtyear`) and for the atmosphere (`1-atmndtyear`), respectively. `month` is the month of the year (1-12).

<i>Structure name^a</i>	<i>Dimensions</i>	<i>Output type</i>	<i>Used in^b</i>
<code>cdf_var_inst_3D</code>	<code>VAR(varid,i,j,k)</code>	Full, instantaneous	<code>diag3*()</code>
<code>cdf_var_inst_2Dh</code>	<code>VAR(varid,i,j)</code>	Full, instantaneous	<code>diag3*()</code>
<code>cdf_var_inst_2Dm</code>	<code>VAR(varid,j,k)</code>	Full, instantaneous	<code>diag3*()</code>
<code>cdf_var_inst_2Ds_oc</code>	<code>VAR(varid,i,j,m)</code>	Full, instantaneous	<code>diag3*()</code>
<code>cdf_var_inst_2Dc_oc</code>	<code>VAR(varid,i,j,m)</code>	Full, instantaneous	<code>*final()</code>
<code>cdf_var_inst_2Dc_atm</code>	<code>VAR(varid,i,j,m)</code>	Full, instantaneous	<code>*final()</code>
<code>cdf_var_inst_2Dc_mon</code>	<code>VAR(varid,i,j,m)</code>	Full, instantaneous	<code>*final()</code>
<code>cdf_var_inst_1D</code>	<code>VAR(varid,i/j/k)</code>	Full, instantaneous	<code>diag3*()</code>
<code>cdf_var_inst_0D</code>	<code>VAR(varid)</code>	Full, instantaneous	<code>diag3*()</code>
<code>cdf_var_inst_0Dc</code>	<code>VAR(varid,m)</code>	Full, instantaneous	<code>*final()</code>
<code>cdf_var_ave_3D</code>	<code>VAR(varid,i,j,k)</code>	Full, averaged	<code>diag99*()</code>
<code>cdf_var_ave_2Dh</code>	<code>VAR(varid,i,j)</code>	Full, averaged	<code>diag99*()</code>
<code>cdf_var_ave_2Dm</code>	<code>VAR(varid,j,k)</code>	Full, averaged	<code>diag99*()</code>
<code>cdf_var_ave_1D</code>	<code>VAR(varid,i/j/k)</code>	Full, averaged	<code>diag99*()</code>
<code>cdf_var_ave_0D</code>	<code>VAR(varid)</code>	Full, averaged	<code>diag99*()</code>
<code>cdf_var_tim_inst</code>	<code>VAR(varid)</code>	Time series, inst.	<code>diag2*()</code>
<code>cdf_var_tim_ave</code>	<code>VAR(varid)</code>	Time series, averaged	<code>diag6*()</code>

^aThe suffixes `2Dh` and `2Dm` refer to 2D horizontal and meridional grids, respectively.

^bTypically data is written to the data structure in this diagnostic routine.

Table E.2: Currently available data structures (`cdf_var_STORAGESUFFIX`) used in the diagnostics code to store data that will be written to NetCDF files by the NetCDF module later. `varid` is the variable ID defined in `netcdf_init()` (i.e. `cdf_vid_3D_tr(tr_VAR)` for standard tracers and `cdf_vid_SUFFIX_VAR` for all other variables).

`constant_name` must be the same name as in the variable definition above and `variable` is the variable actually containing the value.

Note that scalar constants should be written to the file as variables rather than global attributes, in order to make them available for calculations in analysis scripts and to provide the associated units.

E.3 Bern3D NetCDF input

NetCDF input is enabled when the `_netcdf` flag is set and the `_asciirestart` is NOT set. Only the file containing the full instantaneous output is required to restart the model (`RESTARTRUN_YYYYYYY_full_inst.nc`). If `_asciirestart` is set, input data will be read from ASCII files instead and NetCDF input is disabled. Note that the input method is independent of the `_ascii` flag which controls only the output and may be set in addition to `_netcdf` to enable ASCII and NetCDF output simultaneously.

NetCDF input is implemented into file `netcdf_input.F`. It contains the subroutines:

- `netcdf_input()`
- `netcdf_read_restart_year(runname,runnr,year)`
- `netcdf_read_3D(runname,runnr,varid,var)`
- `netcdf_read_2Dh(runname,runnr,varid,var)`
- `netcdf_read_0D(runname,runnr,varid,var)`
- `netcdf_read_2Dc_oc(runname,varid,var)`
- `netcdf_read_2Dc_atm(runname,varid,var)`
- `netcdf_read_0Dc_atm(runname,varid,var)`

The `netcdf_read_3D` reads in the 3D input data of variable `var`. Analogously, `netcdf_read_2Dh` and `netcdf_read_0D` read in horizontal 2D and scalar input data. The `netcdf_read_*Dc_oc/atm` routines are used to read in climatologies.

`varid` is the identity of the variable as defined in `netcdf_init()` (in file `netcdf_output.F`). `runname` and `runnr` are the name and timestep of the restart run and is read in from `RUNNAME____.main.parameter`. When `t00` in `RUNNAME____.main.parameter` is `-1`, `netcdf_read_restart_year(runname,runnr,year)` is called to read in the first year of the model run from the restart file.

Example: reading in the velocity-fields in `netcdf_input()`:

```

subroutine netcdf_input

[...]

c   read in the runname and input-step number of the restart run.

call getstring(lout//'_main.parameter','lin_name',lin_name)
print *, 'NETCDF_INPUT: input filename (a18): ', lin_name
call getint(lout//'_main.parameter','lin_nr',lin_nr)
print *, 'NETCDF_INPUT: input number (i3): ', lin_nr

```

```
!--- (i) Physical variables

[...]

c  velocities
   call netcdf_read_3D(lin_name,lin_nr,cdf_vid_3D_u
$      ,u1(1,0:imax,1:jmax,1:kmax))
   call netcdf_read_3D(lin_name,lin_nr,cdf_vid_3D_v
$      ,u1(2,1:imax,0:jmax,1:kmax))

[...]

return
end
```

Thanks

I would like to thank Fortunat Joos, Thomas Stocker, Thomas Frölicher, Gian-Kasper Plattner, Kuno Strassmann, Scott Doney, Christoph Heinze, Stefan Ritz, Renato Spahni, Anil Bozbiyik, Markus Gerber, Payal Parekh, Tobias Tschumi, Raphael Roth, Beni Stocker, Adrian Schilt, Doris Rätz, Kay Bieri, my colleagues at KUP, my parents, Dominique Rothen, and my friends. Merci!

Publications

- Bozbiyik, A., Steinacher, M., Joos, F., Stocker, T. F., & Menviel, L., 2011. Fingerprints of changes in the terrestrial carbon cycle in response to large reorganizations in ocean circulation, *Clim. Past*, 7(1), 319–338.
- Frölicher, T. L., Joos, F., Plattner, G.-K., Steinacher, M., & Doney, S. C., 2009. Natural variability and anthropogenic trends in oceanic oxygen in a coupled carbon cycle-climate model ensemble, *Global Biogeochem. Cy.*, 23(GB1003), 1–15.
- Gattuso, J.-P., Hansson, L., & the EPOCA Consortium, 2009. European Project on Ocean Acidification (EPOCA): objectives, products and scientific highlights, *Oceanography*, 22(4), 190–201.
- Joos, F., Frölicher, T. L., Steinacher, M., & Plattner, G.-K., 2011. *Ocean Acidification*, chap. 14: Impact of climate change mitigation on ocean acidification projections, pp. 319–338, Oxford University Press, New York, USA.
- Steinacher, M., Frölicher, T. L., & Joos, F., 2009a. Imminent and irreversible ocean acidification, *SOLAS news*, (9), 6–7.
- Steinacher, M., Joos, F., Frölicher, T. L., Plattner, G.-K., & Doney, S. C., 2009b. Imminent ocean acidification in the Arctic projected with the NCAR global coupled carbon cycle-climate model, *Biogeosciences*, 6(4), 515–533.
- Steinacher, M., Joos, F., Frölicher, T. L., Bopp, L., Cadule, P., Cocco, V., Doney, S. C., Gehlen, M., Lindsay, K., Moore, J. K., Schneider, B., & Segschneider, J., 2010. Projected 21st century decrease in marine productivity: a multi-model analysis, *Biogeosciences*, 7(3), 979–1005.

Erklärung

gemäss Art. 28 Abs. 2 RSL 05

Name/Vorname: Marco Steinacher

Matrikelnummer: 99-915-456

Studiengang: Physik

Bachelor Master Dissertation

Titel der Arbeit: Modeling changes in the global carbon cycle-climate system

Leiter der Arbeit: Prof. Dr. Fortunat Joos

Ich erkläre hiermit, dass ich diese Arbeit selbständig verfasst und keine anderen als die angegebenen Quellen benutzt habe. Alle Stellen, die wörtlich oder sinngemäss aus Quellen entnommen wurden, habe ich als solche gekennzeichnet. Mir ist bekannt, dass andernfalls der Senat gemäss Artikel 36 Absatz 1 Buchstabe o des Gesetzes vom 5. September 1996 über die Universität zum Entzug des auf Grund dieser Arbeit verliehenen Titels berechtigt ist.

Bern, 29. November 2011

Curriculum vitæ

Personal Data

Name	Marco Steinacher
Date of birth	November 18, 1979
Place of origin	Basel (BS) and Frutigen (BE)

Education

1986–1992	Primary School, Basadingen, Switzerland
1992–1994	Secondary School, Diessenhofen, Switzerland
1994–1999	Matura Type C at Kantonsschule Schaffhausen, Switzerland
1999–2001	Studies in Computer Science at ETH Zürich, Switzerland
2002–2007	Studies in Physics at the University of Bern, Switzerland (subsidiary subjects: Mathematics and Astronomy)
2006–2007	Master thesis in Physics at the division of Climate and Environmental Physics, Physics Institute, University of Bern, Switzerland (Thesis advisor: Prof. Dr. Fortunat Joos)
2008–2011	Ph.D. thesis at the division of Climate and Environmental Physics, Physics Institute, University of Bern, Switzerland (Thesis advisor: Prof. Dr. Fortunat Joos)

Conferences and Workshops

- 2006 Swiss National Supercomputing Centre (CSCS) User Day, Manno, Switzerland.
- 2006 Parallel Programming Workshop at Swiss National Supercomputing Centre (CSCS), Manno, Switzerland
- 2008 ASLO/AGU 2008 Ocean Sciences Meeting, Orlando, Florida, USA. Talk: “Ocean Acidification in the Arctic over the 21st Century”
- 2008 EPOCA Kickoff Meeting, Nice, France
- 2009 EPOCA First Annual Meeting, Plymouth, UK. Talk: “Imminent ocean acidification in the Arctic projected with the NCAR carbon cycle-climate model”
- 2009 Seminar of Environmental Physics Group, ETH Zürich. Talk: “Imminent and irreversible ocean acidification in the Arctic projected with the NCAR model”
- 2011 ILAMB Workshop, Irvine, California, USA
- 2011 Oeschger Centre WP1/WP2 Meeting, Bern, Switzerland. Talk: “Climate-carbon cycle projections with the Bern3D-LPX model”